Electron Transfer through U-Shaped Donor-Bridge-Acceptor Molecules and Fluorescence Quenching of Conjugated Polyelectrolyte

by

Min Liu

BS, East China University of Science and Technology, P. R. China, 1998

MS, East China University of Science and Technology, P. R. China, 2001

Submitted to the Graduate Faculty of

Arts and Sciences in partial fulfillment

of the requirements for the degree of

Doctor of Philosophy

University of Pittsburgh

2005

UNIVERSITY OF PITTSBURGH

FACULTY OF ARTS AND SCIENCES

This dissertation was presented

by

Min Liu

It was defended on

September 23th, 2005

and approved by

Prof. Kenneth D. Jordan

Prof. Stephane Petoud

Prof. Gilbert C. Walker

Prof. David H. Waldeck
Dissertation Director

Electron Transfer through U-Shaped Donor-Bridge-Acceptor Molecules and Fluorescence Quenching of Conjugated Polyelectrolyte

Min Liu, PhD

University of Pittsburgh, 2005

Abstract

Electron transfer reactions constitute a fundamental chemical process and are of intrinsic importance in biology, chemistry, and the emerging field of nanotechnology. Electron transfer reactions proceed generally in a few limiting regimes: nonadiabatic electron transfer, adiabatic electron transfer and solvent controlled electron transfer. Behavior between some of these regimes was examined by varying the solvents in which the reaction occurs *i.e.*, the different polarization relaxation. In a "fast" solvent, such as acetonitrile, the electron transfer occurs in the nonadiabatic regime over a broad temperature range; in a "slow" solvent, such as N-methylacetamide (NMA) and N-methylpropionamide (NMP), the electron transfer reaction occurs in the nonadiabatic regime of high temperature but occurs in the solvent controlled regime as the temperature decreases. The semiclassical model was compared to the electron transfer rate data in the nonadiabatic regime and the Zusman model was compared to the rate constant in solvent controlled regime. Experimental data was discussed and compared to a theoretical interpretation between the regimes, − how the electron transfer mechanism converts from a nonadiabatic mechanism to a solvent controlled mechanism.

The fluorescence emission of conjugated polyelectrolytes is highly sensitive to their binding with other macromolecules, protein and dendrimers. A detailed investigation on the polyelectrolyte fluorescence intensity changes and the fluorescence quenching mechanism were

explored. These studies confirm that the quenching mechanism is controlled by the electrostatic binding between the macromolecular analytes and the changes in the electronic characteristics of the polyelectrolyte. Three possible electrostatic mechanisms for the polyelectrolyte were explored: electron transfer, energy transfer, and internal conversion. In many cases, the conformational changes of the polyelectrolyte control the internal conversion, hence the fluorescence yield, when binding to other macromolecules, a qualitatively different mechanism from that found for small molecular analytes.

TABLE OF CONTENTS

LIST OF TABLES

LIST OF FIGURES

DEDICATION

This thesis is dedicated to my family for their unconditional support through all these trying years.

Acknowledgements

I would like to acknowledge those many people who have been of tremendous help during these years. First and foremost, I would like to give my deepest gratitude to my advisor, Dr. David. H. Waldeck, whose knowledge, guidance, encouragement and trust always kept me motivated and focused throughout my graduate work, and there are even no appropriate words which can adequately convey my sincerest appreciation to him. I am forever indebted to him for so many reasons: including his constant guidance leads me through my graduate study; his integrity and carefulness toward research shape me as a scientist; his knowledge and vision inspire me to explore science intrepidly. More importantly, Dave's invaluable assistances motivate me to learn the value of independent work and critical analysis, values that not only helped make me a better scientist but also a better person overall. He is not only a research mentor to me, but more like a friend with sense of humor that makes hard work into a delightful experience. Without him, my graduate years would be much more difficult and unimaginable.

I have been very lucky to share the Waldeck group experiences with many wonderful people over the years. My pal Palwinder Kaur, a talented and assiduous graduate student, has been working with me on the study of the fluorescence quenching of polyelectrolyte for two years. We overcame various problems and finally revealed the nature of the quenching mechanism. Subhasis Chakrabarts worked with me on the bulky pendant U-shaped molecules last year. I still remember we celebrated Christmas Eve in the lab with TCSPC. I also want to give many thanks to our former postdoc Dr. Haiying Liu, who synthesized those marvelous polyelectrolytes and made our study of polyelectrolytes possible. I can not forget my young pal, Neil Young, a smart young Scotsman, who was an undergraduate student in our lab when I first joined in the year of 2002. He is my first western friend and we worked together on TCSPC with

many wonderful happy memories. Of my other co-workers, I would like to thank two former graduate students, Hiro and Jianjun for their many helps, and other current group members, Hongjun, Amit, Lei, Li and Dan for sharing many experiences. A working environment with these brilliant young scientists is the only reason to keep our lab growing, developing and succeeding and my time in the graduate school can never be colorful without them.

I also want to give my great appreciation to Dr. Michael Paddon-Row and his group in Australia for the synthesis of those truly amazing U-shaped molecules which were the prerequisite of our electron transfer studies. More importantly, Dr. Paddon-Row's encouragement and affirmation of my work further stimulated my interest in investigating and understanding the nature of the electron transfer mechanism of these molecules.

My solvation Stokes-Shift adventures at the Pennsylvania State University in Professor Mark Maroncelli's lab will be forever imprinted in my mind. It was only with the kind assistance and great patience of Dr. Naoki Ito and Dr. Maroncelli that our experiment made rapid progress in short time. Especially, I also want to thank Dr. Maroncelli for his insightful discussion and prompt responses during our paper drafting process.

Dr. Matthew Zimmt and his talented student Dr. Jorcelyn Nadeau at Brown University also brought many bright sparks in the first year of my graduate work. It was unforgettable to work so hard with Jocelyn in those days and nights, which turned out to be my first experience of how tough it is to be a graduate student. I want to thank Dr. Andrew Napper who gave me many precious advices on how to adjust the laser and measure the fluorescence decays when I started my lab work during his short stay in the group. I also want to thank Dr. Richard Butera, who gave me many valuable suggestions when I built the cryostat, which is an indispensable device in my low temperature experiment.

I also want to express my appreciation to the glass shop blower, Bob, who did me great favors to make and revise sample cell promptly; to the machine shop staff - Dennis, Jeff and Tom - who not only helped me build the high vacuum system, but also patiently and kindly taught me operation and trouble-shooting; to the electronic shop personnel Jim and Chuck who helped me set up the wiring of the vacuum system and repair the power supply of our laser system.

Finally, I would never have made this so far without the unconditional support and love from my family. Whenever I was in deep frustration, their strong love and trust always kept me strong enough to continue with my work, and allowed me to bravely face all difficulties. I miss you so much!

Chapter 1 Introduction

1.1 Brief Retrospective

Electron transfer reactions are one of the most elementary reactions in the field of chemistry. From photosynthesis in plants and nitrogen fixing in microorganisms to metabolic pathways in human beings, electron transfer reactions are essential, directly or indirectly, to all life on Earth. Since the late 1940s, the understanding of electron transfer processes has grown dramatically. In 1952, Willard Libby described the significance of nuclear reorganization in electron transfer[1], and Marcus applied this principle in his formulation of electron transfer theory.[2] It was Marcus' genius work, beginning from 1956, that built the foundation for much of what has been learned in the intervening decades about electron transfer. In recent years, more advances in electron transfer research have taken place because of novel molecular design and synthesis. With the goal of disentangling the forces behind the electron transfer, small, simple molecules have been synthesized in order to impose some constraints on the systems and allow the experimental queries to be focused. Closs and Miller's pioneering work studied through bond effects in intermolecular electron transfer.[3,4] Other scientists, including Wasielewski, Michel-Beyerle and Paddon-Row, have furthered our understanding of intramolecular electron transfer with their clever molecular designs.[5-12]

1.2 Electron Transfer Theory

Electron transfer can be understood as the movement of an electron from a donor molecule to an acceptor molecule, at its most basic level, in the self exchange reaction shown in equation 1.

$$M^n + M^{n+1} \Leftrightarrow M^{n+1} + M^n \quad \textbf{1}$$

Here, the reactants (and products) can be two metal ions that only differ by their oxidation states, *e.g.*, Fe^{2+} and Fe^{3+}. But the process of electron transfer is often far more complex than the example given above and requires an accurately measured approach and an extrapolation for the electron transfer rate.

Marcus' classical theory and more modern semiclassical theories begin with Fermi's Golden Rule expression for the transition rate.

$$k = (2\pi / \hbar)|V|^2 FCWDS \quad \textbf{2}$$

where $\hbar$ is Planck's constant divided by 2π, $|V|$ is the electronic coupling matrix element, and *FCWDS* is the Franck-Condon weighted density of states.[13-15]

Figure 1.1 shows the Marcus curves, an icon of electron transfer theory. Two parabolic curves represent the potential energy of the reactant and the product. λ represents the energy required to reorganize the reactant into the equilibrium geometry of the product without undergoing an electron transfer, and $\Delta_r G$ represents the difference in free energies between the reactant and the product. The activation energy $\Delta G^{\ddagger}$ is the energy difference between the equilibrium position of the reactant curve and the crossing point.

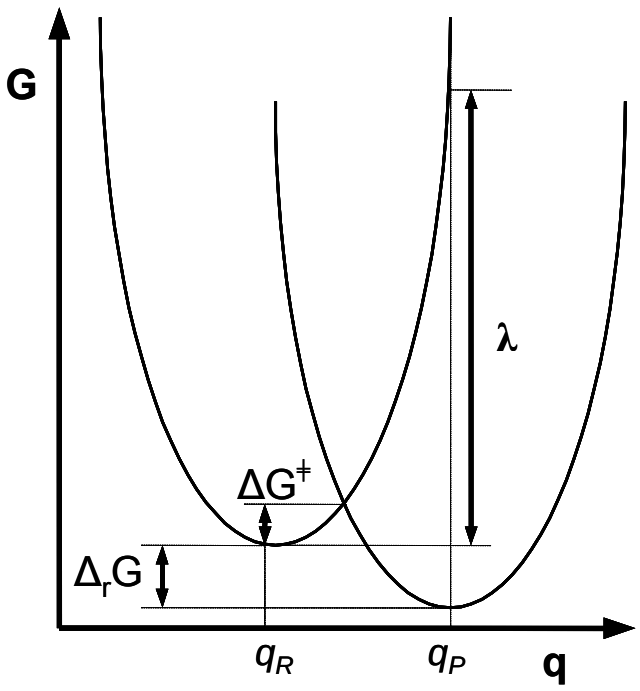

Figure 1.1 Marcus free energy curves for reactant and product states of an electron transfer reaction.

The two limiting electron transfer mechanisms are called nonadiabatic and adiabatic electron transfer reactions. Nonadiabatic electron transfer reactions are described by Fermi's Golden Rule, equation 2. In this case the rate constant is proportional to the electronic coupling $|V|^2$, where the electronic coupling $|V|$ is the interaction between the reactant and the product states at the curve crossing (dashed curve in Figure 1.2). In this case, the rate constant increases with stronger electronic coupling, which represents better overlap of the reactant and the product electronic wave functions. Nonadiabatic electron transfer reactions, *e.g.*, long-distance photoinduced electron transfer reactions where the electron donor and the electron acceptor interact very weakly, have small $|V|$, typically $|V| << k_BT$. When the electronic coupling becomes large enough, the electron transfer reaction occurs along a single electronic state (black

curves in Figure 1.2). Adiabatic electron transfer reactions are characterized by large $|V|$, where $|V| >> k_BT$ (200 cm^{-1}).[4]

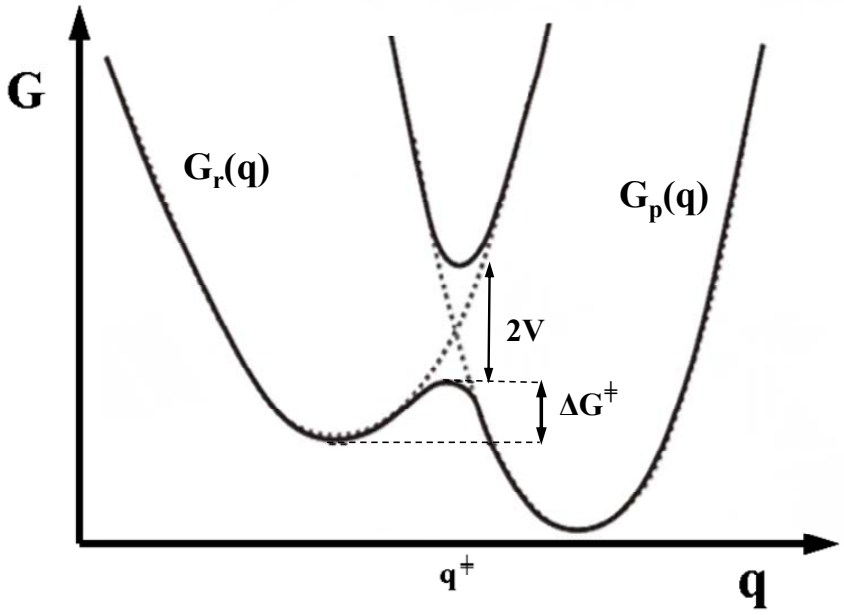

Figure 1.2 Diagram illustrating the two pictures (adiabatic and nonadiabatic) for the electron transfer.

A single one dimensional reaction coordinate illustrates how the electron transfer mechanism differs in these two regimes. In the adiabatic regime (black curve), the electron transfer happens by moving along the lowest energy curve through the transition region and the system's electronic state adiabatically follows the nuclear displacement. In this case the reaction rate is controlled by the activation barriers and dynamics of the nuclear motions. In the nonadiabatic reactions (dashed curves), the electron moves through the transition state region many times (on average) before the electron jumps from the reactant curve to the product curve. In this case the rate constant is controlled by the tunneling probability at the transition state and the Franck-Condon factors.

Jortner's semi-classical expression[16] adequately describes the reaction kinetics of nonadiabatic electron transfer reactions in most situations. He gives the rate constant expression described in equation 3.

$$k_{ET} = \sqrt{\frac{2\pi^3}{\lambda_0 kT}} \cdot |V|^2 \cdot \sum_j e^{-S} \frac{S^j}{j!} \cdot \exp\left(- \frac{(\lambda_0 + \Delta_r G \ + jh\nu)^2}{4\lambda_0 kT} \right) \qquad \mathbf{3}$$

where $S = \frac{\lambda_v}{h\nu}$. This equation is an expanded form of Fermi's Golden rule, where *FCWDS* is defined in terms of four parameters, λ_0, λ_v, $h\nu$, and $\Delta_r G$. This equation takes into account the energy required for high-frequency vibrational reorganization λ_v, when an electron is transferred from an electron donor to an electron acceptor. It also accounts for the low-frequency solvent reorganization energy, λ_0. The $h\nu$ term refers to the average energy spacing of a single effective quantized mode frequency associated with the electron transfer event, which is taken to be a characteristic feature of the solute. The sum is performed over all of the vibrational states in the product based on a single, effective, high-frequency mode model.

The semiclassical theory assumes that the lower frequency modes, which are mostly solvent based, have a low enough energy relative to the thermal bath that they can be treated classically, whereas the higher frequency modes, which arise from intramolecular vibrations, must be treated quantum mechanically, see Figure 1.3.

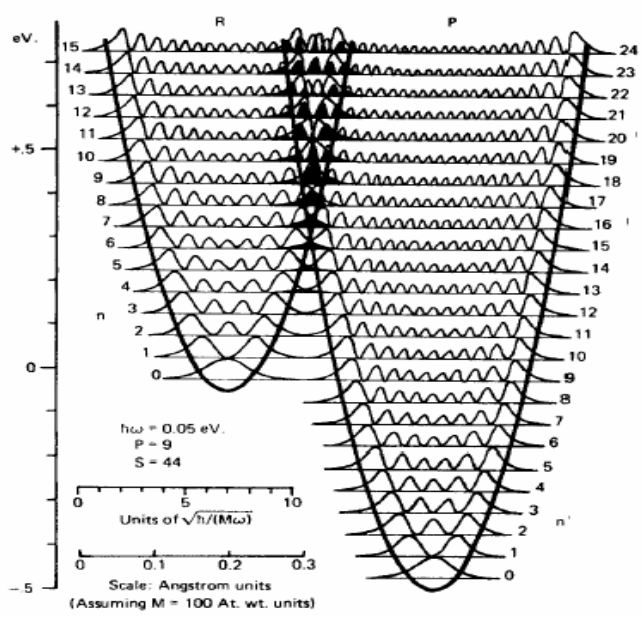

Figure 1.3 Quantum description of the intersection between the reactant and the product vibrational levels. Optimal overlap is achieved between the reactant ν = 0 and the product ν' = 9 product state. This figure is taken from reference DeVault, D. Quart. Rev. Biophys. 1980, 13, 387.

The following sections describe the essentials of three important parameters, reorganization energy, reaction free energy and electronic coupling, in detail. These parameters are used in the semiclassical expression and play a prominent role in modern views of electron transfer reactions.

1.3 Reorganization Energy and Reaction Free Energy

The reorganization energy, λ, is usually divided into two contributions:

$$\lambda = \lambda_0 + \lambda_v \qquad \textbf{4}$$

The solvent-independent inner reorganization energy λ_v arises from structural differences between the equilibrium configurations of the reactant and product states. Because λ_v is related to

the geometry changes of the donor and acceptor groups upon electron transfer, it depends only weakly on the solvation environment around the reactant and product. For example, a value of 0.63 eV was used for λ_v in all the solvents. Also important for understanding the inner reorganization energy is the characteristic frequency *hv,* which is taken to be 1600 cm^{-1} for all of the U-shaped DBA molecules in this study. These parameter values are based on the fitting of molecular charge-transfer absorption and emission spectra, using a single, effective, high-frequency vibrational mode for an electron-transfer reaction. [17]

The outer-sphere reorganization energy λ_0, which is also called the solvent reorganization energy, arises from differences between the orientation and polarization of solvent molecules around the reactant and product states. The solvent reorganization energy and the reaction free energy are determined by solvation characteristics; *i.e.*, solute-solvent interaction energies. We have used two different models to treat the solute-solvent interactions: a dielectric continuum model and a molecular solvation model.

The dielectric continuum model calculates solvation energies using the static dielectric constant ε_s and a high frequency dielectric constant ε_∞.[18-21] The solute is treated as a spherical (or ellipsoidal) cavity containing a point charge. For intramolecular electron-transfer reactions, the dielectric continuum model treats the solute as a cavity containing a dipole moment.

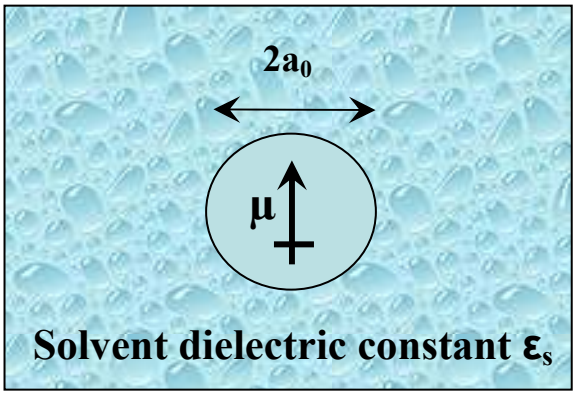

Figure 1.4 The continuum model used to treat intramolecular system

The solvent reorganization energy is described as:

$$\lambda_0 = \frac{(\Delta\mu)^2}{a_o^3}\left(\frac{\varepsilon_s - 1}{2\varepsilon_s + 1} - \frac{\varepsilon_\infty - 1}{2\varepsilon_\infty + 1}\right) \quad \textbf{5}$$

and the reaction free energy from this model is

$$\Delta_r G = \Delta_{vac} G - \frac{\left(\mu_{CS}^2 - \mu_{LE}^2\right)}{a_o^3}\left(\frac{\varepsilon_s - 1}{2\varepsilon_s + 1}\right) \quad \textbf{6}$$

where μ_{LE} is the dipole moment of the initially excited state, μ_{CS} is the dipole moment of the charge-separated state, and a_o is the cavity radius. $\Delta\mu$ is the magnitude of the dipole moment difference vector for the locally excited and the charge separated states; *i.e.* $\Delta\mu \equiv \left|\vec{\mu}_{CS} - \vec{\mu}_{LE}\right|$. $\Delta_{vac} G$ is the reaction Gibbs free energy in the absence of solvation.

Matyushov developed a molecular solvation model, which accounts for the discrete nature of the solute and the solvent and incorporates electrostatic, induction and dispersion interactions between the molecules in the solution, as modeled in Figure 1.5[22]. The solute is considered as a sphere with a point dipole moment μ and polarizability α_0. The solvent is modeled as a polarizable sphere, with an electrostatic charge distribution and includes both a point dipole and a point quadrupole.

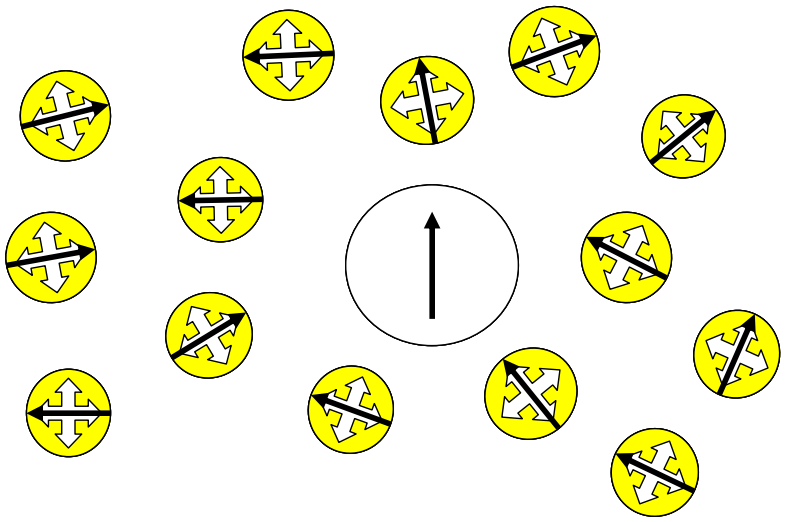

Figure 1.5 The multiple interactions between solvent and solute molecules

In the molecular model, the reaction free energy $\Delta_r G$ is written as a sum of four terms:

$$\Delta_r G = \Delta_{vac} G + \Delta_{dq,i} G^{(1)} + \Delta_{disp} G + \Delta_i G^{(2)} \qquad \textbf{7}$$

where $\Delta_{vac} G$ is the vacuum free energy, $\Delta_{dq,i} G^{(1)}$ contains the first order electrostatic and induction contributions, $\Delta_{disp} G$ contains dispersion terms, and $\Delta_i G^{(2)}$ contains the second order induction terms. The value of $\Delta_{vac} G$ is adjustable. $\Delta_{dq,i} G^{(1)}$ and $\Delta_i G^{(2)}$ make the dominant contributions to the reaction free energy, whereas $\Delta_{disp} G$ is small enough to be ignored. The outer-sphere reorganization energy λ_0 is also written as a sum of three contributions:

$$\lambda_0 = \lambda_p + \lambda_{ind} + \lambda_{disp} \qquad \textbf{8}$$

where λ_p includes contributions from the solvent dipole and quadrupole moments, λ_{ind} includes contributions from the induction forces, and λ_{disp} includes contributions from the dispersion forces. The parameters given above are all temperature dependent except $\Delta_{vac} G$.

The solute molecule's characteristics are highly idealized in the dielectric continuum model. Its electrostatic potential is treated as a point dipole; its polarizability is ignored; and the details of its shape are lost. The molecular model is more appropriate than the continuum model because it includes not only the dipole-dipole interactions, but also the dipole-quadrupole interactions, quadrupole-quadrupole interactions, induction and dispersion interactions among the solute with the solvent molecules and the solvent molecules themselves. The molecular model is especially appropriate to accurately describe the temperature dependence of the reorganization energy and the reaction free energy, and the electron transfer reactions in weakly polar or nonpolar solvents.

1.4 Electronic Coupling

The semi-classical electron transfer rate constant is proportional to the electronic coupling, $|V|^2$, which depends on the overlap of the electron donor and the electron acceptor wavefunctions. For intramolecular electron transfer, the electronic coupling is commonly found to be solvent and temperature independent. Several ways are known in which an electron donor and an electron acceptor can transfer or exchange an electron, including through bonds (σ and π)[23-26], through solvent molecules[12,27-32], and through non-bonded static contacts with organic moieties suspended between electron donor and electron acceptor[17,33].

As for the electronic coupling through non-bonded static contacts in U-shaped DBA molecules, whose existence has been proved by comparing with another reference compound with the same donor and acceptor groups but the electronic coupling through bonded contacts, it is found that the electronic coupling is strongly dependent on the structure of the pendant units, not only the electron donor or acceptor groups. A detail comparison which varies the pendant

units to explore the effect on the electronic coupling has been investigated in this thesis. The electronic coupling values can be obtained by fitting the electron transfer rate data to the semiclassical model. The experiment data demonstrate that the more efficient electron tunneling through the aromatic pendant moiety provides a higher electronic coupling than the alkyl pendant, although they have the same electron donor and acceptor groups.

1.5 Dynamic solvent effects

A solvent molecule can influence a chemical reaction in a number of ways. [34] Basically, it can change the energies of the reactant and product statically; it also can enter into the reaction proceedings in a more dynamic way by exchanging energy and momentum with reacting species. Dynamic solvent effects are mainly associated with the dielectric friction in polar solvents. For electron transfer reactions, static interactions are usually the most important, but dynamic aspects of polar interactions also play an important role in determining reaction rates.

The molecular mechanism of dynamic solvation can be viewed as the reorientation of dipolar solvent molecules in response to the changing charge distribution of a solute. The more polar is the solvent, the stronger is the coupling between the molecules; however the speed of the solvation response depends on features of the intermolecular solvent interactions. Zusman[35] first considered this effect, which has since been studied by several groups.[36-41]

The solvation response function of S(t) reflects the motions required to produce the final equilibrated environment from the unpolarized solvent surroundings of the neutral solute.

$$S(t) = \frac{F(t) - F(\infty)}{F(0) - F(\infty)} \qquad \textbf{9}$$

A number of groups have[42-46] used "simple continuum" models to study solvation. These models treat the solute as a point dipole in a spherical cavity and it is immersed in a continuum solvent which is treated as a continuum, frequency-dependent dielectric. Simple continuum models predict that the solvent has an exponential solvation response function, given by

$$S(t) = \exp(-t/\tau_L) \qquad \textbf{10}$$

The dynamic solvation time is equal to the longitudinal relaxation time (τ_L) of the solvent:

$$\tau_L = \tau_D \frac{\varepsilon_\infty}{\varepsilon_0} \qquad \textbf{11}$$

where ε_0 is the static dielectric constant, ε_∞ is the high-frequency dielectric constant, τ_D is the dielectric (or Debye) relaxation time.

Although predictions based on the continuum dielectric model provide a reasonably good measure of the solvation timescale near room temperature, the single exponential solvation response function is not accurate for describing the solvation dynamics. For example, in many solvents, the relaxation of the solvation energy takes place on two widely separated time scales: a fast relaxation within 0.1 ps range and another slower solvation component in the 1 – 10 ps range or even hundreds of picoseconds for more viscous solvents, to fully relax the solvation energy. At low temperatures or solvents with long lived structure, one finds the very slow processes contributing to the solvation response. Since the more general solvation response is not exponential, the correlation time of the solvation response function, defined as,

$$\langle \tau \rangle = \int_0^\infty S(t)dt \qquad \textbf{12}$$

is used as a measure of the solvation time. Incorporation of molecular aspects of the solute and the solvent interaction substantially modifies continuum predictions. By way of example, Onsager[47] pointed out that only at distances far from the solute is, the continuum dielectric limit

of the longitudinal relaxation time τ_L achieved, because of the slow variation of the electronic field. However, at distance near to the solute, it is more possible to have a slower solvation time and the response function is non-exponential even in Debye solvents. Thus, the molecular solvation predicts a greater value of $<\tau>$ than τ_L.

In intramolecular electron transfer reactions, when the electron tunneling rate is much faster than the reorientation time of the solvent, the electron transfer reaction is limited by the solvent response and the reactant must gain enough energy for successful electron tunneling. In this case, the electron transfer rate is limited by the relaxation rate of the solvent and the reaction is solvent-controlled. In contrast, when the solvent reorientation rate is much faster than the electron transfer rate, the relaxation time of solvent does not effect the electron transfer and it occurs in the nonadiabatic limit, as described by equation 2.

1.6 Fluorescence quenching of polyelectrolyte

The fluorescence of conjugated polyelectrolytes is highly sensitive to the binding of biological or chemical molecules and such materials provide great promise as water soluble fluorescent materials[48] and sensors.[49,50,51] A number of groups are active in using conjugated polymer probes as fluorescence probes, mainly polyphenylvinylene (PPV), polyphenylethynylene (PPE), polyphenylene, and polythiophene. The development of this field has been reviewed recently.[49] The binding of a polyelectrolyte with another molecule can quench the fluorescence of the polyelectrolyte. Three most likely mechanisms dominate this process: electron transfer, energy transfer, and enhancement of the polymer's self-quenching by changing the conformation itself.

As for the electron transfer and energy transfer, the fluorescence quenching originates from the rapid electron or energy transport through the conjugated chain (typically modeled by exciton transport[52,53]) to a trap-site, where an initially created excitation can efficiently and rapidly interact with the trap-site and achieve the fluorescence quenching. The interaction can arise from noncovalent binding, or physical association so that analyte species can quench the excitation by electron transfer or energy transfer. Electron transfer quenching can be controlled by varying the analyte's redox characteristics; energy transfer quenching depends strongly on the polyelectrolyte and the analyte's spectral characteristics, corresponding to a Förster mechanism or a Dexter mechanism.[54] Conformational change in the polyelectrolyte chain, which enhances its intrinsic nonradiative rate constant,[55] can also greatly quench the fluorescence and acts as a third possibility. In this case the quenching would mainly depend on the conformational features of the polyelectrolyte, instead of the redox and spectral properties of the analyte. However, the real situation is more complicated since these mechanisms can exist simultaneously.

This study investigated the fluorescence quenching by studying the binding with macromolecules, such as proteins and dendrimers, to explore the intrinsic quenching mechanism of polyphenylene polyelectrolyte.

1.7 Summary

The work described in this thesis examines electron transfer mechanisms in three different donor-bridge-acceptor systems in detail. Firstly, chapters 2 and 3 illustrate how the electron transfer mechanism converts from a nonadiabatic mechanism at high temperature to a solvent controlled mechanism as the temperature decreases for DBA molecules (Figure 1.6) in slow relaxation solvent – NMA and NMP. The experimental data was compared to the

theoretical interpretations and a detailed discussion revealed the dynamic solvent effect on controlling the electron transfer pathway and varying the electron transfer mechanism.

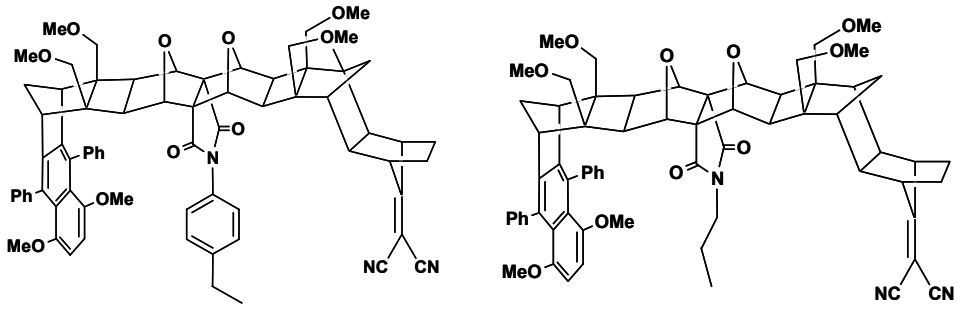

Figure 1.6 Donor-Bridge-Acceptor molecules studied in chapters 2 and 3.

Secondly, chapter 4 explores another system of U-shaped DBA molecules (see Figure 1.7), which provide access to understand how the electronic coupling mediated by the pendant group influences the electron transfer rate. The pendant group lies in direct line of sight in between electron donor and acceptor groups. Variations in solvent choice leads to variations in reaction free energies and solvent reorganization parameters, but little change in the degree of electronic coupling was observed in these different molecules.

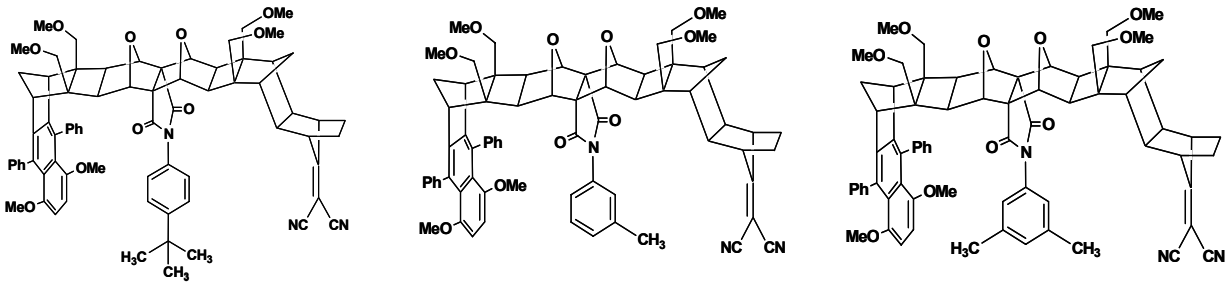

Figure 1.7 Donor-Bridge-Acceptor molecules studied in chapter 4.

Thirdly, chapter 5 studies another type of the electron transfer − hole transfer in the molecule with a 2'-pyrenyl acceptor and a 4'-*N*,*N*-dimethylanilinyl donor. The orientations of the donor and acceptor units, relative to the spacer, are not rigidly constrained, and their torsional motions decreases solvent access to the cleft. Calculations show that rotation of the pyrene group about the bond connecting it to the spacer greatly modulates the magnitude of through-space coupling between the S_1 and CT states. The relationship between the torsional dynamics and the electron-transfer dynamics is discussed.

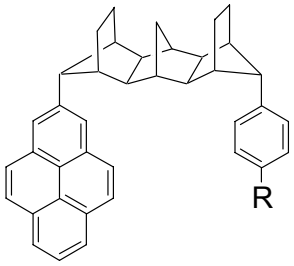

1. R = NMe_2
2. R = H

Figure 1.8 Molecule structure studied in chapter 5.

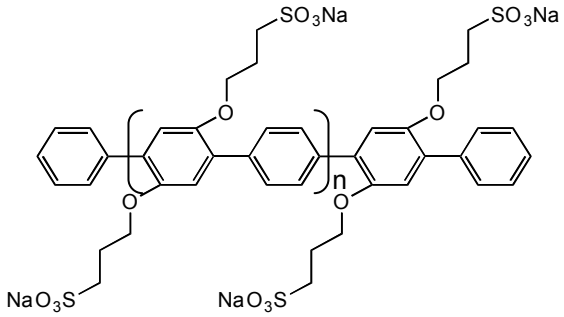

PP1

Figure 1.9 Polyelectrolyte **PP1** studied in chapters 6 and 7.

Lastly, chapter 6 investigates the fluorescence quenching mechanism of the polyelectrolyte **PP1** (Figure 1.9) by the study of the fluorescence emission of **PP1** as a function of the analyte concentrations. A comparison of the different analytes confirms that the quenching mechanism is dominated by the electrostatic binding between the macromolecular analytes and the polyelectrolyte. Chapter 7 further explores how the conformation of **PP1** varies with the variation of the environment by adding several different salt electrolytes as a function of the ionic strength. The comparison of the spectroscopic behaviors of **PP1** in different salt solutions demonstrates an extended and swollen conformation upon increasing the ionic strength.

1.8 References

1. Libby, W. F. J. Phys. Chem., 1952, 56, 863.

2. Marcus, R. A. *J. Chem. Phys.*, **1954**, *24*, 966.

3. Liang, N.; Miller, J. R.; Closs, G. *J. Am. Chem. Soc.*, **1989**, *111*, 8740.

4. Closs, G. L.; Miller, J. R. *Science*, **1988**, *240*, 440.

5. Wasielewski, M. R. *Chem. Rev.*, **1992**, *92*, 435.

6. Lewis, F. D.; Wu, T.; Liu, X.; Letsinger, R. L.; Greenfield, S. R.; Miller, S. E.; Wasielewski, M. R. *J. Am. Chem. Soc.*, **2000**, *122*, 2889.

7. Khundkar, L. F.; perry, J. W.; Hanson, J. E.; Dervoan, P. B. *J. Am. Chem. Soc.*, **1994**, *116*, 9700.

8. Heitele, H.; Michel-Beyerie, M. e. *J. Am. Chem. Soc.*, **1985**, *107*, 8068.

9. Pollinger, F.; Heitele, H.; Michel-Beyerle, M. E. *Chem. Phys. Lett.*, **1993**, *209*, 251.

10. Hush, N. S.; Paddon-Row, M. N.; Cotsaris, E.; Oevering, H.; Verhoeven, J. W.; Heppener, M. *Chem. Phys. Lett.*, **1985**, *117*, 8.

11. Paddon-Row, M. N. *Acc. Chem. Res.*, **1994**, *27*, 18.

12. Lokan, N. R.; Paddon-Row, M. N.; Koeberg, M.; Verhoeven, J. W. *J. Am. Chem. Soc.*, **2000**, *122*, 5075.

13. Levich, V. G. *Adv. Electrochem. Electornchem Engl.*, **1966**, *4*, 249.

14. Zener, C. *Proc. R. Lond. A.*, **1932**, *137*, 696.

15. Landau, L. *Phys. Z. Sowj. U.*, **1932**, *1*, 88.

16. Jortner, J. *J. Chem. Phys.*, **1976**, *64*, 4860.

17. Napper, A. M.; Head, N. J.; Oliver, A. M.; Shephard, M. J.; Paddon-Row, M. N.; Read, I.; Waldeck, D. H. *J. Am. Chem. Soc.*, **2002**, *124*, 10171.

18. Newton, M. D.; Basilevsky, M. V.; Rostov, I. V. *Chem. Phys.*, **1998**, *232*, 201.

19. Sharp, K.; Honig, B. *Annu. Rev. Biophys. Biophys. Chem.*, **1990**, *19*, 301.

20. Sitkoff, D.; Sharp, K. A.; Honig, B. *J. Phys. Chem.*, **1994**, *98*, 1978.

21. Brunschwig, B. S.; Ehrenson, S.; Sutin, N. *J. Phys. Chem.*, **1986**, *90*, 3657.

22. Matyushov, D. V.; Voth, G. A. *J. Chem. Phys.*, **1999**, *111*, 3630.

23. Paddon-Row, M. N.; Shephard, M. J. *J. Am. Chem. Soc.*, **1997**, *119*, 5355.

24. Penfield, K. W.; Miller, J. R.; Paddon-Row, M. N.; Cotasaris, E.; Oliver, A. M.; Hush, N. S. *J. Am. Chem. Soc.*, **1987**, *109*, 5061.

25. Paddon-Row, M. N.; Oliver, A. M.; Warman, J. M.; Smit, K. J.; de Haas, M. P.; Oevering, H.; Verhoeven, J. W. *J. Phys. Chem.*, **1988**, *92*, 6958.

26. Oevering, H.; Cotsaris, M. E.; Verhoeven, J. W.; Hush, N. S. *J. Am. Chem. Soc.*, **1987**, *109*, 3258.

27. Koeberg, M.; De Groot, M.; Verhoeven, J. W.; Lokan, N. R.; Shephard, M. J.; Paddon-Row, M. N. *J. Phys. Chem. A*, **2001**, *105*, 3417.

28. Kumar, K.; Z., L.; Waldeck, D. H.; Zimmt, M. B. *J. Am. Chem. Soc.*, **1996**, *118*, 243.

29. Han, H.; Zimmt, M. B. *J. Am. Chem. Soc.*, **1998**, *120*, 8001.

30. Kaplan, R. W.; Napper, A. M.; Waldeck, D. H.; Zimmt, M. B. *J. Am. Chem. Soc.*, **2000**, *122*, 12039.

31. Kaplan, R. W.; Napper, A. M.; Waldeck, D. H.; Zimmt, M. B. *J. Phys. Chem. A*, **2002**, *106*, 1917.

32. Napper, A. M.; Read, I.; Kaplan, R. W.; Zimmt, M. B.; Waldeck, D. H. *J. Phys. Chem. A*, **2002**, *106*, 5288.

33. Napper, A. M.; Read, I.; Waldeck, D. H.; Head, N. J.; Oliver, A. M.; Paddon-Row, M. N. *J. Am. Chem. Soc.*, **2000**, *122*, 5220.

34. Maroncelli, M.; MacInnis, J.; Fleming, G. R. *Science*, **1989**, *243*, 1674.

35. Zusman, L. D. *Chem. Phys.*, **1980**, *49*, 295.

36. Calef, D. F.; Wolynes, P. G. *J. Phys. Chem.*, **1983**, *87*, 3387.

37. Sumi, H.; Marcus, R. A. *J. Chem. Phys.*, **1986**, *84*, 4272.

38. Sumi., H.; Marcus, R. A. *J. Chem. Phys.*, **1986**, *84*, 4894.

39. Rips, I.; Jortner, J. *Chem. Phys. Lett.*, **1987**, *133*, 411.

40. Marcus, R. A.; Sumi., H. *J. Electroanal. Chem.*, **1986**, *204*, 59.

41. Onuchic, J. N.; Beratan, D. N.; Hopfield, J. J. *J. Phys. Chem.*, **1986**, *90*, 3707.

42. Loring, R. F.; Yan, Y. J.; Mukamel, S. *Chem. Phys. Lett.*, **1987**, *135*, 23.

43. Castner, E. W.; Bagchi, B.; Fleming, G. R. *Chem. Phys. Lett.*, **1988**, *143*, 270.

44. Van der Zwan, G.; Hynes, J. T. *J. Phys. Chem.*, **1985**, *89*, 4181.

45. Barchi, B.; Oxtoby, D. W.; Fleming, G. R. *Chem. Phys.*, **1984**, *86*, 257.

46. Yu, T. M. *Opt. Spectrosc. (USSR)*, **1974**, *36*, 283.

47. Onsager, L. *Can. J. Chem.*, **1977**, *55*, 1819.

48. a) Kim, S.; Jackiw, J.; Robinson, E.; Schanze, K. S.; Reynolds, J. R.; Baur, J.; Rubner, M. F.; Boils, D. *Macromolecules*, **1998**, *31*, 964; b) Tan, C.; Pinto, M. R.; Schanze, K. S. *Chem. Commun.*, **2002**, *446*; c) Liu, B.; Yu, W.-L.; Lai, Y.-H.; Huang, W. *Chem. Commun.*, **2000**, 551.

49. a) Chen, L.; McBranch, D. W.; Wang, H.-Lin; Helgeson, R.; Wudl, F.; Whitten, D. G. *PNAS*, **1999**, *95* 12287; b) DiCesare, N.; Pinto, M. R.; Schanze, K. S.; Lakowicz, J. R.

Langmuir, **2002,** *18*, 7785, c) Harrison, B. S.; Ramey, M. B., Reynolds, J. R.; Schanze, K. S. *J. Am. Chem. Soc.*, **2000,** *122,* 8561.

50. Fan, C.F.; Plaxco, K.W; Heeger, A.J. *J. Am. Chem. Soc.*, **2002,** *124*, 5642.

51. a) Gaylord, B. S.; Heeger, A. J.; Bazan, G. C. *PNAS*, **2002**, *99*,10954; b) Kushon, S.; Bradford, K.; Marin, V.; Suhrada, C.; Armitage, B. A.; McBranch, D.; Whitten, D. *Langmuir*, **2002**, *18*, 7245; c) *ibid*, **2003**, *19*, 6456.

52. a) Hu, D.; Yu, J.; Padmanaban, G.; Ramakrishanan, S. and Barbara, P. F. *Nanoletters***, 2002**, *2,* 1121; b) List, E. J. W.; Creely, C.; Leising, G.; Schulte, N.; Schlueter, A. D.; Scherf, U.; Muellen, K.; Graupner, W. *Chem. Phys. Lett.*, **2000**, *325,*132.

53. van den Bout, D. A.; Yip, W.; Hu, D.; Fu, D.; Swager, T. M. and Barbara, P. F. *Science*, **1997**, *277,* 1074.

54. a) Lakowicz, J. R. "*Principles of Fluorescence Spectroscopy"*, (N.Y., Plenum, **1999**); b) Speiser, S. *Chem. Rev.*, **1996**, *96*, 1953.

55. a) Huser, T.; Yan, M.; Rothberg, L. *PNAS*, **2000**, *97*, 11187; b) Sluch, M.I.; Godt, A.; Bunz, U. H. F.; Berg, M. A. *J. Am. Chem. Soc.*, **2001**, *123*, 6447; c) Hu, D. H.; Yu, J.; Barbara, P. F. *J. Am. Chem. Soc.*, **1999**, *121*, 6936; d) *ibid*, *Science,* **2000**, 289, 1327.

Chapter 2 Observation of Dynamic Solvent Effect for Electron Tunneling in U-Shaped Molecules

This work has been published as M. Liu, D. H. Waldeck, A. M. Oliver, N. J. Head and M. N. Paddon-Row, J. Am. Chem. Soc., 126, 10778, (2004).

The electron transfer rate constant is measured in two U-shaped donor-bridge-acceptor molecules over a wide range of temperature in acetonitrile and N-methylacetamide (NMA). The electron transfer rate at high temperature can be well described by a nonadiabatic model of the reaction, but at low temperatures the rate in NMA becomes controlled by the solvent. The results are discussed in terms of theoretical models for the change in reaction mechanism and its dependence on the solute-solvent frictional coupling.

2.1 Introduction

This work explores intramolecular electron transfer rates in which the electron tunnels through nonbonded contacts between the electron donor and electron acceptor moieties. Tunneling pathways through nonbonded contacts are important for many bimolecular electron transfer reactions in biology and chemistry. The electron transfer is studied as a function of solvent and temperature to elucidate how the mechanism changes from a nonadiabatic electron tunneling behavior to a solvent controlled behavior and to explore how nuclear motion can change the reaction dynamics.

Electron transfer proceeds from a photoexcited dimethoxydiphenylnaphthalene moiety (the electron donor) to a dicyanovinyl moiety (the electron acceptor) in the U-shaped donor-bridge-acceptor (DBA) molecules **1** and **2** (see Figure 2.1). In our earlier work the electron transfer was measured over the temperature range of 273 K to 343 K in five different organic solvents and was well-described by a nonadiabatic electron transfer mechanism.[1,2] In the nonadiabatic limit, the semiclassical rate expression[3],

$$k_{ET} = \frac{4\pi^2}{h} |V|^2 \frac{1}{\sqrt{4\lambda_0 \pi k_B T}} \sum_{n=0}^{\infty} \exp(-S)\left(\frac{S^n}{n!}\right) \exp\left[-\frac{(\Delta_r G + \lambda_0 + nh\nu)^2}{4\lambda_0 k_B T}\right] \qquad \mathbf{1}$$

was used to describe the electron transfer rate of **1** and **2** in different solvents at different temperatures. The five parameters: the reaction free energy $\Delta_r G$, the solvent reorganization energy λ_0, an effective vibrational frequency ν, the electronic coupling $|V|$, and the Huang-Rhys parameter S (defined as $S=\lambda_v/h\nu$ where λ_v is the inner reorganization energy) were quantified through a combination of experimental measurements and modeling. The earlier work quantified these parameters for **1** and **2** at higher temperatures and showed that the solvent effects are only static, that is, the solvent affects the free energies and the energies of activation, but does not participate in the important tunneling pathway(s) between the reactant state and the charge-separated state.[4] The molecular solvation model proposed by Matyushov[5] was shown to account for the observed free energy changes quite well. Lastly, that study showed that the electron tunnels through the pendant moiety (either the 4-ethylphenyl or the propyl group), which lies in the 'line-of-sight' between the donor and acceptor groups. The electronic couplings extracted from that analysis were $|V|$ = 168 cm^{-1} for **1** and $|V|$ = 46 cm^{-1} for **2**, demonstrating that the aromatic pendant group in **1** mediates the electronic tunneling more effectively than the alkyl group in **2**.

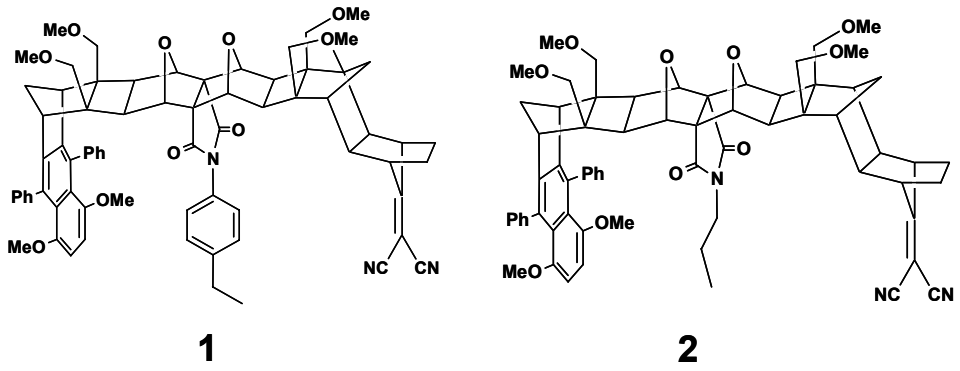

Figure 2.1 Two U-shaped donor-bridge-acceptor molecules

The electronic coupling values extracted from this analysis suggest that the electron transfer mechanism can be manipulated by changing the temperature. This study extends the earlier work to low temperatures to probe the transition from a nonadiabatic electron transfer mechanism (where the rate is controlled by electron tunneling) to a mechanism in which the rate is controlled by nuclear motion, *vide infra*. The electron transfer is compared in two solvents, N-methylacetamide (NMA) and acetonitrile, as a function of temperature. These solvents have very similar indices of refraction and molecular sizes, but have dramatically different solvation relaxation times and static dielectric constants.[6,7] This difference allows us to explore the effect of solvent nuclear motion on the electron transfer rate constant.

The observations show that the electron transfer rate for **1** is significantly faster than for **2** at room temperature and higher, consistent with a nonadiabatic electron transfer process and more efficient electron tunneling via the aromatic pendant group. Upon lowering the temperature to 200 K, the electron transfer rates for **1** and **2** in NMA become similar; *i.e.*, **1** is not much faster than **2**, demonstrating that the electron transfer is controlled by the environment, not the tunneling pathway. In contrast, the rate constant in acetonitrile remains controlled by the tunneling. The Debye relaxation time of the solvent, N-methylacetamide, is 390 ps at 303 K,[6] but

increases dramatically as the temperature decreases, to 13 μs at 201 K, where it is much slower than the electron transfer reaction.[8] In this limit, the electron transfer reaction may be controlled by the relaxation time of solvent, a dynamic solvent effect. This effect is manifest by the similar electron transfer time constants of **1** and **2** at low temperatures, in contrast to their different rate constants at high temperature. These observations demonstrate that the electron transfer mechanism changes with temperature in NMA.

2.2 Electron Transfer mechanisms and the transition between regimes

Figure 2.2 illustrates essential features of the generally accepted view of electron transfer reactions. The electronic energy is sketched as a function of the electron coordinate (on the left) and the nuclear coordinate (on the right); each approximated as an effective one dimensional coordinate. The top panel shows the reactant state, the bottom of the Marcus free energy well, for which the electronic energy of the reactant is lower than that of the product, and reaction does not occur. The bottom panel shows the nuclear coordinate that corresponds to the transition state, for which the electronic energies are degenerate and the electron can tunnel along the electron coordinate (diagram on the left) between the reactant and product wells. This description of the reaction corresponds to the Frank-Condon approximation in which the electronic coupling does not depend on the nuclear coordinate but is purely electronic.

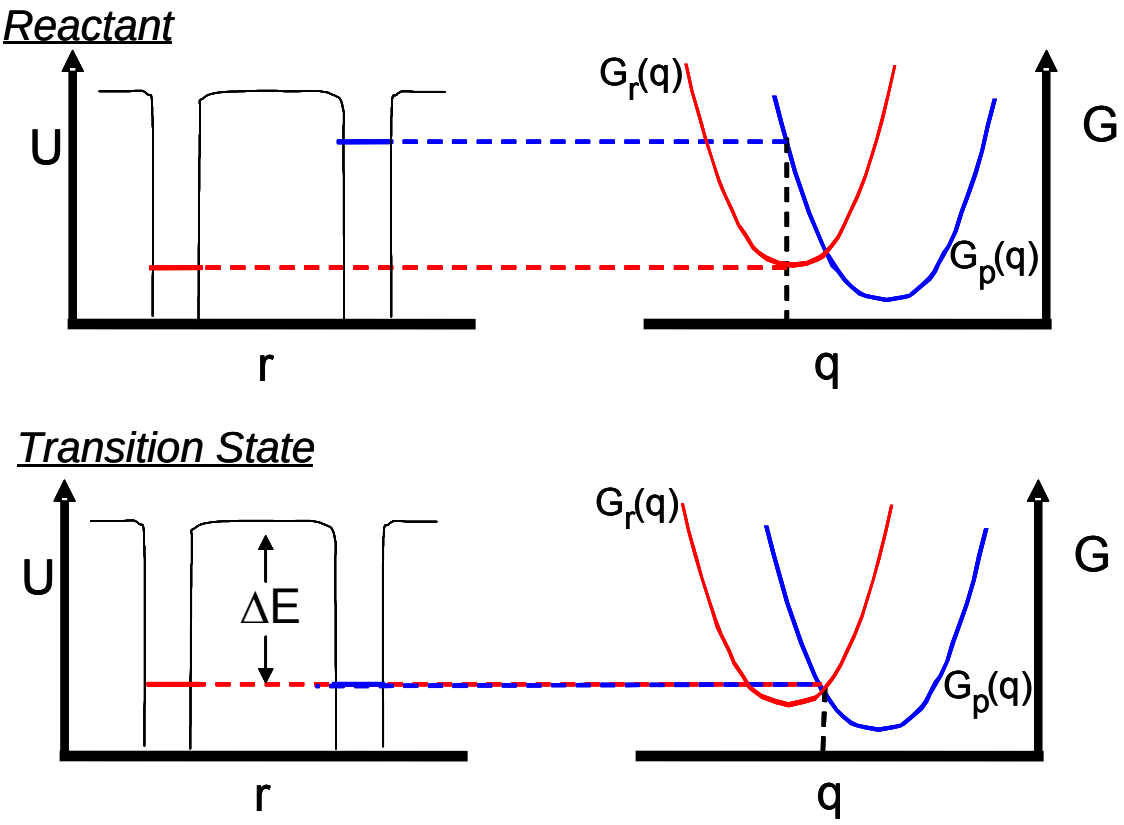

Figure 2.2 Energetics relevant to electron transfer reactions are shown for the reactant state (top panel) and the transition state (bottom panel). Both electronic (**r**) and nuclear (**q**) coordinates are involved in the reaction.

Figure 2.2 underscores the view that a successful electron transfer reaction requires two things to happen: the nuclear coordinate(s) must evolve to the transition state and the electronic coordinate must change from the reactant to the product. The traditional Marcus theory considers two limits for the reaction rate: nonadiabatic and adiabatic. In the nonadiabatic picture the electronic interaction between the product and reactant curves at the transition state is 'weak', and the electron transfer rate is limited by the electronic motion (probability of tunneling from the reactant to product states). In the adiabatic picture the electronic interaction between the product and reactant curves at the transition state is 'strong', and the electron transfer rate is

limited by the nuclear motion to reach the transition state. This traditional view of the reaction does not include the effect of solvent dynamics on either the motion along the nuclear coordinate, in the adiabatic case, or the electron tunneling pathway, in the nonadiabatic case. Earlier work showed that the solvent does not participate in the electron tunneling pathway for these molecules[2], so here we restrict the discussion to the solvent's role in effecting the motion along the nuclear reaction coordinate to the transition state.

The important role of solvent dynamics on electron transfer reactions was first discussed by Zusman.[9] Since that time a number of workers have addressed this problem.[10,11,12] The solvent's role in the reaction mechanism can be elucidated through a consideration of timescales for the molecular dynamics in the transition state region. In the nonadiabatic limit the system moves through the transition state region along the nuclear coordinate many times before a transition occurs from the reactant electronic state to the product electronic state. Hence the rate-limiting step is the electronic tunneling, not the nuclear motion. In the friction (or adiabatic) limit the electronic transition from the reactant state to the product state occurs more rapidly than the nuclear motion through the transition state region because the nuclear motion is slowed by frictional coupling to the environment (or because the electronic coupling is large).

Zusman and others have derived conditions for assessing whether the electron transfer lies in the solvent friction regime. The conditions change somewhat depending on details of the model and shape of the energy surface in the transition state region, but they have the same basic features. When a single effective quantized mode contributes to the reorganization, Zusman[9b] finds that the solvent controlled limit applies if

$$\frac{\pi^2 |V|^2 \tau}{\hbar \lambda_0} \exp\left(-\lambda_v / h\nu\right) >> \sin\left(\frac{\pi}{2}\left(\frac{\Delta_r G}{\lambda_0} + 1\right)\right) \qquad \mathbf{2}$$

in which τ is a characteristic solvent relaxation time. If $|\Delta_r G| << \lambda_0$ and one combines the internal reorganization energy term with the electronic coupling to define an effective electronic coupling $|V_{eff}|$,[13] the inequality 2 reduces to a form like that found by Onuchic,[12] namely

$$g = \frac{|V_{eff}|^2 \tau}{\hbar \lambda_0} >> 1 \qquad \textbf{3}$$

The adiabaticity parameter g compares the characteristic time required for electron tunneling to the characteristic time spent in the transition state (Landau-Zener) region. The reaction is adiabatic when g >> 1, and it is nonadiabatic when g << 1. If these criteria are applied using the parameters in Table 2.3, τ >> 5 ps for **1**, and τ >> 30 ps for **2**.

The observed electron transfer rate is often described by an interpolation formula that connects the nonadiabatic and solvent-controlled (adiabatic) limits, namely

$$\frac{1}{k_{ET}} = \frac{1}{k_{NA}} + \frac{1}{k_{SC}} \qquad \textbf{4}$$

where k_{NA} is the nonadiabatic rate constant, k_{SC} is the rate constant in the solvent-controlled limit, and k_{ET} is the measured electron transfer rate. Equation 4 results because both an electronic state change (rate-limiting for k_{NA}) and nuclear motion to the transition state (rate-limiting for k_{SC}) must occur for reaction, hence the slower process is rate controlling. Although Equation 4 provides a way to interpolate between the two limiting behaviours, it does not describe the dynamics of the reaction accurately. For example, the rate is exponential in the nonadiabatic regime but can be non-exponential in intermediate regimes. More dramatically, if the solute-solvent frictional coupling is strong and slow the reaction trajectory will not go through the transition state. Rather it may occur at a range of different polarization coordinates.[11,14]

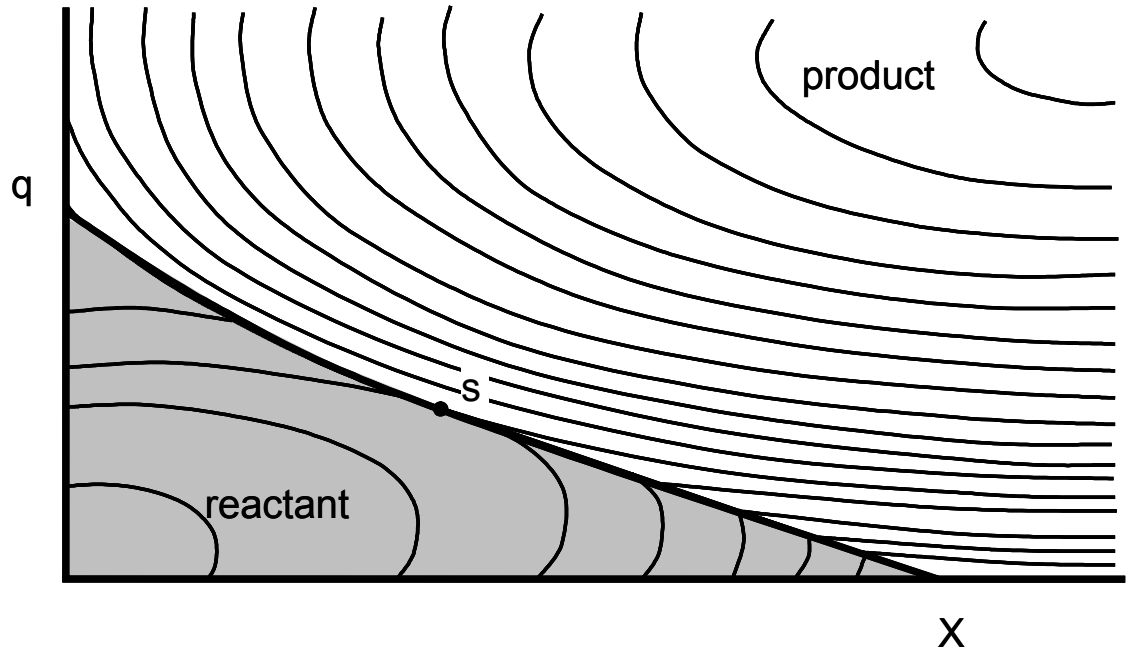

Figure 2.3 A two dimensional V(q,X) reaction coordinate is shown. The shaded area represents the reactant surface. The thick line is the dividing line (ridge) between the reactant and product surfaces. The reactant well is at the bottom left, the product well is at the top right, and point **S** is the saddle point on the ridge line. Adapted from ref 11.

The Sumi-Marcus model of electron transfer explicitly includes solvent dynamics by viewing the reaction as proceeding along a two-dimensional effective potential energy surface, V(q,X) (see Figure 2.3). The coordinate **q** in this reaction surface corresponds to the typical reaction coordinate used in electron transfer reactions (Figure 2.2, right hand panels) and includes internal and low frequency nuclear degrees of freedom that are always 'fast'. The second coordinate **X** is the solvent polarization coordinate; *i.e.*, an effective coordinate that accounts for the polarization response of the medium to the evolving charge distribution of the reactant. They find the reaction rate by solving a Fokker-Planck equation for diffusive motion

along **X** and treat the motion along **q** through a rate constant k(X) which is **X** dependent and depends on the 'fast' motions in the normal way (*e.g.*, Equation 1). In particular, they solve

$$\frac{\partial P(X,t)}{\partial t} = D\frac{\partial^2 P(X,t)}{\partial X^2} + \frac{D}{k_B T}\frac{\partial}{\partial X}\left(P(X,t)\frac{dV(X)}{dX}\right) - k(X)P(X,t) \qquad \mathbf{5}$$

where D is the diffusion coefficient, V(X) is the effective potential for the polarization coordinate, and P(X,t) is a probability distribution function for the reactant; *i.e.*, the concentration. This model treats the time evolution of the reactant probability by diffusion along the **X** coordinate (the first two terms describe diffusion in a potential) and its first order decay at the different **X** values (k(X) acts as a loss term for the probability). The time dependent behavior of P(X,t) should be reflected by the reactant's time evolution in an experiment.

Sumi and Marcus discuss four limiting cases for the reaction. The first case they call the '*slow reaction limit'*. It corresponds to motion along **X** that is fast compared to the motion along **q**, so that the traditional analysis applies (be it nonadiabatic or adiabatic) and the reaction does not depend on solvent frictional coupling. This case applies for the high temperature data (see Figure 2.6). Their second case is called the '*wide reaction window'*. It corresponds to a situation in which the internal reorganization energy is much larger than the solvent reorganization, so that the reaction may proceed at a range of **X** values but the reaction rate at each of the different **X** values is the same. Their third ('*narrow reaction window*') and fourth ('*nondiffusing limit'*) cases may be relevant to the low temperature experiments reported here. Both of these latter cases predict a non-exponential decay of the reactant population because the motion along the polarization coordinate is slow compared to the reaction rate.

In the 'narrow reaction window' case, Sumi and Marcus assume the electron transfer occurs at a particular value of $X = X_0$ and the nonexponentiality arises from the time evolution of the reactant population along **X**. This limit corresponds to motion in **X** being slow, so that the

time behavior is determined by diffusion along **X** to the position X_0 where the electron transfer occurs, given by a 'sink' term in the reaction diffusion equation. Hence the reaction coordinate is **X** and effectively one-dimensional. This limit of the model is useful for understanding dynamic Stokes shift experiments, in which the optical excitation and emission can be viewed as an electron transfer reaction within the chromophore.[6,15]

In the '*nondiffusing limit'* the motion along **X** is frozen and the electron transfer occurs at a range of **X** values so that the nonexponentiality reflects the dispersion in k(X). This limit is quite different from the traditional view of the reaction proceeding through a well-defined transition state. In this case, a range of reaction trajectories are possible and the choice of which to follow is determined dynamically by the medium's polarization response. This limit requires a description with at least two-dimensions.

2.3 Experimental Section

The synthesis of the U-shaped supermolecules is similar to that reported earlier.[16] The solvent acetonitrile (99.9% HPLC) was purchased from Burdick & Jackson. N-methylacetamide (NMA) was purchased from Aldrich and was fractionally distilled three times using a vigreux column under vacuum. The purified fraction was used immediately in all the experiments. Each solution was freeze-pump-thawed a minimum of five times to eliminate dissolved gases.

In our experiment, the sample was excited at 310 nm by the frequency-doubled cavity-dumped output of a Coherent CR599-01 dye laser, using Rhodamine 6G dye, which was pumped by a mode locked Coherent Antares Nd:YAG. The dye laser pulse train had a repetition rate of ca. 300 kHz. Pulse energies were kept below 1 nJ and the count rates were kept below 3 kHz to

prevent pile-up effects. All fluorescence measurements were made at the magic angle and data was collected until a standard maximum count of 10000 is observed at one channel.

Time-resolved fluorescence kinetics of **1**, **2**, and their donor only analogues were measured in acetonitrile and NMA as a function of temperature. The lowest temperature was 200 K and the highest temperature was 338 K. The experimental temperature was controlled by an ENDOCAL RTE-4 chiller in the high temperature range, and the temperature was measured using a Type-K thermocouple (Fisher-Scientific), accurate to within 0.1 ºC. The low temperature experiments were carried out in a VPF-100 Cryostat (Janis Research Company, Inc) and were operated with a $2x10^{-5}$ torr high vacuum during the experiment. For the low temperature experiments, the temperature was measured using a Model 321 Autotuning Temperature Controller (LakeShore Cryotronics, Inc.) which has a silicon diode, accurate to within 0.1 K.

The instrument response function was measured using a sample of colloidal $BaSO_4$. The samples **1** and **2** each contain a small amount of unreacted donor compound. Independent experiments on the donor only molecules were used to characterize its single exponential fluorescence decay, which is much longer than the relaxation time of **1** and **2** at the measured temperatures. The contribution of the donor only impurity was removed from the fluorescence decay curves for **1** and **2** in the analysis.[17] The remaining part of the **1** and **2** decay laws were fit to either one or two exponentials using IBH-DAS6 analysis software. Other fitting and data presentation, *e.g.* Equation 1, was performed using Microsoft Excel XP.

The current work measures the electron transfer kinetics for systems **1** and **2** in acetonitrile and N-methylacetamide (NMA) solvents and combines them with earlier data obtained in polar solvents CH_2Cl_2, tetrahydrofuran, acetonitrile, and the weakly polar solvents toluene and mesitylene.[2] Some properties of NMA and acetonitrile solvents are listed in Table

2.1. NMA has a freezing point of 302 K and allows access to very slow polarization response times for the solvent.[6,8] Electron transfer rate studies in organic solids have been performed previously by other groups, and provide no extraordinary technical difficulties.[18] No unusual features in the reaction kinetics are observed in the region of the freezing point.

Table 2.1 The properties of solvent acetonitrile (ACN) and NMA at 303 K

Solvent	Refractive Index	Static Dielectric Constant	Debye Relaxation Time (ps)	Density (g/ml)	Viscosity (cP)	Dipole Moment (D)
ACN	1.341	34.75	3	0.7696	0.331	3.48
NMA	1.429	178.9	390	0.9503	3.885	5.05[a]

[a] Calculated using Gaussian/MP2/6-31G

2.4 Results

The intramolecular photoinduced electron transfer in **1** and **2** occurs from the locally excited singlet state of the dimethoxydiphenylnaphthalene donor to the dicyanovinyl acceptor. By comparing the fluorescence decay rate of the supermolecule with and without the electron acceptor group it is possible to determine the electron transfer rate.[1]

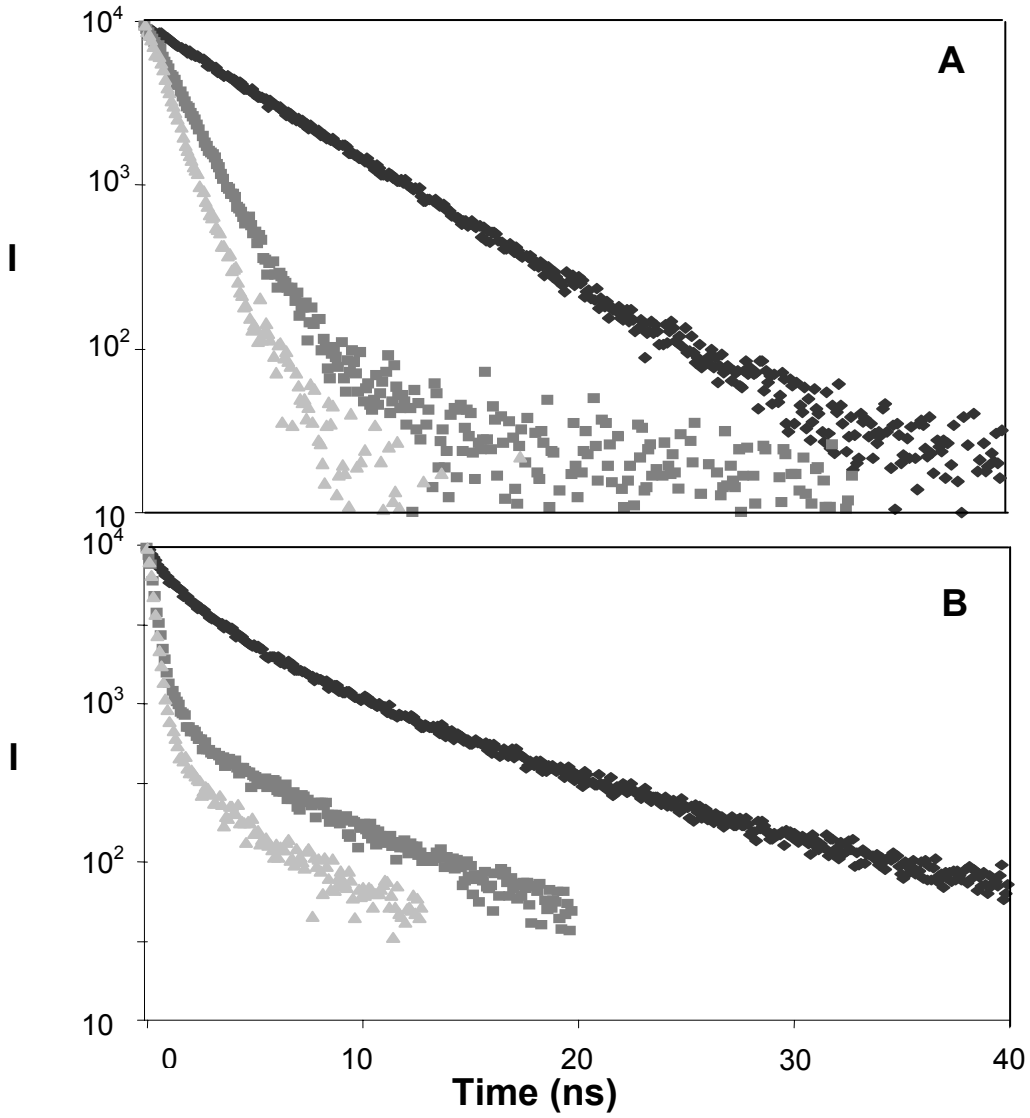

Figure 2.4 Fluorescence decay profiles are shown for **1** in acetonitrile (panel A) at three different temperatures: (diamonds) 200 K, (squares) 295 K, and (triangles) 321 K and NMA (panel B) at: (diamonds) 200 K, (squares) 295 K, and (triangles) 313 K.

2.4.1 Fluorescence Decay

Figure 2.4 presents some representative fluorescence decay curves for **1** in acetonitrile (panel A) and in NMA (panel B), and Table 2.2 presents the corresponding fitting parameters for

these decay curves. The fluorescence decay law in acetonitrile is single exponential over the entire temperature range. In this case the fluorescence decay rate constant k_f can be used to determine the electron transfer rate constant k_{ET}. The electron transfer rate constant is given by $k_{ET} = k_f - k_{\substack{donor \\ only}}$, where $k_{\substack{donor \\ only}}$ is the fluorescence decay constant determined for the analogue molecule without an electron acceptor and provides a good measure of the locally excited state's intrinsic decay rate.

Table 2.2 Fitting parameters for the fluorescence decays in Figure 2.4

	T , K	τ_1 (%), ns[a]	τ_c , ns[b]		T , K	τ_1 (%), ns[a]	τ_c , ns[b]
1 in NMA	200	1.64 (74)	3.06	**2** in NMA	200	2.41 (79)	4.12
1 in NMA	295	0.40 (93)	0.49	**2** in NMA	295	0.67 (97)	0.68
1 in NMA	313	0.27 (94)	0.30	**2** in NMA	313	0.46 (98)	0.46

a τ_1 is the fast time constant and % is its percentage contribution to the total decay curve.

b $\tau_c = \Sigma A_i \tau_i$ where A_i is the percentage of component i and τ_i is the decay time for component i, in a fit of the decay law to a sum of exponentials.

The fluorescence decay law for **1** in NMA is nonexponential (see Figure 2.4B), hence a single rate constant does not fully describe the data. Table 2.2 shows parameters for a double exponential fit and it is evident that the rate law becomes more exponential as the temperature increases. In fact a fit of the fluorescence decay at 313 K has a fast time constant that comprises 94% of the overall decay law. In order to quantify these data, we compute the correlation time τ_c for the decay (see Table 2.2). The fluorescence decay data for **2** shows a trend similar to that found for **1**, except that the nonexponentiality is not as pronounced (see Appendix).

To summarize, the decay law in acetonitrile is well described by a single exponential over the whole temperature range, and the decay law in NMA is well described by a single exponential at high temperatures (above 300 K) but is strongly nonexponential at low temperatures (below 290 K).

2.4.2 Steady-State Spectra

An important difference between NMA and acetonitrile arises from hydrogen-bonding. The hydrogen bonded structures in NMA are largely responsible for the large dielectric constant and slow polarization relaxation of the solvent.[7,8,19] Figure 2.5 shows the steady-state absorption and fluorescence spectra of **1** in acetonitrile and NMA at room temperature. It is evident that the spectral characteristics are very similar in the two solvents. These observations suggest that any difference in the interaction between the solute and the solvents, acetonitrile and NMA, does not involve any significant perturbation of the donor chromophore.

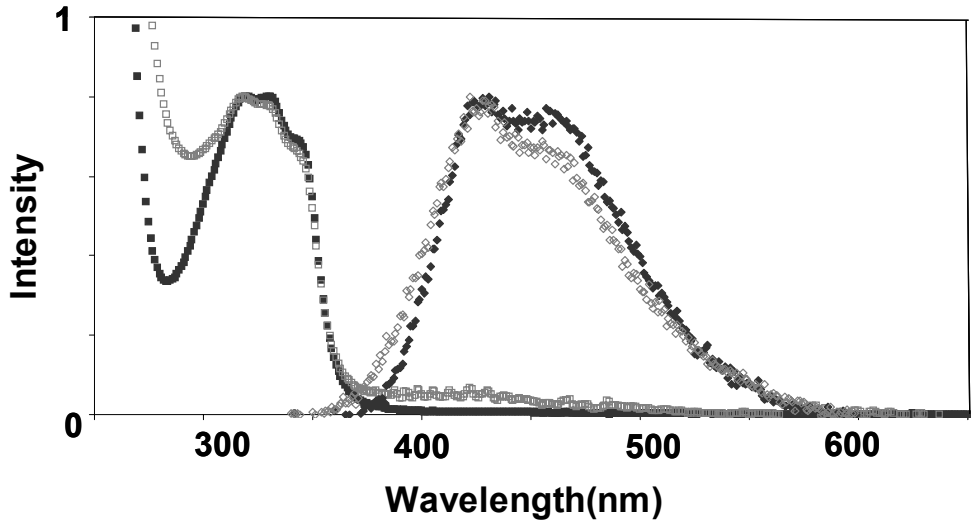

Figure 2.5 The absorption (squares) and fluorescence (diamonds) spectra are shown for **1** in NMA (gray) and acetonitrile (black).

2.5 Data Analysis

2.5.1 High Temperature Results

At high temperatures the rate law in NMA becomes nearly exponential. The worst case scenario is **1** in NMA at 305 K, for which the calculated correlation time is 392 ps and the fast decay time in a double exponential fit is 334 ps, about a 15% difference. As the temperature increases the correspondence between the correlation time and the fast decay component improves. Although not rigorous, it is reasonable to approximate the decay law as single exponential in this regime.

The previous work in our group fit the temperature-dependence of the experimental rate constant to the semiclassical equation and obtained the electronic coupling $|V|$ and solvent reorganization energy λ_0 values. The reaction free energy $\Delta_r G$ was determined from experimental fluorescence lifetime data in weakly polar and nonpolar solvents, from which the forward electron transfer rate and backward rate can both be determined. Electronic structure calculations and the experimental free energies of reaction in the aromatic solvents[4] were used to calibrate a molecular solvation model and determine the values of parameters in the semiclassical electron transfer expression.

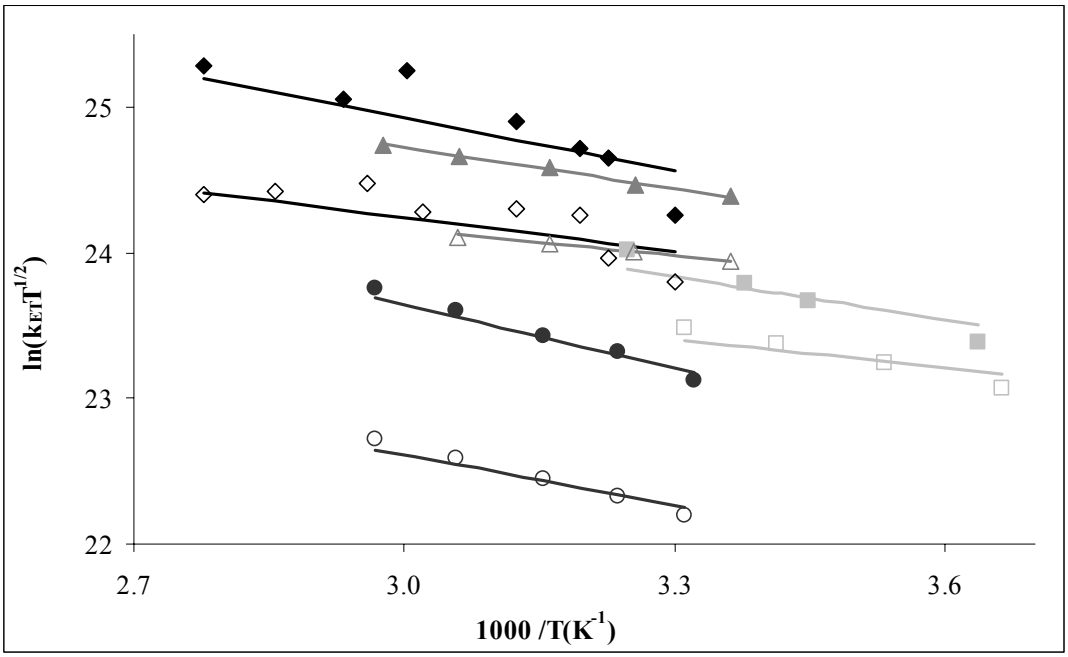

Figure 2.6 Fitting electron transfer rate of **1** (filled symbols) and **2** (open symbols) in different solvents at high temperature: NMA (diamond), THF (triangle), DCM (square), ACN (circule).

Figure 2.6 combines those earlier data with these new data for **1** and **2** in NMA and acetonitrile at high temperatures (> 300 K). When calibrated to the measured free energies in nonpolar solvents, the molecular solvation model and the semiclassical equation (Eqn 1) provide a good representation of the data. This finding supports the identification of nonadiabatic electron transfer for the high temperature mechanism, even in NMA. The experimental electron transfer rate constant of **1** is about 1.7 times faster than that for **2** in NMA, which matches well with the previous conclusion that the aromatic group is better than an alkyl group at mediating the electronic coupling. The fitting was performed in the same manner described previously.[1] Because more data are included in the fit, the best fit parameters changed slightly (see Table 2.3). The electronic coupling values for **1** is 146 cm^{-1} and **2** is 62 cm^{-1}, which is consistent with the earlier analysis.

Table 2.3 Fitting parameters for 1 and 2 to the nonadiabatic model at high temperature.[a]

System	$\lvert V \rvert$,cm^{-1}	CH_3CN		NMA	
		λ_0, eV	$\Delta_r G$, eV	λ_0, eV	$\Delta_r G$, eV
1	146	1.48	-0.54	1.03	-0.35
2	62	1.46	-0.58	1.01	-0.39

a) λ_v= 0.63 eV and $h\nu$ = 1600 cm^{-1} are determined from charge transfer spectra of related species (see ref 1).

2.5.2 Low Temperature Results

Figure 2.7A presents the experimental data in NMA over the temperature range from 200K to 338K. The electron transfer rates of **1** and **2** are plotted versus 1000/T, and the fluorescence decay rate of the donor only molecule is plotted versus 1000/T, as well. This plot illustrates the different electron transfer rate constants for **1** and **2** at temperatures higher than 300 K, and their similar rate constants at lower temperatures, down to 200 K. For temperatures below 200 K the electron transfer appears to be frozen out and the fluorescence decay of **1** and **2** coincides with that of the donor only compound.

These data do not determine whether the rate law is controlled by the solvent or by internal dynamics of the molecule. These two possibilities were analyzed by studying the electron transfer in a solvent which has a very fast relaxation time, acetonitrile. Figure 2.7B shows the rate data for **1** and **2** in acetonitrile over the entire temperature range along with the fluorescence decay rate data for the donor only compound. The plot shows that the electron transfer rates of **1** and **2** remain separated even as the temperature approaches 200 K. Since the rate constants are still quite different in acetonitrile, this finding demonstrates that temperature alone is not the controlling factor for the behaviour in NMA.

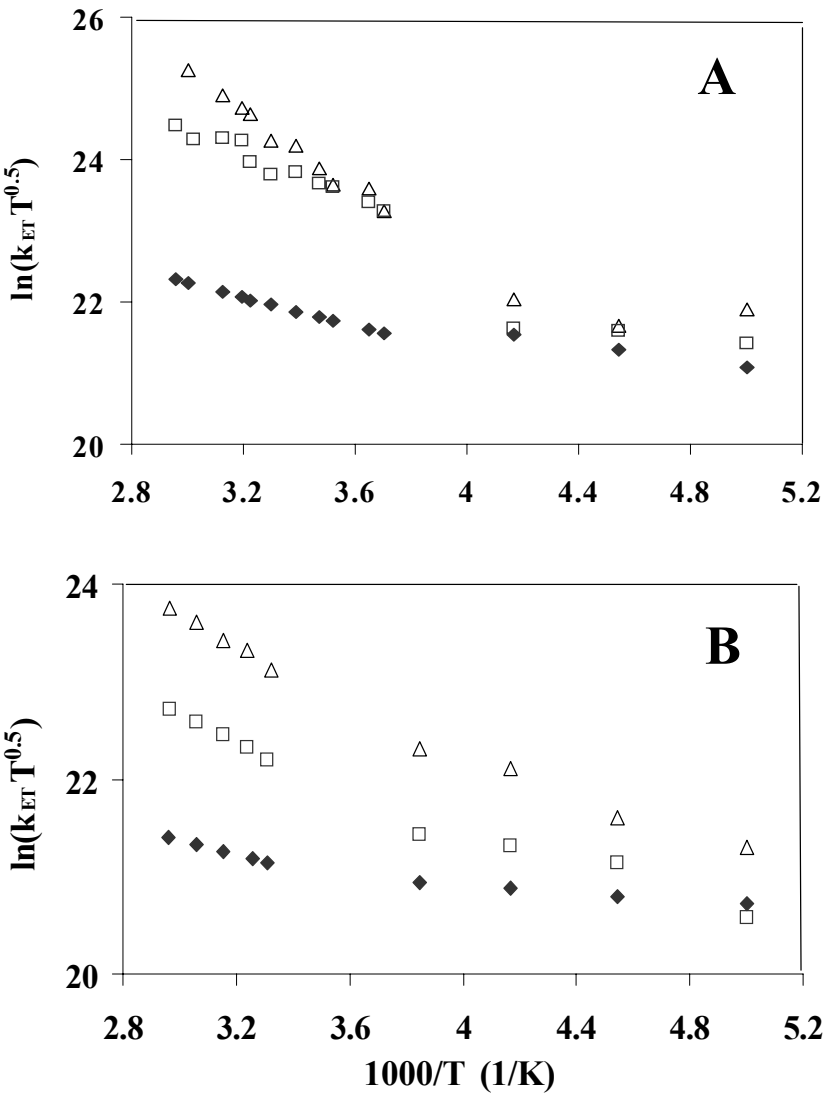

Figure 2.7 The experimental rate constant of **1** (open triangle), **2** (open square) and the donor only compound (filled triangle) is plotted as a function of temperature in NMA (panel A) and in acetonitrile (panel B).

The major difference between acetonitrile and NMA is the solvent polarization relaxation time. In acetonitrile it is 3.2 ps[6] at 298 K which is about 100 times faster than NMA. As the acetonitrile is cooled its relaxation time increases, but is still much faster than NMA at room temperature. Hence the solvent dynamics does not affect the observed electron transfer rate, even

at these low temperatures. In short, the electron transfer rate in acetonitrile follows the same trend at low temperature (295 K – 200 K) as at high temperatures (> 295 K) and is well-described as nonadiabatic.

2.5.3 Mechanism Change

The difference in behavior for the electron transfer rate constant in NMA, compared to that in acetonitrile, implies a change in reaction mechanism that is linked to the slow relaxation dynamics of the NMA solvent. The Sumi-Marcus model can explain this behavior as a transition from the 'slow reaction' limit at high temperature to one of the solvent friction limiting cases at low temperature. In the 'nondiffusing limit' the reaction rate is inhomogeneous and the observed rate behavior depends on the initially prepared distribution of the reactant along **X**. Although no dramatic dependence of the preparation is observed for small changes in the excitation conditions, more extensive studies of this sort need to be examined before this limit can be discounted. For the 'narrow reaction window' limit the dynamics along the solvent coordinate controls the reaction rate. We analyze the implications of this limit for the data and discuss what motion may influence the behaviour.

The transition from the 'slow reaction' limit to the 'narrow reaction window' limit can be approximated by the interpolation formula, Equation 4, for the change in reaction mechanism. This approximation provides a way to extract the rate constant k_{SC} for the solvent controlled rate process when the nonadiabatic rate constant is known. Because the electron transfer reaction for **1** and **2** in acetonitrile appears to follow a nonadiabatic mechanism over the entire temperature range, these data can be used to determine the displacement in the rate constant magnitudes which arises from the different electronic couplings. If the rate constant for **2** in NMA is

assumed to be nonadiabatic over the entire temperature range, then the electronic coupling ratio between **2** and **1** can be used to predict what the nonadiabatic rate constant should be for **1** in NMA. This predicted rate constant is plotted in Figure 2.8.

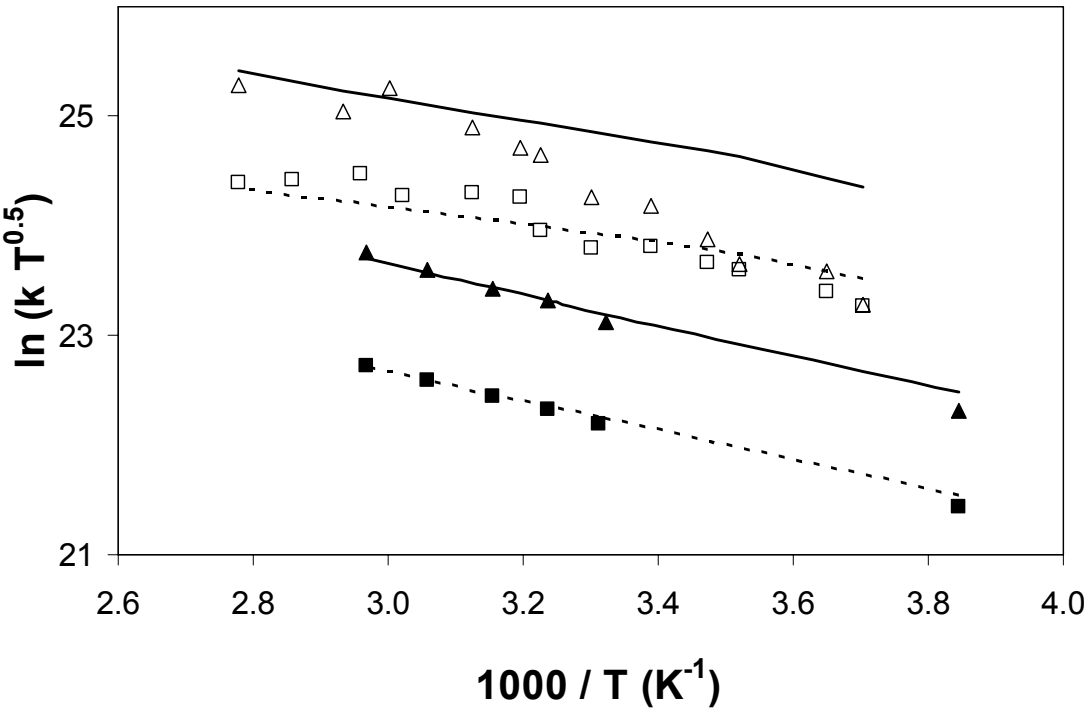

Figure 2.8 Plots of the electron transfer rate constant versus 1000/T for **1** (triangles) and **2** (squares) in NMA (open symbols) and acetonitrile (filled symbols). Straight and dashed lines are fits to Equation 1.

Figure 2.8 plots the $\ln\left(k_{et}\sqrt{T}\right)$ of **1** and **2** in acetonitrile and NMA versus 1000/T. The acetonitrile data are fit to the semiclassical expression (equation 1), with the parameters obtained from fitting the data in Figure 2.6. Because the NMA solidifies below 303 K, the molecular solvation model was not used to determine the solvent reorganization and solute free energy. Instead, the rate data for **2** in NMA are fit to equation 1 with the solvent reorganization and reaction free energy determined by a dielectric continuum model, while the internal

reorganization and electronic coupling parameters are fixed at the values obtained from the high temperature fits. Table 2.3 gives the free energy and reorganization parameters for NMA at high temperature. Taking the offset in electronic coupling and reaction free energy from the fit to the high temperature data in Figure 2.6, the fit for **2** in NMA was used to predict a nonadiabatic rate constant for **1** in NMA (upper curve in Figure 2.8).

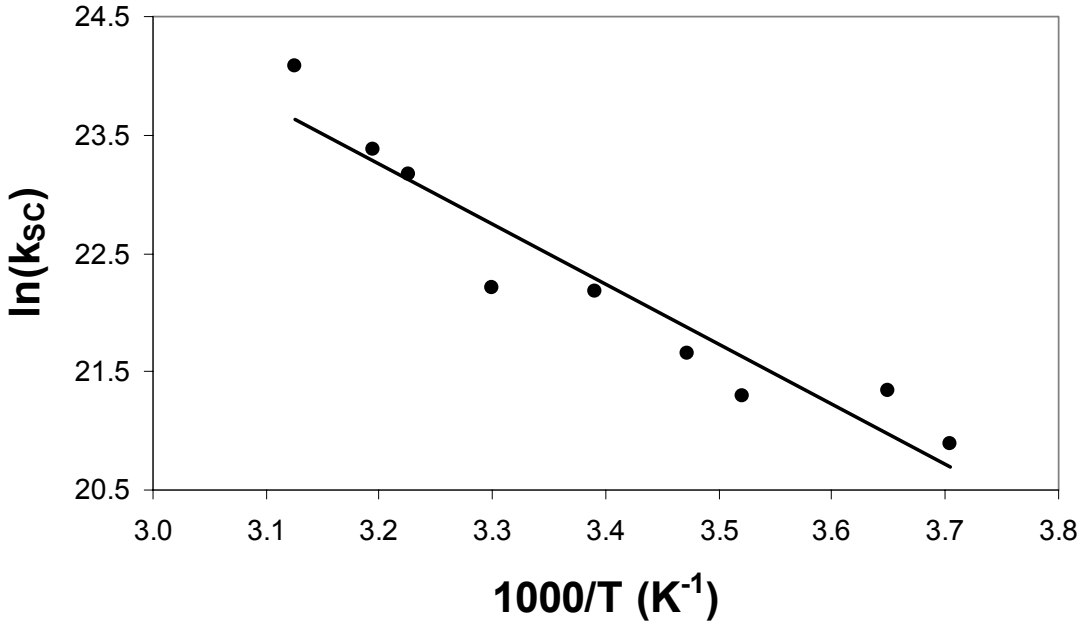

Figure 2.9 An Arrhenius plot is shown for the rate constant k_{SC}. See text for details.

Using this predicted nonadiabatic rate constant, the solvent controlled rate constant of **1** in NMA can be calculated. Figure 2.9 plots the $\ln(k_{SC})$, obtained in this manner, versus 1000/T. The plot shows that the rate constant increases as the temperature increases, and the slope gives an activation energy of 42 kJ/mol. Although data are not available for the solvation dynamics of NMA solid, temperature dependent measurements of NMA's dielectric relaxation time over the range of 201 to 227 K give an activation enthalpy of 84 kJ/mol (70 kJ/mol for the longitudinal

relaxation time). If the solvent's dielectric relaxation is linked to the electron transfer reaction, comparison of these data suggest that the coupling lies in an intermediate regime; *i.e.*, the rate constant is not inversely proportional to the polarization relaxation time but is correlated with it (see references 11 and 20). This comparison is very suggestive and experiments to measure the solvation dynamics in NMA, for comparison with these electron transfer rate constants, are underway.

2.5.4 Phenyl Ring Torsion

An alternative interpretation of the rate constant k_{sc} is conformational gating. This model treats the reaction rate as arising from a conformational rearrangement to an activated state (geometry) from which nonadiabatic electron transfer may occur. A detailed discussion of possible geometrical changes in these electron transfer systems is available elsewhere.[1] To summarize that discussion, the geometry of the system at which electron transfer occurs is different from the reactant geometry. Extrapolating from the computed relaxed geometry of the charge-separated state, the electron transfer transition state structure should differ from the reactant's structure only in the two chromophores being bent toward each other. Those findings indicate that the molecular volume decreases upon reaching the transition state, hence it is unlikely that this change in geometry would be impeded by solvent in the solid state. Because the cavity has very little free space, it is unlikely that any solvent molecules occupy the cavity, and inward motion of the chromophores would not be impeded. On the other hand, torsion of the phenyl group about the imide N-phenyl bond is another likely motion, and may possibly be coupled to the solvent coordinate. For this motion to act as a 'gate' for the electron transfer, the

phenyl torsion must modulate the magnitude of the electronic coupling because of differences in the phenyl ring's interaction with the donor and acceptor groups.

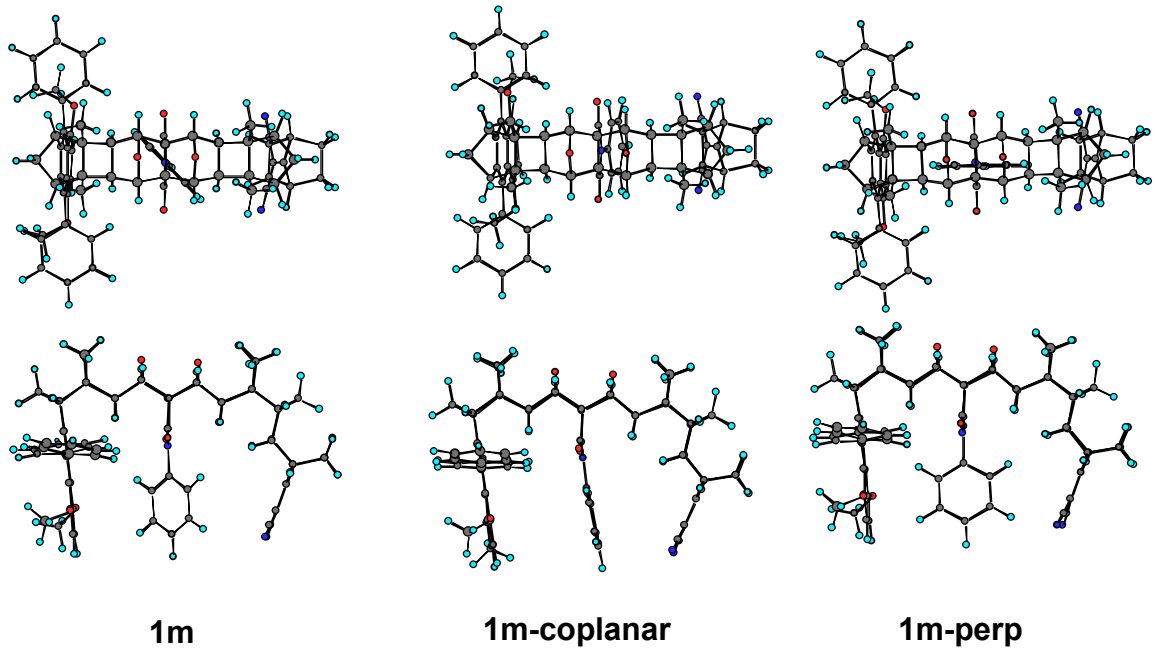

Figure 2.10 Three optimized B3LYP/6-31G(d) gas phase structures of **1m** differing in the conformation of the phenyl ring with respect to the imide group. **1m** differs from **1** only in that the four methoxymethylene groups have been replaced with methyl groups and the ethyl substituent on the phenyl ring has been removed.

To focus the discussion, we compare the magnitude of the electronic coupling for the conformation in which the phenyl ring is nearly coplanar with the imide ring (**1m-coplanar**, Figure 2.10) to that in which the phenyl ring is perpendicular to the imide ring (**1m-perp**, Figure 2.10). On the basis of orbital overlap considerations, the donor to acceptor coupling through the π and π^* molecular orbitals of the central phenyl group might be stronger in the coplanar conformation than in the perpendicular one. Indeed, B3LYP/6-31G(d) Koopmans' Theorem calculations[20] on the B3LYP/6-31G(d) optimized C_{2v} models **3** (Figure 2.11) suggest that the

electronic coupling for the coplanar conformation, **3-coplanar**, is stronger than that for the perpendicular conformation, **3-perp**. The calculations include all types of orbital interactions, however the π-orbital interactions make the largest contribution. The electronic coupling was obtained from one-half of the splitting energies for the symmetric structures in Figure 2.11, in the Koopmans' Theorem limit. The HOMO orbital splitting gives an electronic coupling of 40 cm^{-1} in the coplanar geometry and 23 cm^{-1} in the perpendicular geometry. Similarly, the LUMO orbital splitting gives couplings of 38 cm^{-1} in the coplanar geometry and 11 cm^{-1} in the perpendicular geometry.

In light of this finding, it was deemed necessary to compute the N-phenyl rotational barrier and this was done at the B3LYP/6-31G(d) level of theory using the model system, **1m**, which differs from the experimentally studied one, **1**, by replacement of the four methoxymethylene groups of the latter system by methyl groups and by removing the ethyl substituent from the phenyl ring. All calculations refer to gas phase structures. The fully optimized, global minimum energy, structure for **1m**, has the phenyl ring oriented 43^{o} with respect to the plane of the imide ring. Two distinct rotational barriers for the *N*-phenyl group may be envisaged, namely with the phenyl ring lying either approximately coplanar with the imide ring, or perpendicular to it and the transition structures corresponding to these rotational barriers were duly located – see **1m**-coplanar and **1m**-perp (Figure 2.10). Although they were optimized using no symmetry constraints, both optimized structures closely resemble the expected C_s symmetry. Note that for **1m**-coplanar, the phenyl ring actually bends a little out of coplanarity with the imide ring, towards the dicyanovinyl group.

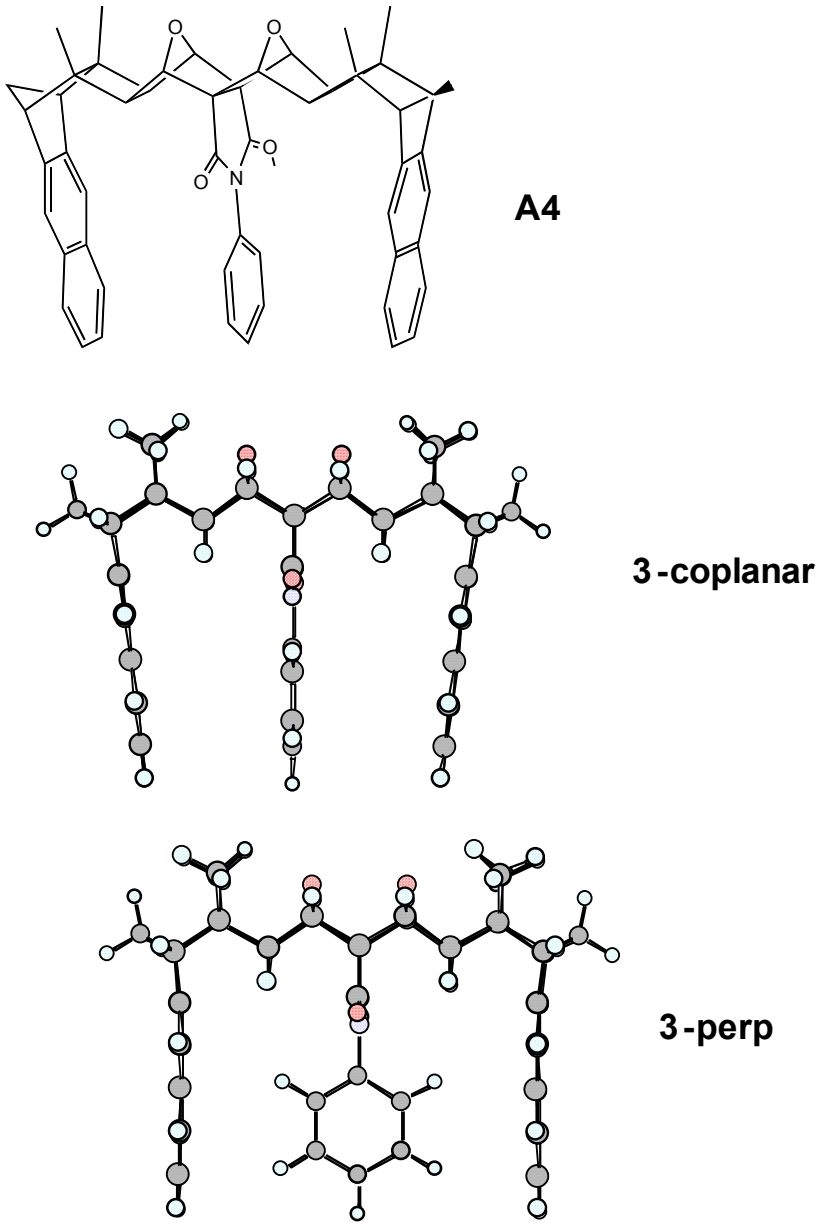

Figure 2.11 B3LYP/6-31G(d) optimized C_{2v} gas phase structures, **3-coplanr** and **3-perp**, in which the phenyl ring is, respectively, coplanar and perpendicular to the imide ring.

The (vibrationless) rotational barriers, calculated from these structures, are 3.3 kJ/mol for passage through **1m-coplanar**, and about 1 kJ/mol or less for the **1m-perp**. These barriers are extremely small and, for all intents and purposes, the phenyl group in **1m** (and **1**) may be

regarded as a free rotor. The magnitude of the electronic coupling between the phenyl group and the donor and acceptor chromophores in **1** is a Boltzmann weighted average, determined by the shape of the rotational barrier, of the different phenyl geometries.[4] Given the extreme shallowness of this barrier, it is likely that the magnitude of this coupling will not change significantly over the range of temperatures used in our electron transfer experiments. Comparison of this small barrier with that obtained from the analysis using equation 4 (*vide supra*), suggests that the phenyl torsion would need to be strongly coupled to the solvent matrix to act as the rate controlling step.

2.6 Discussion and Conclusion

The experimental observations reveal that the electron transfer for **1** in NMA changes from a nonadiabatic mechanism at high temperatures to a solvent controlled (or adiabatic) mechanism at low temperatures. This conclusion is supported by two primary observations. First, the observed excited state decay law changes from a simple exponential in acetonitrile solvent to a nonexponential form in NMA. The nonexponentiality increases with the coupling strength between the donor and acceptor species (**1** versus **2**) and the increase in the solvent relaxation time. Second, when the reaction rate is characterized by the correlation time of the emission decay law, the rate constant for **1** and **2** changes from being displaced in magnitude at high temperature (because $|V|$ is different) to being the same at low temperature. This change to a rate constant that correlates with the solvent relaxation dynamics (characterized by viscosity or polarization relaxation time) rather than the electronic coupling strength and the

nonexponentiality of the decay law are both experimental signatures of a change in the reaction mechanism.

Two possible explanations for the change in reaction mechanism, a transition from nonadiabatic electron transfer to solvent-controlled (adiabatic) electron transfer and conformational gating, are discussed. A change in the reaction mechanism from nonadiabatic to friction controlled could arise from the increasing polarization relaxation time of the NMA solvent as it is cooled. Using the model developed by Zusman[9b] (Eqn 2) and the fitting parameters in Table 2.2, the electron transfer in NMA and acetonitrile solvents at room temperature will be in the solvent friction limit when the solvent's polarization relaxation time $\tau >> 30$ ps for **2** and $\tau >> 5$ ps for **1**. The relaxation time in acetonitrile is significantly faster than this time scale (< 1 ps at room temperature[6]) and the electron transfer rate constant appears to remain nonadiabatic over the entire temperature range. By lowering the temperature and increasing the relaxation time τ in NMA (measured to be 20 to 40 ps at 300 K[6]), we can move the system strongly into the solvent controlled regime. Because the polarization relaxation (solvation) time in NMA has not been measured over this temperature range, it is currently not possible to ascertain if the rate constant correlates with the solvent relaxation time in the predicted manner.

An 'alternative' explanation for the solvent dependent electron transfer is the conformational gating mechanism, which has found wide use in protein electron transfer studies.[21] For example, the torsional motion of the phenyl ring in the cavity can modulate the electronic coupling magnitude. It is possible that other motions, in particular compression of the donor to acceptor distance, might play a role and couple to the phenyl torsional motion. The acetonitrile studies show that such motion is not completely frozen out by the low temperatures,

however the large viscosity in NMA may act to hinder this motion and give rise to solvent control. Independent studies of the phenyl torsional dynamics can be used to assess whether this mechanism is operative.

Both the 'gating' mechanism and the solvation dynamics controlling the electron transfer mechanism correspond to the '*narrow reaction window*' limit of the Sumi-Marcus treatment. In the case of electron transfer controlled by the solvent dynamics the polarization coordinate **X** would be interpreted in the manner described by Sumi and Marcus. In the case of conformational gating, the **X** coordinate should correspond to a conformational (or configurational) change of the reactant; in this case, identified with the phenyl torsional 'gate'. An advantage of using the Sumi-Marcus description is that the nonexponential character of the reactant's population density is included in a natural way, from the diffusion of the system in the solvent coordinate.

By studying the electron transfer kinetics of two U-shaped molecules over a wide range of temperature in acetonitrile and NMA, a change in the electron transfer mechanism is identified. The experimental manifestations of this mechanism change are nonexponential decay laws and rate constants that are controlled by the solvent dynamics.

2.7 Acknowledgements

We thank the Australian Research Council for support and for the award of a senior research fellowship to M.N.P.-R. We thank the Australian Partnership for Advanced Computing (APAC) and the Australian Centre for Advanced Computing and Communications (ac3) for allocation of computing time. We acknowledge support from the U.S. National Science Foundation (CHE-0111435). All experiments and analyses were performed at the University of Pittsburgh and the theoretical calculations were performed in Australia.

2.8 Appendix

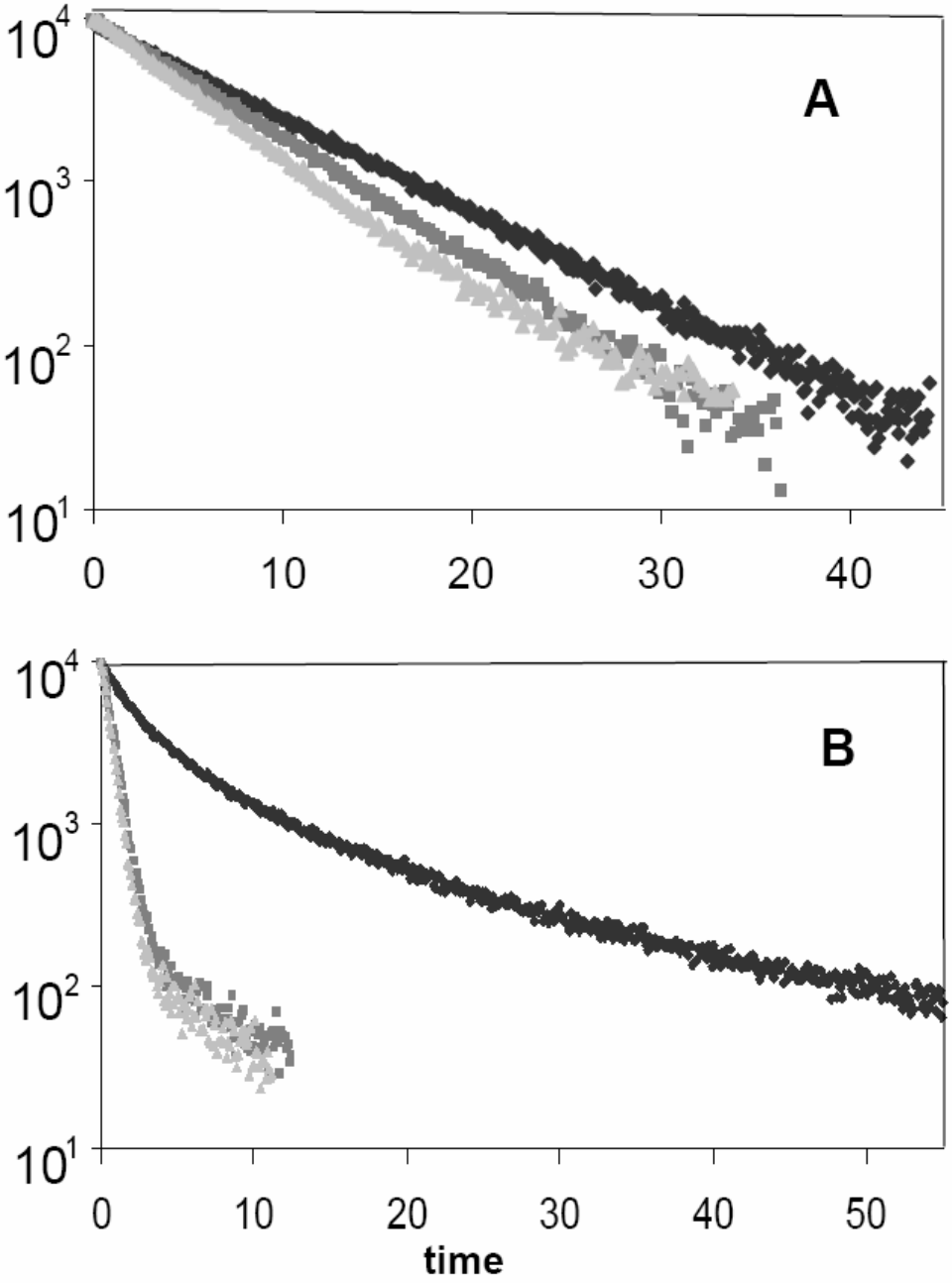

Figure 2.12 Fluorescence decay profiles are shown for **2** in acetonitrile (panel A) at three different temperatures: (diamond) 200 K, (square) 301 K, and (triangle) 317 K and NMA (panel B) at: (diamond) 200 K, (square) 295 K, and (triangle) 313 K.

2.9 References

1. Napper, A. M.; Head N. J.; Oliver A. M.; Shephard, M. J.; Paddon-Row, M. N.; Read, I.; Waldeck, D. H. *J. Am. Chem. Soc.*, **2002**, *124*, 10171.

2. Napper, A. M.; Read, I.; Waldeck, D. H.; Head, N. J.; Oliver, A. M.; Paddon-Row M. N. *J. Am. Chem. Soc.*, **2000,** *122,* 5220.

3. a) Jortner, J. *J. Chem. Phys.*, **1976**, *64*, 4860; b) Barbara, P. F.; Meyer, T. J.; Ratner, M. A. *J. Phys. Chem.*, **1996,** *100,* 13148.

4. Waldeck, D. H.; Zimmt, M. B. *J. Phys. Chem. B*, **2003**, *107*, 3580.

5. Matyushov, D. V.; Voth, G. A. *J. Chem. Phys.*, **1999**, *111*, 3630.

6. Maroncelli, M. *J. Mol. Liq.*, **1993**, *57*, 1.

7. a) Chapman, C. F. ; Fee, R. S.; Maroncelli, M. *J. Phys. Chem.*, **1990,** *94*, 4929; b) Castner, E. W.; Maroncelli, M. *J. Mol. Liq.*, **1998**, *77*, 1.

8. a) Kojima, T.; Kawabe; K. *Technology Reports of the Osaka University*, **1973**, *23*, 187; b) Kojima, T; Kawabe, K. *Oyo Butsuri*, **1973**, *42*, 9.

9. a) Zusman, L. D. *Chem. Phys.*, **1980**, *49*, 295; b) Zusman, L. D. *Z. Phys. Chem.*, **1994**, *186*, 1

10. a) Calef, D. F.; Wolynes, P. G. *J. Phys. Chem.*, **1983**, *87*, 3387; b) Rips, I.; Jortner, J. *Chem. Phys. Lett.*, **1987**, *133*, 411.

11. a) Sumi, H.; Marcus, R. A. *J. Chem. Phys.*, **1986**, *84*, 4272; b) Sumi., H.; Marcus, R. A. *J. Chem. Phys.*, **1986**, *84*, 4894; c) Marcus, R. A.; Sumi., H. *J. Electroanal. Chem.*, **1986**, *204*, 59; d) Sumi, H. *Electron Transfer in Chemistry*; Balzani, V. Ed; Wiley-VCH, New York **2001**, Vol. 1, p 64.

12. a) Onuchic, J. N., *J. Chem. Phys.*, **1987**, *86*, 3925; b) Tanimura, Y.; Leite, B. P.; Onuchic, J. N. *J. Chem. Phys.*, **2002**, *117*, 2172; c) Onuchic, J. N.; Beratan, D. N.; Hopfield, J. J. *J. Phys. Chem.*, **1986**, *90*, 3707.

13. In this case $|V_{eff}| = \sqrt{\pi}\ |V| \exp(-\lambda_v/2h\nu)$.

14. a) Berezhkovskii, A. M.; Zitserman, V. Y. *Physica A*, **1990**, *166*, 585; b) Berezhkovskii, A. M.; Zitserman V. Y. *Chem. Phys. Lett.*, **1990**, *172*, 235; c) Waldeck, D. H. *J. Mol. Liq.*, **1993**, *57*, 127.

15. a) Maroncelli M.; MacInnis, J. and Fleming, G. R. *Science,* **1989**, *243*, 1674; b) Barbara, P. F., Walker, G. C. and Smith, T. P. *Science*, **1992**, *256*, 975; c) Castner, E. W.; Bagchi, B.; Fleming, G. R. *Chem. Phys. Lett.*, **1988**, *143*, 270; d)Van der Zwan, G.; Hynes, J. T. *J. Phys. Chem.*, **1985**, *89*, 4181; e) Bagchi, B.; Oxtoby, D. W.; Fleming, G. R. *Chem. Phys.*, **1984**, *86*, 257.

16. Head, N. J.; Oliver, A. M.; Look, K.; Lokan, N. R.; Jones, G. A.;Paddon-Row, M. N. *Angew. Chem., Int. Ed.*, **1999**, *38*, 3219.

17. The molecular structures for the donor only compounds may be found in reference 1.

18. a) Gaines, G. L. III; O'Neil, M. P.; Svec. W. A.; Niemczyk, M. P.; Wasielewski, M. R. *J. Am. Chem. Soc.*, **1991**, *113*, 719; b) Miller, J. R. *Science*, **1975**, *189*, 221.

19. Knecht, L. A. *Pure and Applied Chemistry*, **1971**, *27*, 281.

20. All calculations reported in this paper were carried out at the B3LYP/6-31G(d) level of theory using the GAUSSIAN 98 package: Frisch, M. J.; Trucks, G. W.; Schlegel, H. B.; Scuseria, G. E.; Robb, M. A.; Cheeseman, J. R.; Zakrzewski, V. G.; Montgomery Jr., J. A.; Stratmann, R. E.; Burant, J. C.; Dapprich, S.; Millam, J. M.; Daniels, A.D.; Kudin, K. N.; Strain, M. C.; Farkas, O.; Tomasi, J.; Barone, V.; Cossi, M.; Cammi, R.; Mennucci, B.;

Pomelli, C.; Adamo, C.; Clifford, S.; Ochterski, J.; Petersson, G. A.; Ayala, P. Y.; Cui, Q.; Morokuma, K.; Malick, D. K.; Rabuck, A. D.; Raghavachari, K.; Foresman, J. B.; Cioslowski, J.; Ortiz, J. V.; Stefanov, B. B.; Liu, G.; Liashenko, A.; Piskorz, P.; Komaromi, I.; Gomperts, R.; Martin, R. L.; Fox, D. J.; Keith, T.; Al-Laham, M. A.; Peng, C. Y.; Nanayakkara, A.; Gonzalez, C.; Challacombe, M.; Gill, P. M. W.; Johnson, B.; Chen, W.; Wong, M.W.; Andres, J. L.; Gonzalez, C.; Head-Gordon, M.; Replogle, E. S.; Pople, J. A. *Gaussian 98, Revision A.7*; Gaussian Inc: Pittsbugh, PA.

21. a) Davidson, V. L. *Acc. Chem. Res.*, **2000**, *33*, 87; b) Davidson, V. L. *Biochemistry*, **2000**, *39* , 4924; c) Jeuken, L. J. C. *Biochim et Biophys. Acta-Bioenergetics*, **2003**, *67*, 1604.

Chapter 3 Solvent Friction Effect on Intramolecular Electron Transfer

U-shaped donor-bridge-acceptor molecules with different electronic couplings have been investigated as a function of temperature in solvents with slow polarization relaxation, in particular N-methylacetamide (NMA) and N-methylpropionamide (NMP). At high temperature, the electron transfer rate is well described by a nonadiabatic model; however, the rate at low temperature is controlled by the solvent friction. The change of the electron transfer mechanism is discussed and compared with theoretical models.

3.1 Introduction

Electron transfer reactions are of broad importance in chemistry, biology, and related technologies. For this reason a large body of work explores electron transfer processes over a broad range of different conditions and systems.[1,2,3,4] Our work addresses fundamental issues in electron transfer by using donor-bridge-acceptor molecules to manipulate the interaction between the electron donor (reductant) and electron acceptor (oxidant) groups. The present work reports studies of two different donor-bridge-acceptor molecules in polar solvents with different solvation timescales and demonstrates how electron transfer proceeds from electron tunneling control to solvent friction control.

Most studies have found that electron transfer reactions proceed in one of a few limiting regimes: nonadiabatic electron transfer, adiabatic electron transfer, or solvent controlled[5] electron transfer. In nonadiabatic electron transfer reactions the reaction rate constant is

appropriately described by a transition state theory rate constant times a transmission factor which depends on the electron tunneling probability. In the adiabatic and solvent-controlled electron transfer regimes the reaction rate is controlled by nuclear motion(s) of the system through the transition state region, rather than by the electron tunneling probability. The current studies are distinguished from other works by the ability to probe how the electron transfer rate constant proceeds from a nonadiabatic mechanism to a solvent-controlled mechanism.

A previous study considered photoinduced intramolecular electron transfer in two U-shaped donor-bridge-acceptor molecules **1** and **2** (see scheme 1). Upon photoexcitation, these molecules transfer an electron from the naphthalenic group to the dicyanovinyl group by electron tunneling through the imide-functionalized cleft.[6] The nature of the chemical group (pendant) in the cleft changes the electron tunneling probability. An earlier study[7] demonstrated the transition between nonadiabatic (electron tunneling) electron transfer and solvent-controlled electron transfer in the system **1**, by comparing the rate constant in acetonitrile to that in N-methylacetamide. The current work extends that study by varying the initial excitation energy of the donor, by performing rate studies in N-methylpropionamide, which has dielectric properties similar to NMA but remains a liquid over the entire temperature range, and by measuring the solvent polarization relaxation times of these solvents, which allows quantitative comparisons of the rate constant behavior with model predictions.

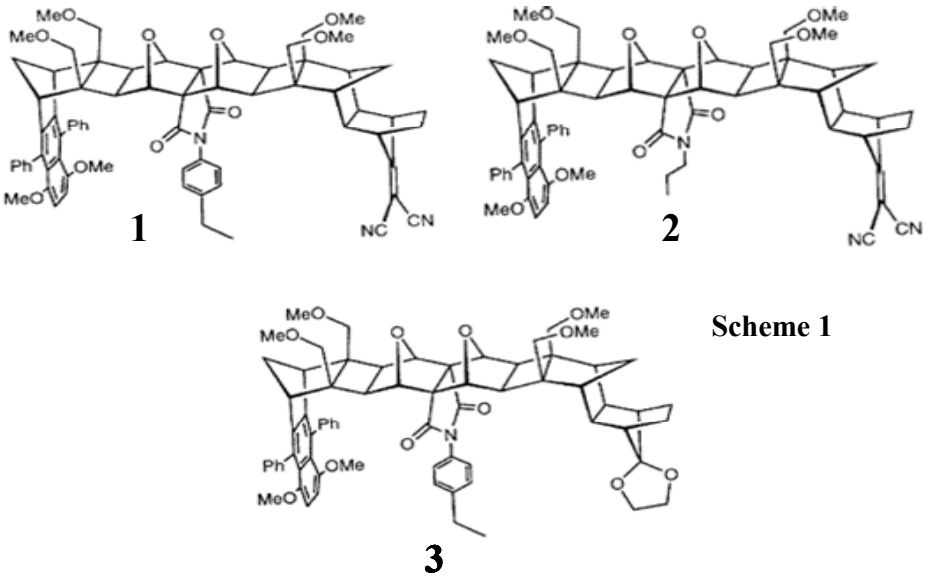

Scheme 1

This report has five major sections. The next section provides background on electron transfer models that account for solvent frictional coupling and briefly describes solvation models. The following section describes the experimental details. The next two sections analyze the experimental results and compare them to models. The last section concludes this work and describes its implications.

3.2 Background

For the U-shaped molecules investigated here the electronic coupling between the donor and acceptor groups is weak enough that a nonadiabatic picture applies. Previous work showed that the Golden Rule rate constant expression k_{NA}[8] with a single effective quantum mode,

$$k_{NA} = \frac{4\pi^2}{h} |V|^2 \frac{1}{\sqrt{4\lambda_o \pi k_B T}} \sum_{n=0}^{\infty} \exp(-S)\left(\frac{S^n}{n!}\right) \exp\left[-\frac{(\Delta_r G + \lambda_o + nh\nu)^2}{4\lambda_0 k_B T}\right] \qquad \mathbf{1}$$

adequately describes the rate behavior in simple solvents with rapid dielectric relaxation times. In Equation 1, λ_0 is the solvent reorganization energy; $\Delta_r G$ is reaction free energy; λ_v is the energy required for high-frequency vibrational reorganization; $|V|$ is the electronic coupling

between the reactant and the product states, and $S = \frac{\lambda_v}{h\nu}$. The $h\nu$ term is the energy spacing of a single effective quantized vibration associated with the electron transfer event, which is taken to be a characteristic feature of the solute. The sum is performed over the vibrational states of the effective quantum mode. The semiclassical theory treats the low frequency modes classically. The electronic coupling $|V|$ in the U-shaped molecules is smaller than k_BT, but not much smaller and it is possible to observe a change in electron transfer mechanism by changing the solvent friction.

Three different regimes, or mechanisms, are observed in electron transfer reactions: nonadiabatic electron transfer, adiabatic electron transfer, and solvent controlled electron transfer. In the nonadiabatic case, the electronic coupling is weak $|V| << k_BT$, the rate constant is proportional to $|V|^2$ and Equation 1 applies. In this limit, the system may move through the curve crossing region $\mathbf{q}^{\ddagger}$ many times before the electronic state changes from **r** to **p** (see Figure 3.1). In the adiabatic case, $|V| >> k_BT$ and the reaction proceeds by nuclear motion through the transition state along a single electronic state. The effect of $|V|$ on the rate constant is only manifest through its role in determining the energy barrier, $\Delta G^{\ddagger}$ (Figure 3.1). In the solvent controlled limit the electronic coupling may still be small; however the rate constant is affected by frictional coupling. In this case, the characteristic time spent in the curve crossing region is long enough that the electronic state changes from **r** to **p** for nearly every approach, even though the coupling is weak. Hence the reactant appears adiabatic in the sense that the rate is limited by nuclear dynamics rather than by the electron tunneling probability.

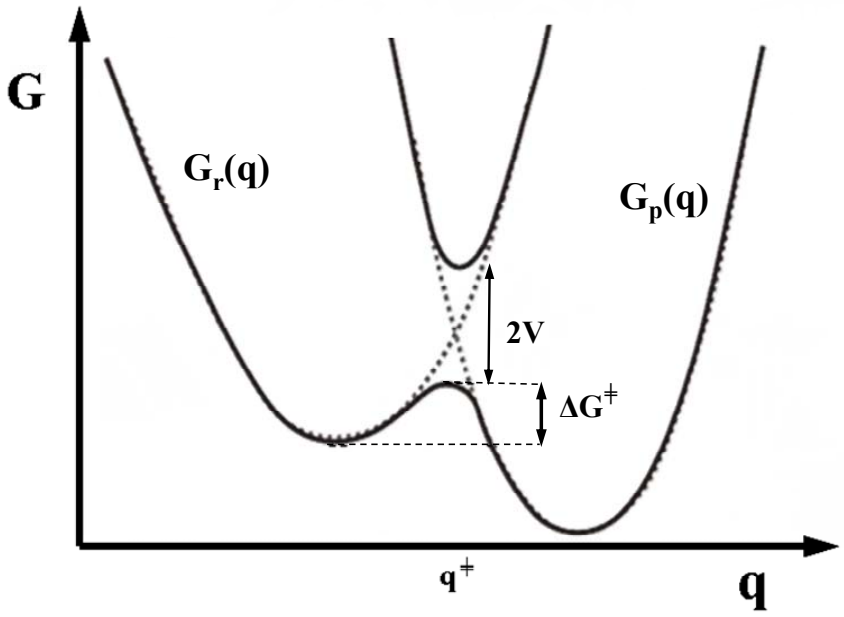

Figure 3.1 Diagram illustrating the adiabatic and nonadiabatic potential surfaces; for adiabatic electron transfer (strong coupling), the solid curves apply, whereas for nonadiabatic electron transfer, the diabatic (dashed) curves apply. (**r** denotes the reactant and **p** denotes the product)

Zusman[9] generalized the rate constant expression for electron transfer k_{ET}, to describe a transition between the normal nonadiabatic limit k_{NA} and a solvent controlled limit k_{SC}, namely

$$\frac{1}{k_{ET}} = \frac{1}{k_{SC}} + \frac{1}{k_{NA}} \qquad \textbf{2}$$

Equation 2 shows that the measured electron transfer rate k_{ET} can be limited by either the electronic motion (k_{NA} is small) or the nuclear motion (k_{SC} is small). The slower process is rate controlling. In the classical limit he found

$$k_{SC} = \frac{1}{\tau_s}\sqrt{\frac{\lambda_0}{\pi^3 k_B T}}\sin(\pi\sqrt{\frac{\Delta G^{\ddagger}}{\lambda_0}})\exp\left(-\frac{\Delta G^{\ddagger}}{k_B T}\right) \qquad \textbf{3}$$

in which the electron transfer rate is proportional to the solvation rate, $1/\tau_s$. Since the solvation time τ_s increases dramatically with decreasing temperature, especially in viscous solvents, the solvation time becomes more important as the temperature is lowered.

Sumi and Marcus[10] considered the combined effects of intramolecular vibrations and diffusive solvent orientational motions on electron transfer. They described the reaction as proceeding along a two-dimensional effective potential energy surface, V(q,X) (see Figure 3.2). The coordinate X corresponds to the solvent polarization (the polarization response of the solvent to changes of the charge distribution), and q is an intramolecular vibrational coordinate, which includes the fast nuclear motions typical of electron transfer reaction in the nonadiabatic or adiabatic limit. In order to find the reaction rate, they solved the Fokker-Planck equation (Eq. 4) for diffusive motion along X and treated the motion along q through a rate constant k(X) that depends on the 'fast' motions in the normal way (e.g., Eq. 1) and depends parametrically on X. In particular, they solved

$$\frac{\partial Q(X,t)}{\partial t} = D\frac{\partial^2 Q(X,t)}{\partial X^2} + \frac{D}{k_B T}\frac{\partial}{\partial X}\left(Q(X,t)\frac{dV(X)}{dX}\right) - k(X)Q(X,t) \qquad \textbf{4}$$

where D is the diffusion coefficient, V(X) is the effective potential for the polarization coordinate, and Q(X,t) is a probability distribution function for the reactant. The decay of the net reactant probability Q(t) determines the fluorescence decays, which are used to measure the electron transfer rates in the U-shaped DBA molecules, **1** and **2**.

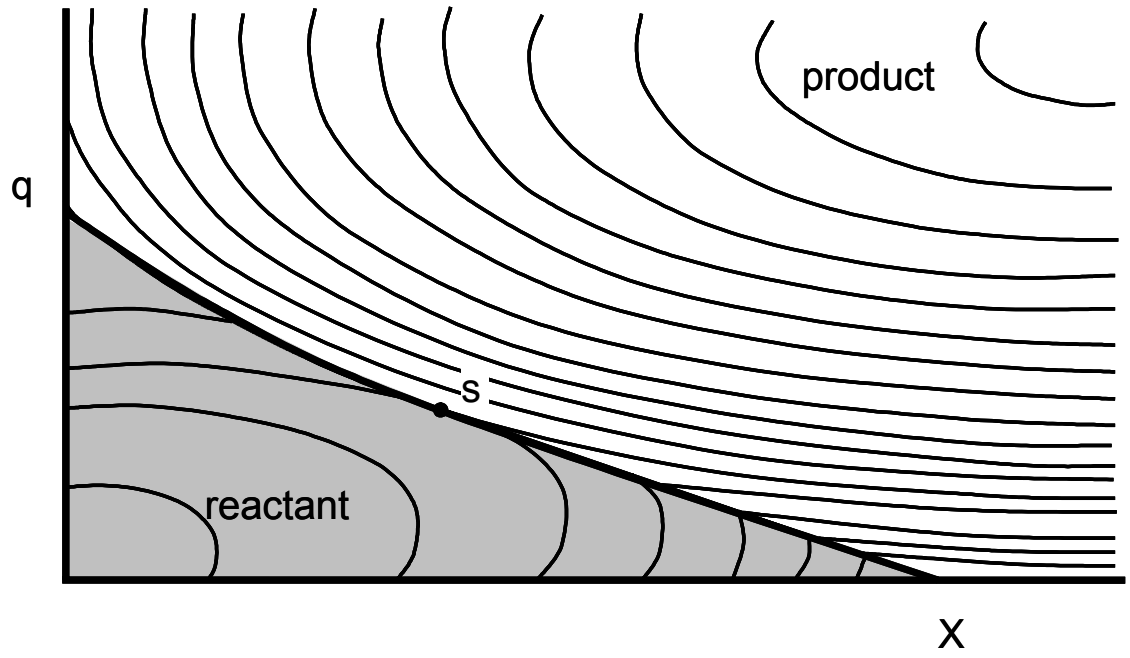

Figure 3.2 A two dimensional V(q,X) reaction coordinate. The shaded area represents the reactant surface. The thick line is the dividing line (ridge) between the reactant and product surfaces. The reactant well is at the bottom left, the product well is at the top right, and point S is the saddle point on the ridge line. Adapted from Ref 10.

Sumi and Marcus proposed four limiting cases for the probability distribution. The first case is the fast diffusion limit, where the polarization coordinate X is at all times proportional to the thermal distribution and Q(t) shows a single exponential decay. In this case, the reaction is either adiabatic or nonadiabatic and it does not depend on solvent friction. The second case is called the slow diffusion limit, where the polarization coordinate X is almost frozen because the solvation time is much longer than the reaction time and the probability distribution decays nonexponentially. The third case is the narrow reaction window, which corresponds to a vanishing contribution of the intramolecular degrees of freedom to the electron transfer reaction. It occurs when the solvent reorganization is much larger than the internal reorganization energy, and nonexponential decays are also predicted in this limit. The last case is called the wide

reaction window, where the internal reorganization energy is much larger than the solvent reorganization energy. More detail on this model is provided in the analysis section as it is needed.

Previous modeling of these U-shaped molecules in fast solvents found an internal reorganization energy λ_v of 0.65 eV and an effective quantum mode frequency of 1600 cm^{-1}. Comparison with solvation models indicates that the solvent reorganization energy λ_0 lies between 1.2 eV and 1.4 eV for **1** and **2** in NMA and NMP (*vide infra*). The ratio λ_v/λ_0 is thus approximately 0.5, which places these reactions in the narrow reaction window limit of Sumi and Marcus. This limit is also one in which Zusman's predictions (Eqs. 2 and 3) should apply. Sumi and Marcus pointed out the nonexponential character in the narrow reaction window limit, however Zusman's treatment does not address this feature.

3.3 Solvation

The solvent reorganization energy and reaction free energy are important determinants of the electron transfer rate in any of the limits, and accurately modeling these solvation energies as a function of temperature is important to properly interpreting the present experiments. Two models are currently popular for describing solvation energies − the dielectric continuum model and a molecular solvation model. The dielectric continuum model[11] calculates solvation energies using the static dielectric constant ε_s and a high frequency dielectric constant ε_∞ of the solvent. In its simplest implementation, the solute is treated as a spherical (or ellipsoidal) cavity containing a point dipole. The solvent reorganization energy is described as:

$$\lambda_0 = \frac{(\Delta\mu)^2}{a_o^3}\left(\frac{\varepsilon_s - 1}{2\varepsilon_s + 1} - \frac{\varepsilon_\infty - 1}{2\varepsilon_\infty + 1}\right) \qquad \textbf{5}$$

and the reaction free energy from this model is

$$\Delta_r G = \Delta_{vac} G - \frac{\left(\mu_{CS}^2 - \mu_{LE}^2\right)}{a_o^3}\left(\frac{\varepsilon_s - 1}{2\varepsilon_s + 1}\right) \qquad \mathbf{6}$$

where μ_{LE} is the dipole moment of the initially excited state, μ_{CS} is the dipole moment of the charge-separated state, and a_0 is the cavity radius. $\Delta\mu$ is the magnitude of the dipole moment difference vector between the locally excited and the charge separated states; i.e. $\Delta\mu \equiv \left|\vec{\mu}_{CS} - \vec{\mu}_{LE}\right|$. $\Delta_{vac}G$ is the reaction Gibbs free energy in the absence of solvation.

The molecular solvation model developed by Matyushov[12] accounts for the discrete nature of the solute and the solvent. Typically, the solute is approximated by a sphere with a point dipole moment and polarizability, and the solvent is modeled as a polarizable sphere, with an electrostatic charge distribution that includes both a point dipole and a point quadrupole. The molecular solvation model is more realistic than the dielectric continuum model because it includes not only the dipole-dipole interactions, but also the dipole-quadrupole interactions between the solute and solvent. Importantly, the molecular model properly accounts for the temperature dependence of the solvation.[13]

Previous reports parameterized the molecular solvation model for **1** and **2** in the weakly polar solvents toluene and mesitylene. In that work, excited state equilibria between the charge separated state and the locally excited state were used to calibrate the molecular solvation model for reaction free energy. This parameterization was shown to provide temperature-dependent reorganization energies in good accord with experiment. In the present work, the molecular solvation model and these previously derived model parameters were utilized to calculate the reaction free energies and solvent reorganization energies of **1** and **2**. This procedure provides a self-consistent analysis for these solute molecules.

3.4 Experimental

The structures of **1**, **2** and **3** are shown in Scheme 1. Synthesis of the U-shaped supramolecules is reported elsewhere.[14] The solvent N-methylacetamide (NMA) was purchased from Aldrich, and N-methylpropionamide (NMP) was purchased from TCI America. NMA and NMP were fractionally distilled three times using a vigreux column under vacuum. The freshly purified fraction was used in all the experiments. Each sample went through a freeze-pump-thaw procedure five or more times to eliminate dissolved oxygen.

Time-resolved fluorescence kinetics of **1** and **2** were measured using Time Correlated Single Photon Counting technique.[15] The instrument used here is based on the frequency-doubled output of a cavity-dumped Coherent CR599-01 dye laser, which was pumped by a mode locked Coherent Antares Nd:YAG laser. The full-width at half maximum of the instrument function is ~ 60 ps. Different dyes were used in this experiment to obtain the different excitation wavelengths: Rhodamine 6G dye was used to obtain 296 nm and 310 nm wavelength, DCM dye was used to obtain 326 nm, and LDS 722 (also named pyridine 2 dye) was used to obtain 359 nm wavelength. The dye laser pulse train had a repetition rate of ca. 300 kHz. Pulse energies were kept below 1 nJ and the count rates were kept below 3 kHz to prevent pile-up effects. All fluorescence measurements were made at the magic angle and data was collected until a standard maximum count of 10000 was observed at one channel.

The experiments for **1**, **2** and their donor-only analogues were carried out in NMA and NMP as a function of temperature at four different excitation energies. The temperature ranged from a low of 226 K to a high of 353 K. At the high end of this range, temperatures were controlled by an ENDOCAL RTE-4 chiller, measured using a Type-K thermocouple (Fisher-Scientific), accurate to within 0.1 ºC. Measurements at lower temperatures employed a VPF-100

Cryostat (Janis Research Company, Inc) and a Model 321 Autotuning Temperature Controller (LakeShore Cryotronics, Inc.) with a silicon diode sensor. The low temperature instrumental setup is shown in the appendix A.

Temperature measurement was improved from the earlier design by including another type-T thermocouple attached on the surface of the cuvette to monitor the temperature, in addition to the silicon sensor used for temperature control, which is not directly in contact with the sample cuvette. The temperatures measured at the cuvette surface are close to those measured when a thermocouple is directly inserted into the liquid sample, within 1 K, but they are systematically higher than the temperature measured from the diode sensor. The worst case was observed at the lowest temperature (220 K) which has a 10 K difference.

3.4.1 Lifetime Measurements

The samples of **1** and **2** each contain a small amount of unreacted donor compound. Independent experiments on the donor-only molecule **3** were used to characterize its single exponential fluorescence decay, which is much longer than the relaxation times of **1** and **2** at the measurement temperatures. To account for emission from this impurity, a component with the lifetime of the donor-only molecule **3** was fixed in the fits to the data collected with compounds **1** and **2**. The impurity component amounted to less than 8% of the overall decay law in all cases. The remaining part of the **1** and **2** decay laws in NMA and NMP were fitted as a double exponential function using IBH-DAS6 analysis software. The instrument response function, measured using a sample of colloidal $BaSO_4$, was convoluted with the decay curves.

3.4.2 Time-resolved Stokes Shift Measurements

For solvation measurements, samples at concentrations providing optical densities of ~ 0.1 for a 1 cm path length were prepared in quartz cuvettes. Samples above 7°C were thermostatted to ± 0.1°C using a circulating water bath and sample holder assembly. For lower temperature measurements, sealed cryogenic cuvettes were enclosed in a copper block mounted on the cold finger of a liquid nitrogen cryostat (Oxford Instruments DN1754). With this system, temperatures between 85 K and 300 K could be maintained constant to within ~ 1 K.

Time-resolved emission measurements were made using a time-correlated single photon counting system previously described.[16] This system employed the doubled output of a femtosecond mode-locked Ti:sapphire laser (Coherent Mira 900F) for excitation at 420 nm or 374 nm, and had an overall response time of 25 ps (FWHM) for higher temperatures and 100 ps for lower temperatures using the cryostat, as measured by scattering. The repetition rate of the excitation was set according to the lifetime of the solvation probe. Emission was collected through a single monochromator (ISA H10) with a 4 nm bandpass. Emission decays were fit with instrumental response functions using an iterative reconvolution least squares algorithm,[17] which enhances the effective time resolution to ~ 5 ps. Time-resolved emission spectra were constructed from a series of nine to twelve magic angle decays recorded at wavelengths spanning the emission spectrum, as previously described.[18]

Steady-state emission spectra were measured on a Spex Fluorolog 1680 (0.22 m double spectrometer with 1 s integration time). The steady-state spectra were utilized to normalize the time-resolved emission spectra at each temperature.

3.5 Results

3.5.1 Steady-State Spectra

Steady-state spectra of **1** in three different solvents (acetonitrile, ACN; N-methylacetamide, NMA; N-methylpropionamide, NMP) are compared in Figure 3.3. It is evident that the spectral shapes are very similar in these three solvents, which suggests that the solvent molecules do not alter the spectroscopic characteristics of the donor group; that is, the three solvents interact similarly with the solute. The higher absorbance of **1** in NMP between 340 − 360 nm arises from the impurity in NMP. Lifetime measurements were carried out at longer wavelengths to avoid interference from this solvent impurity emission.

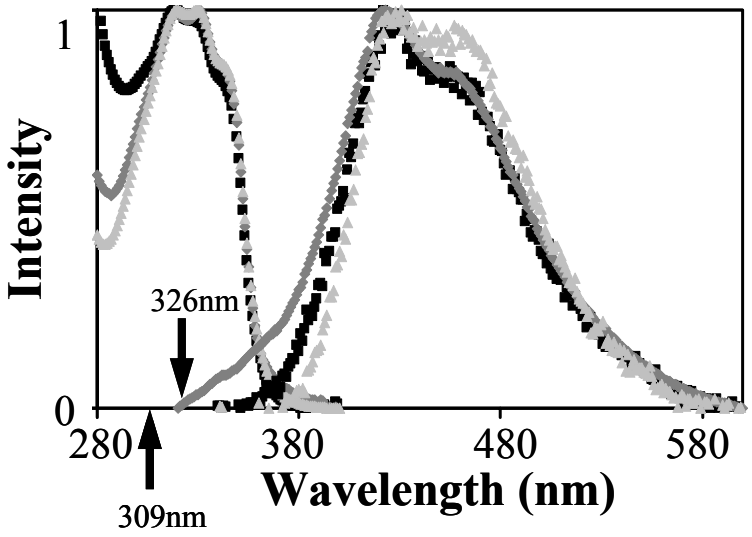

Figure 3.3 Steady-state spectra of **1** in ACN (triangle), NMA (square) and NMP (diamond). The absorption spectra are on the left, and the emission spectra are on the right.

Table 3.1 The properties of solvent ACN, NMA and NMP at 303 K

Solvent	Refractive Index[a]	Static Dielectric Constant[a]	Debye Relaxation Time[19] (ps)	Average Solvation Time(ps)	Viscosity[a] (cP)	Dipole Moment (D)
ACN	1.34	34.75	3	0.9	0.3	3.48
NMA	1.43	178.9	390	35[c]	3.9	5.05[d]
NMP	1.43	164.4	100	42[c]	4.6	4.29[d]

[a] Beilstein database

[b] 298 K, from reference 19

[c] Extracted from the best fit of the dynamic Stoke-shift measurement

[d] Calculated using Gaussian/MP2/6-31G

The solvents ACN, NMA, and NMP have similar static dielectric properties but very different solvation dynamics. Table 3.1 reports some properties of these solvents at 303 K. ACN has very fast relaxation times and low viscosity, so it can reorient much faster than the measured electron transfer rate. As for NMA and NMP, the slow relaxation times mean that polarization fluctuations occur on timescales that are similar to, or slower than, the electron transfer timescale.

3.5.2 Solvent Comparisons

The intramolecular electron transfer in **1** and **2** occurs from the locally excited state of the dimethoxydiphenylnaphthalene donor to generate a non-fluorescent charge separated state. Because the electron transfer competes with the intrinsic fluorescence, the change in the fluorescence decay law with solvent or temperature directly reflects the change in the electron transfer rate if the intrinsic fluorescence rate is unchanging at each temperature in every solvent.

By assuming that this intrinsic fluorescence rate constant is given by the observed decay of the donor-only compound, k_F (**3**) the electron transfer rate constant k_{ET} can be found from the measured fluorescence rate constants k_F; i.e., $k_{ET} = k_F - k_F$ (**3**). Fluorescence lifetime experiments were performed at different temperatures ranging from 360 K to 226 K, in the different solvents NMA, NMP and ACN, and at different excitation energies (296 nm, 309 nm, 326 nm, 359 nm).

Similar to the results reported earlier in NMA, the fluorescence decay of **1** in NMP is nonexponential at low temperature and becomes more exponential at higher temperatures. At 232 K, a fast lifetime component of 1.96 ns with an amplitude of 52% is observed. With increasing temperature, the amplitude of the fast component increases and the overall decay law becomes more like a single exponential function. For example, a fast component of 224 ps with a 94% amplitude ratio is observed at 333 K.

Because the decay law is not single exponential, the electron transfer rate constant is not well-defined. To quantify the rate in terms of an effective rate constant, a correlation time τ_c is computed from the fluorescence decay law, namely $\tau_c = f_1\tau_1 + (1-f_1)\tau_2$. Here, τ_1 and τ_2 are the two time constants obtained from the decay fits, and f_1 is the amplitude of the short time constant, excluding the contribution from the donor-only impurity. By subtracting the donor-only lifetime, an effective electron transfer rate constant is found, *i.e.*, $k_{ET} = 1/\tau_c - k$(**3**). This choice goes smoothly to the proper rate constant as the decay law becomes single exponential.

To compare the behavior in NMA and NMP, the decay curves of **1** in NMA and NMP at two representative temperatures are plotted in Figure 3.4. The difference between the decay curves at 333 K is small. At high temperature, the static dielectric properties of NMA and NMP are similar. If the solvation in the two solvents are similar (Δ_rG and λ), then the nonadiabatic

electron transfer rate of **1** in these solvents should be similar, as observed. Note that the second component in the decay law in Figure 3.4B is only ~ 3% in amplitude. At 250 K, the two decay curves differ more than at high temperature.

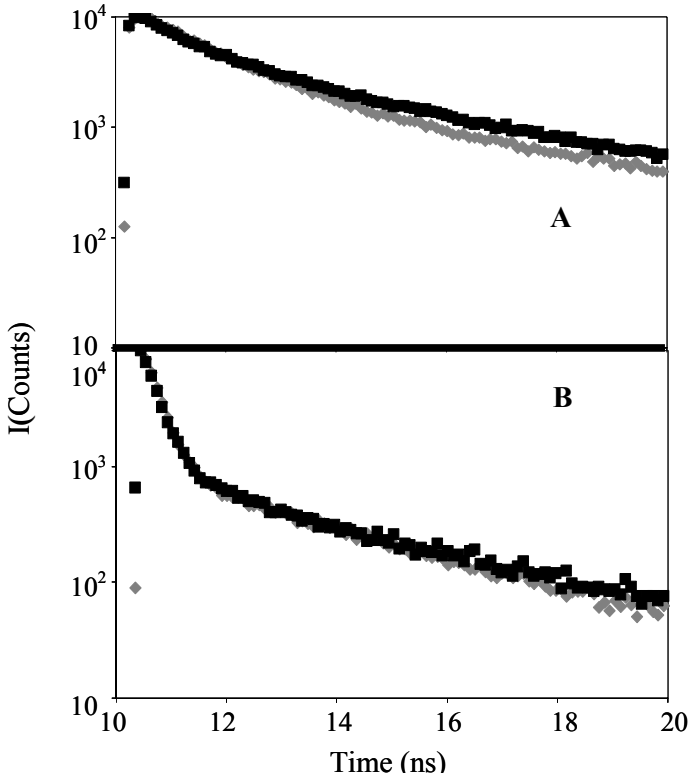

Figure 3.4 The decay curves of **1** in NMA(black) and NMP(gray) at 250 K(A) and 333 K(B) excited at 326 nm.

To better illustrate the differences between electron transfer in NMA and NMP, the temperature-dependence of the experimental rate constants are plotted in Figure 3.5. For a given solute-solvent combination, this plot should be linear if the semiclassical equation for nonadiabatic electron transfer (Eq. 1) is followed, which is supported by the rate data for both **1** and **2** in each solvent at high temperature. The temperature dependence of the rate constants of **1** and **2** in NMP are qualitatively similar to that observed in NMA. As the temperature increases,

the electron transfer rates of **1** and **2** in NMP become more different, but with decreasing temperature, they become more alike. At high temperature, the rate constant of **1** is similar in NMA and NMP (also for **2**), and differences in the solvent are less important. In contrast, the rate constants at low temperature are separated by the solvent type rather than the solute type.

An earlier report[7] compared the electron transfer rate constants in NMA to those in acetonitrile and showed that for acetonitrile the rate constants of **1** and **2** remained displaced over the entire temperature range. Hence the change in character of the k_{ET} versus T plot results from properties of the solvents, not just the temperature.

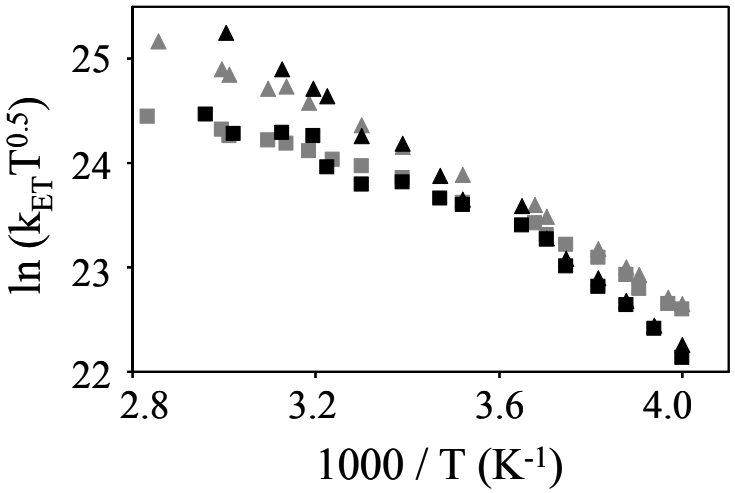

Figure 3.5 Electron transfer rate constants of **1** (triangle) and **2** (square) in NMP(gray) and NMA(black) as a function of temperature excited at 309 nm. The format of this plot is such that the data should be linear if Eq. 1 is obeyed.

Both NMP and NMA are highly polar and have "very slow" dielectric relaxation times (see Table 3.1). At high temperatures, the electron transfer rates of **1** and **2** in NMA and NMP are very similar, suggesting that the reorganization and reaction free energies are similar, a result

which is consistent with the large dielectric constants of these solvents and a nonadiabatic electron transfer mechanism. At low temperatures, the electron transfer appears to be controlled by the solvent and they are different in NMA and NMP. Considering their different physical properties (NMA solidifies at temperatures below 303 K, whereas NMP remains a liquid even at 226 K; see below), it is reasonable to expect that the solvation time of NMA is longer than that of NMP, and that the viscosity of NMA is higher than that of NMP. If the solvent dynamics controls the electron transfer rate, then one expects a smaller rate constant for NMA, as observed.

3.5.3 Excitation Energy

If the solvent is sluggish enough, then the locally excited state may not be equilibrated with the solvent before electron transfer. To test for this nonequilibrium effect on the reaction, the fluorescence decay was studied as a function of excitation energy. Figure 3.6 shows the temperature dependence of the rate constants for **1** and **2** at two different excitation energies, 309 nm and 326 nm. Another excitation wavelength 296 nm was also studied, and its rate is not distinguishable from that of 309 nm and 326 nm. Experiments, using 359 nm excitation were not conclusive because of weak signal levels.

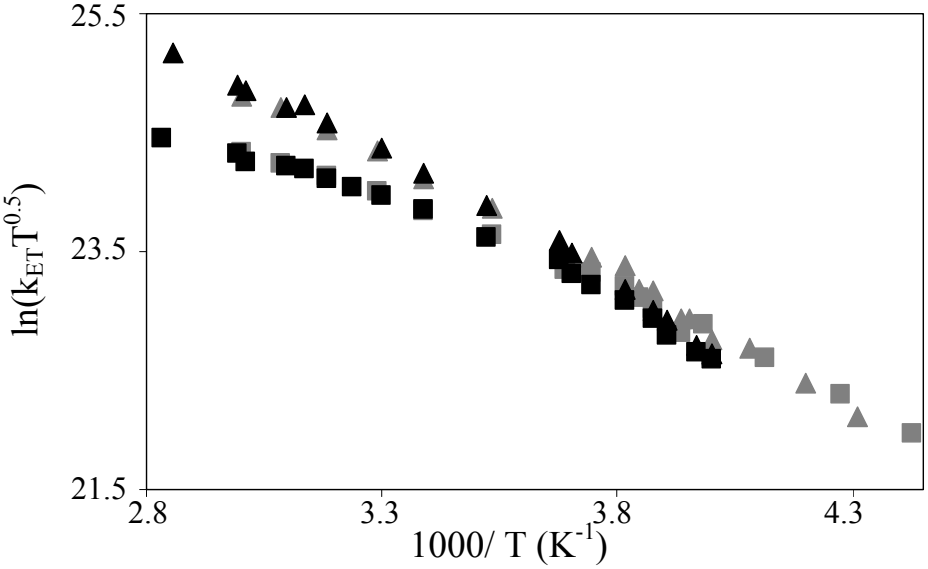

Figure 3.6 Electron transfer rates of **1** (triangle) and **2** (square) in NMP at different temperatures excited at 309 nm(black) and 326 nm(gray).

As illustrated in Figure 3.6, the electron transfer rates for **1** and **2** do not vary significantly with the excitation energy. This behavior is consistent with electron transfer from a locally excited state that is equilibrated with the solvent, i.e., even though the solute is excited with a higher energy, the solute molecules retain no memory of the initial excess energy. In the subsequent analysis, we therefore focus exclusively on data collected using 309 nm excitation.

3.5.4 Dynamic Stokes-Shift

To better quantify how the solvent dynamics affects the electron transfer, dynamic Stokes-shift measurements of solvation times were performed in NMA and NMP. Because the Stokes-shift of **1** and **2** is small, other solute chromophores were used to probe the solvent response. In NMP the solute 4-aminophthalimide was used to measure the solvation time. For temperatures ranging from 240 K to 298 K, the solvation time varies from 719 ps to 56 ps.

Because the relaxation in NMA is so slow, two solutes were used: $Ru(bpy)_2(CN)_2$ at 200 K and 4-aminophthalimide at temperatures ranging from 220 K to 298 K. For $Ru(bpy)_2(CN)_2$ in NMA, the solvation time is approximately 560 ns at 200 K and for 4-Aminophthalimide in NMA, the solvation time varies from 32 ns at 220 K to 70 ps at 298 K.

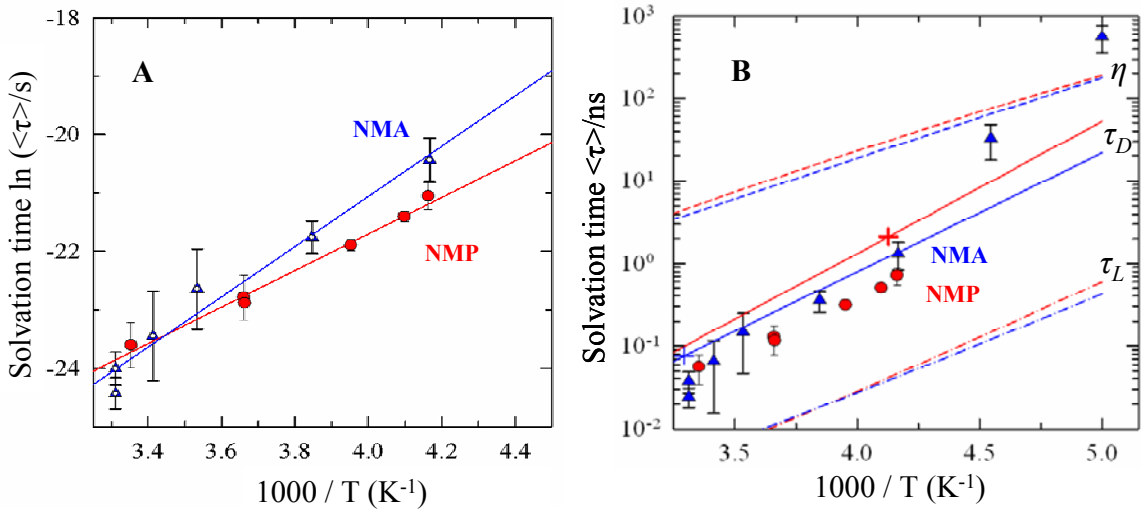

Figure 3.7 The experimental solvation times of NMA (blue triangle) and NMP (red circle) are plotted as a function of temperature. The curves in Panel A are the best fit of the data points. Panel B compares the solvation times for NMA and NMP to the viscosity η, the Debye relaxation time τ_D, and the longitudinal dielectric relaxation time τ_L for the solvents (NMA is blue, NMP is red) from literature data (see Appendix 3.8.2 for details).

Figure 3.7 compares the solvation times measured in NMA and NMP as functions of temperature. The time-dependent Stokes-shift measurements indicate that the solvation time of NMA and NMP are similar at high temperature and become more dissimilar as the temperature decreases. This behavior is consistent with their effect on the electron transfer. It is also evident that solvation in NMA and NMP are slower than the electron transfer rate of **1** and **2** at low temperatures. For example, in NMA at 220 K, the solvation time is 32 ns, whereas the time

constant for electron transfer in both solutes is ~ 3 ns. The slower the solvation time, the slower are the polarization fluctuations, which can lead to a solvent dependence of the electron transfer rates.

3.6 Data Analysis

3.6.1 High Temperature Analysis

At temperatures between 360 K and 295 K, the rate laws for **1** and **2** in NMA and NMP are nearly exponential. For example, for **1** in NMP at 334 K, the midpoint of this range, the fast decay time is 231 ps with amplitude of 94%, whereas the correlation time is 259 ps, an 11% difference. The worst case is the decay time at 295 K for which the correlation time is 504 ps and the fast decay time is 427 ps, a 15% difference. As the temperature increases the correspondence between the correlation time and the fast decay component improves. The molecule **2** in NMA and NMP approximates a single exponential decay law even better than **1**. This latter finding is consistent with the weaker electronic coupling between the donor and acceptor groups in **2**, as compared to **1**.

Previous studies of **1** and **2** applied the Equation 1 to fit the experimental rate constant of **1** and **2** as functions of temperature and extracted values of the electronic coupling $|V|$ for the two systems. At high temperatures, where the decay rate constants of **1** and **2** in NMA and NMP appear to be controlled by the solute molecular properties and the solvents' static dielectric properties, the same analysis can be applied.

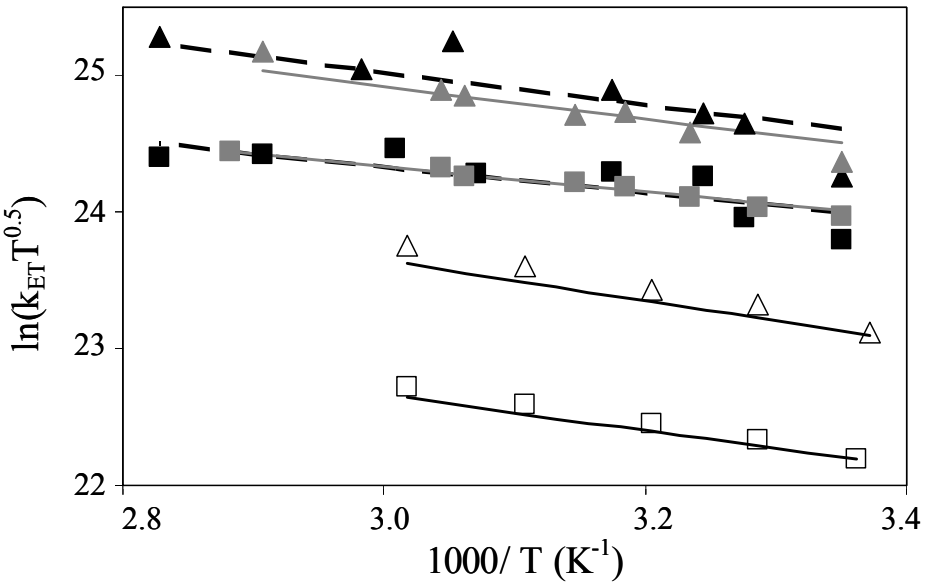

Figure 3.8 Electron transfer rate constants of **1** (triangle) and **2** (square) in ACN(empty), NMA (filled black) and NMP (filled gray) excited at 309 nm. The lines represent fits to Eq. 1.

Figure 3.8 shows a fit to these high temperature data with Equation 1. For comparison purposes, Figure 3.8 includes earlier data for **1** and **2** in acetonitrile with the new data in NMA and NMP at high temperatures (>300 K). The data are fit to Equation 1 and calibrated to the measured free energies in nonpolar solvents as described in Ref.20. The molecular solvation model employed in these fits requires several solvent parameters, which are specified in footnote 21. The values of the electronic coupling $|V|$, λ_v and hv were the same as determined from the previous work, and $\Delta_r G$ and λ_0 were predicted using the calibrated Matyushov model. The experimental electron transfer rate constant for **1** is faster than that for **2** in these solvents, which matches well with the previous conclusion that the aromatic group is better than an alkyl group at mediating the electronic coupling. The fitting parameters for **1** and **2** in NMA and NMP are listed in Table 3.2. Figure 3.8 also reveals that the electron transfer rate for both **1** and **2** in slow solvents NMA and NMP is higher than the rate in acetonitrile. Since the electronic coupling of **1**

and **2** is assumed to be solvent independent, the difference of the rate constants in NMA and NMP with those in acetonitrile is understood as reflecting differences in the activation energies in these solvents, $\Delta G^{\ddagger} \sim (\Delta_r G + \lambda)^2/4\lambda$.

Table 3.2 Fitting parameters for 1 and 2 to the nonadiabatic model at high temperature.[a]

System	$\lvert V \rvert$,cm^{-1}	CH_3CN(295°C)		NMA(303°C)		NMP(295°C)	
		λ_0(eV)	$\Delta_r G$(eV)	λ_0(eV)	$\Delta_r G$(eV)	λ_0(eV)	$\Delta_r G$(eV)
1	146	1.49	-0.54	1.36	-0.56	1.32	-0.52
2	62	1.46	-0.58	1.28	-0.61	1.23	-0.57

a) λ_v= 0.63 eV and hν = 1600 cm^{-1} are determined from charge transfer spectra of related species

3.6.2 Low Temperature Analysis

The semiclassical equation (Eq. 1) does not describe the electron transfer dynamics in the low temperature limit because it does not account for solvent frictional effects. Figure 3.9 compares the low-temperature predictions of Equation 1 using parameters obtained from the high temperature fit in Figure 3.8. In the case of acetonitrile, the nonadiabatic expression (Eq. 1) provides a good description of the rate constant over the whole temperature range studied. In contrast, in the slower solvents NMA and NMP, the low-temperature rates observed fall well below those extrapolated from the high-temperature fits.

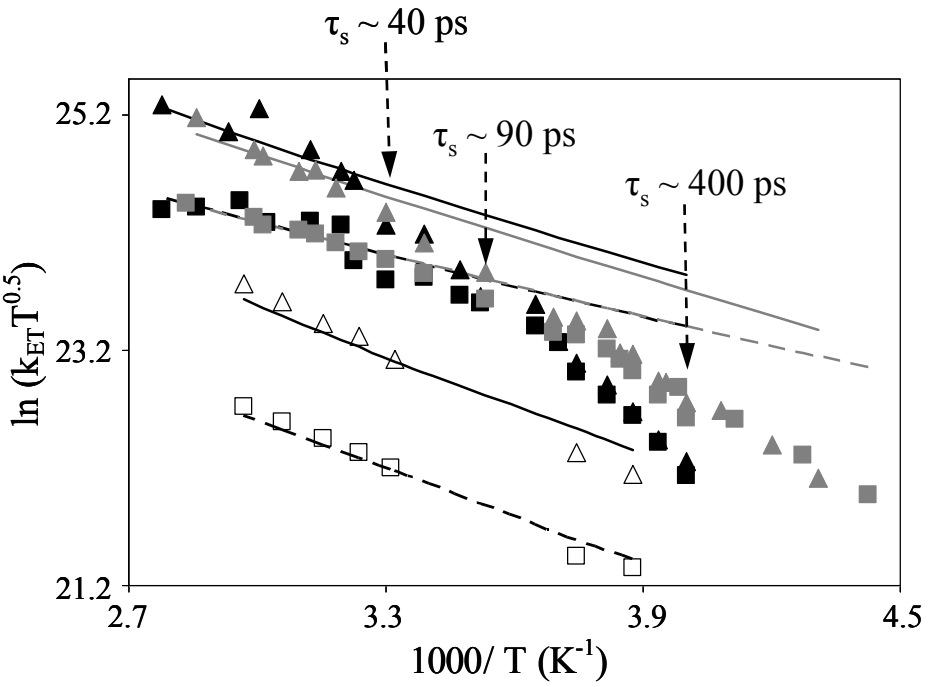

Figure 3.9 Electron transfer rate constants of **1** (triangle) and **2** (square) in acetonitrile (empty black), NMA (filled black) and NMP (filled gray) excited at 309 nm. The lines represent fits to Eq. 1.

Assuming that the rate constant is a serial combination of nonadiabatic and solvent controlled rate constants as in Equation 2, the solvent controlled rate constant k_{SC} can be obtained from the experimental value k_{ET} and the extrapolated nonadiabatic value k_{NA}; i.e.

$$k_{SC} = \Big/ \left(\frac{1}{k_{ET}} - \frac{1}{k_{NA}} \right) \qquad \mathbf{7}$$

Figure 3.10A plots the solvent controlled rate constant for **1** in NMA and NMP as a function of 1000/T. The rate constant increases with temperature and the activation energy is similar for the two solvents, 37 kJ/mol for NMA and 32 kJ/mol for NMP.

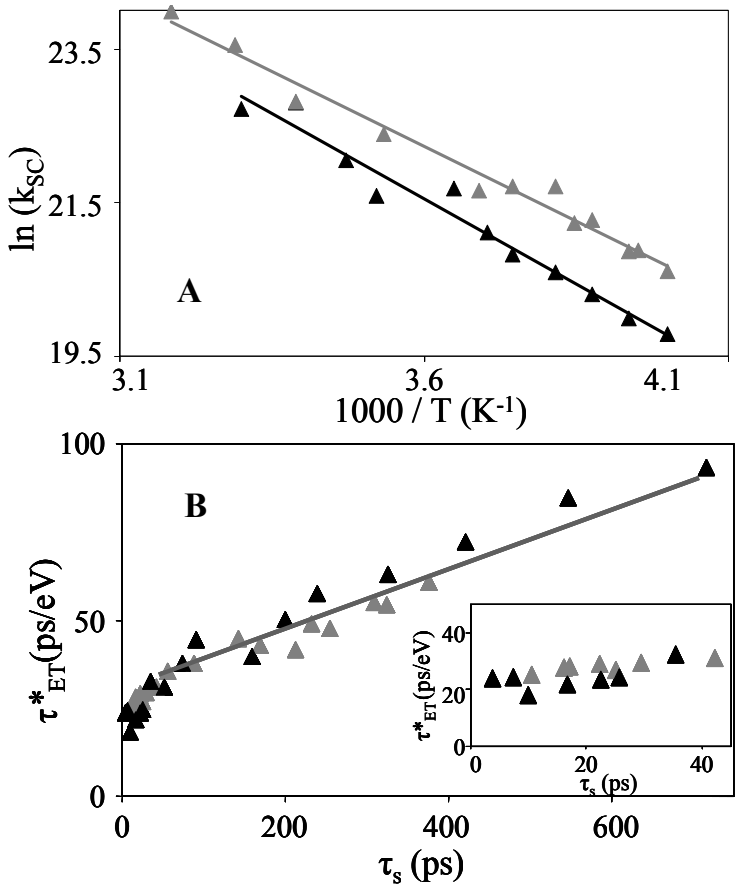

Figure 3.10 (A) Electron transfer rate constant of **1** in NMA (black) and NMP (gray) in the solvent friction region; (B) Interpolation τ^*_{ET} of **1** in NMA (black) and NMP (gray) versus solvation time; the straight line is a linear fit. The insert expands the region $0 \leq \tau_s(ps) \leq 40$ for clarity.

3.6.3 Zusman Model

According to Zusman, the electron transfer rate constant is inversely proportional to the solvation time when the reaction proceeds in the solvent friction regime, but it becomes independent of solvent friction when the solvation time is rapid. The Zusman treatment uses the interpolation formula (Eq. 2). Comparison to this model is facilitated by defining the quantity τ^*_{ET} as,

$$\tau_{ET}^{*} = \sqrt{\frac{1}{\lambda_0 k_B T}} \frac{\exp(-\Delta G^{\ddagger}/k_B T)}{k_{ET}} \qquad \textbf{8}$$

so that Equations 2 and 3 become

$$\tau_{ET}^{*} = \frac{\sqrt{\pi^3}}{\lambda_0 \sin(\pi\sqrt{\frac{\Delta G^{\ddagger}}{\lambda_0}})} \tau_s + \sqrt{\frac{1}{\lambda_0 k_B T}} \frac{\exp(-\Delta G^{\ddagger}/k_B T)}{k_{NA}} \qquad \textbf{9}$$

In the approximation that the first term in the sum over vibronic states in Equation 1 dominates, the form of Equation 1 is the same as the classical expression with an effective electronic coupling $|V_{eff}| = |V| \exp\left(-\frac{S}{2}\right)$ and Equation 9 takes the form of a quasi-linear function of τ_s.

$$\tau_{ET}^{*} = \frac{\sqrt{\pi^3}}{\lambda_0 \sin(\pi\sqrt{\frac{\Delta G^{\ddagger}}{\lambda_0}})} \tau_s + \frac{h}{2\sqrt{\pi^3}} \frac{1}{|V_{eff}|^2} \qquad \textbf{10}$$

This equation is not truly linear because of the temperature dependence of $\Delta_r G$ and λ_0 in the prefactor to τ_s, however their net effect is virtually temperature independent over the range examined here, rendering Equation 10 effectively a linear function of τ_s.

Figure 3.10B plots the value τ^*_{ET} of **1** in NMA and NMP versus the solvation time of NMA and NMP over the temperature range from 250 K to 360 K. For large values of τ_s (> 40 ps), a good linear correlation between τ^*_{ET} and the solvation time at low temperature is found. For smaller values of τ_s (see the inset), τ^*_{ET} is determined by the second term in Equation 10, supporting the conclusion that the electron transfer is nonadiabatic at high temperature. The intercept from the fit to Equation 10 (see Figure 3.10B) gives an electronic coupling $|V_{eff}|$ of 28 cm^{-1}. Using the values of $|V|$ = 146 cm^{-1} and S = 3.2 (Table 3.2), $|V_{eff}|$ = 29 cm^{-1} in agreement with the value obtained from this analysis. But Zusman's model overestimates the magnitude of

the solvent effect observed here. The linear fit in Figure 3.10B has a slope of 0.09 eV^{-1} which is sixty times smaller than the slope predicted from Equation 10, 5.2 eV^{-1}. The behavior of **2** in NMA and NMP is the similar to that of **1** and the fit to Equation 10 gives $|V_{eff}|$ = 11 cm^{-1}, in good agreement with the value of $|V_{eff}|$ = 12 cm^{-1}, calculated from $|V|$ = 62 cm^{-1} used in the high-temperature analysis. The linear fit gives a slope of 0.68 eV^{-1}, which is nine times smaller than the predicted slope, 6.4 eV^{-1}.

Zusman derived a criterion to assess whether the dynamic solvent effect is manifest in the electron transfer. In particular, if the inequality

$$\frac{\pi^2 |V|^2 \tau_s}{\hbar \lambda_o} \exp(-S) >> \sin\left(\frac{\pi}{2}\left(\frac{\Delta_r G}{\lambda_o} + 1\right)\right) \qquad \textbf{11}$$

holds, then the solvent friction should be important. If the reaction occurs in the range of a small driving force, that is $|\Delta_r G| << \lambda_0$, an effective electronic coupling can be defined as $|V_{eff}| = |V| \exp\left(-\frac{S}{2}\right)$. The dynamic solvent effect can be interpreted as an effective change of adiabaticity in the reaction, characterized by an adiabaticity parameter g

$$g = \frac{|V_{eff}|^2 \pi^2 \tau_s}{\hbar \lambda_0} \geq 1 \qquad \textbf{12}$$

A *g* value less than one indicates an essentially nonadiabatic electron transfer process, hence no dynamic solvent effect. By lowering the temperature, the solvation time can increase sufficiently to cause a crossover from nonadiabatic (g < 1) to a solvent friction controlled regime where g>>1. Using the parameters in Table 3.2, the dynamic solvent effect should manifest itself when τ_s >> 7 ps for **1** in NMA, τ_s >> 35 ps for **2** in NMA, τ_s >> 6 ps for **1** in NMP and τ_s >> 33 ps for **2** in NMP. The fit to the experimental data predicts that g ~ 1 (i.e., $k_{SC} \sim k_{NA}$) for **1** in NMP when the solvation time is ~ 309 ps at 254 K and NMA is ~ 201 ps at 270 K. As with the analysis of

the full Equation 10, the transition (g ~ 1) occurs at a value of τ_s about ten times larger than that predicted by Zusman.

The Zusman analysis provides a qualitatively consistent description for the rate constant over the entire temperature range. At high temperature, the solvation dynamics is fast and the rate constant is limited by the electron tunneling step; i.e., k_{NA}. At low temperature, the solvation is slow and the electron transfer depends on the solvent friction.

3.6.4 Sumi-Marcus Model [,22]

Electron transfer of **1** and **2** at high temperatures appears to lie in the fast diffusion limit, where the electron transfer is nonadiabatic (*vide supra*). At lower temperatures, these molecules have $\lambda_v/\ \lambda_0 \sim 0.5$ and appear to lie closer to the narrow reaction window limit of Sumi and Marcus. The reaction rate can be quantified by considering the average survival probability Q(t) of the locally excited state. Q(t) is the fraction of reactant molecules that have not transferred their electron by time *t*, and is obtained directly from the fluorescence decay law. Sumi and Marcus consider both the correlation time $\tau_c = \int_0^\infty Q(t)dt$ and the average decay time $\bar{\tau} = \frac{1}{\tau_c}\int_0^\infty tQ(t)\,dt$. These survival times provide valuable information about the timescale and temporal characteristic of the reaction rate. For example, if $\tau_c = \bar{\tau}$ then Q(t) is a single exponential decay, whereas $\tau_c \neq \bar{\tau}$ indicates a nonexponential decay law.

Figure 3.11 plots $\tau_c\, k_{ET}$ (panel A) and $\bar{\tau}\, k_{ET}$ (panel B) as functions of $\tau_s k_{ET}$ in NMP and NMA. k_{ET} is extracted from the fit of the high temperature data to the nonadiabatic model. $\bar{\tau}$ is calculated using a fit to a sum of exponentials. [23] If the reaction proceeded solely in the narrow

reaction window limit, the slope of the log-log plot would be unity. However for $0 < \lambda_v/\lambda_0 < 1$, the slope should lie between zero and unity.[22] In fact, the slope is less than one, 0.58 in NMP and 0.72 in NMA (Figure 3.11A), which suggests that the reaction occurs close to the narrow reaction window limit. The fact that τ_c is different from $\bar{\tau}$ supports the interpretation that the reaction proceeds away from the fast diffusion limit. Comparison of the average survival times τ_c and $\bar{\tau}$ reveals that τ_c always deviates from $\bar{\tau}$ for **1** in NMA and NMP, the population decay is nonexponential and controlled by the solvent friction. In contrast, τ_c and $\bar{\tau}$ are similar for **2** in NMP, suggesting a single exponential decay, and a weak dynamic solvent effect. Figure 3.11 shows considerable noise for the $\bar{\tau}$ plot of **1** so that the conclusions from it must be qualitative only. From Figure 3.11, it is evident that k_{SC} is smaller than the rate of solvation, $1/\tau_s$, and this occurs because of the activation energy, which also contributes to k_{SC}.

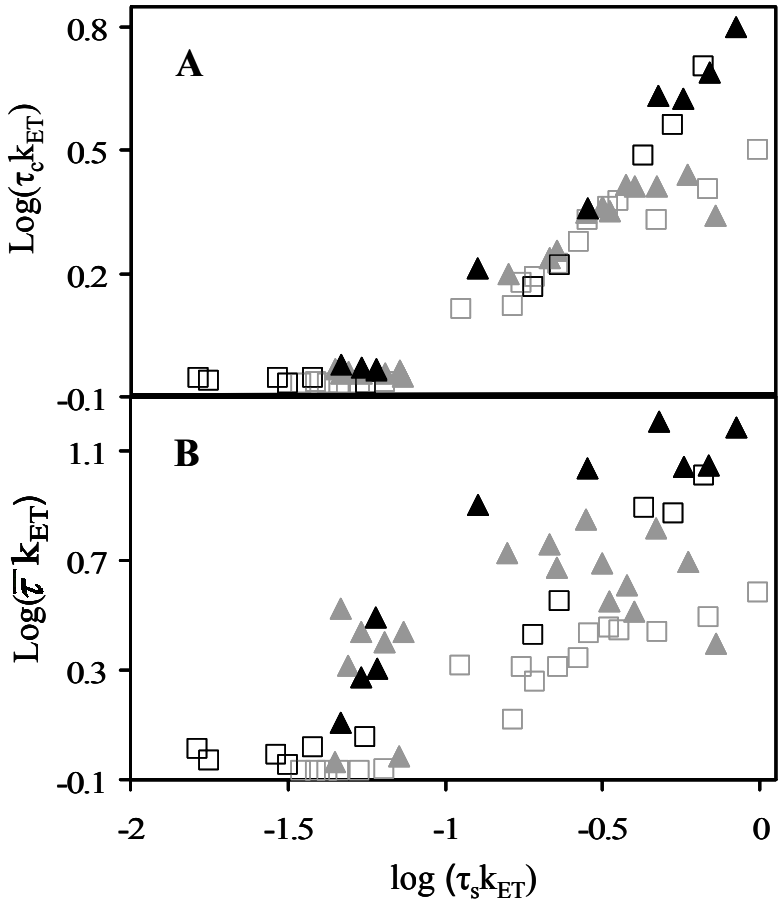

Figure 3.11 Plot of log ($\tau_c k_{ET}$) (A) and log ($\bar{\tau}\, k_{ET}$) (B) versus log $\tau_s k_{ET}$ for **1** (filled triangle) and **2** (empty square) in NMA (black) and NMP (gray). k_{ET} is extracted from the fit of the high temperature data to the nonadiabatic model.

3.7 Discussion and Conclusion

The photoinduced intramolecular electron transfer in **1** and **2** displays a dynamic solvent effect in NMA and NMP, even though the electronic coupling is small (see Table 3.2). By studying the rate constant over a large range of temperature, the electron transfer mechanism can be followed from one in which the electronic coupling dominates the reaction to one in which the solvent friction controls the reaction. Since the electronic coupling is mediated by the pendant

group, which is different in **1** and **2**, the change of fluorescence decay law from a single exponential decay at high temperature to a nonexponential decay at low temperature occurs differently for these two molecules. The experimental rate constants differ for **1** and **2** at high temperature, but tend to be the same at low temperature. This trend is a consequence of the slowdown in solvation dynamics with decreasing temperature, as probed by dynamic Stokes-shift experiments, as the temperature decreases.

A curious feature revealed by both the electron transfer and the solvation dynamics measurements reported here is the qualitative similarity of the dynamics observed in NMA and NMP at low temperatures. This similarity is curious because neat NMA crystallizes below 303 K, whereas NMP remains liquid to 226 K. Most of the data in NMA was collected using polycrystalline samples. Clearly both the solutes used for the solvation measurements and the electron transfer molecules sense a local environment which is much more fluid than crystalline. Evidently these "impurities" in the NMA solid exist in regions where the fluidity is similar to that in liquid NMP. These regions have reproducible properties that are comparable to what is expected for supercooled liquid NMA.

Because the solvation dynamics is relatively slow at low temperatures, experiments with different excitation energies were used to assess whether or not the locally excited state was equilibrated with the solvent. The rate constants do not change significantly with the excitation energy. This behavior confirms that when an electron transfers from the locally excited state to the charge separated state, the solute molecule retains no memory of the initial excess energy of the excitation.

Zusman's model for the effect of solvent friction on electron transfer was compared to the observations. The low temperature rate constants correlate with the solvation rate, $1/\tau_s$, as

determined through dynamic Stokes-Shift measurements. At high temperature the rate constant is independent of τ_s. Quantitative comparison with the model gave an effective electronic coupling that is in good agreement with that found using Equation 1 at high temperature (when high frequency modes are included), and the adiabaticity parameter g, which can be defined from Zusman's criterion, predicts that the solvent friction limit applies. The plot of τ^*_{ET} versus the solvation time τ_s reveals a linear correlation at low temperatures, however, the slope does not match the theoretical prediction.

Three different possibilities can be identified for the discrepancy between the predictions of Zusman's model and the observed dependence of τ^*_{ET} on τ_s. One limitation of the Zusman description (Eq. 3) is the failure to explicitly include quantum modes for the reorganization energy. This possibility was noted earlier by Walker et al,[24] who studied electron transfer in betaines and found that the theoretically predicted value was 10^6 times slower than their experimental value. In that case the electron transfer proceeded in the inverted regime and quantum effects are expected to be critically important. They found that electron transfer in the slow solvent limit was controlled by vibrational motion. A second limitation of the Zusman treatment arises from the use of the high friction (Smoluchowski) limit for the solvent frictional coupling. Recently, Gladkikh et al[25] extended Zusman's ideas to the intermediate friction regime and different barrier shapes. They found that the Zusman model overestimated the transfer rate by up to 10^3 and that the dynamics is a sensitive function of $|V|$ (or distance). A third limitation is the description of the solvation dynamics by a single relaxation time constant, whereas the solvation in these hydrogen bonding solvents is non-exponential. It may be that the faster components of the solvation response control the electron transfer dynamics.[26,27] Although

quantitative details of the Zusman description may be questioned, it appears to capture the physical picture of the process and approaches the correct nonadiabatic limit.

The electron transfer in **1** and **2** appears to lie in the narrow reaction window limit of the Sumi-Marcus treatment. Supporting this conclusion is the ratio of $\lambda_v/\lambda_0 \sim 0.5$ and the nonexponentiality of the locally excited state's population decay. In this limit, the electron transfer reaction occurs predominantly at a particular solvent polarization value of X_0 and the nonexponentiality arises from the time evolution of the reactant population along X. The deviation of the correlation time τ_c and the average time $\bar{\tau}$ verifies the characteristics of nonexponential decay law for the reaction. Other considerations of the Sumi-Marcus treatment, e.g. the electron transfer rate is proportional to the solvation rate, are similar to the Zusman prediction. The important difference between the two models in this limit is that Sumi-Marcus predicts a nonexponential decay law, as observed, whereas the Zusman model does not address the issue.

By exploring the electron transfer dynamics of two U-shaped molecules as a function of temperature in the slowly relaxing solvents NMA and NMP, the change in electron transfer mechanism from a nonadiabatic reaction to a friction controlled reaction is observed. Comparison to the theoretical model of Sumi-Marcus, shows that the decay law is nonexponential in the solvent friction limit. This study provides new insights into the factors governing the dynamics of electron transfer through non-bonded contacts.

3.8 Acknowledgements

We acknowledge support from Pennsylvania State University for fluorescence dynamic Stokes-Shift experiment, funded by The Office of Basic Energy Sciences, U.S. Department of Energy. We thank The Australian Research Council, The Australian Partnership for Advanced Computing (APAC) and The Australian Centre for Advanced Computing and Communications (ac3) for allocation of computing time. We acknowledge support from the U.S. National Science Foundation (CHE-0415457) and thanks R. A. Butera for technical assistance.

3.9 Appendix

3.9.1 Electron Transfer Rate Constant

1 in NMP excited at 309nm

T(K)	Donor k_D (s^{-1})	k_{ET} (s^{-1})
250	1.01×10^8	4.32×10^8
252	1.02×10^8	4.61×10^8
256	1.08×10^8	5.66×10^8
258	1.14×10^8	6.09×10^8
262	1.24×10^8	7.19×10^8
270	1.34×10^8	9.67×10^8
272	1.38×10^8	1.07×10^8
284	1.63×10^8	1.40×10^8
295	1.85×10^8	1.80×10^8
303	2.09×10^8	2.19×10^8
314	2.37×10^8	2.67×10^8
319	2.51×10^8	3.09×10^8
323	2.62×10^8	3.01×10^8
332	2.91×10^8	3.41×10^8
334	2.92×10^8	3.57×10^8
350	3.39×10^8	4.57×10^8

2 in NMP excited at 309nm

T(K)	Donor k_D (s^{-1})	k_{ET} (s^{-1})
250	1.01×10^8	4.12×10^8
252	1.02×10^8	4.35×10^8
256	1.08×10^8	4.94×10^8
258	1.14×10^8	5.66×10^8
262	1.24×10^8	6.61×10^8
267	1.35×10^8	7.45×10^8
270	1.34×10^8	8.10×10^8
272	1.38×10^8	9.08×10^8
284	1.63×10^8	1.08×10^9
295	1.85×10^8	1.33×10^9
303	2.09×10^8	1.48×10^9
309	2.24×10^8	1.56×10^9
314	2.37×10^8	1.68×10^9
319	2.51×10^8	1.79×10^9
323	2.62×10^8	1.83×10^9
332	2.91×10^8	1.88×10^9
334	2.92×10^8	2.00×10^9
353	3.48×10^8	2.21×10^9

1 in NMP excited at 326nm

T(K)	Donor k_D (s^{-1})	k_{ET} (s^{-1})
232	7.74×10^7	2.65×10^8
238	8.46×10^7	3.44×10^8
245	9.34×10^7	4.54×10^8
250	1.00×10^8	4.84×10^8
253	1.04×10^8	5.72×10^8
254	1.04×10^8	5.75×10^8
258	1.11×10^8	7.19×10^8
260	1.13×10^8	7.23×10^8
262	1.16×10^8	8.85×10^8
267	1.22×10^8	9.36×10^8
271	1.32×10^8	9.56×10^8
283	1.50×10^8	1.37×10^9
295	1.72×10^8	1.73×10^9
304	1.91×10^8	2.15×10^9
314	2.15×10^8	2.52×10^9
324	2.38×10^8	3.01×10^9
333	2.63×10^8	3.26×10^9

2 in NMP excited at 326nm

T(K)	Donor k_D (s^{-1})	k_{ET} (s^{-1})
226	7.04×10^7	2.31×10^8
234	7.98×10^7	3.18×10^8
243	9.08×10^7	4.24×10^8
250	1.00×10^8	4.22×10^8
251	1.01×10^8	5.50×10^8
254	1.04×10^8	5.08×10^8
258	1.11×10^8	6.19×10^8
260	1.13×10^8	6.79×10^8
262	1.16×10^8	7.38×10^8
267	1.22×10^8	8.25×10^8
271	1.32×10^8	8.42×10^8
283	1.50×10^8	1.10×10^9
295	1.72×10^8	1.32×10^9
304	1.91×10^8	1.54×10^9
314	2.15×10^8	1.71×10^9
324	2.38×10^8	1.87×10^9
333	2.63×10^8	2.02×10^9

1 in NMA excited at 309nm

T(K)	Donor k_D (s^{-1})	k_{ET} (s^{-1})
250	1.28×10^8	2.93×10^8
254	1.24×10^8	3.50×10^8
258	1.27×10^8	4.41×10^8
262	1.41×10^8	5.45×10^8
267	1.53×10^8	6.49×10^8
270	1.40×10^8	7.83×10^8
274	1.47×10^8	1.06×10^9
284	1.64×10^8	1.11×10^9
288	1.71×10^8	1.39×10^9
295	1.83×10^8	1.86×10^9
303	1.99×10^8	1.97×10^9
310	2.07×10^8	2.87×10^9
313	2.16×10^8	3.08×10^9
320	2.31×10^8	3.63×10^9
333	2.57×10^8	5.08×10^9

2 in NMA excited at 309nm

T(K)	Donor k_D (s^{-1})	k_{ET} (s^{-1})
250	1.28×10^8	2.59×10^8
254	1.24×10^8	3.39×10^8
258	1.27×10^8	4.24×10^8
262	1.41×10^8	5.01×10^8
267	1.53×10^8	6.06×10^8
270	1.40×10^8	7.76×10^8
274	1.47×10^8	8.83×10^8
284	1.64×10^8	1.06×10^9
288	1.71×10^8	1.12×10^9
295	1.83×10^8	1.28×10^9
303	1.99×10^8	1.24×10^9
310	2.07×10^8	1.45×10^9
313	2.16×10^8	1.94×10^9
320	2.31×10^8	1.99×10^9
331	2.53×10^8	1.93×10^9
338	2.68×10^8	2.31×10^9

3.9.2 Solvation Dynamics Fitting

The viscosities and dielectric properties of the liquid amides plotted here are from parameterizations of the form:

$$\varepsilon(T) = a_0 + a_1(10^3\,\mathrm{K}/T) + a_2(10^3\,\mathrm{K}/T)^2 \qquad \varepsilon_\infty(T) = a_0$$

$$\ln\{\eta(T)/\mathrm{cP}\} = a_0 + a_1(10^3\,\mathrm{K}/T) + a_2(10^3\,\mathrm{K}/T)^2$$

$$\log_{10}\{\tau_D(T)/\mathrm{ns}\} = a_0 + a_1(10^3\,\mathrm{K}/T) + a_2(10^3\,\mathrm{K}/T)^2 \qquad \tau_L(T) = \frac{\varepsilon_\infty(T)}{\varepsilon(T)}\tau_D(T)$$

with the parameters:

N-Methylpropionamide

Property	a_0	a_1	a_2
ε	99.5	-114	39.8
ε_∞	6	---	---
τ_D	-3.26	1.60	---
η	-7.58	3.14	-.114

N-Methylacetamide

Property	a_0	a_1	a_2
ε	69.1	-84.8	35.9
ε_∞	10.5	---	---
τ_D	-2.86	1.44	---
η	-6.08	2.25	---

These parameterizations are based on fits to the data contained in the references 1-8:

1. Firman, P.; Eyring, E. M.; Xu, M.; Marchitti, A.; Petrucci, S. *J. Phys. Chem.* **1992**, *96*, 41.

2. Maroncelli, M.; Fleming, G. R. *J. Chem. Phys.* **1990**, *92*, 3251.

3. Bennetto, H. P.; Evans, G. F.; Sheppard, R. J. *J. Chem. Soc., Faraday Trans. I.* **1983**, *79*, 245.

4. Brownsell, V. L.; Price, A. H. *J. Phys. Chem.* **1970**, *74*, 4004.

5. Millero, F. J. *J. Phys. Chem.* **1968**, *72*, 3209.

6. Gopal, R.; Rizvi, S. A. **1966**, *43*, 179.

7. Bass, S. J.; Nathan, W. I.; Meighan, R. M.; Cole, R. H. *J. Phys. Chem.* **1964**, *68*, 509.

8. Hoover, T. B. *J. Phys. Chem.* **1964**, *68*, 876.

3.10 References

1. P. F. Barbara, T. J. Meyer, M. A. Ratner, *J. Phys. Chem.*, *100*, 13148, **1996**

2. M. B. Zimmt and D. H. Waldeck, *J. Phys. Chem. A*, *107*, 3580, **2003**

3. J, Jortner, "*Advances In Chemical Physics - Electron Transfer-From Isolated Molecules To Biomolecules"*, Series #2, **1999**, Vol. *107*, New York : Wiley.

4. H. Sumi in Topics Topics "*Adiabatic versus Non-Adiabatic Electron Transfer in Electron Tranfer in Chemistry",* Volume *1*, Chapter 2, **2001**, edited by V. Balzani, pp. 65-108, New York: Wiley

5. We need to distinguish the case of solvent control from adiabatic control

6. a) A. M. Napper, N. J. Head, A. M. Oliver, M. J. Shephard, M. N. Paddon-Row, I. Read, D. H. Waldeck, *J. Am. Chem. Soc*, *124*, 10171, **2002**; b) A. M. Napper, I. Read, D. H. Waldeck, N. J. Head, A. M. Oliver, M. N. Paddon-Row, *J. Am. Chem. Soc.*, *122*, 5220, **2000**

7. M. Liu, D. H. Waldeck, A. M. Oliver, N. J. Head, M. N. Paddon-Row, *J. Am. Chem. Soc.*,*126*, 10778, **2004**

8. J. Jortner, *J. Chem. Phys.*, *64*, 4860, **1976**

9. a) L. D. Zusman, *Chem. Phys.*, *49*, 295, **1980**; b) L. D. Zusman, *Chem. Phys.*, *80*, 29, **1983**; c) L. D. Zusman, *Zeitschrift fűr Physikalische Chemie*, *186*, 1, **1994**

10. H. Sumi and R. A. Marcus, *J. Chem. Phys.*, *84*, 4894, **1986**

11. a) M. D. Newton, M. V. Basilevsky, I. V. Rostov, *Chem. Phys*., *232*, 201, **1998**; b) K. A. Sharp, B. Honig, *Annu. Rev. Biophys. Biophys. Chem*, *19*, 301, **1990**; c) D. Sitkoff, K. A. Sharp, B. Honig, *J. Phys. Chem*, *98*, 1978, **1994**; d) B. S. Brunschwig, S. Ehrenson, N. Sutin, *J. Phys. Chem*, *90*, 3657, **1986**

12. a) D. V. Matyushov and G. A. Voth, *J. Chem. Phys*, *111*, 3630, **1999**; b) D. V. Matyushov, *Chem. Phys.*, *174*, 199, **1993**; c) D. V. Matyushov, *Mol. Phys.*, *79*, 795, **1993**

13. P. Vath, M. B. Zimmt, D. V. Matyushov, G. A. Voth, *J. Phys. Chem. B.*, *103*, 9130, **1999**

14. a) N. J. Head, A. M. Oliver, K. Look, N. R. Lokan, G. A. Jones, M. N. Paddon-Row, *Angew. Chem., Int. Ed.*, *38*, 3219, **1999**; b) Supporting information of Ref 6a.

15. D. V. O'Connor and D. Phillips, *"Time-Correlated Single Photon Counting"*, **1984**, London; Orlando: Academic Press

16. M. P. Heitz and M. Maroncelli, *J. Phys. Chem. A, 101***,** 5852, **1997**

17. D. J. S. Birch and R. E. Imhof, in *Topics in Fluorescence Spectroscopy, Vol. 1: Techniques*, edited by J. R. Lakowicz (Plenum, New York, **1991**), pp. 1-95

18. M. Maroncelli and G. R. Fleming, *J. Chem. Phys. 86***,** 6221, **1987**

19. M. Maroncelli, *J. Mol. Liq.*, *57*, 1, **1993**

20. I. Read, A. Napper, R. Kaplan, M. B. Zimmt, D. H. Waldeck, *J. Am. Chem. Soc.*, *121*, 10976, **1999**

21. The molecular solvation model requires several solvent parameters in the fit of Equation 1, specifically:

	Dipole moment (D)[a]	Sigma (Å)[b]	Polarizability	Lennard-Jones energy (K)[e]	Quad moment (D)[a]
NMA	5.05	5.0	7.8[c]	304	9.54
NMP	4.29	5.4	8.0[d]	355	7.73

a. MP2 (6-31G) Gaussian calculation

b. D. Ben-Amotz and K. G. Willis, *J. Phys. Chem.*, *97*, 7736, **1993**

c. CRC handbook of chemistry and physics, 75th edition, CRC press, New York, **1994**

d. guess number

e. D. V. Matyushov and R. Schmid, *J. Chem. Phys.*, *104*, 8627, **1996**

22. W. Nadler and R. A. Marcus, *J. Chem. Phys.*, *86*, 3906-3924, **1987**

23. $\overline{\tau} = \Sigma f_i \tau_i^2 / \tau_c$ where f_i is the percentage of component i and τ_i is the decay time for component i, in a fit of the decay law to a sum of exponentials. τ_c is the correlation time.

24. G. C. Walker, E. Akesson, A. E. Johnson, N. E. Levinger, P. F. Barbara, *J. Phys. Chem.*, *96*, 3728, 1992

25. V. Gladkikh, A. I. Burshtein and I. Rips, *J. Phys. Chem. A*, *109*, 4983, **2005**

26. J. T. Hynes, *J. Phys. Chem.*, *90*, 3701, **1986**

27. T. Fonseca, *Chem. Phys. Lett.*, *162*, 491, **1989**

Chapter 4 Pendant Unit Effect on Electron Tunneling in U-Shaped Molecules

The electron transfer reactions of three U-shaped donor-bridge-acceptor molecules with different pendant groups have been studied in different solvents as a function of temperature. The pendant group mediates the electronic coupling and varies the electron tunneling efficiency through nonbonded contacts with the donor and acceptor groups. Quantitative analysis of the temperature dependent rate data provides the electronic coupling. The influence of steric changes on the electronic coupling magnitudes is explored by structural variation of the pendant groups.

4.1 Introduction

Electron transfer reactions are one of the most fundamental reactions in chemistry and play important roles in biology and in the emerging field of molecular electronics. Electron transfer reactions are distinguished from other chemical reactions by their ability to proceed even when the reductant (electron donor) and oxidant (electron acceptor) are not in direct contact, although they are in contact through some kind of intervening medium (*e.g.* hydrocarbon groups, protein segments). For example, photosynthesis reaction centers in plants use light driven electron transfer to produce a charge separated state across a membrane. This electron transfer occurs by a sequence of electron transfer steps, each one proceeding by a super-exchange mechanism in which the donor – acceptor electronic coupling is mediated by the interaction of the donor and acceptor states with virtual ionic states of the intervening medium.

Over the past four decades, rigid, covalently linked donor-bridge-acceptor (DBA) molecules, in which the donor and acceptor chromophores are held at well-defined separations and orientations with respect to each other, have been successfully used to explore the dependence of electron transfer dynamics on a variety of factors,[1] including interchromophore distance[2] and orientation,[3] bridge configuration[4] and orbital symmetry.[5] These studies have revealed that the electronic interaction between the donor (reductant) group and the acceptor (oxidant) group is controlled by the covalent linkages in the molecules. Changes in the bonding patterns in the bridging group and their energetics may be used to manipulate the electronic coupling magnitude and hence the electron transfer rate.[6]

In the past ten years, electron transfer kinetics in highly curved DBA molecules[7], where the distances between two redox centers are significantly larger than the sum of their van der Waal's radius, has been used to investigate electron tunneling through nonbonded contacts. When the electron transfer is nonadiabatic, the tunneling probability is proportional to the electronic coupling squared, $|V|^2$. Previous work[8] shows that the placement and electronic properties of the pendant group in U-shaped DBA molecules can strongly affect the electron tunneling efficiency. Corresponding studies on C-shaped molecules which display electron tunneling by way of solvent molecules located in the cleft are also available.[9,10] These studies show that the electron tunneling efficiency correlates with the electron affinity of the solvent molecules and their ability to fit in the cleft, *i.e.* steric constraints.

Scheme 1

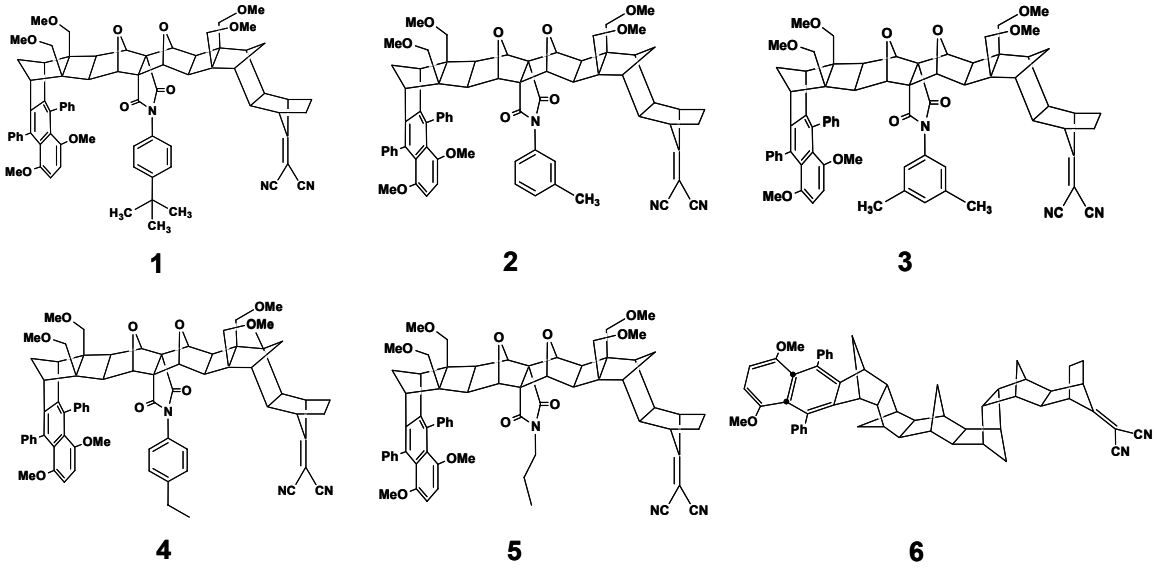

The current work studied electron transfer in three U-shaped molecules (**1**, **2** and **3**) and compared them to the previously studied compound **4** to explore how steric properties of the pendant group affect the electronic coupling. The U-shaped DBA molecules (**1**−**5**) have a highly curved and rigid bridge, which holds the donor and an acceptor groups at a fixed distance and orientation. A pendant group is covalently attached to the bridge and occupies the space between the donor and acceptor unit. Previous studies explored how the electron transfer rate constants and electronic couplings vary amongst the compounds **4**, **5** and **6**. The results revealed that the coupling for **4** is 2.5 times larger than that for **5**[8b]. The electronic coupling is enhanced by an aromatic pendant group, compared to an alkyl group, in the "line-of-sight" between the donor and acceptor, because the virtual ionic states of the pendant aromatic ring in **4**, being mainly of π character, are energetically closer to the naphthalene donor and dicyanovinyl acceptor states than are the virtual ionic σ states of the pendant alkyl group in **5**. The photoinduced electron transfer rate constant of **4** is 15 times faster than compound **6** in toluene[8a]. Compound **6** has a bridge, with the same number of bonds linking the donor and acceptor units as do **4** and **5**, but it is not

U-shaped. Thus, the electronic coupling between the naphthalene and dicyanovinyl groups in **6** can only occur by way of a superexchange mechanism operating through the bridge and is weaker than the corresponding electronic coupling in **4** and **5** which takes place more directly, through superexchange involving the pendant group.

The schematic energy diagram in Figure 4.1 shows an effective one-dimensional nuclear reaction coordinate. Two possible electron transfer regimes are distinguished by the strength of the electronic coupling $|V|$, the interaction between the reactant and the product states at the curve crossing. When the electronic coupling is weak $|V| << k_BT$, the reaction is nonadiabatic (dashed curve in Figure 4.1) and the rate constant is proportional to $|V|^2$. In this regime, the system may move through the curve crossing region $\mathbf{q}^{\ddagger}$ many times before the electronic state changes. The second regime is adiabatic electron transfer, where $|V| >> k_BT$ (solid curves in Figure 4.1). In this limit, the electronic state change evolves as the nuclear motion proceeds; *i.e.*, the strong coupling mixes the donor and acceptor states and the reaction proceeds along a single electronic state.

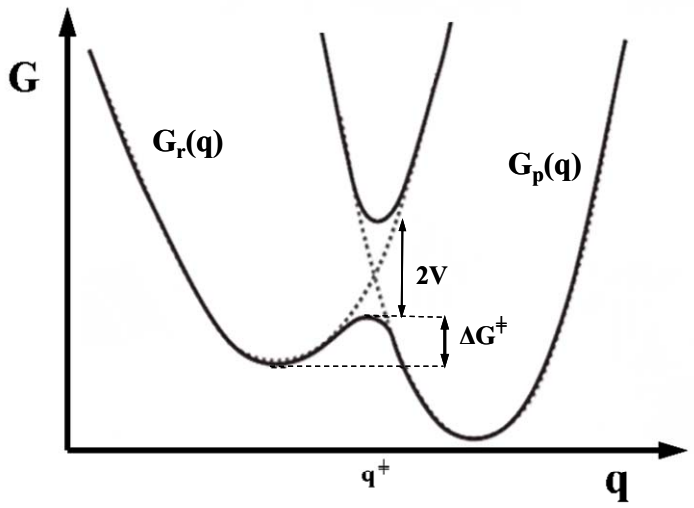

Figure 4.1 Diagram illustrating the adiabatic (the solid curves) − strong coupling − and nonadiabatic (the diabatic dashed curves) – weak coupling.

For the U-shaped molecules, the electronic coupling between the donor and acceptor moieties is weak enough that the electron transfer lies in the nonadiabatic limit. The semiclassical model for electron transfer in the nonadiabatic limit begins with a Fermi's Golden Rule expression for the transition rate; namely

$$k = (2\pi / \hbar)\left|V\right|^2 FCWDS \qquad \textbf{1}$$

where $\hbar$ is Planck's constant divided by 2π, $|V|$ is the electronic coupling matrix element, and FCWDS is the Franck-Condon weighted density of states. The FCWDS term accounts for the probability that the system achieves a nuclear configuration in which the electronic state can change. The square of the coupling, $|V|^2$, measures the probability of changing from the reactant to product electronic state.

4.2 Modelling the Rate Constant

Previous work successfully applied the Golden Rule rate constant expression with a single effective quantum mode, and described k_{ET} by the semiclassical rate equation.

$$k_{ET} = \frac{4\pi^2}{h} |V|^2 \frac{1}{\sqrt{4\lambda_0 \pi k_B T}} \sum_{n=0}^{\infty} \exp(-S)\left(\frac{S^n}{n!}\right)\exp\left[-\frac{(\Delta_r G + \lambda_0 + nh\nu)^2}{4\lambda_0 k_B T}\right] \qquad \textbf{2}$$

where λ_0 is the solvent reorganization energy; $\Delta_r G$ is the reaction free energy; $S = \frac{\lambda_v}{h\nu}$ and λ_v is the internal reorganization energy. The *hν* term refers to the average energy spacing of a single effective quantized mode frequency in the electron transfer reaction and is a characteristic of the solute. The sum is performed over the vibrational states of the effective quantum mode.

The quantities *hν* and λ_v are determined primarily by the donor and acceptor groups and is not sensitive to their separation. Charge-transfer absorption and emission measurements of

compound **7** in hexane, in conjunction with theoretical calculations[11] were used to quantify *hv* and λ_v. This analysis provided a value of 1600 cm^{-1} for the single effective quantized mode and 0.63 eV for the solute reorganization energy λ_v. This effective frequency is comparable to typical carbon-carbon stretching frequencies in aromatic ring systems, such as the naphthalene, which primarily show stretching modes of ~ 1600 cm^{-1} upon formation of the cation.[8a] A lower frequency of 1088 cm^{-1} [7b,12] is associated with out-of-plane bending of the dicyanovinyl group. A previous study[8a] showed that inclusion of this mode frequency affected the absolute magnitude of $|V|$, that is extracted from the data but did not affect the relative magnitude of $|V|$, for **4** and **5**. The internal reorganization energy is dominated by the dicyanovinyl acceptor which provides values in a range of 0.30 – 0.50 eV from the charge transfer emission experiment[7b]. The values of *hv* and λ_v are consistent with those reported for charge transfer complexes of hexamethylbenzene with tetracyanoethylene in CCl_4 and cyclohexane.[13] In the current work, these two parameters are kept fixed in the fit of the rate constant to equation 2.

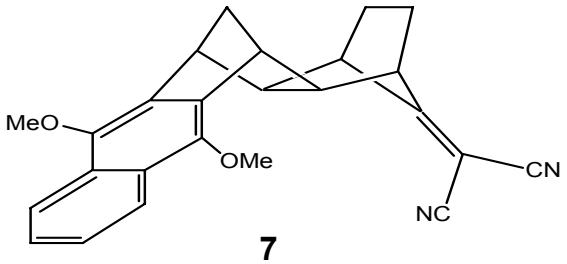

7

The values of the three remaining parameters contained in the semiclassical rate expression (Eqn 2), namely λ_0, $|V|$ and Δ_rG, need to be determined. The solvent reorganization energy λ_0 and the reaction free energy Δ_rG are determined by calibration of Matyushov's molecular solvation model[14] with experimental Δ_rG data. The reaction free energy Δ_rG in weakly polar or non-polar solvents can be experimentally measured from an analysis of the equilibrium

between the locally excited state and the charge-separated state. Previous reports[8a] parameterized the molecular solvation model for **4** in the solvents toluene and mesitylene and used it to predict the reaction free energy and the solvent reorganization energy in polar solvents. This model, parameterized in the same way, was used to fit the electron transfer reaction rate constant in the new U-shaped molecules, **1**, **2** and **3**.

The Matyushov solvation model accounts for the discrete nature of the solute and the solvent. The solute is treated as a sphere with a point dipole moment and polarizability. The solvent is modeled as a polarizable sphere with an electrostatic charge distribution that includes both a point dipole and a point quadrupole. The model incorporates the interactions between the solute and the solvent molecules and amongst the solvent molecules themselves, including the dipole-dipole interactions, the dipole-quadrupole interactions, the quadrupole-quadrupole interactions, the induction, and dispersion interactions. The molecular model properly describes the temperature dependence of the solvation[15], as compared to a continuum model, and is superior for analyzing these data.

The current work reports the electron transfer behavior of three new U-shaped molecules (**1** – **3**) with pendant groups having different steric properties, compared to compound **4**. Compound **4** has a *para* ethyl group on the phenyl ring, **1** has a *para t*-butyl unit, **2** has one methyl at a *meta* position of the phenyl ring; and **3** has two methyl groups, one at each *meta* position. The rate constant model described above is used to compare the electronic coupling in these U-shaped molecules. The similarity found for the electronic coupling in these dissimilar substitution patterns suggests that the average orientation of the phenyl ring, with respect to the donor and acceptor, is similar.

4.3 Experimental Section

4.3.1 Time-Resolved Fluorescence Studies

Each sample was dissolved in the different solvents at a peak optical density of less than 0.2 in all of the experiments. The solvent acetonitrile (99.9% HPLC) was purchased from Burdick & Jackson without further purification. The solvents toluene, mesitylene and *p*-xylene were fractionally distilled two times using a vigreux column under vacuum after purchased from Aldrich. The purified fraction was used immediately in all the experiments. Each solution was freeze-pump-thawed a minimum of five cycles.

Each sample was excited at 326 nm by the frequency-doubled cavity-dumped output of a Coherent CR599-01 dye laser, using DCM (4-dicyanomethylene-2-methyl-6-p-dimethylamino-styryl-4H-Pyran) dye, which was pumped by a mode locked Coherent Antares Nd:YAG. The dye laser pulse train had a repetition rate of 300 kHz. Pulse energies were kept below 1 nJ, and the count rates were kept below 3 kHz to prevent pile up effect. All fluorescence measurements were made at the magic angle, and data were collected until a standard maximum count of 10,000 was observed at one channel.

The time-resolved fluorescence kinetics for **1**, **2** and **3** and their donor only analogues were carried out in different solvents as a function of temperature. The temperature ranged from 273 K to a high of 346 K. The experimental temperature was controlled by an ENDOCAL RTE-4 chiller and the temperature was measured using a Type-K thermocouple (Fisher-Scientific), accurate to within 0.1 ºC.

The instrument response function was measured using a sample of colloidal $BaSO_4$. The fluorescence decay curve was fit by a convolution and compare method using IBH-DAS6

analysis software. Independent experiments on individual donor only molecules at the measured temperatures, always a single exponential fluorescence decay, was used to determine the intrinsic fluorescence decay rate of the locally excited state. The DBA molecules **1** – **4** have a small amount of donor only impurity. The measurement of the donor only molecule's characteristic in each solvent and temperature allowed their contribution to be subtracted from the decay law of their DBA molecules**.** The decay law of **1** – **4** in acetonitrile was a single exponential function and in weakly polar solvents toluene, mesitylene and *p*-xylene was a double exponential function. Fitting to the semiclassical equation (equation 2) was performed using Microsoft Excel 2003.

4.4 Results and Analysis

4.4.1 Steady-State Spectra

The U-shaped molecules **1**, **2**, **3** and **4** have been studied in the polar solvent acetonitrile, the weakly polar solvent toluene, and the nonpolar solvents mesitylene and *p*-xylene. The spectra of the DBA molecules are the same as those of the donor only analogues, hence the spectroscopic properties of the donor units in these molecules dominate the spectral features. Figure 4.2 shows the absorption and emission spectra of these molecules in acetonitrile and mesitylene.

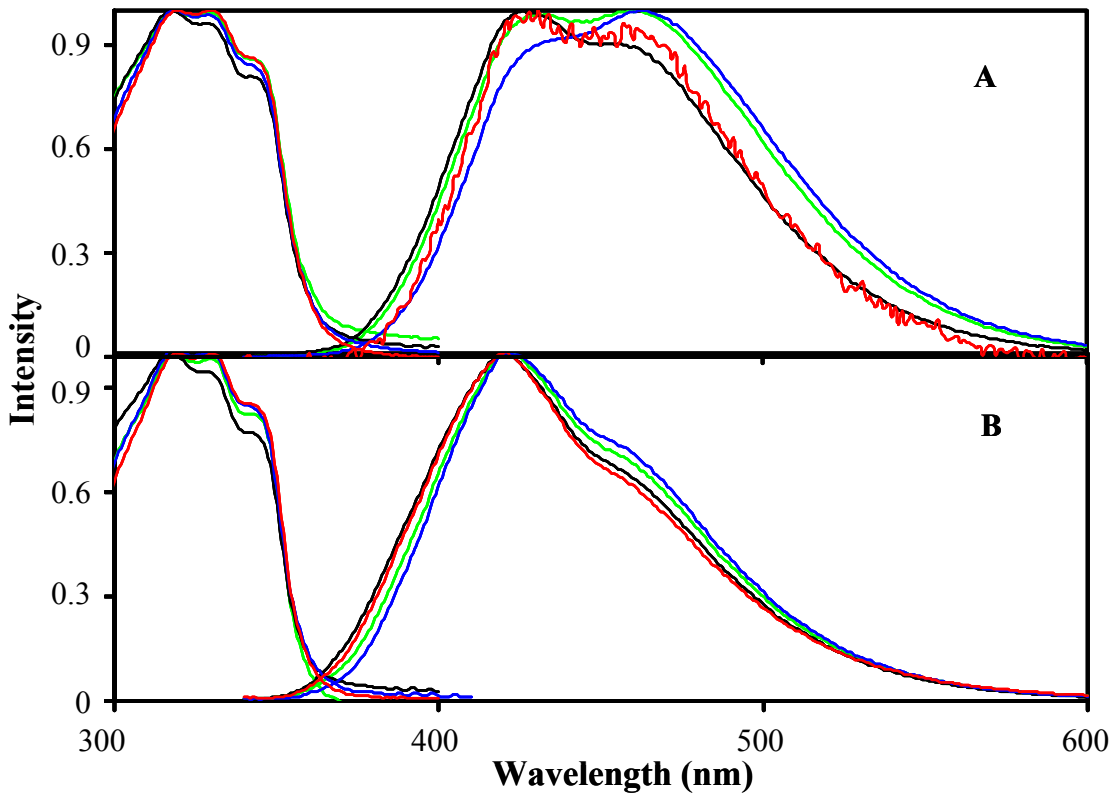

Figure 4.2 Absorption spectra (left) and emission spectra (right) of **1** (black), **2** (green), **3** (blue) and **4** (red) in acetonitrile (A) and mesitylene (B)

The donor unit of compounds **1** through **4** is the same, 1,4–dimethoxy-5,8-diphenylnaphthalene, and accounts for the similarity of the spectra in a given solvent. The naphthalene chromophore has two close lying excited electronic states, ^1L_a and ^1L_b in the Platt notation, that are accessed in the ultraviolet. The red shift of the donor spectrum and the loss of vibronic structure, as compared to naphthalene, are consistent with the methoxy group (and phenyl) substitution.[16] Although 1-substituted naphthalenes typically have the ^1L_b state below the ^1L_a state (transition is polarized along the short axis), high-resolution spectra of 1-aminonaphthalene in a jet expansion show a reversal of this ordering; *i.e.*, the ^1L_a state is below

the ^1L_b state.[17] This example underscores the sensitivity of the relative ordering of the ^1L_b and ^1L_a states to perturbations.

The variations in the spectral substructure must arise from changes in the excited state properties with changes in the solvent and the pendant group. The spectra in mesitylene solvent (Figure 4.2B) are shown because it is expected to perturb the chromophore the least of all the solvents and illustrate the spectral perturbations that arise from the changes in the pendant groups. Polar solvent molecules, such as acetonitrile (Figure 4.2A) interact with the solute to stabilize the excited ^1L_b state and this changes the relative intensity of the two peaks in the emission spectrum. Despite the change in intensity of these two emission peaks the fluorescence decay law does not change with emission wavelength; *i.e.*, it is the same across the band.

Although the absorption spectra show different absorption bands, the fluorescence spectrum and lifetime do not depend on the excitation energy. It is understood that both electronic configurations involve π-π* single electron excitations and the energy difference is small enough that the ^1L_a and ^1L_b states are strongly mixed. This claim is supported by the identical emission spectra that were obtained at different excitation energies for each compound and by the fact that the lifetime of compound **4** does not change with the excitation energy from 296 nm to 359 nm.

4.4.2 Fluorescence Kinetics

In polar solvents, like acetonitrile, the fluorescence decay of the U-shaped molecules is single exponential with rate constant k_{obs}, and the electron transfer rate constant can be determined from $k_{ET} = k_{obs} - k_f$, where k_f is the fluorescence decay rate of the donor only molecule and k_{ET} is the electron transfer rate.

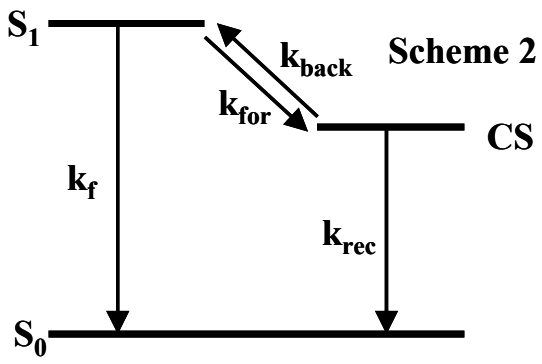

In toluene and nonpolar solvents, mesitylene and *p*-xylene, the fluorescence decay is double exponential. The biexponential kinetic arises because the free energy of the charge separated state is close to zero and an equilibrium between the locally excited state (LE) and the charge separated state (CS) occurs (see scheme 2). The double exponential kinetics can be analyzed to extract the reaction free energy, $\Delta_r G$, from the experiment. By writing the fluorescence intensity as

$$I(t) = a_+ \exp(-k_+ t) + (1 - a_+) \exp(-k_- t) \quad \textbf{3}$$

the forward electron transfer rate constant is

$$k_{for} = a_+ (k_+ - k_-) + k_- - k_f \quad \textbf{4}$$

and the backward electron transfer rate constant is

$$k_{back} = \frac{(k_+ - k_-)^2 - [(k_f + k_{for}) - (k_{back} + k_{rec})]^2}{4k_{for}} \quad \textbf{5}$$

The free energy difference between the locally excited state (LE) and the charge separated state (CS) is

$$\Delta_r G = -RT \ln\left(\frac{k_{for}}{k_{back}}\right) \quad \textbf{6}$$

The experimentally determined reaction free energy for all these U-shaped molecules as a function of temperature in toluene, mesitylene and *p*-xylene are used to calibrate the solute parameters in this model.

4.4.3 Reaction Free Energy $\Delta_r G$

A number of solvent parameters (some of them are listed in Table 4.1) are required to analyze the molecular solvation model. The polarizability of toluene, mesitylene and acetonitrile were kept the same as used previously[8a] and the polarizability of *p*-xylene was obtained from literature. [18] The dipole moments and quadrupole moments of the different solvents were computed using Gaussian 2003 at the MP2/6-31 G level. Rather than use the quadrupole moment tensor, an effective axial moment $\langle Q \rangle = (\frac{2}{3}\sum_i Q_{ii}^{\ 2})^{1/2}$ was evaluated.[19] The sizes (sigma) of the solvents and the Lennard-Jones energies were obtained from the literature. [20,21]

Table 4.1 Solvent parameters used in the Molecular Solvation Model

Solvent	Polarizability (Å^3)	Quad Moment (D Å)	Dipole Moment (D)	Sigma (Å)	Lennard-Jones energy (K)
Toluene	12.32	8.76	0.363	5.68	603
Mesitylene	16.14	8.58	0.0671	6.40	720
Acetonitrile	4.48	3.37	4.0664	4.24	405
p-xylene	14.23	8.77	0.0542	6.04	725

The best fit of the experimental reaction free energies to the solvation model provides the solute parameters listed in Table 4.2. Details of the analysis are available elsewhere. Because the bridge is so rigid and the size changes on the pendant group are small compared to the overall

molecular size, the radius of solute was kept constant at 7.66 Å for the different molecules. The solute's ground and excited state dipole moments were kept the same as the previous calculation[8a], 5.75 D for the ground state and 28.64 D for the charge-separated state. The polarizabilities of **1** – **4** were adjusted slightly to account for changes in the pendant group.[22] The polarizability of **4** is 128 $Å^3$; the same as previously.[8a] The ΔG_{vac} value was chosen independently for the four solutes and treated as an adjustable parameter when fitting the experimental free energy to the molecular solvation model. The best fit provides similar ΔG_{vac} values for these solutes, see Table 4.2.

Table 4.2 Solute parameters used in the Molecular Solvation Model

System	Radius[a](Å)	$\Delta\gamma^a$ ($Å^3$)	μ_{ex} (D)	μ_{gs} (D)	Polarizability ($Å^3$)	$\Delta G_{vac}{}^a$ (eV)
1	7.66	5.29	28.64	5.75	133	0.19
2					128	0.18
3					130	0.17
4					128	0.18

[a.] obtained from the best fit of the molecular solvation model

Figure 4.3 plots the reaction free energy of **1**, **2**, **3** and **4** in mesitylene as a function of temperature. The model fits the experimental data well in each case where the Gibbs energy change could be measured experimentally. The reaction free energy for these U-shaped molecules in mesitylene changes systematically with temperature from -0.10 to -0.05 eV (see Figure 4.3). Similar behavior was observed in toluene and *p*-xylene.

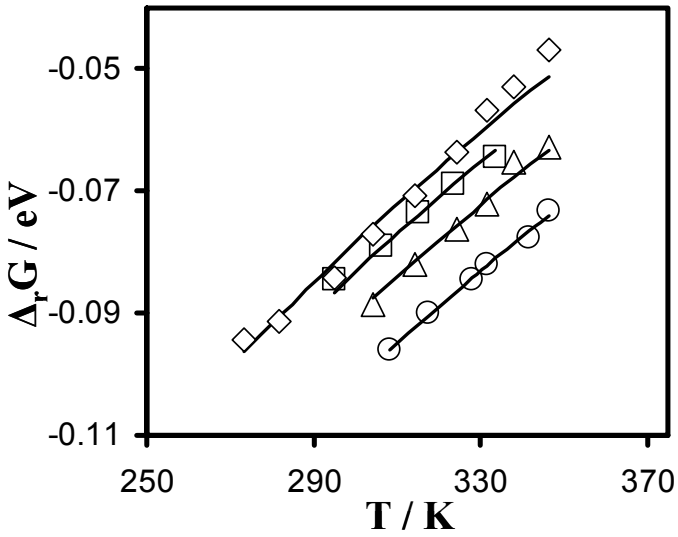

Figure 4.3 The experimental $\Delta_r G$ values are plotted for **1** (diamond), **2** (triangle), **3** (circle) and **4** (square) in mesitylene. The lines show the $\Delta_r G$ values predicted from the molecular model with the solvent parameters given in Table 4.1.

After parameterization, the reaction free energies of these molecules in acetonitrile were predicted. Table 4.3 compares the free energies of these compounds at 295 K in different solvents. The free energy becomes more negative as the solvent becomes more polar. Mesitylene and *p*-xylene which have no dipole moment have the most positive $\Delta_r G$. Toluene has a small dipole moment and the $\Delta_r G$ becomes more negative, whereas the strongly polar acetonitrile has the most negative reaction free energy.

Table 4.3 Best fit of $\Delta_r G$ (295 K) values for U-shaped molecules

System	$\Delta_r G$, eV (295 K)			
	Toluene	Mesitylene	*p*-xylene	Acetonitrile
1	-0.11	-0.082	-0.087	-0.55
2	-0.12	-0.094	-0.099	-0.55
3	-0.13	-0.10	-0.11	-0.57
4	-0.12	-0.087	-0.092	-0.55

For molecules **1** – **4** in weakly polar and nonpolar solvents, $\Delta_r G$ becomes more negative as the size of the phenyl ring's substituent increases; in the more polar acetonitrile the variation of $\Delta_r G$ with the pendant group is not apparent. Although the molecular model provides a means for estimating $\Delta_r G$ as a function of temperature, it contains significant simplifying assumptions; for example, it treats the solute as a sphere containing a point dipole moment and polarizability. In comparing the model with the experimental $\Delta_r G$ for compounds **1** – **4** in mesitylene (see Figure 4.3), the $\Delta_r G$ difference in **1** varies from -8.4% to 2.1%; **2** varies from -3.7% to 1.2%; **3** varies from -0.89% to 1.3%; and **4** varies from -2.5% ~2.1%. Although this finding suggests some slight systematic error in the model fitting, the overall agreement is excellent. A previous analysis reported a $\Delta_r G$ of -0.52 eV for **4** in acetonitrile[8a], whereas the current value is -0.55 eV (see Table 4.3), a 5% deviation. Although the fit of the molecular model to the $\Delta_r G$ data depends on three adjustable solute parameters, the ability to fit a range of different solvents and use very similar solute parameters for compounds **1** to **4** indicates that the molecular model provides a reliable and consistent description of the reaction free energy.

4.4.4 Kinetic Analysis

With the reaction free energy obtained from the model and the internal reorganization energy parameters from the previous studies,[8a] it is possible to fit the temperature dependent rate constant data to equation 2 and extract the electronic coupling $|V|$ and the solvent reorganization energy λ_0. $|V|$ is treated as a temperature independent quantity. The solvent reorganization energy has a temperature dependence because the solvation is temperature dependent. The temperature dependence of the solvent reorganization energy was predicted from the molecular solvation model and the best fit was used to extract the solvent reorganization energy at 295 K.

The fit of the temperature dependent rate constant data to equation 2 (see Figure 4.4) was used to determine the electronic coupling $|V|$ and λ_0 (295 K), listed in Table 4.4. Figure 4.4 shows fits of the experimental rate constant to the model for these four molecules in mesitylene and acetonitrile. The rate data in toluene and *p*-xylene behave similarly. Table 4.4 lists the solvent reorganization energies, λ_0, at 295 K and electronic couplings $|V|$ that are obtained for the four solutes by fitting to the temperature dependent rate constant expression, equation 2.

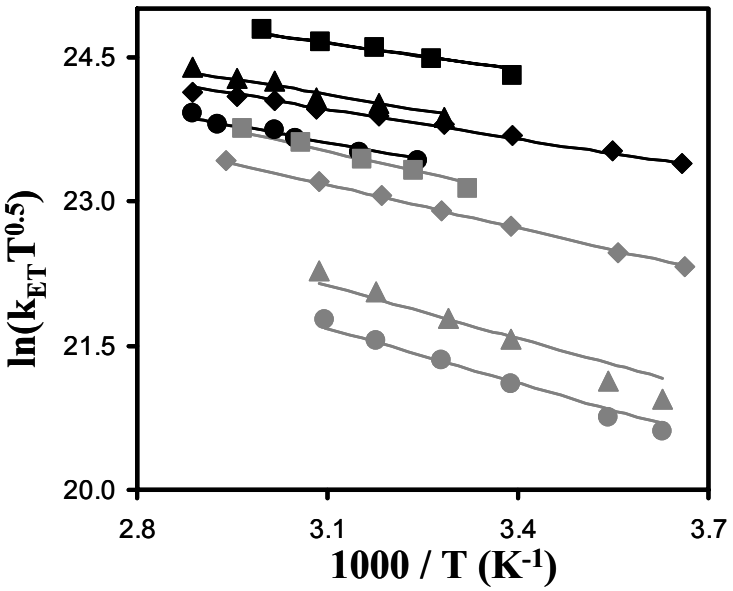

Figure 4.4 Experimental rate constant data are plotted versus 1/T, for **1** (diamond), **2** (triangle), **3** (circle) and **4** (square) in mesitylene (black) and acetonitrile (gray). The lines represent the best fits to equation 2.

The reorganization energies in weakly polar and nonpolar solvents at 295 K lie in the range of 0.66 to 0.85 eV; in acetonitrile they are considerably higher within 1.50 to 1.72 eV. In these analyses, the solvent reorganization λ_0 is modeled as temperature dependent and an adjustable λ_0 offset is used to fit the data. From the molecular model prediction, λ_0 is associated

with both solvent rotational degrees of freedom, which increase slightly with increasing temperature, and solvent translational degrees of freedom, which decrease with increasing temperature.[23] For compounds **1** – **4** in mesitylene from 273 K to 346 K, the net decrease in λ_0 is 10% to 13% of the adjustable λ_0 offset. The previous molecular model fitting of λ_0 (295) for **4**[8a] reported a value of 0.69 eV in mesitylene and 1.50 eV in acetonitrile, which are consistent with the current fit (Table 4.4). The values of λ_0 for compounds **1** – **3** are close to those found for **4**, as expected.

Table 4.4 Best fit of $|V|$ and λ_0 (295 K) values for U-shaped molecules

System	$\|V\|$, cm^{-1}	λ_0, eV (295 K)			
		Toluene	Mesitylene	*p*-xylene	Acetonitrile
1	139	0.75	0.71	0.72	1.53
2	147	0.78	0.73	0.75	1.67
3	130	0.85	0.77	0.80	1.72
4	147	0.70	0.66	0.67	1.50

Table 4.4 lists the values of $|V|$ for **1** – **4** obtained from the best fit to equation 2. Compound **1** with a *t*-butyl substituent on the phenyl ring gives a $|V|$ of 139 cm^{-1}; **2** has one methyl group and a $|V|$ of 147 cm^{-1}; **3** has two methyl substituents and a somewhat lower $|V|$ of 130 cm^{-1}. In comparison with a $|V|$ value of 168 cm^{-1}, for **4** reported previously[8a], a 13% smaller value of 147 cm^{-1} was obtained from the current fit. The disparity of the electronic coupling from the different fits is within expected errors in the analysis. Although the steric properties of the pendant group in these U-shaped molecules may change the phenyl ring geometry, the values of the electronic couplings are similar.

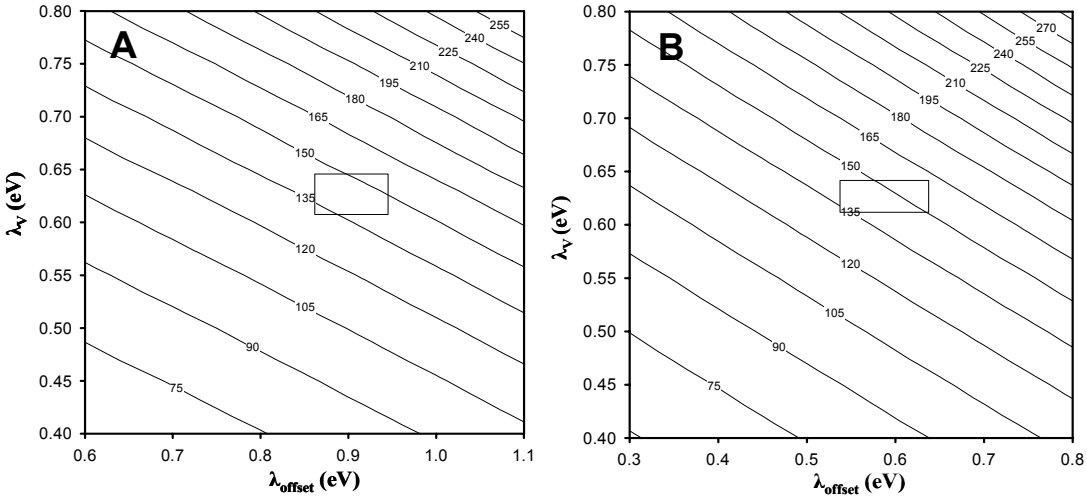

Figure 4.5 Contours of constant $|V|$ are shown for **4** in acetonitrile (panel A) and mesitylene (panel B). The rectangular region contains parameter values for which the χ^2 parameter in the fit is ≤ 3 times its optimal value. Outside of this region the fits to the rate data visibly deviate.

Although $|V|$ is treated as independent of the solvent, it strongly relies on the value of the parameters λ_0, λ_v, $\Delta_r G$ and $d\lambda_0/dt$ in the fit. Figure 4.5 illustrates how the best fit value of the electronic coupling changes with the magnitude of the internal reorganization energy and the outer sphere reorganization energy used in the analysis. The contours represent different values of the electronic coupling. The boxed region in each case identifies the range for λ_v and λ_{offset} over which the χ^2 changes by a factor of three.

4.5 Theoretical Calculations

Structural features of the U-shaped systems were investigated by carrying out geometry optimizations of the ground states of **1** − **3** at the B3LYP/6-31G(d) level of theory, which has been demonstrated previously to be acceptable for these types of systems. Complete geometry optimizations were carried out with no imposed constraints using Gaussian 03.[24] Each system

was found to have two stable conformations differing in the orientation of the naphthalene methoxy groups. The lowest energy conformation for each system, exemplified by **1a** (Figure 4.6), has both methoxy groups lying in the plane of the naphthalene ring, whereas in the other conformation, exemplified by **1b**, one of the methoxy groups is twisted out of the plane of the naphthalene ring. Unsurprisingly, conformation **b** in each system is 8 - 9 kJ/mol less stable than conformation **a,** and therefore is expected not to play a significant role in the electron transfer dynamics. In any case, apart from the differences in methoxy group orientation, conformations **a** and **b** have very similar structural features, particularly with respect to interchromophore separation and pendant group twisting about the N-C (phenyl) bond. Two additional conformations were located for each of **2a** and **2b**, distinguished by the different direction of twisting of the pendant 3-methylphenyl ring about the N-C (phenyl) bond. In one conformation, the 3-methyl side of the pendant group is twisted towards the naphalene ring whereas in the other conformation, it is twisted towards the dicyanovinyl group. The former conformation is slightly more stable than the latter, by about 1.5 kJ/mol.

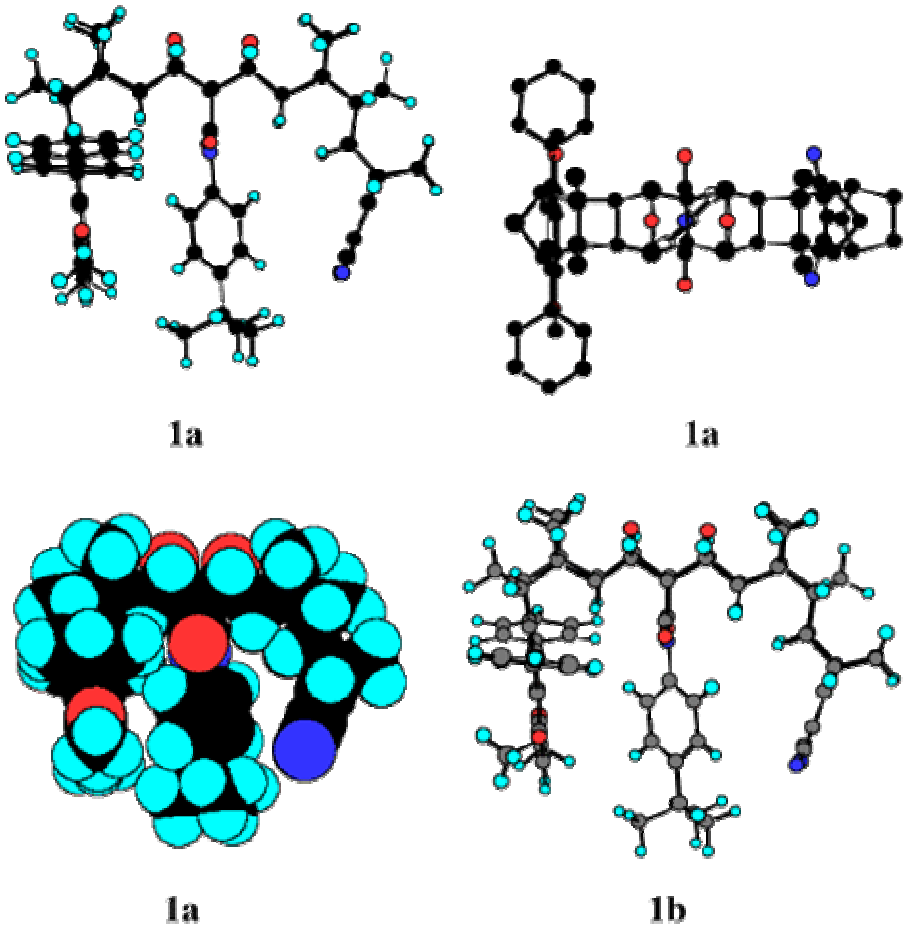

Figure 4.6 B3LYP/6-31G(d) optimized geometries of two conformations of **1**, namely **1a** (more stable), in which both OMe groups of the 1,4-dimethoxy-5,8-diphenylnaphthalene ring approximately lie in the plane of the naphthalene and **1b** (less stable), in which one of the methoxy groups is twisted out of the naphthalene plane. A planee view of **1a** is shown (minus all H atoms and the *tert*-butyl group for clarity) which depicts the degree of twisting of the N-*tert*-butylphenyl pendant group about the N-C(phenyl) bond. A space-filling depiction of **1a** is also shown (using standard van der Waals atomic radii).

The following discussion of geometries refers to the lowest energy conformation for each system. The space-filling depiction of **1a** is representative of all three molecules and shows that the pendant group is fairly close to both the donor and acceptor moieties. Another important

geometric parameter, which is linked to the distances between the pendant and donor and acceptor groups, is the torsional (twist) angle about the C-N bond connecting the pendant group to the succinimide ring. The twist angle is equal to 0^o when the planes of the pendant aromatic ring and succinimydyl ring coincide and it is equal to 90^o when the two planes are orthogonal to each other. The twist angle and closest distances between the donor, pendant and acceptor groups for the lowest energy conformation of each molecule are given in Table 4.5. The pendant group in **8** is the unsubstituted phenyl group (*i.e.* **8** is **1** with *tert*-butyl replaced by H).

Table 4.5 Twist angles (degrees) and closest distances (Å) between the pendant group and acceptor and donor groups and the closest distance between the donor and acceptor.

Molecule	Twist[a]	*r*(dcv-ar)[b]	*r*(nap-ar)[c]	*r*(dcv-napd)[b]
1	44	3.8	4.0	9.4
2	40	3.8	4.2	9.6
3	32	4.5	4.2	9.9
4[e]	47	3.8	3.9	9.4
8[f]	48	3.8	3.9	9.5

[a] Torsional angle about the N-C(aromatic pendant group) bond. [b] Closest distance between the dicyanovinyl and the aromatic pendant groups. [c] Closest distance between the naphthalene and the aromatic pendant groups. [d] Closest distance between the dicyanovinyl and thenaphthalene groups. [e] The pendant group has a methyl substituent rather than the ethyl substituent of 4. [f]phenyl (C_6H_5).

In none of the stable molecular conformations are the pendant and succinimide rings coplanar, a consequence of steric repulsions between the two *ortho* C-H hydrogens of the pendant aromatic ring with the carbonyl groups of the succinimide ring which are present in the coplanar conformation. The twist angle decreases along the series **1** > **2** > **3** and this trend reflects the increasing steric bulk at the *meta* positions of the pendant aromatic ring, by the

presence of methyl substituents. Reducing the magnitude of the twist angle therefore reduces destabilizing steric interactions of the pendant group with the acceptor and donor groups. This increasing steric interaction along the series **3** > **2** > **1** is also probably responsible for the slight increases in the closest distances between the various groups along the series **1** < **2** < **3** (Table 4.5). The placement of a *tert*-butyl group (or an ethyl group **4**) at the *para* position of the pendant aromatic ring has little effect on the molecular geometry (*c.f.* **1** and **8**). This is understandable because the *para* substituent is remote (> 4 Å) from the donor and acceptor groups.

It is difficult to predict the trend in the strengths of the electronic coupling term in the series of U-shaped systems because it seems to depend, not only on the closest distances between the pendant group and the donor and acceptor groups, but also on the type of overlap between the π orbitals of the pendant group with those of the donor and acceptor. Thus, model calculations reported previously[8c] suggested that the coupling is stronger when the plane of the pendant ring is parallel to those of the donor and acceptor (twist angle = 0^o) than when it is perpendicular to those planes (twist angle = 90^o). In the former case, the overlap of the π orbitals is of σ-type whereas for the latter case, it is a mixture of σ- and π-types. The data shown in Table 4.5 indicate that as the twist angle *decreases* along the series **1** > **2** > **3**, the closest distances between the pendant ring and the donor and acceptor groups *increase* slightly. Thus, the electronic coupling term may well be approximately constant along the series.

4.6 Discussion

The electron transfer rate constants in compounds **1** through **3** behave similarly to changes in temperature and solvent as does **4**. The electron transfer rate constants in these molecules are not the same; *e.g.*, at 298 K **4** is ten times faster than **3** in acetonitrile and three

times faster in mesitylene. The differences in the electron transfer rate constants arise from changes in the energetics rather than changes in the couplings. The difference in the electron transfer energetics is apparent from Figure 4.3 and Table 4.3 which shows the experimentally determined reaction free energy for the four solutes in mesitylene. Because the only change between the compounds is alkylation of the pendant phenyl ring, these energetic differences likely arise from changes in the pendant polarizability and the extent of Coulomb stabilization of the charge separated state.

A fit of the rate constant data as a function of temperature to Equation 2 was used to extract values for the solvent reorganization energy and the electronic couplings (see Table 4.4). The reorganization energies in the aromatic solvents range from 0.66 eV to 0.85 eV, whereas those in acetonitrile range from 1.5 eV to 1.7 eV. The reorganization energy for **1**, **2**, and **3** are similar in size to those reported previously for **4**. The magnitudes of the reorganization energies reported here are larger than those reported for analogous systems containing a methoxyanthracene donor and a diacetylvinyl acceptor, however this difference can be attributed to differences in size of the donor and acceptor moieties and distortion of the dicyanovinyl acceptor group in the charge separated state. In particular, the distortion of the dicyanovinyl group may contribute up to 0.5 eV [25] in reorganization energy. The trend in solvent reorganization energy correlates with the changes in solvent polarity. The variations in the reorganization energy between solutes is consistent for the different solvent systems, however they are small enough compared to the expected error that they are not interpreted here.

In the nonadiabatic picture the electron transfer rate constant is directly proportional to the electronic coupling squared $|V|^2$, which gives the probability for electron tunneling from the locally excited state to the charge separated state. For the four solutes studied here (**1** through **4**)

the electronic couplings are all very similar, ranging from 130 cm^{-1} to 150 cm^{-1}. This observation is consistent with electron affinities of alkyl benzenes that do not vary much with substitution pattern.[26] Previous work demonstrated that the electronic coupling in systems of this type occurs by electron mediated superexchange.[27,28] The similar $|V|$ values are consistent with the computational studies and may reflect a compensation between a decrease of the electronic coupling as the phenyl ring twists away from 0° and an increase of the electronic coupling as the donor and acceptor groups distance decreases with the phenyl twist (*vide supra*).

Studies of electron tunneling through nonbonded contacts in related compounds, containing a dimethoxyanthracene donor and a diacetylvinyl acceptor separated by a 7 angstrom gap found a significant variation of the electronic coupling with the substitution pattern and steric bulk of the molecule in the gap between the donor and acceptor group.[9,10] In those studies the alkylated phenyl moiety was a solvent molecule and not tethered to the bridge, hence the change in electronic coupling could reflect either intrinsic changes arising from electronic state differences of the alkylbenzene or geometric changes arising from steric constraints. The current studies show that placement of the aromatic moiety in the cleft gives electronic couplings that do not vary significantly with alkylation and supports the conclusions made in reference 9 that the electronic coupling variation results from steric constraints rather than intrinsic electronic differences.

The small changes in the electronic coupling magnitudes for the different systems studied here bears on studies of **4** in the slowly relaxing solvent N-methylacetamide. That study[8c] reported that **4** and **5** have different electron transfer rates at high temperatures, arising from differences in the electronic coupling, but have similar rates at low temperature. The possibility that phenyl ring rotation in **4** can conformationally gate the electron transfer in that system was

proposed as a possible explanation. The small variation of the electronic coupling with the amount of alkyl substitution and the related geometric changes of the pendant group in the cleft suggest that modulation of the electron tunneling probability by changes in the phenyl ring geometry is not the cause of that behavior.

4.7 Conclusion

The electron transfer in U-shaped molecules containing a pendant group in the line of sight between an electron donor and an electron acceptor was studied. In each case the pendant group was an alkylsubstituted phenyl and had the aromatic moiety in the same location, although twisted at different average angles. The electronic coupling in these systems does not vary significantly.

4.8 Acknowledgements

We acknowledge the support from the Australian Research Council and we thank the U.S. National Science Foundation (CHE-0415457) for support. We gratefully acknowledge support from the Australian Partnership for Advanced Computing (APAC) and the Australian Centre for Advanced Computing and Communications (ac3) for allocation of computing time. All of experiments and analyses were performed at the University of Pittsburgh and the theoretical calculations were performed in Australia.

4.9 Appendix

System	Toluene							
	T(K)	Donor τ (ps)	A1%	τ_1 (ps)	τ_2 (ps)	k_{for} (s^{-1})	k_{back} (s^{-1})	$\Delta_r G$ (eV)
4	295.0	4203	99.0	399	25515	2.24×10^{9}	2.59×10^{7}	-1.13×10^{-1}
	305.6	3980	98.5	355	39882	2.52×10^{9}	4.63×10^{7}	-1.05×10^{-1}
	314.7	3814	98.0	324	41885	2.77×10^{9}	6.58×10^{7}	-1.01×10^{-1}
	323.9	3663	97.0	279	42236	3.21×10^{9}	1.15×10^{7}	-9.30×10^{-2}
	336.6	3479	95.8	264	38555	3.35×10^{9}	1.70×10^{7}	-8.64×10^{-2}
1	295.0	3610	99.2	642	18894	1.27×10^{9}	1.45×10^{7}	-1.14×10^{-1}
	304.6	3449	98.9	595	25233	1.37×10^{9}	2.13×10^{7}	-1.09×10^{-1}
	314.0	3262	98.3	541	36867	1.51×10^{9}	3.76×10^{7}	-9.99×10^{-2}
	324.3	3115	97.6	506	35573	1.61×10^{9}	5.51×10^{7}	-9.43×10^{-2}
	338.1	2914	95.8	425	32979	1.91×10^{9}	1.13×10^{7}	-8.25×10^{-2}
2	295.0	4352	99.2	706	20376	1.18×10^{9}	1.22×10^{7}	-1.16×10^{-1}
	304.4	4181	99.0	634	17595	1.32×10^{9}	1.69×10^{7}	-1.14×10^{-1}
	313.6	3995	98.8	565	35721	1.50×10^{9}	2.50×10^{7}	-1.11×10^{-1}
	324.4	3809	98.0	484	51482	1.77×10^{9}	4.59×10^{7}	-1.02×10^{-1}
	338.0	3602	96.8	436	52504	1.94×10^{9}	8.27×10^{7}	-9.20×10^{-2}
3	295.0	5452	94.7	1214	1764	6.26×10^{8}	5.32×10^{6}	-1.21×10^{-1}
	304.4	5216	98.1	1127	5836	6.81×10^{8}	1.43×10^{6}	-1.01×10^{-1}
	313.6	4981	99.2	1044	46604	7.50×10^{8}	9.42×10^{6}	-1.18×10^{-1}
	324.4	4720	99.0	928	38192	8.56×10^{8}	1.28×10^{7}	-1.18×10^{-1}
	338.1	4407	98.4	820	45718	9.73×10^{8}	2.31×10^{7}	-1.09×10^{-1}

System	Mesitylene							
	T(K)	Donor τ (ps)	A1%	τ_1 (ps)	τ_2 (ps)	k_{for} (s^{-1})	k_{back} (s^{-1})	$\Delta_r G$ (eV)
4	295.0	3474	97.2	407	28211	2.10×10^{9}	7.59×10^{7}	-8.44×10^{-2}
	306.3	3294	96.1	349	28426	2.45×10^{9}	1.23×10^{8}	-7.90×10^{-2}
	314.9	3174	94.8	316	28059	2.69×10^{9}	1.78×10^{8}	-7.36×10^{-2}
	323.7	3063	93.5	296	27106	2.84×10^{9}	2.40×10^{8}	-6.89×10^{-2}
	333.7	2950	91.8	260	25142	3.19×10^{9}	3.39×10^{8}	-6.45×10^{-2}
1	273.3	4392	98.8	897	42871	8.74×10^{8}	1.59×10^{7}	-9.44×10^{-2}
	281.7	4139	98.5	809	37068	9.76×10^{8}	2.26×10^{7}	-9.15×10^{-2}
	294.9	3792	97.6	702	43591	1.13×10^{9}	4.11×10^{7}	-8.42×10^{-2}
	304.4	3588	96.5	639	41463	1.23×10^{9}	6.56×10^{7}	-7.70×10^{-2}
	314.3	3407	95.2	584	36678	1.34×10^{9}	9.79×10^{7}	-7.08×10^{-2}
	324.3	3241	93.3	543	31378	1.41×10^{9}	1.46×10^{8}	-6.35×10^{-2}
	331.5	3120	91.1	498	26001	1.51×10^{9}	2.08×10^{8}	-5.67×10^{-2}
	338.1	3020	89.6	473	22567	1.57×10^{9}	2.56×10^{8}	-5.28×10^{-2}
	346.3	2921	86.9	443	18316	1.63×10^{9}	3.39×10^{7}	-4.69×10^{-2}
2	304.5	3928	97.6	616	47992	1.33×10^{9}	4.56×10^{7}	-8.85×10^{-2}
	314.6	3739	96.5	541	46466	1.52×10^{9}	7.38×10^{7}	-8.20×10^{-2}
	324.8	3951	95.4	513	41172	1.58×10^{9}	1.03×10^{8}	-7.63×10^{-2}
	331.5	3462	94.2	437	36195	1.87×10^{9}	1.50×10^{8}	-7.21×10^{-2}
	339.4	3342	92.4	423	31387	1.89×10^{9}	2.03×10^{8}	-6.52×10^{-2}
	346.3	3266	91.2	379	27944	2.10×10^{9}	2.57×10^{8}	-6.28×10^{-2}
3	308.3	4873	98.2	936	54290	8.45×10^{8}	2.29×10^{7}	-9.59×10^{-2}
	317.4	4624	97.5	869	49846	9.07×10^{8}	3.38×10^{7}	-9.00×10^{-2}
	327.8	4354	96.6	762	46523	1.04×10^{9}	5.22×10^{7}	-8.45×10^{-2}
	331.5	4258	96.1	707	47701	1.13×10^{9}	6.39×10^{7}	-8.20×10^{-2}
	341.5	4025	95.2	672	41206	1.17×10^{9}	8.36×10^{7}	-7.77×10^{-2}
	346.3	3958	94.1	606	38478	1.30×10^{9}	1.12×10^{8}	-7.33×10^{-2}

System	*p*-Xylene							
	T(K)	Donor τ (ps)	A1%	τ_1 (ps)	τ_2 (ps)	k_{for} (s^{-1})	k_{back} (s^{-1})	$\Delta_r G$ (eV)
4	295.0	4051	97.9	418	48039	2.10×10^9	5.53×10^7	-9.24×10^{-2}
	305.1	3834	97.0	364	46308	2.40×10^9	8.94×10^7	-8.66×10^{-2}
	314.6	3641	96.1	339	44762	2.56×10^9	1.26×10^8	-8.18×10^{-2}
	323.1	3488	94.9	306	41869	2.82×10^9	1.80×10^8	-7.66×10^{-2}
	333.6	3317	93.4	265	36500	3.23×10^9	2.69×10^8	-7.14×10^{-2}
1	295.0	3851	97.8	722	82187	1.10×10^9	3.72×10^7	-8.60×10^{-2}
	305.3	3672	96.8	666	69655	1.18×10^9	5.77×10^7	-7.95×10^{-2}
	313.6	3496	95.5	611	59909	1.28×10^9	8.73×10^7	-7.26×10^{-2}
	323.5	3329	94.0	565	46653	1.37×10^9	1.27×10^8	-6.62×10^{-2}
	335.0	3128	91.7	512	34368	1.48×10^9	1.92×10^8	-5.89×10^{-2}
2	295.0	4217	98.7	763	38878	1.06×10^9	1.95×10^7	-1.02×10^{-1}
	305.3	4011	98.0	653	52550	1.25×10^9	3.50×10^7	-9.42×10^{-2}
	313.1	3860	97.3	578	59762	1.43×10^9	5.34×10^7	-8.87×10^{-2}
	323.7	3675	96.3	508	57896	1.62×10^9	8.37×10^7	-8.27×10^{-2}
	334.4	3497	94.6	448	49157	1.83×10^9	1.36×10^8	-7.49×10^{-2}
3	295.0	5377	98.9	1299	5377	5.77×10^8	6.57×10^6	-1.14×10^{-1}
	305.1	5072	98.9	1120	50337	6.86×10^8	1.18×10^7	-1.07×10^{-1}
	315.3	4824	98.5	1006	57091	7.72×10^8	1.85×10^7	-1.01×10^{-1}
	323.3	4585	97.8	898	64473	8.72×10^8	2.92×10^7	-9.47×10^{-2}
	333.9	4326	97.0	789	62787	9.99×10^8	4.58×10^7	-8.87×10^{-2}

System	Acetonitrile			
	T(K)	Donor τ (ps)	τ_1 (ps)	k_{ET} (s^{-1})
4	301	11375	1382	6.36×10^8
	309	11102	1172	7.63×10^8
	317	10472	1069	8.40×10^8
	327	9897	918	9.88×10^8
	337	9389	806	1.13×10^9
1	273	10900	2575	2.97×10^8
	281	10492	2286	3.42×10^8
	295	10478	1879	4.37×10^8
	305	10049	1662	5.02×10^8
	314	8985	1446	5.80×10^8
	324	9089	1295	6.62×10^8
	340	8401	1085	8.02×10^8
2	276	12828	6542	7.49×10^7
	282	12335	5858	8.96×10^7
	295	11432	4501	1.35×10^8
	304	11071	3893	1.67×10^8
	315	10448	3225	2.14×10^8
	324	10098	2775	2.61×10^8
3	276	14211	8040	5.40×10^7
	282	13952	7498	6.17×10^7
	295	13488	6265	8.55×10^7
	305	13218	5487	1.07×10^8
	315	12929	4848	1.29×10^8
	323	12757	4245	1.57×10^8
	338	12370	3467	2.08×10^8

4.10 Reference

1. a) Closs, G. L.; Miller, J. R. *Science*, **1988**, *240*, 440; b) Paddon-Row, M. N. *Acc. Chem. Res.*, **1994**, *27*, 18. c) Barbara, P. F.; Meyer, T. J.; Ratner, M. A. *J. Phys. Chem.*, **1996**, *100*, 13148; d) Paddon-Row, M. N., In "*Electron Transfer In Chemistry"*; Balzani, V., Ed.; Wiley-VCH: Weinheim, **2001**; Vol. Vol. 3, Part 2, Chapter 1; p.179.
2. a) Hush, N. S.; Paddon-Row, M. N.; Cotsaris, E.; Oevering, H.; Verhoeven, J. W.; Heppener, M. *Chem. Phys. Lett.*, **1985**, *117*, 8; b) Penfield, K. W.; Miller, J. R.; Paddon-Row, M. N.; Cotsaris, E.; Oliver, A. M.; Hush, N. S. *J. Am. Chem. Soc.*, **1987**, *109*, 5061; c) Pispisa, B.; Venanzi, M.; Palleschi, A. *J. Chem. Soc. Far. Trans.*, **1994**, *90*, 435; d) Closs, G. L.; Calcaterra, L. T.; Green, N. J.; Penfield, K. W.; Miller, J. R. *J. Phys. Chem.*, **1986**, *90*, 3673; e) Leland, B. A.; Joran, A. D.; Felker, P. M.; Hopfield, J. J.; Zewail, A. H.; Dervan, P. B. *J. Phys. Chem.*, **1985**, *89*, 5571.
3. a) Helms, A.; Heiler, D.; McClendon, G. *J. Am. Chem. Soc.*, **1991**, *113*, 4325; b) Sakata, Y.; Tsue, H.; O'Neil, M. P.; Wiederrecht, G. P.; Wasielewski, M. R. *J. Am. Chem. Soc.*, **1994,** *116*, 6904; c) Guldi, D. M.; Luo, C.; Prato, M.; Troisi, A.; Zerbetto, F.; Scheloske, M.; Dietel, E.; Bauer, W.; Hirsch, A. *J. Am. Chem. Soc.*, **2001**, *123*, 9166.
4. a) Kroon, J.; Oliver, A. M.; Paddon-Row, M. N. and Verhoeven, J. W. *Rec, Trav. Chim. Pays-Ba*, **1988**, *107*, 509; b) Oliver, A. M.; Craig, D. C.; Paddon-Row, M. N.; Kroon, J. and Verhoeven, J. W. *Chem. Phys. Lett.*, **1988**, *150*, 366; c) Lawson, J. M.; Craig, D. C.; Paddon-Row, M. N.; Kroon, J. and Verhoeven, J. W. *Chem. Phys. Lett.*, **1989**, *164*, 120.
5. a) Zeng Y. and Zimmt, M. B. *J. Am. Chem. Soc.*, **1991**, *113*, 5107; b) Oliver, A. M.; Paddon-Row, M. N.; Kroon, J. and Verhoeven, J. W. *Chem. Phys. Lett.*, **1992**, *191*, 371.

6. Paddon-Row, M. N., Shephard, M. H. *J. Am. Chem. Soc*., **1997**, *119*, 5355.

7. a) Kumar, K.; Lin, Z.; Waldeck, D. H.; Zimmt, M. B. *J. Am. Chem. Soc.*, **1996**, *118*, 243; b) Kumar, K.; Kurnikov, I.; Beratan, D. N.; Waldeck, D. H.; Zimmt, M. B. *J. Phys. Chem. A*, **1998**, *102*, 5529; c) Lokan, N. R.; Craig, D. C.; Paddon-Row, M. N. *Synlett*, **1999**, 397; d) Lokan, N. R.; Paddon-Row, M. N.; Koeberg, M.; Verhoeven, J. W. *J. Am. Chem. Soc.*, **2000**, *122*, 5075; e) Jolliffe, K. A.; Bell, T. D. M.; Ghiggino, K. P. ; Langford, S. J. ; Paddon-Row, M. N. *Angew. Chem., Int. Ed.*, **1998**, *37*, 915; f) Bell, T. D. M.; Jolliffe, K. A.; Ghiggino, K. P.; Oliver, A. M.; Shephard, M. J.; Langford, S. J.; Paddon-Row, M. N. *J. Am. Chem. Soc.*, **2000**, *122*, 10661; g) Bell, T. D. M.; Ghiggino, K. P.; Jolliffe, K. A.; Ranasinge, M. G.; Langford, S. J.; Shephard, M. J.; Paddon-Row, M. N. *J. Phys. Chem. A*, **2002**, *106*, 10079; h) Smith, T. A.; Lokan, N.; Cabral, N.; Davies, S. R.; Paddon-Row, M. N.; Ghiggino, K. P. *J. Photochem. Photobiol. A: Chem.*, **2002**, *149*, 55.

8. a) Napper, A. M.; Head, N. J.; Oliver, A. M.; Shephard, M. J.; Paddon-Row, M. N.; Read, I.; Waldeck, D. H. *J. Am. Chem. Soc*, **2002**, *124*, 10171; b) Napper, A. M.; Read, I.; Waldeck, D. H.; Head, N. J.; Oliver, A. M.; Paddon-Row, M. N. *J. Am. Chem. Soc.*, **2000**, *122*, 5220; c) Liu, M.; Waldeck, D. H.; Oliver, A. M.; Head, N. J.; Paddon-Row, M. N. *J. Am. Chem. Soc.*, **2004**, *126*, 10778.

9. Read, I.; Napper, A. M.; Kaplan, R.; Zimmt, M. B.; Waldeck, D. H. *J. Am. Chem. Soc.*, **1999**, *121*, 10976.

10. Zimmt, M. B. and Waldeck, D. H. *J. Phys. Chem. A*, **2003**, *107*, 3580.

11. a) Oevering, H.; Verhoeven, J. W.; Paddon-Row, M. N.; Warman, J. M. *Tetrahedron*, **1989**, *45*, 4751; b) Oevering, H.; Paddon-Row, M. N.; Heppener, H.; Oliver, A. M.; Cotsaris, E.; Verhoeven, J. W.; Hush, N. S. *J. Am. Chem. Soc.*, **1987**, *109*, 3258.

12. Wong, M. W. *Chem. Phys. Lett.*, **1996**, *256*, 391.

13. Kulinowski, K.; Gould, I. R.; Myers, A. B. *J. Phys. Chem.*, **1995**, *99*, 9017.

14. Matyushov, D. V. and Voth, G. A. *J. Chem. Phys.*, **1999**, *111*, 3630.

15. Vath, P.; Zimmt, M. B.; Matyushov, D. V.; Voth, G. A. *J. Phys. Chem. B.*, **1999**, *103*, 9130.

16. Birks, J. B. *Photophysics of Aromatic Molecules* (Wiley, NY, **1970**).

17. Berden, G.; Meerts, W. L.; Plusquellic, D. F.; Fujita, I.; Pratt, D. W. *J. Chem. Phys.*, **1996**, *104*, 3935.

18. Martin, B.; Geneck, P.; Clark, T. *International Journal of Quantum Chemistry*, **2000**, *77*, 473.

19. Gray, C. G.; Gubbins, K. E., "*Theory of Molecular Fluids", Vol. 1*; Clarendon Press: Oxford, **1984**

20. Ben-Amotz, D. and Willis, K. G. *J. Phys. Chem.*, **1993**, *97*, 7736.

21. Matyushov, D. V. and Schmid, R. *J. Chem. Phys.*, **1996**, *104*, 8627.

22. The pendant's polarizability was estimated from Ma, B.; Lii, J.-H.; Allinger, N. L. *J. Comput. Chem.*, **2000**, *21*, 813. The perpendicular polarizability, 5.7 $Å^3$ was used for the propyl group; the polarizability perpendicular to the phenyl axis was taken to be 7.4 $Å^3$; the average polarizability of toluene (12.30 $Å^3$), 2-methylpropene (8.29 $Å^3$), methane (2.56 $Å^3$) were used to approximate the polarizability of compound **1** – **3**. The change of the polarizability matches with the increasing size of the pendant groups in compound **1- 4**. This similar calculation predicts a shift in the reaction free energy amongst compound **1** – **4**.

23. a) Matyushov, D. V. *Chem. Phys.*, **1993**, *174*, 199; b) Matyushov, D. V. *Mol. Phys.*, **1993**, *79*, 795.

24. Gaussian 03, Revision A.1, Frisch, M. J.; Trucks, G. W.; Schlegel, H. B.; Scuseria, G. E.; Robb, M. A.; Cheeseman, J. R.; Montgomery, Jr., J. A.; Vreven, T.; Kudin, K. N.; Burant, J. C.; Millam, J. M.; Iyengar, S. S.; Tomasi, J.; Barone, V.; Mennucci, B.; Cossi, M.; Scalmani, G.; Rega, N.; Petersson, G. A.; Nakatsuji, H.; Hada, M.; Ehara, M.; Toyota, K.; Fukuda, R.; Hasegawa, J.; Ishida, M.; Nakajima, T.; Honda, Y.; Kitao, O.; Nakai, H.; Klene, M.; Li, X.; Knox, J. E.; Hratchian, H. P.; Cross, J. B.; Adamo, C.; Jaramillo, J.; Gomperts, R.; Stratmann, R. E.; Yazyev, O.; Austin, A. J.; Cammi, R.; Pomelli, C.; Ochterski, J. W.; Ayala, P. Y.; Morokuma, K.; Voth, G. A.; Salvador, P.; Dannenberg, J. J.; Zakrzewski, V. G.; Dapprich, S.; Daniels, A. D.; Strain, M. C.; Farkas, O.; Malick, D. K.; Rabuck, A. D.; Raghavachari, K.; Foresman, J. B.; Ortiz, J. V.; Cui, Q.; Baboul, A. G.; Clifford, S.; Cioslowski, J.; Stefanov, B. B.; Liu, G.; Liashenko, A.; Piskorz, P.; Komaromi, I.; Martin, R. L.; Fox, D. J.; Keith, T.; Al-Laham, M. A.; Peng, C. Y.; Nanayakkara, A.; Challacombe, M.; Gill, P. M. W.; Johnson, B.; Chen, W.; Wong, M. W.; Gonzalez, C.; and Pople, J. A.; Gaussian, Inc., Pittsburgh PA, 2003.

25. Rothenfluh, D. F. and Paddon-Row, M. N. *J. Chem. Soc. Perkin. Trans. 2*, **1996**, 639.

26. Jordan, K. D.; Michejda, J. A.; Burrow, P. D. *J. Am. Chem. Soc.*, **1976**, *98*, 1295.

27. a) Napper, A. M.; Read, I.; Kaplan, R.; Zimmt, M. B. and Waldeck, D.H. *J. Phys. Chem. A*, **2002**, *106*, 5288; b) Kaplan, R.; Napper, A. M.; Waldeck, D. H. and Zimmt, M. B. *J. Phys. Chem. A*, **2002**, *106*, 1917.

28. Koeberg, M.; de Groot, M.; Verhoeven, J. W.; Lokan, N. R.; Shephard, M. J. and Paddon-Row, M. N. *J. Phys. Chem. A*, **2001**, *105*, 3417; b) Goes, M.; de Groot, M.; Koeberg, M.;

Verhoeven, J. W.; Lokan, N. R.; Shephard, M. J. and Paddon-Row, M. N. *J. Phys. Chem. A*, **2002**, *106*, 2129.

Chapter 5 Hole Transfer in a C-shaped Molecule: Conformational Freedom Obviates Solvent Mediated Coupling

This work has been published as J. M. Nadeau, M. Liu, D. H. Waldeck, M. B. Zimmt, J. Am. Chem. Soc., 125, 15964, (2003).

The electronic coupling matrix elements attending the charge separation reactions of a C-shaped molecule containing an excited pyrene as the electron acceptor and a dimethylaniline as the donor are determined in aromatic, ether, and ester solvents. Band shape analyses of the charge-transfer emission spectra ($CT \rightarrow S_0$) provide values of the reaction free energy, the solvent reorganization energy, and the vibrational reorganization energy in each solvent. The free energy for charge separation in benzene and toluene solvent is independently determined from the excited state equilibrium established between the locally excited pyrene S_1 state and the charge-transfer state. Analysis of the charge separation kinetics using the spectroscopically determined reorganization energies and reaction free energies indicate that the electronic coupling is solvent independent, despite the presence of a cleft between the donor and acceptor. Hence, solvent molecules are not involved in the coupling pathway. The orientations of the donor and acceptor units, relative to the spacer, are not rigidly constrained, and their torsional motions decreases solvent access to the cleft. Generalized Mulliken-Hush calculations show that rotation of the pyrene group about the bond connecting it to the spacer greatly modulates the magnitude of through-space coupling between the S_1 and CT states. The relationship between the torsional dynamics and the electron-transfer dynamics is discussed.

5.1 Introduction

The great progress in understanding unimolecular electron-transfer processes during the past two decades has occurred by combining experiments and theoretical calculations on well-defined donor-spacer-acceptor molecules.[1] In these studies, the electron-transfer rate constant is described by a Golden Rule expression which treats nuclear and electronic degrees of freedom as independent quantities.[2] This rate formulation is appropriate when the donor-acceptor electronic coupling (which is a measure of these groups' quantum mechanical mixing) is small and the same every time the transition state is accessed. This criterion (the Condon approximation) is best satisfied in conformationally restricted systems, such as "rigid", linear donor-bridge-acceptor molecules. The dependence of electronic coupling magnitude on bridge structure in a variety of "rigid" systems has been investigated and is well understood.[3] In contrast to such systems, the C-shaped molecule studied here has two potential sources of nuclear coordinate-dependent electronic coupling: (i) a direct, through-space interaction that is modulated by the conformational freedom of the donor and acceptor groups and (ii) an indirect, solvent-mediated interaction that is modulated by a solvent molecule's placement in the cleft that lies between the donor and acceptor. The influence of these nuclear coordinates on the overall electronic coupling and on the electron-transfer process is explored in this investigation.

The dynamical consequences of nuclear coordinate-dependent electronic coupling have been addressed in a number of limiting cases. When interconversion rates between a predominant system conformation and a number of highly reactive conformations are slow, the experimental transfer rate constant reflects conformational dynamics more than intrinsic electron-transfer rate constants; that is, the system is conformationally gated.[4] Additional kinetic complexity arises in systems when interconversion rates among multiple reactive conformations

are comparable to the transfer rate constants of the individual conformations. A different category of complexity arises if a set of nuclear coordinates influences the barrier to electron transfer (*i.e.*, the nuclear Franck-Condon factors) and also strongly modulates the donor-acceptor electronic coupling. This produces an explicit nuclear dependence of the coupling matrix element, which violates the Condon approximation and may invalidate use of the Golden Rule rate expression. Systems that may fall into this category include protein electron transfers,[5] symmetry forbidden but vibronically allowed electron transfers,[6] and solvent-mediated electron transfers.[7] In the latter systems, different placements of solvent molecules generate different values of the donor-acceptor coupling matrix element, thus altering the electron tunneling probability, and at the same time contribute to the activation barrier through solvation and reorganization effects.

During the past few years, we have analyzed electron-transfer dynamics from a number of systems in which coupling is primarily solvent mediated. These investigations employ rigid C-shaped structures with a solvent-accessible cleft directly between the donor and acceptor groups. The rigidity guarantees that each molecule populates only one conformation. The length and topology of the spacers, in conjunction with the attachment geometries of the donor and acceptor, were designed to reduce through-bond coupling magnitudes so that solvent-mediated coupling dominates. In these systems, solvent molecules within the cleft constitute the electron tunneling pathway between the donor and acceptor group. Striking evidence for the solvent's participation in the electron tunneling pathway comes from the strong correlation between the experimentally derived electronic coupling magnitude and the solvent's LUMO energy.[8] Because the electron-transfer reaction within the C-shaped molecule is initiated by photoexcitation of the donor, the transferring electron originates in the donor LUMO. The energetic proximity of vacant solvent

orbitals to the LUMO of the excited donor provides a rationale for the observed correlations. Solvent molecules with a lower energy LUMO enhance the excited donor to acceptor coupling because they provide lower energy excited configurations (resonance structures), such as D^+S^-A, that more effectively mix into the donor excited state and, simultaneously, increase the acceptor's proximity to the transferring electron.[9] This explanation suggests that a C-shaped molecule employing an electronically excited acceptor might display solvent-mediated coupling magnitudes that correlate with solvent HOMO energy; that is, energetic proximity of solvent valence orbitals to the transferring hole in the HOMO of an excited acceptor should enhance electron tunneling from D to A*.

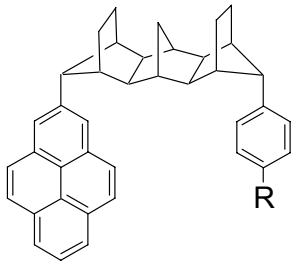

1. R = NMe_2
2. R = H

Scheme 1

This manuscript analyzes the electron-transfer kinetics and charge-transfer emission spectra from a C-shaped molecule containing an excited acceptor and a ground state donor. Molecule **1** (Scheme 1) has a 2'-pyrenyl acceptor (A) and a 4'-*N*,*N*-dimethylanilinyl donor (D) that are connected by single bonds to the terminal, CH_2 bridges of a tetradecahydro-1,4:5,8:9,10-trimethanoanthracene spacer. Eight σ bonds separate the acceptor and donor groups. In the molecule's lowest energy conformation, the pyrene and dimethylaniline groups lie in roughly parallel planes displaced by 6.7 Å. Molecular mechanics calculations indicate that the cleft

defined by the donor, spacer, and acceptor is just large enough to accommodate aromatic or other nearly planar solvent molecules. The gas phase, vertical ionization potential of dimethylaniline is ~7.4 eV.[10] The gas phase, vertical ionization potentials of the solvents employed in this investigation range from 8.4 eV (anisole) to 10.4 eV (ethyl acetate). The energy of a virtual (A^-)-($solvent^+$)-D superexchange[9a,b] configuration changes substantially across this set of solvents, as should its mixing with the acceptor excited state.[8] If donor-acceptor coupling in **1** is predominantly solvent mediated, the experimentally determined coupling value ought to decrease as the energy of the virtual[9a] A^--($solvent^+$)-D configuration increases, that is, from anisole to ethyl acetate. In contrast to this prediction, the experimentally determined coupling magnitudes are solvent independent, exhibiting no correlation with solvent ionization potential (HOMO level) or solvent electron affinity (LUMO level). This is evidence against the involvement of solvent in the electron tunneling pathway. Surprisingly, calculations reveal negligible electronic coupling in the lowest energy conformation of molecule **1**, indicating that through-space and through-bond tunneling pathways are inactive. Instead, the calculations predict large donor-acceptor* electronic coupling in conformations formed by twisting the pyrene or the dimethylaniline about the σ bonds connecting these groups to the spacer. Taken together, the experiments and calculations indicate that donor-acceptor electronic coupling in **1** is strongly modulated by the conformational degrees of freedom of the molecule.

5.2 Experimental Section

The preparation of **1** and its acceptor only analogue **2** are reported elsewhere.[11] Samples used for steady-state spectroscopy had optical densities of 0.05-0.15 at the excitation wavelength (331 nm) in freshly dried and distilled solvents. Spectra were recorded on a SPEX F111X1

fluorimeter using 0.1 mm slits and were corrected for the detection system response. Samples for nanosecond time-resolved fluorescence spectroscopy (λ_{exc} 331 nm) and picosecond time-resolved photon counting (λ_{exc} 321 nm) were freeze-pump-thaw degassed a minimum of four cycles. Samples investigated at temperatures above 25 ºC were back-filled with high purity argon to prevent solvent distillation. The apparatus for both time-resolved fluorescence methods was previously described.[12] Fluorescence decays of the excited pyrene were recorded at 380 nm to eliminate contributions from the charge-transfer (CT) emission band. Fluorescence decays of the CT band were detected at wavelengths longer than 490 nm. Fluorescence decays were fit by iterative convolution of a mono-, bi-, or triexponential expression with an instrument response function obtained from a $BaSO_4$-glycerol colloid. Fits to a triexponential expression were realized by adjusting three amplitudes and two decay rate constants. The slowest decay rate constant was independently determined from a single-exponential fit of the final 100 ns of the photon counting data or from a 500 ns data set obtained with the nanosecond apparatus.

Samples of compound **1** contained trace amounts of an unidentified impurity and of a pyrene-spacer molecule that lacked an active donor group. HPLC purification reduced but did not eliminate these impurities from the sample. The emission spectrum of the unidentified impurity overlapped significantly with that of pyrene; however, its decay rate constant, which varied with solvent between 0.2 and 0.5 ns^{-1}, was considerably slower than the charge separation rate constants for **1** and much faster than the decay rate constants of the CT state. The impurity's presence necessitated a triexponential analysis of the fluorescence decay, but otherwise provided little interference in the kinetic analyses or in the analyses of charge-transfer emission line shapes. The pyrene-spacer impurity contributed 3.3% of the pyrene fluorescence decay amplitude detected at 380 nm. This value was determined in polar solvents, where the $S_1 \rightarrow$ CT

transition is irreversible. The contribution of this impurity was removed prior to determination of the charge separation free energy, $\Delta_r G$ ($S_1 \rightarrow$ CT), from the ratio of the fast and slow pyrene decay amplitudes.[8]

5.3 Results and Discussion

5.3.1 Emission Spectroscopy

The steady-state emission spectrum of **1** exhibits structured, pyrene-like peaks between 370 and 470 nm and a broad, featureless band that extends to wavelengths greater than 600 nm (Figure 5.1).

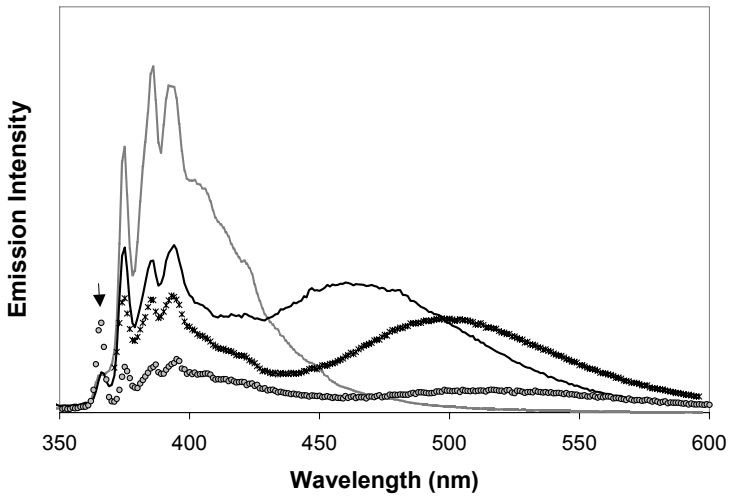

Figure 5.1 Steady state fluorescence spectra from **1** in cyclohexane (gray line, intensity × 0.4), benzene (black line), anisole (cross), tetrahydrofuran (shaded circles, intensity × 3.0). The arrow points to Raman peaks (C-H) from the solvent.

The latter emission is obscured partially by the red edge of the pyrene-like emission. The overall intensity of the structured region varies with solvent, but the positions of the peaks remain constant at 375, 386, and 394 nm. The structured emission from **1** is assigned as fluorescence from the lowest excited singlet state (S_1, LE) of the pyrene acceptor on the basis of its similarity to the spectrum from the pyrene-spacer analogue, **2**. The intensity and position of the broad featureless emission is strongly solvent dependent. The large red shift of this band with increasing solvent polarity identifies it as a charge-transfer (CT → S_0) emission.

The solvatochromic shift of a CT band can be analyzed using the Lippert-Mataga relationship,[13,14]

$$\nu_{max} = \left[\frac{-2\mu_{dip}^{\ 2}}{a^3}\right]\left[\frac{\varepsilon - 1}{2\varepsilon + 1} - \frac{n^2 - 1}{4n^2 + 2}\right] + \nu^0_{max} \qquad \mathbf{1}$$

where ν_{max} is the CT emission maximum in a given solvent (expressed in cm^{-1}), ν^0_{max} is the CT emission maximum for $\Delta f = 0$ (where $\Delta f = [(\varepsilon - 1)/(2\varepsilon + 1)] - [(n^2 - 1)/(4n^2 + 2)]$), a is the effective spherical radius of the cavity that the donor-spacer-acceptor molecule occupies in the solvent, μ_{dip} is the CT state dipole moment, ε is the solvent dielectric constant, and n is the refractive index of the solvent. This form of equation 1 is appropriate because the ground-state dipole moment of **1** is small (< 1.5 D). CT spectra and emission maxima were determined in ether and ester solvents (Table 5.1). The data points (Figure 5.2) deviate somewhat from a straight line, with the values in acyclic ethers somewhat offset from those in the ester solvents. The slope obtained from a linear fit to the data is -30 560 cm^{-1} and yields $\mu_{dip}(D) = (3.03 \times a^3)^{1/2}$. Assuming a cavity radius of 6 or 7 Å produces a charge-separated state dipole moment of 25.6 or 32.3 D, respectively.[15] These values correspond to transfer of a full electron over a distance of 5.3 and 6.7 Å, which is consistent with the ground state, donor-acceptor separation. The spectral

analysis is too crude to determine whether charge separation induces a significant reduction of the donor-acceptor separation in **1**.

Table 5.1 CT emission maxima (ν_{max}) of 1 in dipolar solvents at 295 K.[a] Solvent polarity parameters, n, ε_s, and Δf, are listed for each solvent.[b,c]

Solvent	*n*	ε_s	Δf	Experimental ν_{max} (cm^{-1})
n-butyl ether	1.40	3.1	0.194	21,500
n-propyl ether	1.38	3.4	0.214	21,200
isopropyl ether	1.37	3.9	0.238	20,800
ethyl ether	1.35	4.3	0.255	20,300
n-butyl propionate	1.40	4.83	0.261	19,300
n-butyl acetate	1.39	5.1	0.269	19,200
n-propyl acetate	1.38	5.5	0.281	19,000
ethyl acetate	1.37	6.0	0.292	18,700
THF	1.41	7.5	0.307	18,300

[a] An instrument correction factor for the monochromator and detector response was applied to each spectrum.[b] n_D values were obtained from the Aldrich Handbook of Fine Chemicals and Laboratory Equipment, 2001-2002.[c] ε_s values were obtained from either: (a) Kaplan, R.; Napper, M.; Waldeck, D. H.; Zimmt, M. B. *J. Phys. Chem. A* **2002**, *106*, 1917-1925 or (b) Madelung, O. *Landolt-Börnstein Numerical Data and Functional Relationships in Science and Technology, New Series IV*; Springer-Verlag: New York, 1991; Vol. 6.

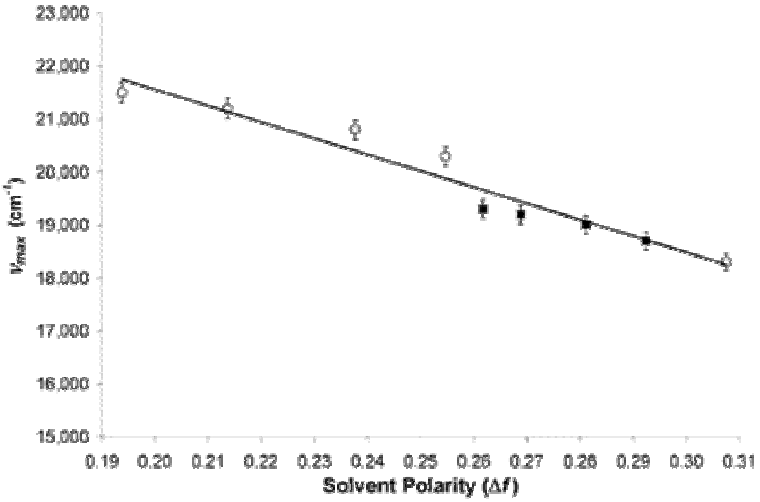

Figure 5.2 Lippert-Mataga plot for the CT emission band of **1** (see eq 1). Ether solvents are indicated by empty circle. Ester solvents are indicated with black square.

5.3.2 Electron-Transfer Thermodynamics and Reorganization Parameters.

The charge recombination driving force, $\Delta_r G$ (CT → S_0), for **1** dissolved in weakly and moderately polar solvents may be estimated through simulation of the CT emission line shape.[16,17] Such fits provide estimates of $\Delta_r G$ (CT → S_0) and other electron-transfer parameters included in the semiclassical model: λ_0, the solvent (low frequency) reorganization energy; λ_v, the vibrational (high frequency) reorganization energy; and $\hbar\omega$, the average mode spacing associated with the high frequency reorganization. Many combinations of the four parameters accurately reproduce the experimental line shapes. Fortunately, **1** exhibits LE ⇔ CT equilibrium in weakly polar solvents, and analysis of the kinetic data (*vide infra*) provides an independent value of the charge separation free energy, $\Delta_r G$ (S_1 → CT), in benzene (-0.11 eV) and toluene (-0.05 eV). These free energies were used to constrain fits to the CT spectra so as to obtain more accurate reorganization parameters.

The CT line shape analysis for **1** in benzene and toluene was constrained by setting $\Delta_r G$ (CT → S_0) = -$\Delta_r G$ (S_1 → CT) − 3.33 eV, where 3.33 eV is the pyrene excited state energy. The CT emission spectra from these two solvents were fit simultaneously with a single λ_v parameter for both solvents, a separate λ_0 parameter for each solvent, and a single fixed value of $\hbar\omega$.[18] The procedure was repeated with $\hbar\omega$ fixed to values between 0.12 and 0.22 eV in steps of 0.02 eV. The best fits were obtained with $\hbar\omega$ between 0.18 and 0.22 eV (Figure 5.3). The analysis yielded five ($\hbar\omega$, λ_v) pairs correlated to one of five values of λ_0 for benzene and for toluene. In general, larger assumed values of $\hbar\omega$ produced smaller λ_v and larger λ_0 values. Line shape analyses for **1** in the remaining solvents employed the five ($\hbar\omega$, λ_v) pairs and generated five corresponding pairs of ($\Delta_r G$ (CT → S_0), λ_0) for each solvent.

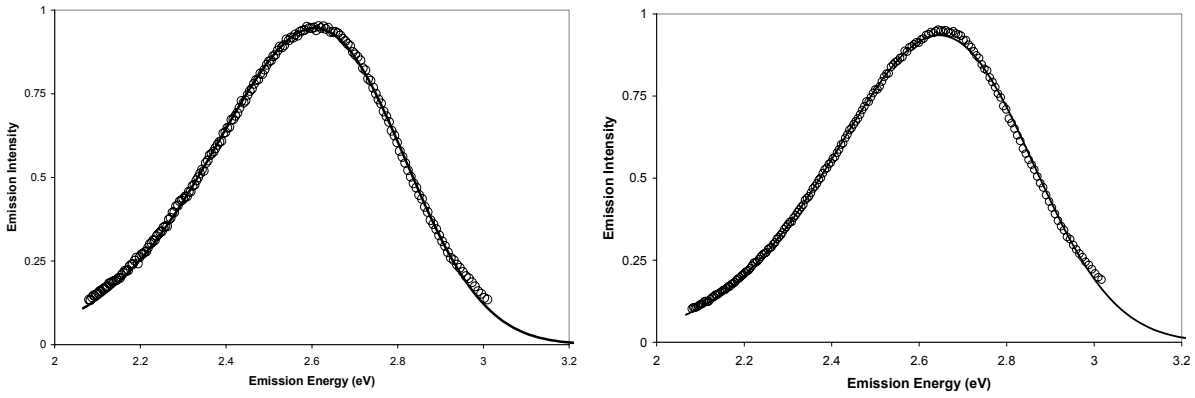

Figure 5.3 Experimental (circle) and calculated (lines) charge transfer emission spectra from **1** in Benzene (left) and Toluene (right). The spectra were calculated using λ_v = 0.15 eV, $\hbar\omega$ = 0.20 eV and Δ_rG (CT→S_0) = -3.22 eV (benzene) and -3.28 eV (toluene). Fitting yielded λ_0 = 0.54 eV (benzene) and 0.56 eV in toluene.

Table 5.2 lists mean values and the range of values, as an error, for $\Delta_r G$ (CT → S_0) and λ_0 in the eight solvents. The solvent dependence of $\Delta_r G$ (CT → S_0) determined via line shape

analysis for the nonaromatic solvents (Table 5.2) is in reasonable agreement (within 0.1 eV) with predictions of a continuum solvation model (eq 2) using the slope of the Lippert-Mataga analysis (μ^2/a^3) and $\Delta_r G$ (CT → S_0)$_{VAC}$ = -3.83 eV.

$$\Delta_r G(CT \rightarrow S_0)(cont.) = \Delta_r G(CT \rightarrow S_0)_{VAC} + \frac{\mu^2}{a^3}\left(\frac{\varepsilon - 1}{2\varepsilon + 1}\right) \qquad \mathbf{2}$$

By contrast, the experimental values of $\Delta_r G$ (CT → S_0) in the aromatic solvents are 0.3 − 0.4 eV less exoergic than the continuum predictions, indicating that these solvents stabilize the charge-transfer state to a greater extent than predicted by their static dielectric constants. This additional solvation arises from the aromatic solvents' large quadrupole moments.[19] In the case of chlorobenzene, other factors may be involved (*vide infra*). Generally, the energy of a CT emission band maximum (Franck-Condon maximum[18]) can be approximated as $h\nu_{FC\text{-}max} \approx -\Delta_r G$ (CT → S_0) – λ_0 – λ_v.[20] For each solvent in Table 5.2, $-\Delta_r G$ (CT → S_0) – λ_0 determined from the fit parameters is 0.1 eV larger than $h\nu_{FC\text{-}max}$.[18] This suggests an approximate value of 0.1 eV for λ_v, in agreement with the value used in the fitting procedure (*vide infra*).

Table 5.2 Charge Recombination Free Energy and Solvent Reorganization Energy Determined from the CT Emission Analyses and from a Continuum Solvation Model[a]

Solvent	ε (ε$_{EFF}$[b])	CT FC$_{MAX}$ (eV)	Δ_rG(CT→S_0) (line shape) eV[c]	Δ_rG(CT→S_0) (cont.) eV[e]	λ_0 (lineshape) eV[c]	λ_0 (cont.)[f] eV
Benzene	2.3 (4.4)	-2.57	-3.22 ± 0.00[d]	-3.61 (-3.18)	0.54 ± 0.02	0.22
Toluene	2.4 (3.6)	-2.65	-3.28 ± 0.00[d]	-3.59 (-3.23)	0.56 ± 0.02	0.18
Anisole	4.3 (6.4)	-2.38	-3.10 ± 0.01	-3.40 (-3.09)	0.60 ± 0.02	0.30
Ethyl Ether	4.3	-2.52	-3.24 ± 0.01	-3.35	0.61 ± 0.02	0.32
Butyl Acetate	5.1	-2.36	-3.17 ± 0.01	-3.14	0.70 ± 0.02	0.33
Chlorobenzene	5.7 (5.7)	-2.45	-3.03 ± 0.01	-3.34 (-3.34)	0.46 ± 0.02	0.28
Ethyl Acetate	6.0	-2.30	-3.12 ± 0.01	-3.10	0.75 ± 0.02	0.38
THF	7.5	-2.26	-3.09 ± 0.01	-3.06	0.72 ± 0.03	0.39

[a] Mean value of $\hbar\omega$ = 0.20 eV; mean value of λ_v = 0.15 eV. [b] See text for ε_{EFF} definition. [c] Errors represent one standard deviation for the five ($\hbar\omega$, λ_v) pairs. [d] Value not varied. [e] Continuum value calculated using eq 2; values in parentheses calculated using ε_{EFF}. [f] Continuum values calculated using eq 3 and ε for the nonaromatic solvents or ε_{EFF} for the aromatic solvents.

Independent estimates of vibrational reorganization energies are available from ionization energies and from theory. The difference between the vertical and adiabatic ionization potentials for aniline, ~ 0.33 eV, and for *N*,*N*-dimethylaniline, 0.2 − 0.45 eV, indicate significant vibrational reorganization upon oxidation of aromatic amine donors.[21] AM1 calculations predict vibrational reorganization energies, λ_v for pyrene reduction and dimethylaniline oxidation of 0.13 and 0.23 eV, respectively. The nitrogen of dimethylaniline is pyramidal in the neutral structure and planar in the equilibrated radical cation geometry. Vibrational frequencies related to this motion are low (< 200 cm^{-1})[22] and can be treated as a low frequency (solvent) contribution in a single quantized mode model.[23] The calculated λ_v for dimethylaniline is only 0.06 eV if the dimethylamino group's improper torsion angle is constrained to the value for the neutral structure. Combined with the pyrene reorganization, this yields a total, calculated high-frequency reorganization energy of 0.19 eV, in reasonable agreement with the average value, 0.15 eV, derived from CT line shape analysis for **1** in benzene and toluene. This internal reorganization energy is associated with the planar aromatic groups, whose C=C vibrations lie near 1600 cm^{-1}. The remaining 0.17 eV of the AM1 calculated internal reorganization energy for dimethylaniline is coupled to the low frequency, pyramidalization coordinate of the dimethylamino group.

The line shape derived estimates of λ_0 increase with increasing solvent dielectric constant, with the notable exception of chlorobenzene (Table 5.2). Overall, the values are somewhat large for the moderately polar solvents used here. The slope of the Lippert-Mataga analysis (μ^2/a^3) in

combination with eq 3 provides independent, continuum model estimates of λ_0 for the nonaromatic, dipolar solvents (eq 3, Table 5.2).

$$\lambda_o\left(cont.\right)=\frac{\mu^2}{a^3}\left(\frac{\varepsilon-1}{2\varepsilon+1}-\frac{n^2-1}{2n^2+1}\right) \qquad \textbf{3}$$

The λ_0 values determined by line shape analyses are 0.29 − 0.37 eV larger than the continuum estimates. A significant part of this discrepancy derives from the vibrational reorganization involving the dimethylamino group (~ 0.17 eV, *vide supra*). The origin of the residual 0.1 − 0.2 eV difference is not clear. The other solvents in Table 5.2 are weakly polar aromatics. Continuum model predictions of λ_0 for these solvents are usually too small because quadrupolar solvation is not included.[19] One can define "effective" dielectric constants, ε_{EFF}, for the aromatic solvents using the Lippert-Mataga slope, the solvent refractive indices, and the CT emission maxima (Table 5.2). This procedure doubles benzene's dielectric constant, enhances those of toluene and anisole by 50%, but leaves chlorobenzene's unchanged. The "continuum" λ_0 values calculated using the ε_{EFF} for the aromatic solvents (Table 5.2) are smaller than the line shape values by 0.18 − 0.38 eV. The underestimates for the aromatic solvents are comparable to those found for the nonaromatic solvents and may be explained similarly.

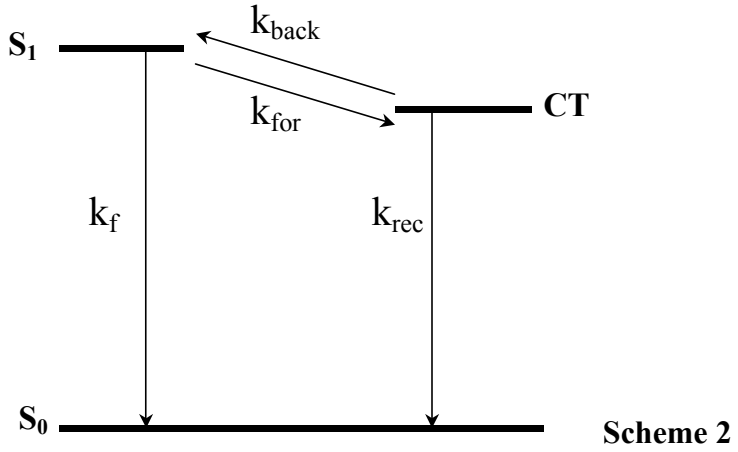

Scheme 2

The CT emission full width at half-maximum is smallest in chlorobenzene. Fitting the CT line shape in this solvent yields the smallest value of λ_0 and the lowest CT state energy (Table 5.2). This contrasts with the continuum estimates of λ_0 and the CT state energy for chlorobenzene, which lie roughly in the middle of the ranges predicted for all of the solvents. The small λ_0 and low CT state energy translate into a small activation barrier and a large driving force for electron transfer in chlorobenzene. Analysis of the kinetic data using these spectral fitting parameters produces a small value of the electronic coupling in chlorobenzene (*vide infra*). The origin of the small CT spectral width in chlorobenzene is unknown.

5.3.3 Electron-Transfer Rate Constants and Coupling Magnitudes

The shape of the time-resolved fluorescence signal from **1** depends strongly on the detection wavelength, sample temperature, and solvent. If fluorescence is detected at a wavelength where the charge-transfer band dominates, for example, 540 nm, the emission intensity rises and reaches a maximum within a few nanoseconds after excitation. The subsequent decay of the emission intensity requires many hundreds of nanoseconds. By contrast, the fluorescence intensity decays to a small fraction of its peak value within a few nanoseconds following excitation when detecting at 380 nm where pyrene emission dominates. The residual emission intensity requires many hundreds of nanoseconds to decay. Increasing the sample temperature reduces the time required for the fast intensity decay (growth) observed at 380 (540) nm. In toluene and benzene, increasing the sample temperature increases the amplitude of the long-lived component detected at 380 nm. In solvents more polar than benzene or toluene, the amplitude of this long-lived component (~ 3%) is temperature independent.

The solvent and temperature dependences of the emission decay profile indicate the establishment of an excited-state equilibrium between the pyrene S_1 and CT states of **1** (Scheme 2).[24] The initially prepared pyrene S_1 state evolves to an interconverting mixture of S_1 and CT. The equilibrium constant for this step depends on the charge separation driving force, $\Delta_r G$ ($S_1 \rightarrow$ CT) and the sample temperature. Back transfer from CT to S_1 occurs to a measurable extent only if $\Delta_r G$ ($S_1 \rightarrow$ CT) is more positive than -0.12 eV. The equations relating the observed fluorescence decay parameters to the four rate constants in Scheme 2 are well known.[8] The intrinsic decay rate constants of the pyrene S_1 and CT states (k_f and k_{rec}) are so small that the observed fast decay rate constant is equal to $k_{for} + k_{back}$ and the ratio of the fast decay amplitude to the slow decay amplitude detected at 380 nm is equal to k_{for}/k_{back}. Figure 5.4 displays the temperature dependence of k_{for}, k_{back}, and $\Delta_r G$ ($S_1 \rightarrow$ CT) determined by analyzing the picosecond photon counting data for **1** in toluene.

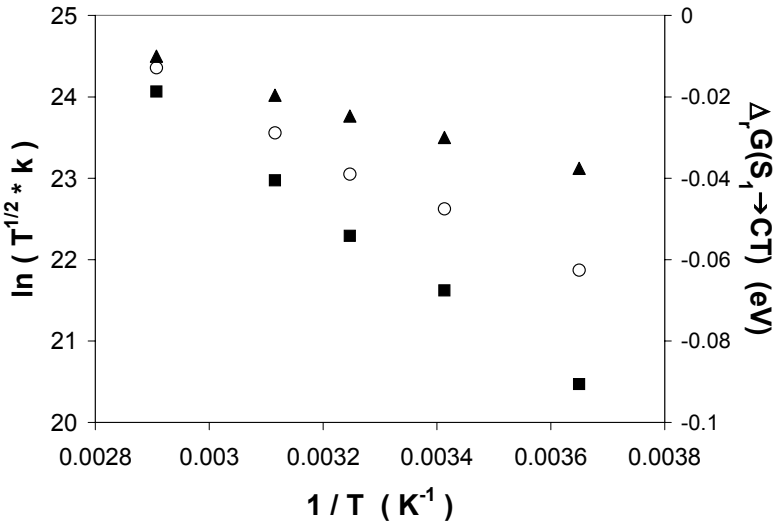

Figure 5.4 Left axis: Arrhenius type plot of k_{for} (black triangle) and k_{back} (black square) for **1** in toluene versus the reciprocal temperature. Right axis: Plot of $\Delta_r G$ ($S_1 \rightarrow$CT) (circule) versus the reciprocal temperature.

The value of $\Delta_r G$ ($S_1 \rightarrow$ CT) determined for **1** from the excited-state equilibrium is -0.05 eV in toluene at 293 K and is -0.11 eV in benzene at 295 K. These two experimental values were used to extract values of ($\hbar\omega$, λ_v, λ_0) from the CT spectra in these two solvents and, ultimately, ($\Delta_r G$ (CT $\rightarrow S_0$), λ_0) values for the other solvents (*vide supra*). These reorganization parameters characterize the charge recombination to ground-state reaction, and their use for analyzing the S_1 $\rightarrow$ CT electron-transfer reaction is not rigorously justified. Nevertheless, the CT $\rightarrow S_0$ reorganization parameter sets provide the best estimates for the $S_1 \rightarrow$ CT reaction and will be used in the absence of other information.[25]

Table 5.3 lists the charge separation free energy, $\Delta_r G$ ($S_1 \rightarrow$ CT), and charge separation rate constants (k_{for}) determined for **1** at 295 K. The solvents are ordered from smallest to largest vertical ionization potential (column 2). The rate constants vary by less than a factor of 7 from the largest value in anisole to the smallest value in toluene. The small reaction free energy in the latter solvent likely is responsible for the slow transfer rate. Values of the donor-acceptor electronic coupling were determined from the charge separation rate constant[8] using the single high-frequency mode, semiclassical rate equation[26] and the free energy and reorganization parameters determined from the CT spectra. Excluding the chlorobenzene result, the coupling magnitudes exhibit no clear solvent dependence (mean value for seven solvents, 23 ± 3 cm^{-1}). The values determined for the aromatic solvents are, perhaps, slightly smaller than the values for the nonaromatic solvents, but the difference is comparable to the systematic uncertainties and to the accuracy that this sort of analysis produces. The coupling exhibits no obvious dependence on the solvent ionization potential (HOMO energy) or on the solvent's electron affinity (LUMO energy, data not shown). If solvent mediates donor-acceptor coupling for **1**, its contribution is either minor or weakly solvent dependent.

Table 5.3 Charge separation rate constants and electronic coupling magnitudes determined as a function of solvent for 1 at 295 K.

Solvent	IP_{VERT} (eV)	$k(S_1 \rightarrow CT)$ / s^{-1}	$\Delta_r G$ ($S_1 \rightarrow CT$) eV	$\lvert V \rvert$ cm^{-1}
Anisole	8.4	6.5×10^9	-0.23 ± 0.01	19 ± 1
Toluene	8.9	9.4×10^8	-0.05 ± 0.00	23 ± 1
Chlorobenzene	9.1	5.6×10^9	-0.30 ± 0.01	7.2 ± 0.5
Benzene	9.2	2.2×10^9	-0.11 ± 0.00	19 ± 1
THF	9.6	4.0×10^9	-0.24 ± 0.01	25 ± 3
Ethyl Ether	9.6	1.4×10^9	-0.09 ± 0.01	27 ± 3
Butyl Acetate	10.1	1.3×10^9	-0.16 ± 0.01	24 ± 3
Ethyl Acetate	10.4	1.8×10^9	-0.21 ± 0.01	22 ± 3

5.3.4 Theoretical Calculations of Electronic Coupling Magnitudes for 1

Because the experimental results indicate that a solvent insensitive pathway is the dominant source of electronic coupling in the charge separation reaction of **1**, through-bond and through-space coupling pathways were evaluated by quantum chemical calculation. The ZINDO[27]/Generalized Mulliken Hush (GMH)[28] method was used to calculate electronic coupling magnitudes between (i) the CT state and the ground state and (ii) the CT state and the S_1 state, which is an equal mixture of the HOMO → LUMO + 1 and HOMO − 1→ LUMO configurations. For **1** in its ground-state equilibrium conformation, both calculated couplings magnitudes are at least 1 order of magnitude smaller than the experimental value of the $S_1 \Leftrightarrow$ CT coupling (Figure 5.5: Eq. Geom.). Through-bond coupling and direct through-space interaction (6.7 Å) at the equilibrium geometry of **1** do not impart coupling comparable to the experimentally determined values. Consequently, conformational distortions, involving the donor and acceptor groups, were explored to investigate whether higher energy conformations provide larger electronic coupling.

Eq. Geom: Side View	Eq.Geom: End View	17º wag: End View

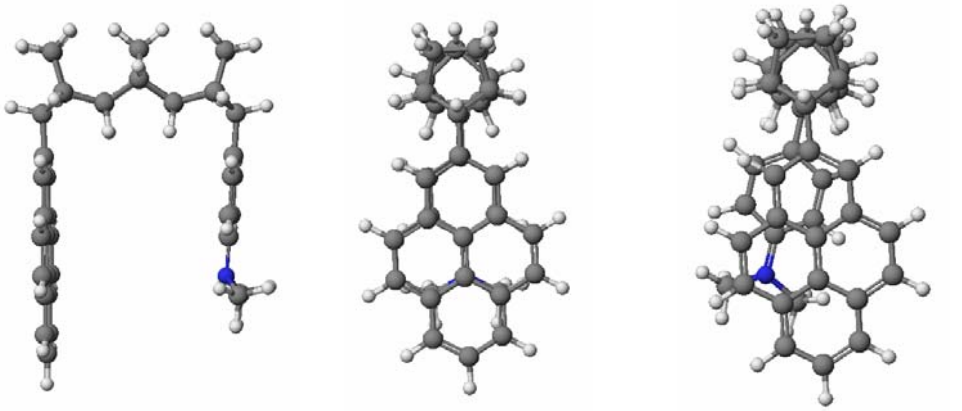

States Coupled	Equilibrium Geometry	17º Wag
$\|V\|$ ($S_0 \Leftrightarrow$ CT)	1.5 cm^{-1}	6 cm^{-1}
$\|V\|$ ($S_1 \Leftrightarrow$ CT)	0.6 cm^{-1}	0.5 cm^{-1}

Figure 5.5 ZINDO / GMH calculated couplings for the equilibrium and "17º wag" conformations.

Calculations have been performed for three types of structural deformation. Twisting the spacer such that the donor and acceptor remain in parallel planes but that a 17º dihedral angle is formed by the atoms in the σ bonds connecting these groups to the spacer (Figure 5.5: 17º wag) barely alters the $S_1 \Leftrightarrow$ CT coupling, although it increases the $S_0 \Leftrightarrow$ CT coupling 4-fold. Starting from the equilibrium geometry, compression of the donor-acceptor separation by 1.5 Å increases $|V|$ ($S_1 \Leftrightarrow$ CT) by only 2 cm^{-1}. In contrast to these ineffectual distortions, rotation of the pyrene about the bond connecting it to the spacer strongly modulates the pyrene/DMA electronic coupling magnitude (Figure 5.6). A structure in which the pyrene group is rotated by 45º generates $S_1 \Leftrightarrow$ CT coupling comparable to the experimental values. This rotation positions the edge of the pyrene closer to the dimethylaniline. The source of the coupling increase is discussed below.

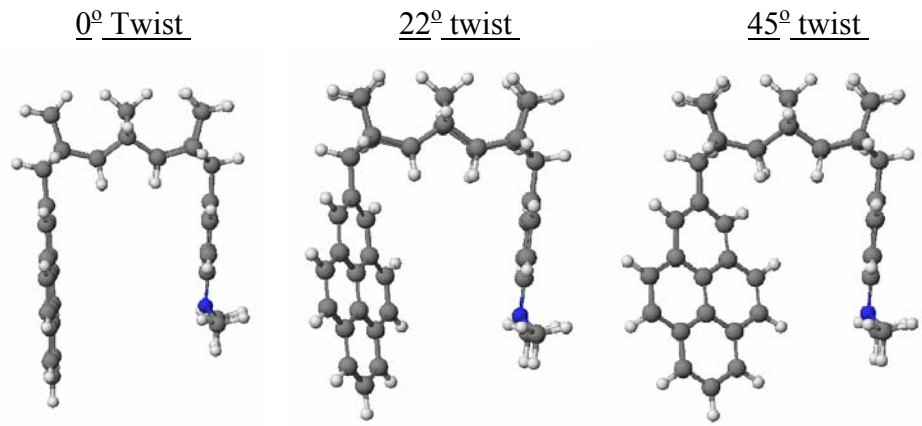

$\|V\|$ ($S_0 \Leftrightarrow$ CT)	1.5 cm^{-1} (0.2 cm^{-1})	34 cm^{-1} (11cm^{-1})	171 cm^{-1} (110 cm^{-1})
$\|V\|$ ($S_1 \Leftrightarrow$ CT)	0.6 cm^{-1} (1.6 cm^{-1})	4 cm^{-1} (3 cm^{-1})	23 cm^{-1} (26 cm^{-1})

Figure 5.6 ZINDO / GMH calculated couplings for the equilibrium, "22º twist" and "45º twist" conformations. Removal of the central norbornane unit of the spacer generates the couplings listed in parentheses.

Assessing whether twisted pyrene conformations are relevant to the electron-transfer event requires an estimate of their energy and probability of formation. Molecular mechanics calculations indicate that a 22º twist about the bond connecting pyrene to the spacer (the "22º twist" conformer) lies 1.6 kcal/mol above the lowest energy ("0º twist") conformer and the "45º twist" conformer lies 8.3 kcal/mol above the lowest energy conformer (Scheme 4). Thus, it is feasible that twisting of the aryl groups could be an important nuclear motion for generating electronic coupling.[29] Evaluation of the thermally averaged coupling magnitude in a conformationally unconstrained system requires a molecular dynamics/electronic coupling calculation.[30] An estimate of the coupling generated by pyrene rotations alone was obtained from the calculated GMH couplings and molecular mechanics energies as a function of the twist angle (Figure 5.7).

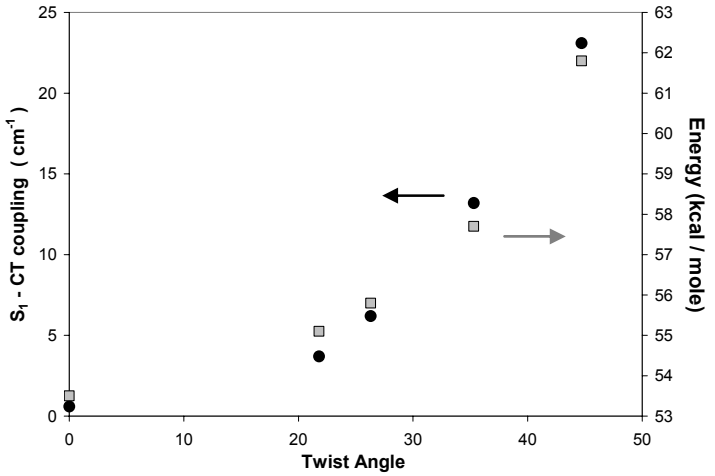

Figure 5.7 Influence of rotation of the pyrene spacer bond on the $S_1 \Leftrightarrow$ CT electronic coupling (left axis, circle) and the molecular mechanics energy (right axis, square) of molecule **1**. A 0^o twist angle corresponds to the lowest energy conformer of molecule **1**.

The $S_1 \Leftrightarrow$ CT coupling magnitude and the conformer energy vary quadratically with twist angle (between 0º and 45º). Using this dependence on twist angle, a Boltzmann weighted, root-mean-square value of the coupling may be calculated[8] using

$$\sqrt{\left\langle |V|^2 \right\rangle} = \sqrt{\frac{\sum_j |V_j|^2 \exp\left(-(E_j - E_0)/kT\right)}{\sum_j \exp\left(-(E_j - E_0)/kT\right)}} \qquad \textbf{4}$$

where E_j is the energy of a particular conformation, $|V_j|$ is the $S_1 \Leftrightarrow$ CT coupling in that conformation, and E_0 is the energy of the most stable conformation. This yields a V_{rms} of 6.6 cm^{-1} at 295 K and 8.4 cm^{-1} at 360 K.[29] It is possible that combinations of distortions, for example, pyrene and dimethylaniline rotations and compression, might generate V_{rms} values that approach the experimental values. Interestingly, higher energy conformers of **1** that offer larger $S_1 \Leftrightarrow$ CT coupling most likely cannot be populated when solvent molecules are situated in the cleft

directly between the donor and acceptor. Thus, solvents that easily enter the cleft might actually reduce the coupling. As both pyrene and dimethylaniline are relatively electron rich, electron-deficient solvents would have the greatest propensity for cleft insertion.[31] Although the preceding analysis uses a crude molecular mechanics model for the conformer energetics and neglects the energetics of solvent-substrate interactions,[32] it illustrates that the conformational freedom of the minimally constrained donor and acceptor groups is a likely source of significant donor acceptor electronic coupling.

The enhanced coupling attending twisting of the pyrene can be dissected to ascertain whether it arises from changes in through-bond pathways, through-space pathways, or both. ZINDO/GMH values of $|V|(S_1 \Leftrightarrow CT)$ are unchanged by removal of the spacer's central norbornane unit (Scheme 4, values in parentheses) when the donor and acceptor geometries are otherwise maintained as in the full calculation. This finding implicates direct, through-space, donor-acceptor interactions as the primary pathway for $S_1 \Leftrightarrow CT$ coupling in the twisted conformers. Through-bond coupling contributions are minimal. This contrasts with the results for $S_0 \Leftrightarrow CT$ coupling following clipping of the spacer unit, where through-bond and through-space interactions interfere constructively to generate the coupling. Thus, the S_0 and S_1 states of pyrene in **1** employ different combinations of coupling pathways to interact with the same CT state.

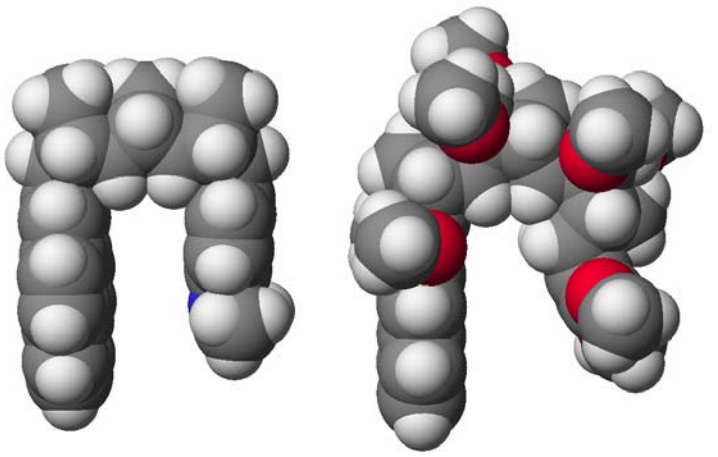

Figure 5.8 CPK models of the pyrene containing, C-shaped hole transfer molecule, **1** (left) and the anthracene containing, C-shaped electron transfer molecule, **3** (right).

The ZINDO/GMH calculations suggest that the charge separation reactions of **1** obtain $S_1 \Leftrightarrow$ CT coupling from thermally populated, twisted conformers. If this is correct, the electronic coupling in **1** should be temperature dependent.[8] The charge separation driving force for **1** in benzene at 295 K is the same as for a 7 Å C-shaped molecule, **3**, previously characterized (Figure 5.8).[8] The temperature dependence of $\Delta_r G$ ($S_1 \rightarrow$ CT) in both systems are similar.[33] Despite these similarities, the charge separation rate constants for **1** and **3** exhibit very different temperature dependences: k_{for} in **1** increases with temperature ($E_A \approx 1.8$ kcal/mol), but k_{for} in **3** decreases with temperature ($E_A \approx$ -1.4 kcal/mol). The apparent barrier to charge separation is significantly larger for **1** than for **3**. The low-frequency reorganization energy for **1** in benzene is larger than the λ_0 attributed to **3** and certainly contributes to the more positive activation energy observed for **1**. A contribution to the larger activation energy from a temperature-dependent electronic coupling in **1** cannot be ruled out, however.

5.3.5 Charge Recombination Reactions

Although the $S_1 \leftrightarrow$ CT electron-transfer kinetics are the primary focus of this investigation, the CT state decay kinetics are noteworthy. The CT state is formed with greater than 98% efficiency, and its decay rate constant, which ranges from 4×10^6 s^{-1} in tetrahydrofuran to 9×10^6 s^{-1} in chlorobenzene, is ~ 1000 times smaller than the CT state formation rate constant.[34] Numerous processes potentially depopulate the charge-transfer state. Nonradiative CT $\rightarrow S_0$ charge recombination lies deep within the Marcus inverted region: $\Delta_r G$ (CT $\rightarrow S_0$) $\approx$ -3.1 eV. Using the reorganization parameters obtained from the charge-transfer band line shape fitting, the $|V|$ ($S_0 \Leftrightarrow$ CT) coupling magnitude would need to be larger than 2000 cm^{-1} to produce the observed decay rate constants. Although couplings of this magnitude are known for contact ion pairs and short donor-bridge-acceptor molecules,[35] the calculated GMH couplings are not close to this magnitude. Thus, nonradiative CT $\rightarrow S_0$ transitions are not the dominant CT decay process. The charge-transfer emission quantum yield is less than 0.05, so radiative CT $\rightarrow S_0$ charge recombination is also not the dominant decay process. Diffusion-controlled, intermolecular charge shift reactions are too slow because the DSA concentration is less than 10 μM. Other possible contributors to the decay of the CT emission include charge recombination with direct formation of the pyrene triplet[36] and a two-step process for formation of the pyrene triplet involving intersystem crossing to the ^{3}CT state followed by charge recombination.[37] The pyrene triplet state energy is 2.1 eV; thus CT $\rightarrow T_1$ charge recombination processes lie close to the peak of the Marcus curve in these solvents. Donor-acceptor coupling $|V|$ ($T_1 \Leftrightarrow {}^{1,3}$CT) of $1 cm^{-1}$ or less is sufficient to produce the observed rate constants using the estimated reorganization parameters. Pyrene triplet is likely the dominant product formed from the CT state.

5.4 Conclusion

For the C-shaped pyrene*-spacer-dimethylaniline molecule investigated here, the coupling is essentially solvent independent. No correlation between coupling magnitude and solvent HOMO or LUMO energy is discernible. The shape of molecule **1** in its equilibrium geometry is similar to that of a C-shaped molecule, **3**, previously used extensively in investigations of solvent-mediated electronic coupling (Figure 5.8). Two structural differences between these molecules are likely responsible for their disparate sensitivity to solvent-mediated coupling. The donor and acceptor "walls" defining the solvent-accessible cleft in the lowest energy conformation of molecule **1** are parallel to each other and separated by 6.7 Å. The corresponding "walls" in **3** are angled slightly, generating a cleft whose static width varies between 6.9 and 7.4 Å. In both molecules, the thickness of the donor and acceptor excludes ~ 3.5 Å of the cleft. Thus, the wider, wedge-shaped cleft **3** may be more amenable to solvent entry. Mixed solvent NMR studies confirm that benzene entry into the cleft of **1** is not facile.[11] The second major structural difference between these molecules is the connection to the spacer. The donor and acceptor in **3** are each "rigidly" attached to the spacer by two σ bonds, so there is only one thermally accessible conformation of the molecule. By contrast, the donor and acceptor in **1** are each attached to the spacer by a single σ bond. The barriers to rotation about these σ bonds are small, and rotation of the donor and acceptor groups sharply reduces the cleft size of **1**, making solvent entry more difficult, and brings the edges of the donor and acceptor into proximity, enhancing the direct through-space electronic interaction. The failure to observe solvent-mediated coupling for **1** likely results from the small separation of the donor and acceptor groups (< 6.7 Å) and because of their conformational freedom.

Although the donor and acceptor group conformational mobility obviates significant solvent-mediated coupling pathways, it allows the donor and acceptor moieties to approach near van der Waals contact and enable direct, through-space electronic interaction. This importance of this process was evaluated through a combination of GMH/ZINDO and molecular mechanics calculations. The GMH calculations reveal that twisted pyrene conformers have significant electronic coupling magnitudes. Although only a small sample of **1**'s conformations is explored here, they illustrate the enhanced coupling afforded in some higher energy conformations and suggest that a more extensive theoretical study will demonstrate significant dependence of the electronic coupling on nuclear geometry. Within this model, the experimentally derived electronic couplings reported in Table 5.3 must correspond to ensemble averages of different donor to acceptor geometries.

Most electron-transfer investigations tacitly assume that any variation of the donor acceptor electron coupling with nuclear structure is unimportant. Both this and prior investigations of electron transfer in C-shaped molecules find coupling variations with nuclear structure to be of considerable importance. The most appropriate framework within which to interpret the dynamics of such systems has yet to be established. One particular case, conformational gating of electron-transfer reactions, has been treated theoretically and analyzed in a number of protein systems.[4] The dynamics of **1** fall into a different limit and delineate a new direction of investigation. Beratan and Onuchic analyzed the role of nuclear dynamics in determining the adiabatic or nonadiabatic character of an electron-transfer process.[38] Their analysis highlighted the importance of two time scales: the characteristic time a system spends in the Landau-Zener (transition state) region, τ_{LZ}, and the time required to interconvert the reactant electronic state to the product electronic state, $\tau_H = \hbar / |V|$. Provided $\tau_{LZ} << \tau_H$, a reaction is

nonadiabatic. Analysis of the electron-transfer reactions of **1**, using the nonadiabatic approximation, generated $|V| \approx 20$ cm^{-1} so that $\tau_H \approx 10^{-11}$ s. The polarization relaxation times for the solvents employed here limit τ_{LZ} to time scales of $10^{-12} - 10^{-13}$ s or less. Comparison of these time scales indicates that the electron-transfer reactions of **1** lie in the nonadiabatic regime. However, the electron-transfer process for **1** is coupled to torsional (and other) motions of the donor and acceptor units. Given a torsional frequency of $6X10^{11}$ Hz,[39] we estimate a 1 ps correlation time, τ_v, for fluctuations of the electronic coupling due to the nuclear motions of **1**. Hence, the three relevant time scales are ordered $\tau_{LZ} \leq \tau_v < \tau_H$, and the following picture of the dynamics for **1** is proposed.

During any single entry into the transition state region, the electronic coupling is relatively constant and the transition probability is small. Thus, the transfer event should remain nonadiabatic. However, each time the transition state region is accessed, the value of the coupling is different due to its strong dependence on nuclear structure. As a result, the experimentally determined coupling value is a root-mean-square average (eq 4) over the thermally accessible conformations. In this limit, the dependence of the electronic coupling on the nuclear coordinate is not immediately obvious in the kinetics. It should be possible to reveal the nuclear coordinate dependence of the coupling by modifying the relative ordering of the three time scales. For example, a significant increase of τ_v, such that $\tau_v >> \tau_H > \tau_{LZ}$, would produce a distribution of persistent coupling magnitudes and generate a range of transfer rate constants.[5h] The fluorescence decay kinetics in such a system would appear nonexponential.

The role of nuclear dynamics in accessing the electron-transfer transition state is well understood. By contrast, the implications of the electronic coupling itself being coupled to nuclear dynamics are not well established. Future studies, in which the conformational motion is

inhibited, should allow exploration of an electron-transfer mechanism that is controlled by the torsional motion of the donor and acceptor groups and investigation of the dynamics in the regime $\tau_v / \tau_H \approx 1$ to $\tau_v / \tau_H >> 1$.

5.5 Acknowledgements

We thank the National Science Foundation (CHE-0108945 to M.B.Z. and CHE-0111435 to D.H.W.), Professor V. Fidler (Prague) for enlightening discussions, Dr. Andrew Napper for invaluable assistance with the SPC experiments, and Dr. M. Newton for assistance with GMH calculations.

5.6 References

1. (a) Closs, G. L.; Miller, J. R. *Science* **1988**, *240*, 440; (b) Barbara, P. F.; Meyer, T. J.; Ratner, M. A. *J. Phys. Chem*., **1996**, *100*, 13148; (c) Lewis, F. D.; Letsinger, R. L.; Wasielewski, M. R. *Acc. Chem. Res*., **2001**, *34*, 159; (d) Davis, W. B.; Ratner, M. A.; Wasielewski, M. R. *Chem. Phys*., **2002**, *281*, 333; (e) Jordan, K. D.; Paddon-Row, M. N. *Chem. Rev.*, **1992**, *92*, 395; (f) Newton, M. D. *Chem. Rev.* **1991**, *91*, 767.
2. (a) Reimers, J. R.; Hush, N. S. *Chem. Phys*., **1989**, *134*, 323; (b) Todd, M. D.; Nitzan, A.; Ratner, M. A. *J. Phys. Chem*., **1993**, *97*, 29; (c) Rips, I.; Jortner, J. *Jerusalem Symp. Quantum Chem. Biochem*., **1990**, *22*, 293-9; (d) Baym, G. *Lectures on Quantum Mechanics*; Benjamin-Cummings: London, **1981**; pp 248-58.
3. (a) Oevering, H.; Paddon-Row, M. N.; Heppener, M.; Oliver, A. M.; Cotsaris, E.; Verhoeven, J. W.; Hush, N. S. *J. Am. Chem. Soc.*, **1987**, *109*, 3258; (b) Winkler, J. R.; Gray, H. B. *J. Biol. Inorg. Chem.*, **1997**, *2*, 399; (c) Helms, A.; Heiler, D.; McLendon, G. *J. Am. Chem. Soc.*, **1991**, *113*, 4325; (d) Shin, Y.-G. K.; Newton, M. D.; Isied, S. S. *J. Am. Chem. Soc*., **2003**, *125*, 3722; (e) Kang, Y. K.; Rubtsov, I. V.; Iovine, P. M.; Chen, J.; Therien, M. J. *J. Am. Chem. Soc.*, **2002**, *124*, 8275.
4. (a) Cartling, Bo. *J. Chem. Phys.*, **1985**, *83*, 5231; (b) Blair, D. F.; Gelles, J.; Chan, S. I. *Biophys. J.*, **1986**, *50*, 713; (c) Hoffman, B. M.; Ratner, M. A. *J. Am. Chem. Soc.*, **1987**, *109*, 6237; (d) McLendon, G.; Pardue, K.; Bak, P. *J. Am. Chem. Soc.*, **1987**, *109*, 7540.
5. (a) Beratan, D. N.; Hopfield, J. J. *J. Chem. Phys*., **1984**, *81*, 5753; (b) Skourtis, S. S.; Archontis, G.; Xie, Q. *J. Chem. Phys.*, **2001**, *115*, 9444; (c) Skourtis, S. S. *Chem. Phys. Lett.*, **2003**, *372*, 224; (d) Medvedev, E. S.; Stuchebrukhov, A. A. *J. Chem. Phys.*, **1997**, *107*, 3821; (e) Ungar, L. W.; Newton, M. D.; Voth, G. A. *J. Phys. Chem. B*, **1999**, *103*, 7367; (f)

Mikkelsen, K. V.; Ulstrup, J.; Zakaraya, M. G. *J. Am. Chem. Soc.*, **1989**, *111*, 1315. Related treatments not specific to proteins include: (g) Tang, J. *J. Chem. Phys.*, **1993**, *98*, 6263; (h) Bixon, M.; Jortner, J. *Russ. J. Electrochem.*, **2003**, *39*, 3.

6. (a) Reimers, J. R.; Hush, N. S. *Chem. Phys*., **1990**, *146*, 105; (b) Jones, G. A.; Paddon-Row, M. N.; Carpenter, B. K.; Piotrowiak, P. *J. Phys. Chem. A*, **2002**, *106*, 5011.
7. (a) Lawson, J. M.; Paddon-Row, M. N.; Schuddeboom, W.; Warman, J. M.; Clayton, A. H. A.; Ghiggino, K. P. *J. Phys. Chem*., **1993**, *97*, 13099; (b) Kumar, K.; Lin, Z.; Waldeck, D. H.; Zimmt, M. B. *J. Am. Chem. Soc.*, **1996**, *118*, 243; (c) Read, I.; Napper, A.; Kaplan, R.; Zimmt, M. B.; Waldeck, D. H. *J. Am. Chem. Soc.*, **1999**, *121*, 10976; (d) Napper, A. M.; Read, I.; Waldeck, D. H.; Kaplan, R. W.; Zimmt, M. B. *J. Phys. Chem. A*, **2002**, *106*, 4784; (e) Milischuk, A.; Matyushov, D. V. *J. Chem. Phys.*, **2003**, *118*, 5596.
8. Zimmt, M. B.; Waldeck, D. A. *J. Phys. Chem. A*, **2003**, *107*, 3580.
9. The energy of D^+S^-A electronic configurations are too far above the D*SA configuration to allow significant thermal population. D^+S^-A configurations act as "virtual" states that enhance D*A coupling via superexchange. See: (a) McConnell, H. M. *J. Chem. Phys*., **1961**, *35*, 508; (b) Liang, C.; Newton, M. D. *J. Phys. Chem*., **1993**, *97*, 3199.
10. (a) Kobayashi, T.; Nagakura, S. *Bull. Chem. Soc. Jpn*., **1974**, *47*, 2563; (b) Baker, A. D.; May, D. P.; Turner, D. W. *J. Chem. Soc. B*, **1968**, 22. The adiabatic IP is 6.95 eV according to NIST and Mautner(Meot-Ner), M.; Nelsen, S. F.; Willi, M. R.; Frigo, T. B. *J. Am. Chem. Soc*., **1984**, *106*, 7384.
11. Nadeau, J. M. Ph.D. Thesis, Brown University, **2003**.
12. (a) Zeglinski, D. M.; Waldeck, D. H. *J. Phys. Chem*., **1988**, *92*, 692; (b) Zeng, Y.; Zimmt, M. B. *J. Phys. Chem*., **1992**, *96*, 8395.

13. (a) Mataga, N.; Kaifu, Y.; Koizumi, M. *Bull. Chem. Soc. Jpn.*, **1955**, *28*, 690; (b) Mataga, N.; Kaifu, Y.; Koizumi, M. *Bull. Chem. Soc. Jpn.*, **1956**, *29*, 465.

14. (a) Lippert, E. *Z. Naturforsch., A*, **1955**, *10a*, 541; (b) Lippert, E.; Schneider, F. *Ber. Bunsen-Ges.*, **1970**, *74*, 624; (c) Lippert, E. In *Organic Molecular Photophysics*; Birks, J. B., Ed.; John Wiley and Sons: New York, **1975**; Vol. 2, pp 18-19.

15. A CPK model of molecule **1** overlaps substantially with a CPK model of the 7 Å cleft, C-shaped molecule, **3**, previously studied (see Scheme 5).[8] A 7.5 Å cavity radius accurately reproduced the experimental free energy data **3**. Thus, a cavity radius of 6-7 Å is reasonable for **1**.

16. Electron transfer from dimethylaniline to excited pyrene is more than 0.5 eV exoergic in nitrile solvents: Finckh, P.; Heitele, H.; Volk, M. Michel-Beyerle, M. E. *J. Phys. Chem.*, **1988**, *92*, 6584.

17. (a) Marcus, R. A. *J. Phys. Chem.*, **1989**, *93*, 3078; (b) Gould, I. R.; Young, R. H.; Moody, R. E.; Farid, S. *J. Phys. Chem.*, **1991**, *95*, 2068.

18. CT spectra were obtained from the experimental data by subtracting a scaled acceptor only spectrum and a scaled impurity emission spectrum. The CT Franck Condon line shape was obtained from the CT spectra through division by ν^3. This accounts for the ν^3 dependence of the Einstein transition probability, the ν^{-2} dependence of the transition moment, and the ν^2 that accompanies conversion from nm to cm^{-1} units. The energy of the CT Franck-Condon maximum, $h\nu_{FC\text{-}max}$, was determined from a quadratic fit to the top 15% of the Franck-Condon line shape.

19. (a) Matyushov, D. V.; Voth, G. A. *J. Chem. Phys.*, **1999**, *111*, 3630; (b) Reynolds, L.; Gardecki, J. A.; Frankland, S. J. V.; Horng, M. L.; Maroncelli, M. *J. Phys. Chem.*, **1996**, *100*,

10337; (c) Read, I.; Napper, A.; Zimmt, M. B.; Waldeck, D. H. *J. Phys. Chem. A*, **2000**, *104*, 9385.

20. (a) Matyushov, D. V.; Voth, G. A. *J. Phys. Chem. A*, **2000**, *104*, 6485; (b) Vath, P.; Zimmt, M. B.; Matyushov, D. V.; Voth, G. A. *J. Phys. Chem. B*, **1999**, *103*, 9130.
21. NIST Chemistry WebBook, NIST Standard Reference Database Number 69 - March, 2003 Release. http://webbook.nist.gov/chemistry/.
22. (a) Vibrational modes and frequencies determined using the Hartree-Fock method and the 6-31G** basis set[22b] as implemented in TITAN.[22c] (b) Hehre, W. J.; Radom, L.; Schleyer, P. V. R.; Pople, J. A. *Ab Initio Molecular Orbital Theory*; Wiley: New York, **1986**. (c) TITAN, Wavefunction, Inc., Irvine, CA.
23. (a) Marcus, R. A.; Sutin, N. *Biochim. Biophys. Acta*, **1985**, *811*, 265; (b) Sutin, N. *Acc Chem. Res*., **1982**, *15*, 275.
24. The pyrene-spacer impurity is the source of the long-lived component detected at 380 nm in the solvents more polar than benzene. The absence of a pyrene $S_1 \leftrightarrow$ CT equilibrium in these solvents was confirmed by the addition of tetrabutyammonium hexafluorophosphate. The salt increased the decay rate constant of the long-lived, CT emission (detected at 520 nm) but did not alter the decay rate constant of the long-lived pyrene emission detected at 380 nm. In benzene and toluene, the long-lived component detected at 380 nm has contributions from both the pyrene-spacer impurity and the pyrene S_1 state in equilibrium with the CT state. The excited-state lifetime of the pyrene-spacer model, **2** (~ 300 ns), and of the CT state of **1** (~ 200 ns, detected at 520 nm) are both longer than the window used to resolve the initial fluorescence decays with picosecond photon counting.

25. Carter, E. A.; Hynes, J. T. *J. Phys. Chem.*, **1989**, *93*, 2184. Carter and Hynes determined that the solvent force constants characterizing fluctuations of a polar solvent about neutral and ion pair states in the same geometry are similar. If the donor-acceptor separations of **1** in the ground, locally excited (S_1) and charge-transfer states (CT) are similar, λ_0 should be similar for the $S_1 \rightarrow CT$ and $CT \rightarrow S_0$ reactions.

26. Kestner, N. R.; Logan, J.; Jortner, J. *J. Phys. Chem.*, **1974**, *78*, 2148.

27. Ridley, J.; Zerner, M. *Theor. Chim. Acta*, **1973**, *32*, 111.

28. (a) Cave, R. J.; Newton, M. D. *Chem. Phys. Lett.*, **1996**, *249*, 15; (b) Cave, R. J.; Newton, M. D. *J. Chem. Phys.*, **1997**, *106*, 9213.

29. Semiempirical PM3 calculations place the 22° and 45° twist calculations less than 1 kcal/mol above the lowest energy conformation. Neither the molecular mechanics nor the semiempirical calculation provide the proper Boltzmann weighting for the twisted conformations. However, both calculations demonstrate that twisted conformations are thermally accessible. Use of the PM3 energies yields 13 cm^{-1} as the root-mean-square coupling value at 295 K.

30. (a) Castner, E. W., Jr.; Kennedy, D.; Cave, R. J. *J. Phys. Chem. A*, **2000**, *104*, 2869; (b) Troisi, A.; Ratner, M. D.; Zimmt, M. B. *J. Am. Chem. Soc.*, **2004**, *126*, 2215.

31. (a) Klärner, F.-G.; Burkert, U.; Kamieth, M.; Boese, R.; Benet-Buchholz, J. *Chem.-Eur. J.*, **1999**, *5*, 1700. (b) Klärner, F.-G.; Panitzky, J.; Blaser, D.; Boese, R. *TetrahedronI*, **2001**, *57*, 3673.

32. Sinnokrot, M. O.; Sherrill, C. D. *J. Phys. Chem.*, **2003**, *107*, 8377.

33. (a) $(\partial \Delta_r G)/(\partial T)$ = -1 meV/K for **3**;[7c] $(\partial \Delta_r G)/(\partial T)$ = -1.1 meV/K for **1**.

34. The CT state decay rate constants for **1** in other solvents are benzene 7.0×10^6 s^{-1}; anisole 7.6×10^6 s^{-1}, BuOAc 7.7×10^6 s^{-1}; ethyl ether 5.6×10^6 s^{-1}.

35. (a) Gould, I. R.; Young, R. H.; Mueller, L. J.; Albrecht, A. C.; Farid, S. *J. Am. Chem. Soc.*, **1994**, *116*, 8188; (b) Pasman, P.; Rob, F.; Verhoeven, J. W. *J. Am. Chem. Soc.*, **1982**, *104*, 5127; (c) Oevering, H.; Verhoeven, J. W.; Paddon-Row, M. N.; Warman, J. M. *Tetrahedron*, **1989**, *45*, 4751.

36. The dimethylaniline triplet state is slightly higher in energy than the CT state in these solvents. Murov, S. L.; Carmichael, I.; Hug, G. L. *Handbook of Photochemistry*, 2nd ed.; Marcel Dekker: New York, **1993**.

37. (a) Liddell, P. A.; Kuciauskas, D.; Sumida, J. P.; Nash, B.; Nguyen, D.; Moore, A. L.; Moore, T. A.; Gust, D. *J. Am. Chem. Soc.*, **1997**, *119*, 1400; (b) Roest, M. R.; Oliver, A. M.; Paddon-Row, M. N.; Verhoeven, J. W. *J. Phys. Chem. A*, **1997**, *101*, 4867; (c) Lukas, A. S.; Bushard, P. J.; Weiss, E. A.; Wasielewski, M. R. *J. Am. Chem. Soc.*, **2003**, *125*, 3921.

38. (a) Onuchic, J. N.; Beratan, D. N.; Hopfield, J. J. *J. Phys. Chem.*, **1986**, *90*, 3707; (b) Sumi, H.; Marcus, R. A. *J. Chem. Phys.*, **1986**, *84*, 4894.

39. The moment of inertia about the pyrene long axis is 498 amu $Å^2$. The curvature, C, according to molecular mechanics is 7.21×10^4 J/(mol rad^2). The frequency of the pyrene oscillation about its long axis is $\omega = (2C/I)^{1/2} = 3.8 \times 10^{12}$ rad/s $= 6 \times 10^{11}$ Hz.

Chapter 6 The Fluorescence Quenching Mechanism of a Polyphenylene Polyelectrolyte with Other Macromolecules: Cytochrome *c* and Dendrimers

This work has been published as M. Liu, P. Kaur, D. H. Waldeck, C. Xue, H. Liu, Langmuir, 21, 1687, (2005).

This study investigates the fluorescence quenching of a polyphenyl based polyelectrolyte by positively charged macromolecules (proteins and dendrimers). This work shows that the fluorescence quenching of the dendrimer materials does not involve energy transfer or electron transfer, but is correlated to the overall charge on the dendrimer and its size. The quenching is hypothesized to result from conformational changes that occur upon binding the polyelectrolyte to the protein, or dendrimer. This mechanism is qualitatively different from that invoked for small molecule analytes.

6.1 Introduction

Conjugated polyelectrolytes offer great possibilities as water soluble fluorescent materials[1] and sensors,[2,3,4] especially for small molecule analytes.[5] A number of groups are active in using conjugated polymers as fluorescence probes and this field has been reviewed recently.[6] Typically, a trap-site is created when an analyte molecule binds to the polymer, sometimes via a receptor, and quenches the emission by electron transfer or energy transfer. The sensitivity of these materials arises from the presence of many binding sites, of which only one

or a few need to be occupied to quench the polymer's intrinsic fluorescence. More recently, conjugated polyelectrolytes are being used for the detection of proteins and oligonucleotides, however the mechanism of fluorescence quenching has not been as thoroughly studied.

Fluorescence quenching of a polyelectrolyte by binding with another macromolecule can occur from a number of different processes, but three are likely to dominate. These are electron transfer, energy transfer, and enhancement of the polymer's self-quenching, *eg.* internal conversion. Electron transfer quenching is often invoked with these sensor materials and can be controlled by changing the analyte's redox characteristics. Energy transfer quenching should depend strongly on the polyelectrolyte and the analyte's spectral characteristics, whether it is a Förster mechanism or a Dexter mechanism.[7] A third possibility for the quenching mechanism is a binding event that induces a conformational change in the polymer which enhances its intrinsic nonradiative rate constant.[8] In this case the quenching would not depend on the redox and spectral properties of the analyte, but would depend on conformational features of the binding. Lastly, these mechanisms are not exclusive; they could operate simultaneously.

This study compares the quenching mechanism for the protein cytochrome *c* with a polyphenylene polyelectrolyte to that observed for similarly sized dendrimers with the same polyelectrolyte. The fluorescence of poly[sodium 2,5-(3-sulfopropoxy)-1,4-phenylphenylene] (identified as **PP1**) is quenched by positively charged dendrimers and the protein cytochrome *c*. Cytochrome *c* is a positively charged heme protein that acts as an electron carrier in the respiratory chain of aerobic organisms[9] and has been implicated in apoptosis.[10] A recent report by Fan demonstrated the utility of using a PPV based polyelectrolyte (poly[lithium 5-methoxy-2-(4-sulfobutoxy)-1,4-phenylenevinylene) to detect cytochrome *c* and concluded that the quenching occurs by electron transfer in that case.

6.2 Experimental Details

Poly[2,5-bis(3-sulfonatopropoxy)-1,4-phenylene-alt-1,4-phenylene) was prepared in a manner similar to that reported in the literature.[11] The molecular weight was found to be 9900 and the polydispersity was 1.26, as determined by size exclusion chromatography.[12]

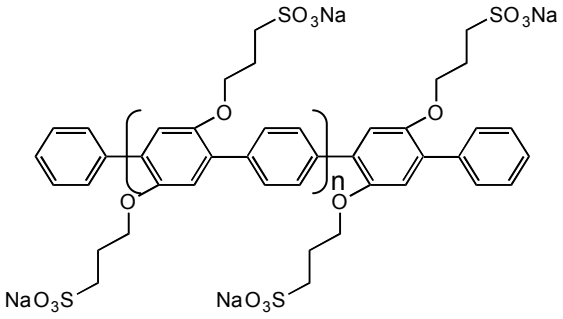

PP1

Both proteins and dendrimer materials were studied as analytes. The ferric cytochrome *c* was purchased from Sigma and purified in the manner described previously.[13] The ferric material was chemically reduced to ferrous with sodium dithionate.[14] The myoglobin was purchased from Sigma and used without further purification. The PAMAM (polyamidoamine) and the DAB (DAB-Am-32, Polypropylenimine dotriacontaamine Dendrimer, Generation 4.0) dendrimer materials were obtained from Dendritech and Sigma-Aldrich, respectively.

Steady-state absorption spectra were measured on an Agilent 8453 spectrometer and the steady-state emission spectra were measured on a Spex Fluorolog 0.22 m double spectrometer. The time-resolved fluorescence data were collected using the time-correlated single photon counting method; see reference 15 for details of the apparatus.

6.2.1 Quenching with Proteins

The steady-state electronic spectra of **PP1** and cytochrome *c* are presented in Figure 6.1. The absorption spectrum of **PP1** has a λ_{max} at 338 nm, significantly blue of the Soret band of the cytochrome *c*. The shift in absorption wavelength of cytochrome *c* is consistent with the native state of the ferrous and ferric forms of the protein. In aqueous solution at pH = 7 (20 mM phosphate buffer) **PP1** is highly fluorescent. The fluorescence spectrum in Figure 6.1 was taken with an excitation wavelength of 338 nm. The overlap of the polyelectrolyte's emission band with the absorption band of the protein shows that energy transfer quenching is possible for this system.

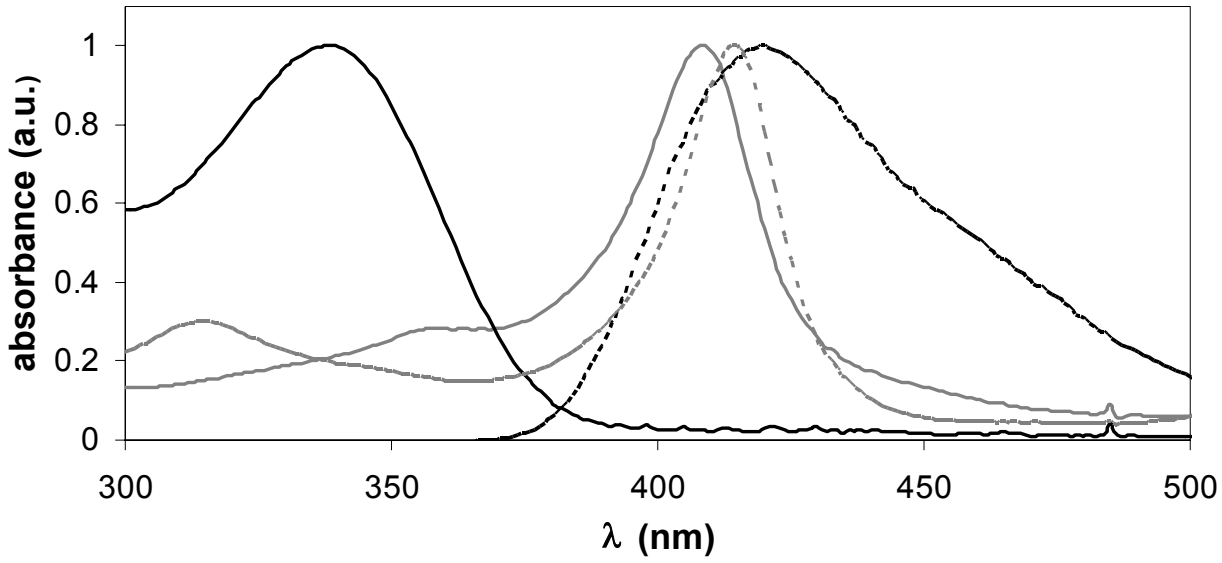

Figure 6.1 The absorption spectrum (solid black line) and fluorescence spectrum (dashed black line) of the polymer are shown. The absorption spectrum of ferric (solid gray line) and ferrous (dashed gray line) are also shown.

Upon addition of cytochrome *c* to a solution of **PP1**, the fluorescence emission intensity decreases. Figure 6.2A shows Stern-Volmer plots for a 0.3 μM solution of **PP1** with cytochrome *c* and another heme protein, myoglobin. At low concentrations of analyte good linear fits to the data are found.[16] Table 6.1 presents the Stern-Volmer constants that are obtained by analyzing these data. The quenching of the emission by ferric cytochrome *c* is greater than that by ferrous cytochrome *c*, and the quenching by cytochrome *c* is stronger than that for myoglobin; a finding that correlates with the smaller surface charge for myoglobin.

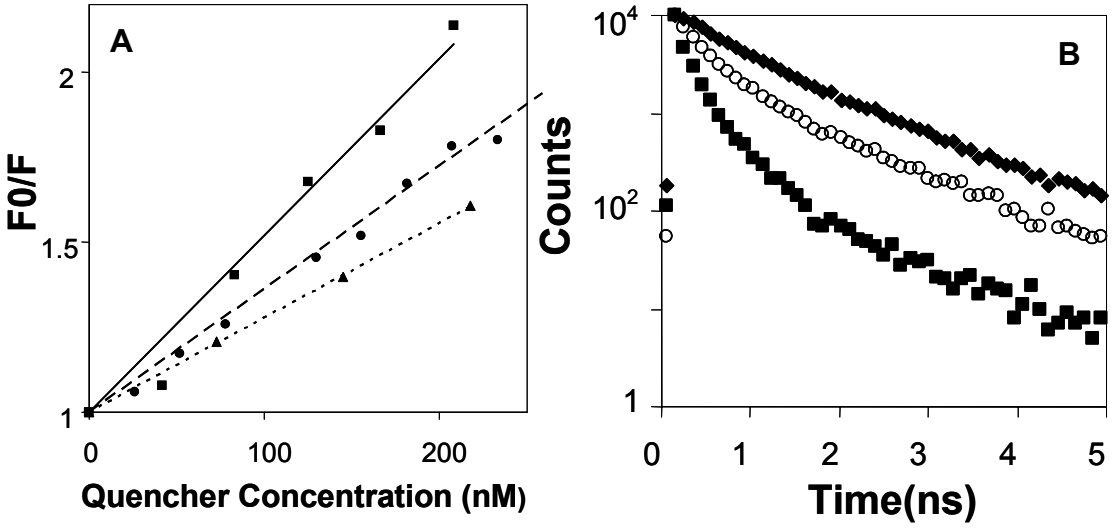

Figure 6.2 Panel A shows Stern-Volmer plots for **PP1** with ferric cytochrome *c* (squares), ferrous cytochrome *c* (circles) and myoglobin (triangles). The lines show fits corresponding to the Stern-Volmer constants in Table 6.1. Panel B shows the fluorescence decay of **PP1** with cytochrome *c* at 0.0 M (diamonds), 0.46 mM (circles), and 0.92 mM (squares).

Figure 6.2B shows the fluorescence decay curves for solutions of **PP1** with cytochrome *c*. The fluorescence decay of **PP1** in aqueous solution is nonexponential with an average fluorescence lifetime of 857 ps. In a methanol/water mixture the same polymer sample displays a

single exponential fluorescence decay law (see Figure 6.3B). Because the polymer is highly soluble in both systems, the different behavior is not ascribed to fractionation of the sample, but is believed to arise from differences in **PP1**'s conformation in the two solvents. As cytochrome *c* is added to the aqueous **PP1** solution, the fluorescence decay profile becomes more highly nonexponential. A fit of the data to a sum of exponentials shows that the fast relaxation component (*ca.* 100 ps lifetime) increases in amplitude as the concentration of cytochrome *c* increases. Although the lifetime distribution appears to be inhomogeneous, the short time component was ascribed to quenching of the polymer emission by static quenching.

The quenching mechanism for the polymer with cytochrome *c* was analyzed in several ways. Table 6.1 shows that the quenching of the ferrous and ferric forms of the protein are similar, suggesting that electron transfer quenching is not dominant. The influence of molecular geometry on the quenching was studied by denaturing the protein. The ferric form of the protein was heated to 353 K and cooled back to room temperature (denaturation was verified by measuring CD and UV/visible spectra, see Appendix). This form of the protein also quenched the polymer fluorescence but with about 71% the efficiency of the native protein, $K_{SV} = 3.7 \times 10^6$ M^{-1}. In a second experiment, apocytochrome *c* was prepared.[17] The CD spectrum for this form of the protein was similar to that reported earlier, and it did not display any heme features, as expected. The K_{SV} for the apocytochrome c was 6.3×10^5 M^{-1}, which is about six times smaller than that for the denatured protein and eight times smaller than that for the native protein.

Assuming that the **PP1**'s self-quenching and energy transfer quenching are independent relaxation processes, comparison of these two K_{SV} values suggest that the energy transfer quenching mechanism is more important than the conformational quenching mechanism for the denatured cytochrome *c*.[18]

Table 6.1 The Stern-Volmer constants for PP1 with some different macromolecules

Protein Analyte	K_{SV} (M^{-1})	Net Charge	Size
Fe^{2+}- cytochrome c	0.36×10^7	+5e	14 nm^3
Fe^{3+}- cytochrome c	0.52×10^7	+6e	14 nm^3
Fe^{3+}- myoglobin	0.28×10^7	0	20 nm^3
PAMAM 3G	1.0×10^7	+32e	24 nm^3
DAB 4G	1.1×10^7	+32e	5.0 nm^3

6.2.2 Quenching with Dendrimers

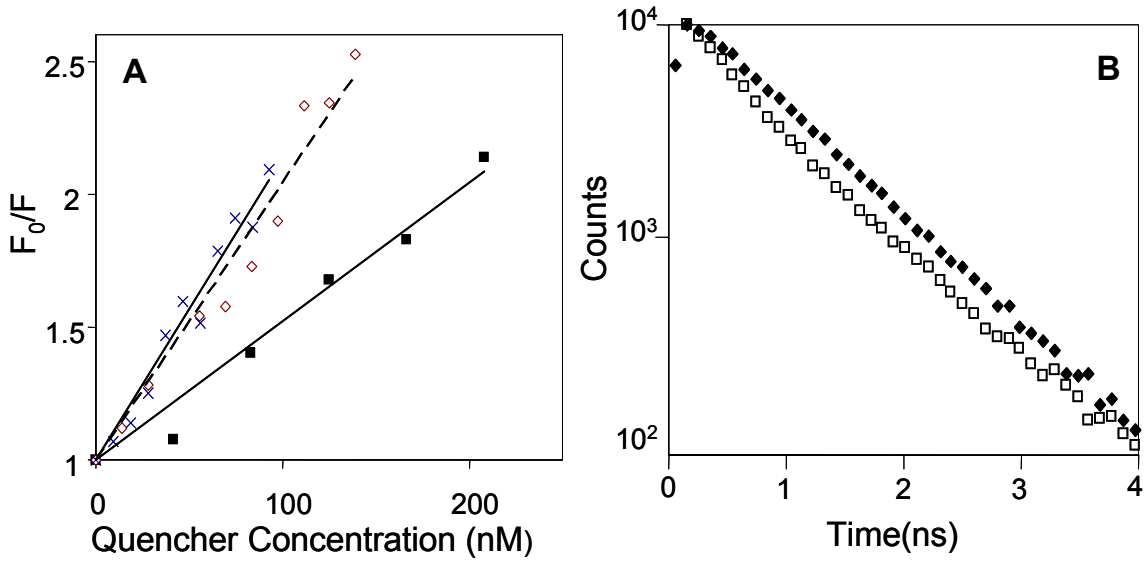

Figure 6.3 Panel A shows Stern-Volmer plots for **PP1** with different macromolecular quenchers: DAB 4G (X), PAMAM 3G (diamonds), and ferric cytochrome *c* (squares). The lines show fits corresponding to the Stern-Volmer constants in Table 6.1. Panel B shows the fluorescence decay law of **PP1** in water/methanol mixtures at PAMAM 3G concentrations of 0.0 M (diamonds) and 0.21mM (squares).

Figure 6.3A shows Stern-Volmer plots for **PP1** with PAMAM 3G and DAB 4G dendrimers. Interestingly the quenching by the dendrimers is even stronger than that of the

cytochrome *c*. Each of these dendrimers contains 32 ammonium groups in its outer shell and they are expected to bind strongly to **PP1**. Figure 6.3B shows the fluorescence decay of **PP1** with PAMAM 3G in methanol/water solutions. These data reveal that the quenching mechanism is static; *i.e.*, the unbound polyelectrolyte has a single exponential decay law with a 843 ps lifetime and the bound polyelectrolyte has a 210 ps fast component lifetime. The relative amplitude of the two components changes with PAMAM 3G concentration, but the lifetimes are the same. The change in quenching efficiency for each of the analytes correlates with the expected change in electrostatic binding for the macromolecules (see Table 6.1). Such a correlation was identified by Wang et al[19] for binding of PPV with differently charged viologens.

Although the dendrimer molecules PAMAM 3G and DAB 4G have the largest Stern Volmer constants, they do not possess visible chromophores. A Förster energy transfer quenching mechanism between **PP1** and the analyte requires an overlap of **PP1**'s emission spectrum with the analyte's absorption spectrum, and hence this mechanism is clearly not operative for the dendrimer molecules. A comparison of the absorption spectra are provided in Appendix.

An electron transfer quenching mechanism was also discounted. The dendrimers do not possess good electron acceptor groups, but possess primary and tertiary amines which might quench the fluorescence by an electron transfer mechanism.[7a] The importance of this mechanism was probed by changing the pH of the solution. A titration curve of PAMAM 3G dendrimer showed that the ammonium groups on the dendrimer are almost fully ionized at pH 7 ($\geq$ 30 of the 32 groups). To assess the importance of this mechanism the pH was raised to 12 in order to reduce the surface charge and generate more amines. In this latter case, no quenching was found. At intermediate pH values, between 7 and 12, the Stern-Volmer constant decreases from its value

at pH = 7 because the net positive charge on the dendrimer surface is decreasing. By lowering the solution pH, it is possible to fully protonate the surface amines and significantly protonate the 'interior' tertiary amines of the dendrimer. The Stern-Volmer constants do not change much, less than a factor of 2, as the pH is lowered − $K_{SV} = 6.8 \times 10^6$ M^{-1} at pH = 4 and $K_{SV} = 1.8 \times 10^7$ M^{-1} at pH = 2.15. These studies show that the quenching is not sensitive to amine availability (hence electron transfer quenching is not important) but is sensitive to the dendrimer charge.

The data in Table 6.1 show a correlation of the quenching efficiency with the positive charge on the analyte, however the quenching also depends on the analyte's size. This dependence is evident when comparing different generations of the same dendrimer material, for example the quenching efficiency of the PAMAM 3G dendrimer with that of the PAMAM 0G dendrimer. By increasing the PAMAM 0G dendrimer concentration to eight times that of PAMAM 3G the same equivalents of ammonium groups are made available to **PP1**, however the quenching efficiency is very low. The K_{SV} for the PAMAM 0G is $< 3.3 \times 10^3$ M^{-1}. If this value is modified to account for the number of ammonium groups (multiplied by eight), it is $< 2.7 \times 10^4$ M^{-1}, more than 400 times smaller than that found for PAMAM 3G. The Stern-Volmer constant observed for PAMAM 0G is also much smaller than that obtained for the common electron transfer quencher, methylviologen (for which K_{SV} was found to be 1.0×10^6 M^{-1}), corroborating the unimportance of electron transfer quenching for PAMAM.

6.3 Discussion and Conclusion

These observations demonstrate that the fluorescence quenching of conjugated polyelectrolyte **PP1** by charged macromolecules need not involve the typically used mechanisms of electron transfer or energy transfer. The dependence of the quenching efficiency on the

dendrimer size and charge suggests that the polyelectrolyte changes conformation upon binding. When the dendrimer size is small (zero or one generation) the charged units on the dendrimer probably interact with only two sequentially charged units on the polymer backbone. The larger analyte molecules allow for more interactions with the **PP1** backbone, so that the **PP1** can distort and/or 'wrap' itself onto the analyte's surface. This process should cause conformational changes in the **PP1** and create conditions for enhanced coupling between the electronically excited state and the ground state, increasing the internal conversion rate.

This work investigated the mechanism of fluorescence quenching in a conjugated polymer electrolyte when it binds with other macromolecules, in particular proteins and dendrimers. The binding constants can be quite large, supporting the promise of these materials as fluorescence sensors. A comparison of the different analytes confirms that the quenching mechanism is controlled by the electrostatic interactions between the macromolecular analytes and the polyelectrolyte. This study demonstrates that electron transfer and electronic energy transfer need not be present to cause quenching. The dependence of the quenching efficiency for a particular polyelectrolyte on the size and charge of the dendrimer analyte suggests a mechanism in which the polyelectrolyte has multiple 'contacts' with the dendrimer surface. We hypothesize that the multiple interactions between the polymer and the dendrimer changes the polymer's conformation and enhances the internal conversion, 'self-trapping'.

6.4 Acknowledgements

We acknowledge support from the U.S. National Science Foundation (CHE-0415457).

6.5 Appendix

The spectra shown below demonstrate that the dendrimer absorption spectrum is blue shifted from that of the PPP polyelectrolyte.

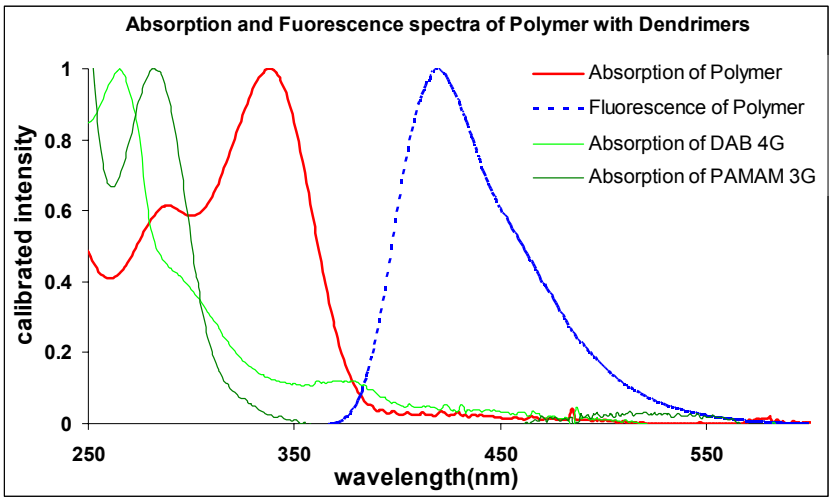

Figure 6.4 Absorption and fluorescence spectra of PP1 with dendrimers

Shown below are CD spectra for the native cytochrome c, denatured cytochrome c, and the apocytochrome c.

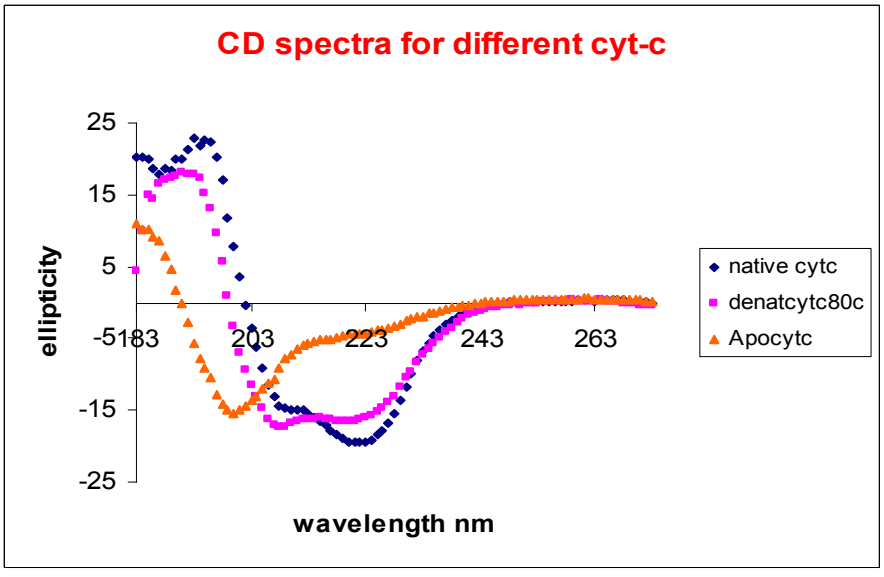

Figure 6.5 CD spectra for different cytochrome c

6.6 References

1. a) Kim, S.; Jackiw, J.; Robinson, E.; Schanze, K. S.; Reynolds, J. R.; Baur, J.; Rubner, M. F.; Boils, D. *MacromoleculesI*, **1998**, *31*, 964; b) Tan, C.; Pinto, M. R.; Schanze, K. S. *Chem. Commun*., **2002**, 446; c) Liu, B.; Yu, W.-L.; Lai, Y.-H.; Huang, W. *Chem. Commun.*, **2000**, 551.

2. a) Chen, L.; McBranch, D. W.; Wang, H.-Lin; Helgeson, R.; Wudl, F.; Whitten, D. G. *PNAS*, **1999**, *95* 12287; b) DiCesare, N.; Pinto, M. R.; Schanze, K. S.; Lakowicz, J. R. *Langmuir*, **2002,** *18*, 7785; c) Harrison, B. S.; Ramey, M. B., Reynolds, J. R.; Schanze, K. S. *J. Am. Chem. Soc.*, **2000,** *122,* 8561.

3. Fan, C. F.; Plaxco, K. W; Heeger, A. J. *J. Am. Chem. Soc.*, **2002,** *124*, 5642.

4. a) Gaylord, B. S.; Heeger, A. J.; Bazan, G. C. *PNAS*, **2002**, *99*, 10954; b) Kushon, S.; Bradford, K.; Marin, V.; Suhrada, C.; Armitage, B. A.; McBranch, D.; Whitten, D. *Langmuir*, **2002**, *18*, 7245; c) *ibid*, **2003**, *19*, 6456.

5. a) Zhou, Q.; Swager, T. M. *J. Am. Chem. Soc.*, **1995,** *117*, 12593.

6. a) McQuade, D. T.; Pullen, A.E.; Swager, T. M. *Chem. Rev.*, **2000**, *100*, 2537; b) Swager, T. M. *Acc. Chem. Res.*, **1998**, *31*, 201.

7. a) Lakowicz, J. R. "*Principles of Fluorescence Spectroscopy"* (N.Y., Plenum, **1999**); b) Speiser, S. *Chem. Rev.*, **1996**, *96*, 1953.

8. a) Huser, T.; Yan, M.; Rothberg, L. *PNAS*, **2000**, *97*, 11187; b) Sluch, M. I.; Godt, A.; Bunz, U. H. F.; Berg, M. A. *J. Am. Chem. Soc.*, **2001**, *123*, 6447; c) Hu, D. H.; Yu, J.; Barbara, P. F. *J. Am. Chem. Soc.*, **1999**, *121*, 6936; d) *ibid*, *Science*, **2000**, *289*, 1327.

9 . Moore, G. R.; Pettigrew, G. W. *Cytochromes c, "Evolutionary, Structural and Physicochemical Aspects"*; Springer-Verlag: Berlin, Germany, **1990**.

10. Dove, A. *Nature Biotech*., **2001**, *19*, 615.

11. Kim, S.; Jackiw, J.; Robinson, E.; Schanze, K. S.; Reynolds, J. R.; Baur, J.; Rubner, M. F. ; Boils, D. *Macromolecules*, **1998**, *31*, 964.

12. GPC studies were performed by Polymer Source Inc., Quebec CANADA.

13. Yamamoto, H.; Liu, H.; Waldeck, D. H. *Chem. Commun. B*, **2001**, 1032.

14. Trewhella, J;. Carlson, V. A. P.; Curtis, E. H.; Heidorn, D. B. *Biochemistry*, **1988**, *27*, 1121.

15. Liu, M.; Waldeck, D. H.; Oliver, A. M.; Head, N. J. and Paddon-Row, M. N. *J. Am. Chem. Soc.*, **2004**, *126*, 10778.

16. At higher concentrations of analyte deviations from the linear Stern-Volmer behavior are found and will be described elsewhere.

17. Fisher, W.R.; Taniuchi, H.; Anfinsen, C. B. *J. Biol. Chem.*, **1973**, *248*, 3188.

18. If the electrostatic binding is the same for the two protein forms, the difference would be a factor of ten. However, the apocytochrome has a smaller net charge and this will contribute to a decrease in binding also.

19. Wang, D.; Wang, J.; Moses, D.; Bazan, G. C.; Heeger, A. J. *Langmuir*, **2001**, *17*, 1262.

Chapter 7 Ionic Strength Effect on the Rigidity of a Conjugated Polyelectrolyte

The properties of polyelectrolytes and their origin in molecular structure and conformation have been a challenge for many decades. This work studies the spectroscopic behavior of a polyelectrolyte with a polyphenylene backbone and a sodium sulfopropoxy side chain. Study of the variation in fluorescence with ionic strength and the electrolyte nature is used to probe changes in molecular conformation, albeit indirectly. The observed fluorescence and absorption spectra indicate that the conjugated polyelectrolyte chain becomes extended and more rigid because of the Coulomb interactions with the salt counterions. An explicit discussion of the experimental data and its interpretation is provided.

7.1 Introduction

Polyelectrolytes are a special class of polymers which contain a large number of charged groups. The biopolymers DNA, RNA, and polysaccharides are polyelectrolytes and have attracted considerable attention because of their fundamental role in biological systems.[1,2] Although the understanding of polyelectrolyte solutions is desirable, it is still limited both theoretically and experimentally.[3,4,5]

When a polyelectrolyte dissolves in a polar solvent like water, it dissociates into charged counterions, and a charged polyion. The counterions and polyion are subject to long-range Coulomb interactions which provide a rich variety of effects not found in neutral polymer solutions. As a result, the addition of electrolyte is a key means to alter the properties of solution

containing polyions and allows the influence of the ionic distribution on the polyion chains to be investigated.

Experimental characterization of polyelectrolyte chain conformation in solution has been studied extensively with a variety of techniques; intrinsic viscosity[6], static and dynamic light scattering[7] and small angle neutron scattering (SANS)[8] are prominent ones. Wang et al used the SANS technique to show that the addition of excess electrolyte screens the repulsive interchain interaction and increases the polymer's persistence length, presumably by a combination of the intrinsic rigidity of the conjugated backbone and a stiffening from the charges along the polyelectrolyte chain. However, these techniques require high concentrations (40 mg/ml) of the solute in order to get a good detection signal. As a result, the interactions between polyion chains are likely to be important and may cause deviations from the conformation of isolated chains. Highly sensitive spectroscopic methods, such as fluorescence and absorption techniques are able to probe dilute solutions of a polyelectrolyte (lower than 2×10^{-3} mg/ml). This work investigates how the polyphenylphenylene polyelectrolyte's spectra change upon varying the solution's ionic strength.

This study contains four major sections. The next section provides the description of the theoretical models. The following section describes the experimental details. The next section analyzes the experimental results and compares them to models. The last section concludes this work and describes its implications.

7.2 Theoretical Models

Over the past few decades, the evolution of theoretical models for understanding neutral polymers in solution has been widely developed, largely by employing modern scaling

concepts.[9] Compared to neutral polymers an understanding of the properties of polyelectrolytes is still limited, however ideas and methods have been developed for many years for charged colloidal systems. Direct experimental tests of the theoretical models are typically not possible because of idealizing assumptions in the theory and the lack of detailed control over the experimental system. Therefore, computer dynamics simulations play a key role in mimicking the experimental system and in testing the theoretical models. Although the accuracy of simulations is still below that obtained from neutral polymers, they provide a useful means to understand the properties of polyelectrolytes.

Molecular dynamics simulations of salt-free polyelectrolyte systems have been developed to overcome major theoretical difficulties[10,11] one of which is to calculate the ionic density on the polyelectrolyte chain. Almost all calculations which study polyelectrolyte conformation apply the Debye-Hückel approximation[12], which is a linearization of the Poisson-Boltzmann equation[13] (see equation 1) and assumes that the Coulomb interaction energy is much less than the average thermal energy k_BT.

$$\frac{1}{r^2}\frac{d}{dr}\left(r^2\frac{d\Psi_j}{dr}\right) = -\frac{\rho_j}{\varepsilon_0\varepsilon_r} \qquad \mathbf{1}$$

In equation 1, the solvent is treated as a dielectric continuum of dielectric constant $\varepsilon_r\varepsilon_0$. $\psi_j(r)$ is the mean electrostatic potential around an ion of charge z_je positioned at the origin and ρ_j is the charge density defined by

$$\rho_j(r) = \sum_i z_i e\rho_i \exp(-z_i e\psi_j / k_BT) \qquad \mathbf{2}$$

where ρ_i is the number density of ionic species i in solution.

Stevens et al[14] performed molecular dynamics simulations on polyelectrolytes for different chain lengths and different ionic strengths, and compared the time averaged end-to-end distance, R, to the inverse Debye length κ. The inverse Debye length κ is defined as

$$\kappa^2 = \frac{4\pi e^2}{\varepsilon k_B T} \sum_i \rho_i z_i^2 \qquad \mathbf{3}$$

They simulated the conformation of the polyelectrolyte with several different repeat units (N) and salt concentrations and found that for a given N, R depends only on the value of κ. The densities studied there are mainly in the dilute regime. However, the Poisson-Boltzmann approximation fails quantitatively and qualitatively in cases with higher densities, larger coupling strengths, and multivalent salt and counterions[15,16,17] because the Coulomb interaction is much stronger than k_BT. Because of strong attractive interactions, counterions buildup in the volume surrounding the polyions, whereas ions with the same sign as the polyions are excluded out of this area. The Debye-Hückel model is not accurate enough to explain the strong influence of salt on the environment of the polyions in this regime.

Vlachy[18] discussed the salt effect beyond the Poisson-Boltzmann theory and used three basic models to interpret the experimental results for polyelectrolyte solutions: the cell model, the one component model and the isotropic model. The cell model[19,20,21] assumes that the Coulomb repulsion between polyions is so strong that the polyions stay far away from each other, on average. As a result, the solution is treated as an assembly of noninteracting cells and the model only considers the interaction between a polyion and counterions. Each polyion is approximated as spherical or cylindrical in shape, and uniformly spread throughout the solution. The cell model considers the size and charge asymmetry between the polyion and small ions in solution. The cell model is not adequate for describing solutions containing divalent counterions because of the strong spatial correlations between divalent counterions, a feature not included in

the cell model. However, it can be applied to model the effect of the monovalent counterions on the polyelectrolyte in the current study.

The second model is called the one component model[22,23,24] and it further develops the cell model, by considering spatial correlations between polyions. It treats the solution as an effective one-component fluid in which the polyions interact via a screened Coulomb potential. In conjunction with the Mean Spherical Approximation (MSA)[25,26] or HyperNetted Chain (HNC) approximation[27], the one-component model can somewhat predict the structure of the solution or extract the number of charges on a polyion. However, neither the cell model nor one component model provides information about all the interparticle correlations.

The isotropic model[28,29] treats the particles as charged hard (soft) spheres but considers all the ionic species on an equal level, immersed in a dielectric continuum. Although the isotropic model realistically includes all ionic species in solution, it requires that an integral equation theory[29], MSA and HNC approximation, be used to model the structure. Valchy et al[30] compared Monte Carlo results to the HNC approximation and found that the HNC approximation predicts a counterion to polyion distance that is too small; in short it underestimates the repulsive interactions between polyions. Overall, a comprehensive and simple model for interpreting the salt effect on polyelectrolytes is not available.

The current study compares the behavior of the experimental fluorescence intensities in variable electrolyte solutions as a function of the inverse Debye length κ, and the dependence of this correlation on the size and charge of the counterions.

7.3 Experimental

Poly[2,5-bis(3-sulfonatopropoxy)-1,4-phenylene-alt-1,4-phenylene) (identified as **PP1**) was prepared in a manner similar to that reported in the literature.[31] The molecular weight was found to be 9900 and the polydispersity was 1.26, as determined by size exclusion chromatography. [32] Steady-state absorption spectra were measured on an Agilent 8453 spectrometer and the steady-state emission spectra were measured on a Spex Fluorolog 0.22 m double spectrometer.[33] The time-resolved fluorescence data were collected using the time-correlated single photon counting method.[34]

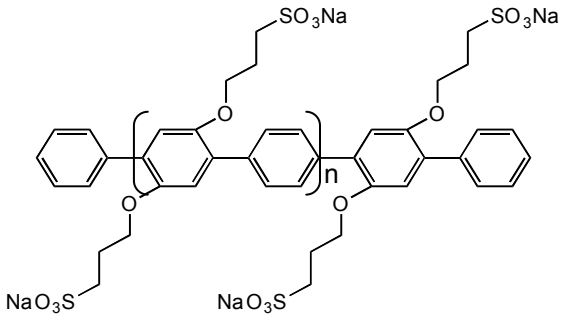

PP1

Figure 7.1 Structure of **PP1**

PP1 is a polyelectrolyte with negative charges on its side chains in every other phenyl ring. In order to avoid intermolecular interactions between **PP1** chains, the experimental concentration was dilute, 3 x 10^{-3} mg/ml, ~ 3 x 10^{-7} M assuming 9900 g/mol molecular weight. Since the concentration of electrolyte is comparable or higher than the concentration of **PP1**, the properties of the electrolyte solution, such as the charges and the sizes of the ions and the magnitude of the ionic strength, can be explored. In the current experiment, the ionic strength of electrolyte was varied from 10^{-5} M to 0.1 M.

The electrolyte solutions are separated into three groups. The first group is composed of cations with a single charge, such as Li^+, Na^+, K^+, Cs^+ and Cl^-, I^-, phosphate counterions. The second group contains three organic electrolytes which are tetrabutylammonium tetrafluoroborate (TBAF), tetraethylammonium tetrafluoroborate (TEAF) and ammonium tetrafluoroborate (AF). The last group is composed of cations with a double charge, such as Mg^{2+}, Ca^{2+} and Ba^{2+}.

7.4 Results and Analysis

7.4.1 Singly charged ions (Li^+, Na^+, K^+, Cs^+, I^-, Phosphate, Cl^-)

Absorption and fluorescence spectra of **PP1** (concentration fixed at 3×10^{-7} M) were measured in different ionic strength solutions. Figure 7.2 shows the absorption spectra of **PP1** in LiCl solutions for ionic strengths from 0.5 mM to 100 mM. The absorption spectrum of **PP1** in water has an absorption peak λ_{max} at 338 nm, which red-shifts with increasing ionic strength as shown in Figure 7.2. When the ionic strength is less than 1.25 mM, the absorption peak is close to the 338 nm value measured for **PP1** in water and it has a similar absorbance. Upon further increasing the ionic strength, the absorbance increases and an isosbestic point is observed at 339 nm. As the ionic strength increases above 8 mM, the absorbance peak slightly shifts to a redder wavelength while preserving the isosbestic point. The absorbance at high ionic strength remains constant, even with further increase of the ionic strength by up to ten times.

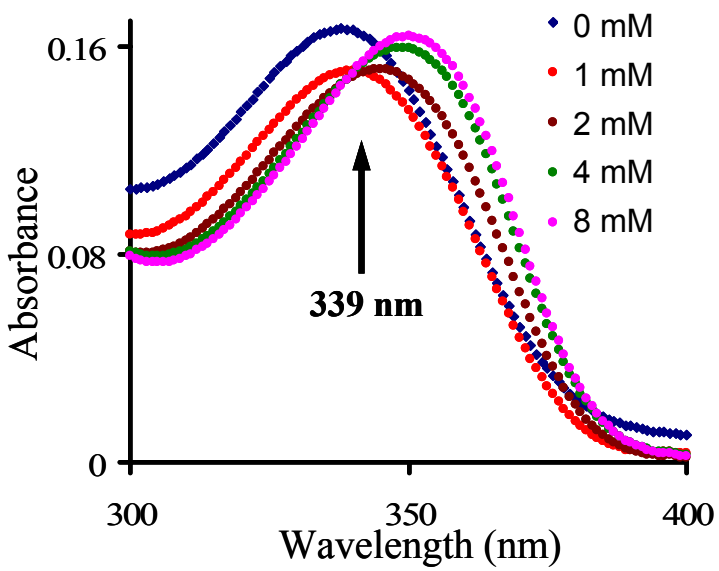

Figure 7.2 Absorption spectra of **PP1** in LiCl solutions. Ionic strength varies from 0 mM to 8 mM. The absorbance increases with increasing the ionic strength, accompanying with the spectrum red-shift. The different color represents the different ionic strength.

The spectroscopic behavior of **PP1** in NaCl, KCl, CsCl electrolyte solutions are similar to that in LiCl. The observed isosbestic points lie at 340 nm, 341 nm and 342 nm, respectively and it red-shifts in the order of increasing radii from Li^+ (0.59 Å), Na^+ (1.02 Å), K^+ (1.33 Å) to Cs^+ (1.74 Å). The change on the absorption spectrum is stronger at lower ionic strength and stops at higher ionic strength.

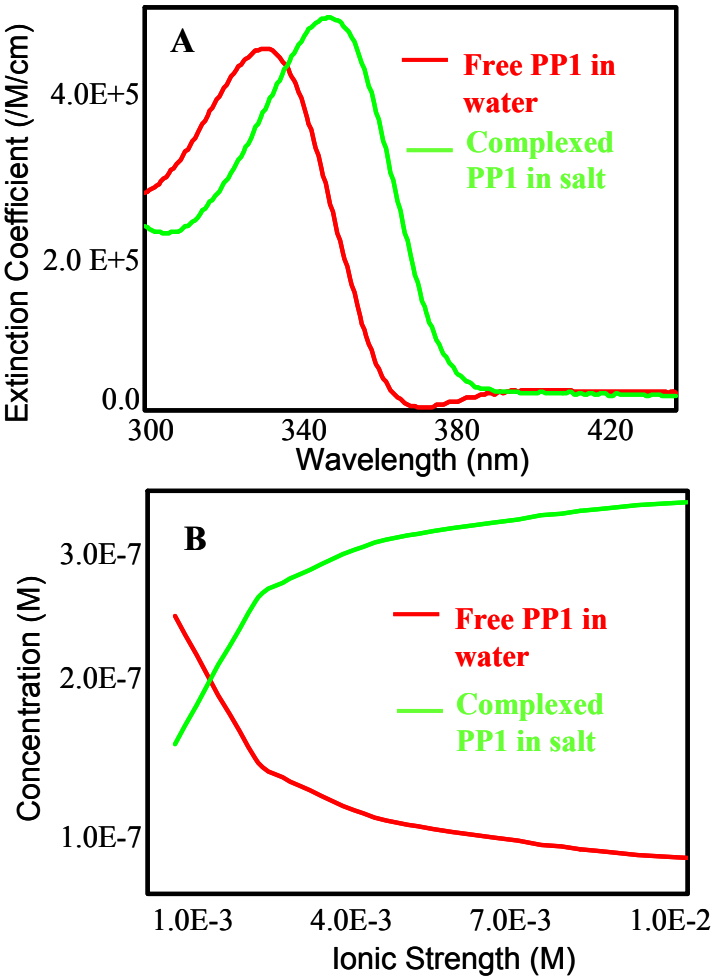

Figure 7.3 Theoretical fit to a two states model for the absorption spectrum of **PP1** in LiCl solutions. A) extinction coefficient versus absorption wavelength; B) change of concentration versus ionic strength. Red line represents the free **PP1** species and green line represents the complexed species.

Table 7.1 Theoretical fit of the absorption spectrum of PP1 in MCl, a two species model.

Salt	Reactant λ_{max} (nm)	Product λ_{max} (nm)	Stability Constant (ln K)	Percentage of Free **PP1** in 0.01 M Salt (%)
LiCl	334	352	6.9	9
NaCl	338	354	6.0	20
KCl	334	352	7.3	7
CsCl	335	355	6.6	12

By assuming a two species equilibrium reaction, the absorption spectrum was fit to obtain an equilibrium constant, K, or, stability constant. Figure 7.3 gives an example of the fitting results for **PP1** in LiCl solutions. Figure 7.3A shows the theoretical absorption spectra for each of two species in the equilibrium reaction. Figure 7.3B shows the change in concentration of the two species with increasing the ionic strength. Table 7.1 summarizes the equilibrium constant K and gives the absorption peaks of the two species from the fit for all singly charged cations. The absorption peak of the free **PP1** varies from 334 nm to 338 nm, and the absorption peak of the complexed **PP1** varies from 352 nm to 355 nm. The concentration of the free **PP1** varies from 85% in free-salt solution to 7% in 0.01 M salt solution. This observation indicates one species appearing and simultaneously another species disappearing with ionic strength.

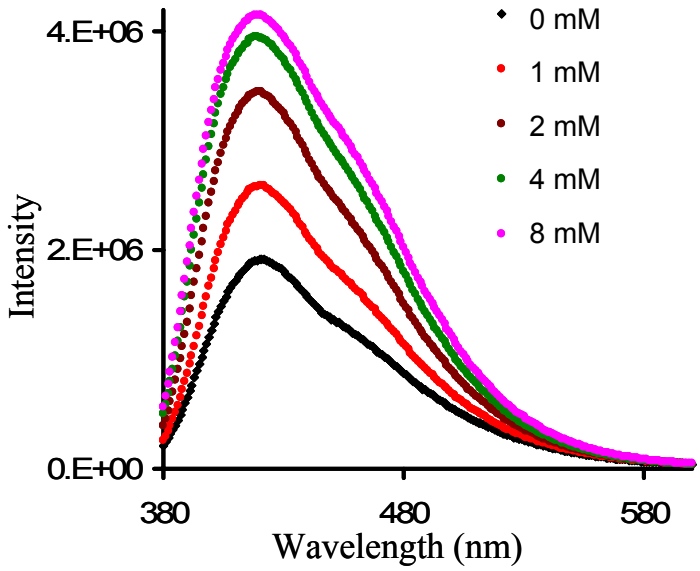

Figure 7.4 Fluorescence spectra of **PP1** in LiCl solutions. Ionic strength varies from 0 mM to 8 mM. The fluorescence intensity enhances with increasing the ionic strength. The different color represents the different ionic strength.

The fluorescence spectrum of **PP1** in LiCl solution was measured as a function of increasing ionic strength, shown in Figure 7.4. The peak of the fluorescence spectrum for **PP1** remained at 420 nm; the fluorescence intensity increases with increasing the ionic strength. In comparison with the changes in absorbance at different ionic strengths, the fluorescence intensity increases more dramatically; e.g. the quantum yield of **PP1** increases 1.3 times in 1 mM salt and increases by 2.3 times in 8 mM ionic strength, as compared to that in water. From the absorption spectrum fits (see Figure 7.3), the two species have different radiative rates, 3.6×10^6 s^{-1} and 4.8×10^6 s^{-1}. This increase is not large enough to account for the change in the fluorescence yield, implying that the nonradiative rates of the two species must decrease. This result indicates that the increase of the fluorescence intensity is not caused only by the effect of the oscillator strength of the transition in **PP1** from the absorption spectrum, but it is affected also by the change of the internal conversion rate of the excited state.

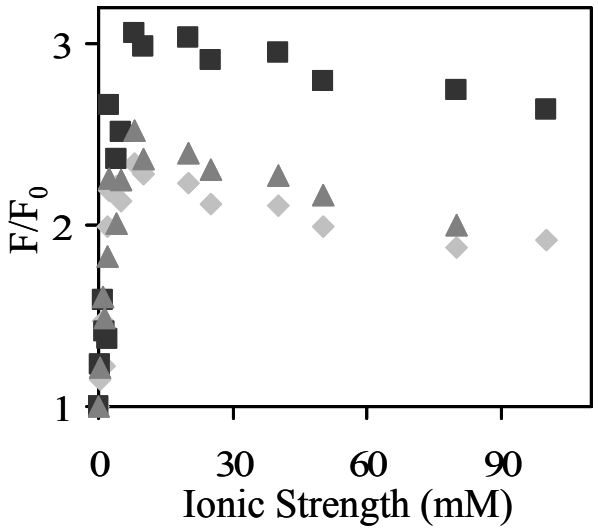

Figure 7.5 Fluorescence intensity ratio of **PP1** in ionic LiCl solutions (F) to that in water (F_0) versus the ionic strength. The fluorescence intensity was summed up the whole spectrum area. The spectrum was obtained by exciting three excitation wavelengths, the peak absorption

wavelength (diamond), the 20 nm shorter than the peak wavelength (square) and the 20 nm longer than the peak wavelength (triangle).

Figure 7.5 plots the fluorescence intensity ratio of **PP1** in LiCl solution to its intensity in deionized water versus the ionic strength. The fluorescence intensity ratio curves in Figure 7.5 are shown for three excitation wavelengths: the peak absorption wavelength, a wavelength 20 nm shorter than the peak wavelength and a wavelength 20 nm longer than the peak wavelength. Each data set shows that the fluorescence intensity increases rapidly at low ionic strength (below 2 mM), and then stops increasing before it starts to weakly decrease. This behavior corresponds to the red-shift of the absorption spectrum, crossing an isosbestic point at low ionic strength with the intensity increasing and preserving the isosbestic point at high ionic strength. For the spectrum collected at 20 nm shorter exciting wavelength than the peak wavelength, the fluorescence intensity is the highest; for exciting at 20 nm longer and exciting at peak wavelength, the fluorescence intensities are similar. The wavelength dependence can be predicted using the two state model. In this equilibrium the two species have different absorbance at every wavelength, see Figure 7.3A, hence different excitation wavelengths can cause exciting different percentage of the two species in the excited state.

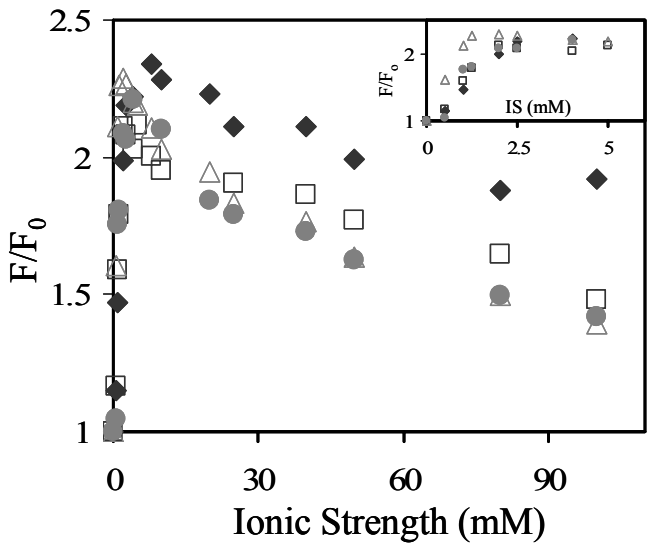

Figure 7.6 Fluorescence intensity ratio of **PP1** in LiCl (diamond), NaCl (square), KCl (triangle) and CsCl (circle) to **PP1** in water versus the ionic strength.

To better understand the ionic strength effects, the fluorescence of **PP1** in other singly charged cation electrolyte solutions was also studied. The comparison of F/F_0 for different singly charged ions is shown in Figure 7.6. The fluorescence spectrum was collected by exciting at the peak absorption wavelength for each ionic solution. Like the observed behavior of **PP1** in LiCl solutions, the fluorescence intensities of other monocations increases rapidly at low ionic strength, then saturates at higher ionic strength before decreasing. Comparing their fluorescence behavior, the fluorescence intensity increases with a similarly fast extent, however when the intensity saturates, the solutions with the smaller Li^+ shows a higher fluorescence intensity than the other ions. The larger cations K^+ and Cs^+ behave similarly. Although the smaller cation can get closer to the polyion chain, causing a stronger Coulomb interaction than bigger cations, the difference among these singly charged ions is small. After the spectrum saturates, further increasing the ionic strength causes the fluorescence to decrease, however the order is preserved $Li^+ > Na^+ > K^+, Cs^+$.

Figure 7.7 compares the fluorescence intensity ratio for different counter anions: phosphate, Cl^- and I^-. These data show that the size of the anion affects the fluorescence intensity of **PP1**. In particular, I^- has the smallest charge to size ratio and the largest fluorescence yield, whereas Cl^- has the largest charge to size ratio and the smallest fluorescence yield. This trend is opposite to that observed for the cations. To summarize, the fluorescence intensity increases with the charge to size ratio of the cationic counterions, but decreases with the charge to size ratio of the anionic counterions.

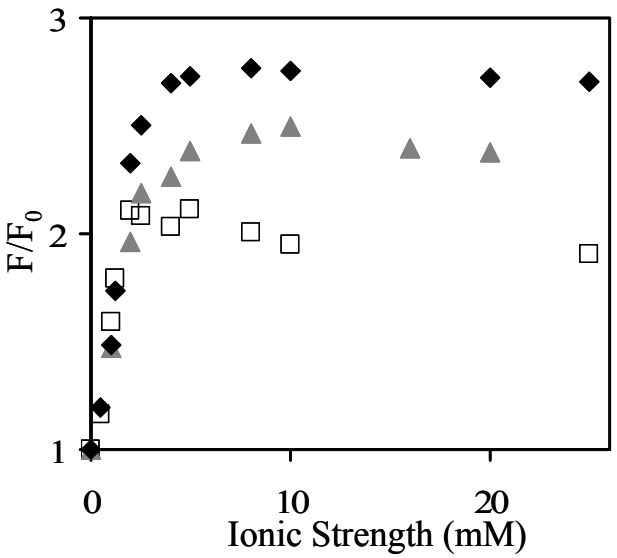

Figure 7.7 Fluorescence intensity ratio of **PP1** in NaCl (square), sodium phosphate buffer at pH = 7 (triangle) and NaI (diamond) verse **PP1** in water.

As a whole, all of the different singly charged salt ions show a similar behavior on the ionic strength of a solution. The different magnitudes appear to be related to their different sizes for both cations and anions.

7.4.2 Organic charged ions (TBAF, TEAF, AF)

Three organic singly charged ions TBAF, TEAF and AF were studied to further explore the ionic strength effect on **PP1**. Compared to the inorganic ions, the organic ions have a large steric size. Figure 7.8 shows the absorption spectrum of **PP1** in TBAF solution, which red-shifts with increasing ionic strength and displays an isosbestic point at 351 nm. The isosbestic point in TEAF and AF is 345nm and 339nm, respectively.

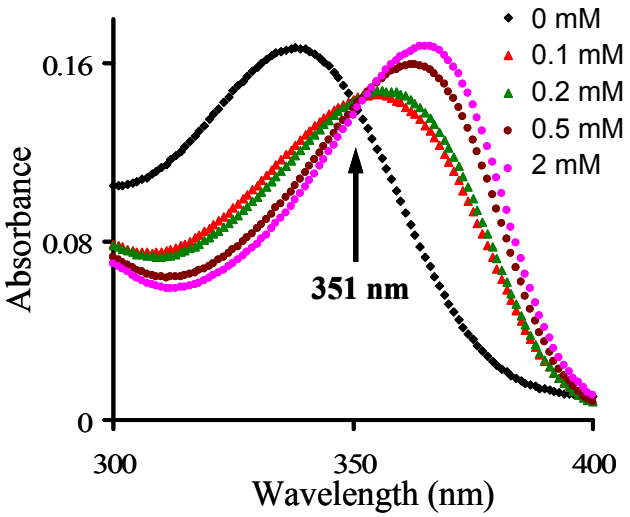

Figure 7.8 The absorption spectra of **PP1** for aqueous solutions with different TBAF concentrations

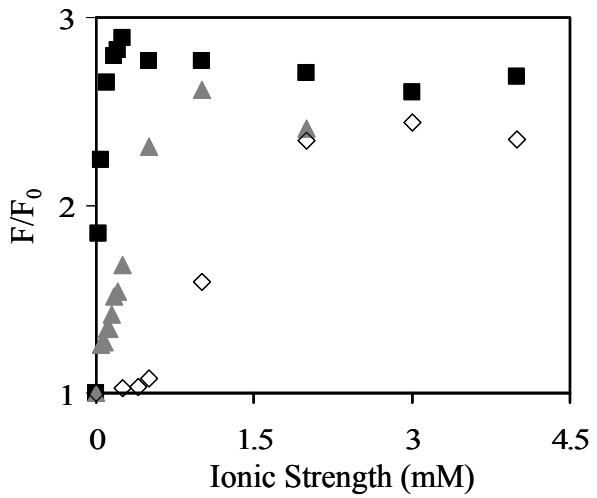

Figure 7.9 Fluorescence intensity ratio of **PP1** in AF (diamond), TEAF (triangle) and TBAF (square) to **PP1** in water as a function of the ionic strength. The ionic strength range is small due to the weak solubility of TBAF in water.

Figure 7.9 shows that the fluorescence intensity ratio increases in all the solutions and by an amount between 2.5 to 3 times as a function of ionic strength. The ratio increases with different slopes, *e.g.* faster in TBAF at low ionic strength than it does in AF solutions. The slope correlates with the size of the cation, namely TBAF > TEAF > AF. The fluorescence intensity ratios in TBAF as a function of ionic strength at three different excitation wavelengths were also compared. The data showed a similar trend to that for the LiCl solutions (Figure 7.5), that is, the highest fluorescence ratio is collected at a 20 nm shorter excitation wavelength.

Four different ionic strengths (0 mM, 0.25 mM, 0.5 mM and 15 mM) of TBAF were studied in detail. Figure 7.10 shows the normalized absorption spectrum of **PP1** in solutions of these four ionic strengths. The spectra reveal two features, a dominant 'red' peak and a weaker 'blue' (ca. 290 nm) peak. The relative intensity of this 'blue' peak decreases with increasing ionic strength. In comparison with biphenyl, *p*-terphenyl and *p*-quaterphenyl in heptane, which have S1 structure at 246 nm, 278 nm and 296 nm, respectively[35], it suggests that the small bump

might be a more localized (two to three phenyl rings) transition of the polymer backbone. As the ionic strength increases, this transition decreases in intensity relative to the major peak. The red-shift in the localized transition with increasing ionic strength could correspond to the red-shift of the aromatic hydrocarbons as the size of the molecule increases, (for example, from biphenyl to *p*-quaterphenyl[36]), demonstrating that the **PP1** chain becomes more extended with increasing ionic strength.

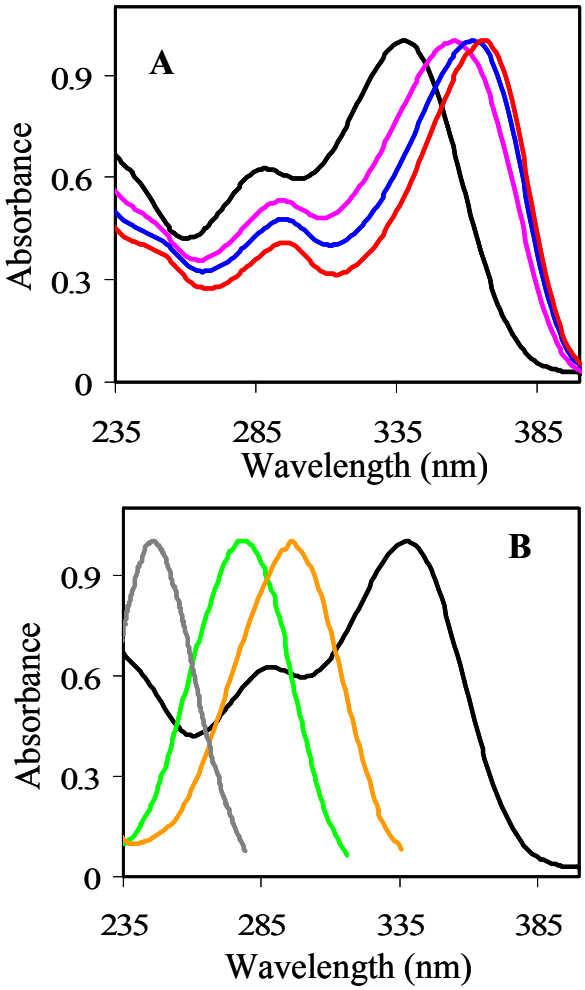

Figure 7.10 A) Normalized absorption spectra of **PP1** in 0 mM (black, peaks at 388 nm and 288 nm), 0.25 mM (pink, peaks at 356 nm and 293 nm), 0.5 mM (blue, peaks at 362 nm and 295 nm) and 15 mM (red, peaks at 365 nm and 295 nm) TBAF solutions; B) comparison of the absorption

spectrum of biphenyl (gray, peak at 246 nm), *p*-terphenyl (green, peak at 278 nm) and *p*-quaterphenyl (orange, peak at 296 nm) with **PP1** in water (0 mM).

7.4.3 Doubly charged ions (Ca^{2+}, Mg^{2+}, Ba^{2+})

Doubly charged ions, Mg^{2+}, Ca^{2+} and Ba^{2+}, have cation radii 0.72 Å, 1.00 Å and 1.42 Å, respectively. Comparing the size of doubly charged ions with singly charged ions, Mg^{2+} is slightly bigger than Li^{+} (0.59Å); Ca^{2+} is close to Na^{+} (1.02 Å), and Ba^{2+} is similar to K^{+} (1.33 Å). Figure 7.11 shows the absorption spectrum of **PP1** in Mg^{2+} solution. The absorption spectrum of **PP1** in doubly charged electrolyte solutions also red-shifts with increasing ionic strength. The isosbestic point appears for $MgCl_2$ and $CaCl_2$ at 345 nm and 346 nm, respectively. Comparing to the isosbestic point obtained from the similar sizes of the singly charged ions, they shift 6 nm more toward red wavelengths. These data show that the magnitude of the charge also affects the spectral shift.

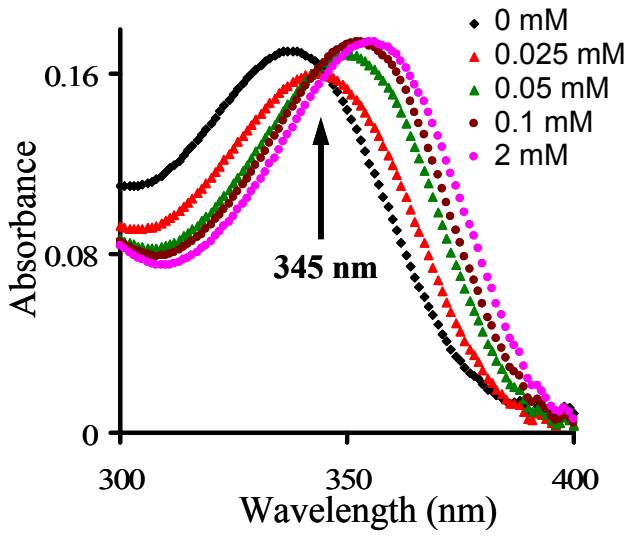

Figure 7.11 Absorption spectra of **PP1** in different ionic strength of $MgCl_2$ solution.

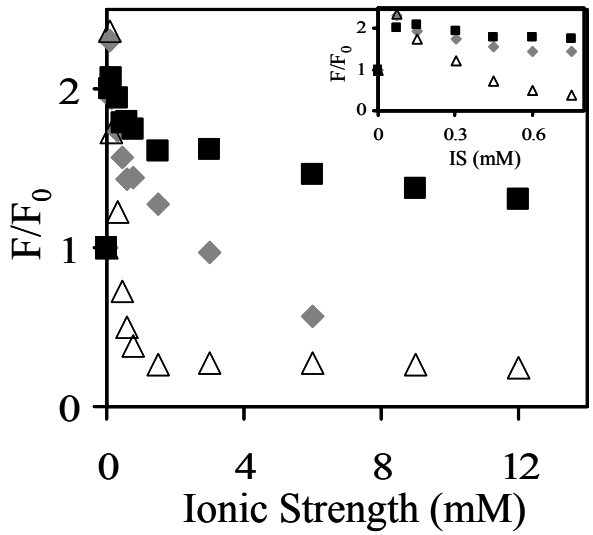

Figure 7.12 Fluorescence intensity ratio of **PP1** in $MgCl_2$ (square), $CaCl_2$ (diamond) and $BaCl_2$ (triangle) ionic solutions to the intensity in water as a function of ionic strength.

Figure 7.12 plots the fluorescence intensity ratio of **PP1** as a function of the ionic strength for the doubly charged ions. The intensity ratio rapidly increases at low ionic strength (below 0.075 mM) and the magnitude of the increased fluorescence between 2 to 2.5 times is comparable to the effect of singly charged ions. Mg^{2+} with the smallest size and the highest charge density, increases the fluorescence intensity the strongest compared to other doubly charged ions, the same trend as seen for Li^{+}. In contrast to the slow decrease of fluorescence intensity which is observed from the singly charged ions, a dramatic fluorescence decrease is found for the doubly charged ions. This quenching increases with the size of the cation.

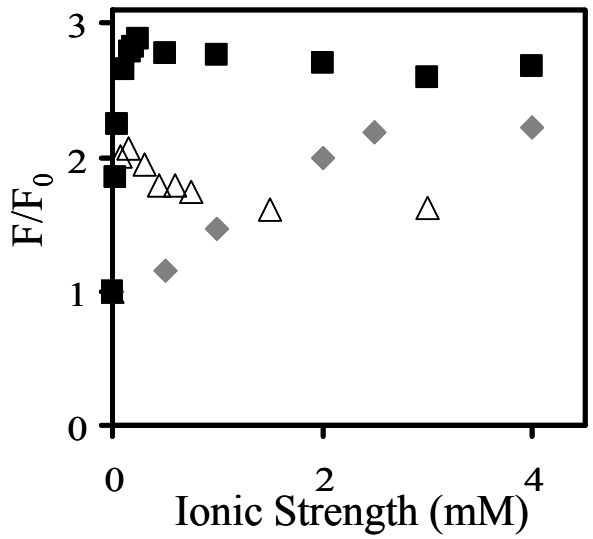

Figure 7.13 The comparison of the fluorescence intensity ratio of **PP1** in TBAF (square), $MgCl_2$ (triangle) and LiCl (diamond) to **PP1** in water.

Figure 7.13 compares the fluorescence of **PP1** in different kinds of electrolytes at small ionic strength, where it is increasing. The data show that the organic salt TBAF has the steepest slope and the slope of the doubly charged cation Mg^{2+} is steeper than that of the singly charged ion Li^{+}. This comparison suggests that TBAF enhances the fluorescence intensity of **PP1** more than the other electrolytes. In comparison with the properties of these electrolytes, TBAF has the biggest size and the smallest charge to size ratio, hence TBAF should have the weakest interactions with polyion. The experiment shows a most dramatic fluorescence increasing in TBAF solutions as the ionic strength increases, however this behavior suggests that the Coulomb interactions between salt and the polyelectrolyte is not the only origin for the change in the fluorescence yield of **PP1**.

7.4.4 Lifetime measurements

The time-resolved fluorescence of **PP1** at ten TBAF ionic strengths was collected at two emission wavelengths 420 nm and 500 nm. The data could be well described by fitting to a sum of two exponential decay functions. Table 7.2 provides the lifetime fitting parameters.

Table 7.2 The lifetime fits for PP1 in TBAF ionic solutions at 500 nm emission

Ionic Strength(mM)	τ_1 (ps)[a]	τ_2 (ps)	A_2 (%)	τ_c (ps)[b]	χ^2
0	217	860	9.3	277	1.06
0.025	263	848	34.4	464	0.86
0.05	287	802	43.5	511	1.10
0.1	291	817	65.2	634	1.05
0.2	271	833	76.1	699	1.21
2	187	833	86.5	746	1.01
4	253	848	81.8	739	0.94
5	213	838	86.4	752	0.91
10	255	837	85.5	752	0.91
15	285	847	81.8	745	1.06

a. The fluorescence decay is fit to a double exponential function: τ_1 is the fast time constant, τ_2 is the slow time constant and A2 % is its percentage contribution to the total decay curve.

b. The Correlation time is defined as $\tau_c = \Sigma A_i \tau_i$ where τ_i is the decay time for component i and A_i is the percentage of decay time i in a fit of the decay law to a sum of two exponentials.

The fluorescence decay of **PP1** was fit to a double exponential function, in which one fast time component 217 ps dominates 90.7% for **PP1** in water. With increasing ionic strength, the fast time component varies from 217 ps to 291 ps and its contribution drops to 18% at high ionic strength. Another slow time component (average 837 ps) becomes dominant as the ionic strength increases and the decay curve becomes nearly single exponential at high ionic strength. These

data suggest that two species exist in solution, one with a lifetime of about 254 ps and one with a lifetime of 837 ps, and the amount of the longer lived species increases with the ionic strength.

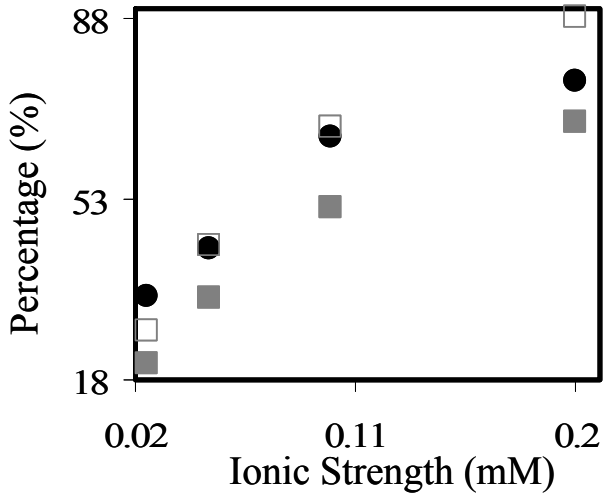

Figure 7.14 The A_2% percentage (circle) of the longer lived component obtained from the lifetime measurements compares with the concentration ratio (square) of the new complexed species obtained from the theoretical fit on the absorption spectrum as a function of ionic strength. The open squares adjust the data for the absorbance difference of the two species at the excitation wavelength.

The result obtained from the lifetime measurements has the same trend as the theoretical fit of the absorption spectrum, see Figure 7.14. For example, when the ionic strength is 0.025 mM, the complexed species is 21% of the total concentration and corresponds to the longer-lived component with a 34% amplitude percentage. When the ionic strength increases to 0.2 mM, the complexed species has a concentration ratio of 68% from the absorption spectra and a value of 76% amplitude contribution from longer-lived component. Although Figure 7.14 shows similar trend for these two different percentages obtained from absorption spectrum and lifetime data, at each ionic strength, two percentages do not fall on a same curve. The reason is that the

fluorescence decay was excited at one specific excitation wavelength (326 nm), at which two species have different absorbance, but the absorption spectrum includes concentration of the whole wavelength region. From the simulated absorption spectra for two species at 326 nm wavelength, the absorbance ratio of **PP1** in TBAF to free **PP1** is 1.3. Accounting for this absorbance difference, the concentration ratio can be corrected; the open squares fall on a similar curve as the percentage obtained from the lifetime data, see Figure 7.14. Therefore, the increasing amplitude of the long lived component from the fluorescence lifetime fits corresponds to the increasing concentration of the new species from the absorption spectrum fits.

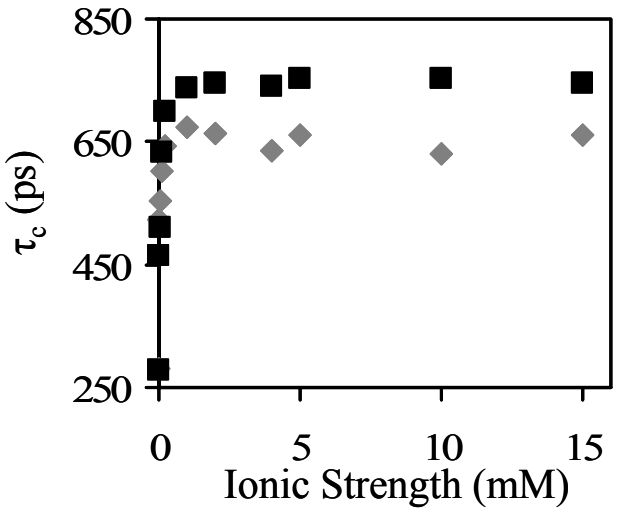

Figure 7.15 The average lifetime τ_c of **PP1** as a function of TBAF ionic strengths. The fluorescence decay was excited at 326 nm and the emission was collected at 420 nm (diamond) and 500 nm (square).

The correlation time τ_c is plotted versus the ionic strength in Figure 7.15. The correlation time of **PP1** collected at longer wavelength (500 nm) is slower than that at a shorter wavelength (420 nm) in each ionic strength solution. Assuming that the less conjugated conformation

contributes more to the emission at blue wavelengths and the more conjugated conformation contributes more at red wavelengths, these data indicate that the more conjugated form ('red') has a long lifetime and the flexibility of the chain (internal conversion rate) decreases with increasing ionic strength. However, comparing with the plot of F/F_0 versus ionic strength in Figure 7.9, the fluorescence intensity slightly decreases at high ionic strength, unlike the behavior of the correlation time which keeps flat at high ionic strength, see Figure 7.15.

Like the fluorescence decay of **PP1** in TBAF, the correlation time in LiCl behaves with a similar trend, that is, a longer lifetime collected at the wavelength of 500 nm corresponds to a shorter lifetime at a shorter wavelength 420 nm. As a whole, the correlation time becomes longer as the ionic strength increases.

7.5 Discussion

The current work explores how the absorption and fluorescence properties of **PP1** change with ionic strength. Varying the charge and the size of ions (singly charged inorganic ions, organic ions and doubly charged inorganic ions), different spectroscopic behaviors were observed and studied.

The absorption spectrum of **PP1** shows an isosbestic point in all of these salt solutions and the isosbestic point red-shifts with increase in the size and charge of the counterions. It indicates that with adding salt, a new species is forming by the equilibrium reaction. For the fluorescence spectrum, the intensity increases at low ionic strength and reaches a maximum, then decreases upon further increasing ionic strength. These changes follow the order of the size to charge ratio. The increase of the fluorescence intensity confirms that the new species has a high quantum yield, probably from forming a more conjugated polymer chain. The fluorescence

lifetime data shows a growing percentage of a long-lived species with increasing ionic strength and this behavior demonstrates that **PP1**'s chain becomes more rigid and conjugated.

A two states model is applied to simulate the absorption spectrum in the current study. This model uses the idea of the equilibrium existing between one state, the free **PP1**, and another state, the complexed **PP1**. The theoretical fit gives a value of the stability constant, K and hence a $\Delta_r G$ to form a new complex when adding the salt into the polyion solution. For the different cations, $\Delta_r G$ varies from 15 kJ/mol to 18 kJ/mol for singly charged small ions, an averaged value around 25 kJ/mol for the doubly charged ions, a value close to 23 kJ/mol for the biggest TBAF. This variation confirms that the charge density and size of cation are key factors to describing the interaction with polyion. Higher charge density interacts strongly with polyion, as well as a bigger size of cation. The two state model oversimplifies the actual case, i.e., a large number of conformations and species exist at every ionic strength. Nevertheless, it appears that the system can be divided into two subpopulations based on their fluorescence lifetimes and absorption spectra which do not change with ionic strength; only their percentages vary with adding salt.

Using molecular dynamics simulation, Stevens demonstrated that the end-to-end distance of a polyelectrolyte in dilute salt solution, in which ln $\kappa\sigma$ varies from -4 to 2, depends on the product of the Debye screening length κ and the ion radius σ; $\kappa\sigma$. This finding suggests that the conformation changes of the **PP1** polyelectrolyte should correlate with the parameter $\kappa\sigma$. If the spectroscopic data also correlate with $\kappa\sigma$, then it supports the interpretation that the spectroscopic changes result from conformational changes.

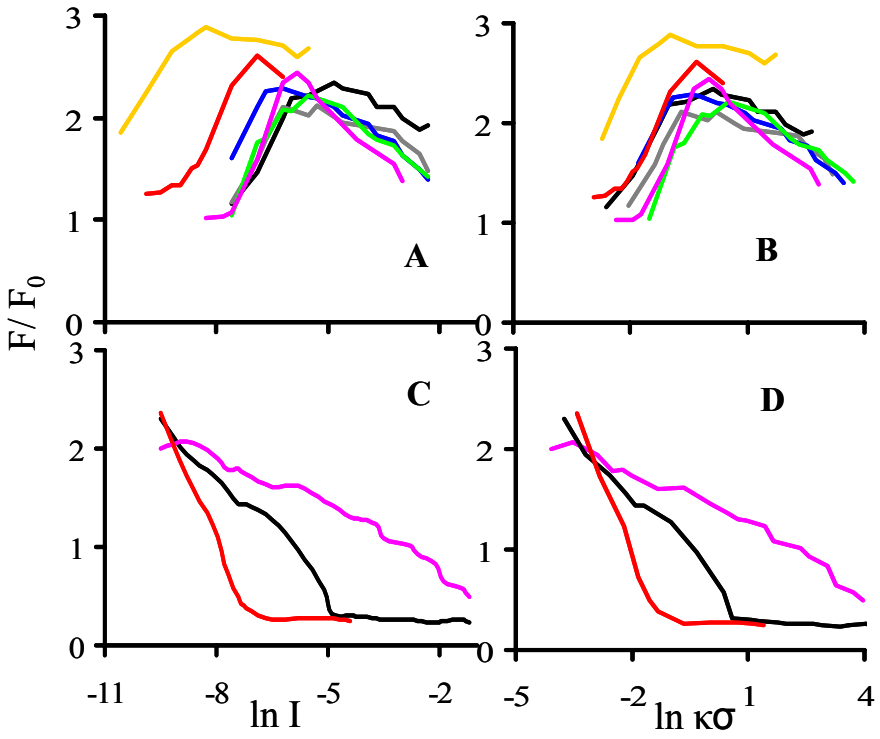

Figure 7.16 The fluorescence intensity ratio of **PP1** in (A) and (B) monovalent salt solutions including Li^+ (black), Na^+ (gray), K^+ (blue), Cs^+ (green) and ammonium solutions including AF (pink), TEAF (red) and TBAF (orange); and in (C) and (D) divalent salt solutions including Mg^{2+} (pink), Ca^{2+} (black), Ba^{2+} (red). (A) and (C) are the plots of ln (ionic strength) versus F/F_0; (B) and (D) are the plots of ln (κσ) versus F/F_0. σ accounts for the diameter of the cation, Li^+ 1.18 Å, Na^+ 2.04 Å, K^+ 2.66 Å, Cs^+ 3.48 Å, NH_4^+ 2.86 Å, TEA^+ 6.07 Å, TBA^+ 11.65 Å, Mg^{2+} 1.44 Å, Ca^{2+} 2.00 Å, and Ba^{2+} 2.84 Å, respectively. Diameters of organic salts were optimized using CAChe (PM3 in water).

Figure 7.16 shows the fluorescence ratio of **PP1** in different electrolytes as a function of ln (κσ) (shown in Figure 7.16B and D) and ln (ionic strength) (shown in Figure 7.16A and C). The fluorescence of **PP1** in monovalent salts (both organic and inorganic) behaves similarly upon increasing the charge density. At small κ (low charge density) or low ionic strength, the fluorescence is enhanced (a regime in which the chain length extends); further increase of κ

(increase ionic strength) causes the fluorescence to approach a maximum. At high κ (high ionic strength) the electrostatic interactions are screened and the chain length decreases, corresponding to the decrease of the fluorescence intensity. Stevens shows that the ionic density increases significantly near the polyelectrolyte chains with increasing ionic strength. This result corresponds similarly to what is observed in Figure 7.16.

In comparison with individual monovalent cation, the plot of ionic strength shows different curves for TBAF and TEAF to the other small cations, but the plot of ln κσ adjusts the size difference of these cations, shown a single curve for all of small cations in Figure 7.16B. The distance of a counterion from a polyion chain depends on the size and the magnitude of the counterions charge. Particularly, TBAF has the biggest size, hence it is far from the chain in comparison with the inorganic ions. The fluorescence intensity in TBAF changes much stronger than that in other salts, however. It suggests that the Coulomb interaction is not the only effect on changing the spectroscopic behavior of **PP1**. Instead, TBAF can 'trap' more binding sites which can produce another possibility to interact strongly with polyions.

Figure 7.16B and D show the fluorescence trends of **PP1** in divalent counterions. As well as the monovalent counterions, small κ (low ionic strength) enhances the fluorescence of **PP1**. But the fluorescence is found to increase dramatically and then decrease rapidly. These observations are consistent with modeling studies that show strong ionic interactions to polyion at low charge density, then charge screening at high ionic strength. The data do not rescale and lie on a single curve as seen in singly charged ions, rather they show a consistent trend which is proportional to the size of the cations. Mg^{2+} has the smallest size and provides the least electrostatic screening interactions and Ba^{2+} has the largest size with the strongest interactions.

7.6 Conclusion

The current work studies the fluorescence and absorption characteristics of the polyelectrolyte − **PP1** as a function of ionic strength. The ionic solutions differ by the charge and the size of the cation. In general, the fluorescence intensity of **PP1** is enhanced by adding a small amount of electrolyte to the solution until the fluorescence approaches a maximum. At large ionic strength the fluorescence yield decreases, presumably because of a strong electrostatic screening effect from extra ionic species. The absorption spectrum reveals an isosbestic point for different electrolytes and the wavelength of the isosbestic point is associated with the strength of the ionic effect on the change of the chain conformation.

The time-resolved fluorescence studies show that the lifetime of **PP1** also varies with ionic strength. The fluorescence decay law is well described by a double exponential function and the shorter lifetime dominates under salt free conditions. With increasing ionic strength, the longer lifetime component becomes dominant and it also causes the correlation time τ_c to increase with ionic strength. The change of τ_c is fast at low ionic strength and saturates at high ionic strength. The fluorescence lifetime at different emission wavelengths reveals that a red component has a longer correlation time. The fluorescence lifetime of **PP1** in inorganic electrolyte solution also gives the similar behavior as that of the organic electrolyte, that is, the correlation time increases with ionic strength.

The spectroscopic behavior of **PP1** with salt concentration is interpreted to result from changes in the chain rigidity, which is expected to be influenced strongly by the properties and composition of the salt. At the same ionic strength, the ionic effect of the monovalent cations is much gentler than the divalent cations because of the lower charge density. Monocations of different ion size interact with the chain differently. For example, for singly charged inorganic

ions, the smaller sized Li^+ ions can be closer to the polyion chain and cause a stronger Coulomb attraction, in comparison with other inorganic ions. However, the biggest size of TBAF shows the highest fluorescence which might arise from the interaction with multiple chain sites. For doubly charged inorganic ions, the high charge density interacts strongly enough that the fluorescence intensity of **PP1** increases very fast at low ionic strength.

The fluorescence yield was compared to a product of the inverse Debye length and the ionic radius σ. The comparison shows a consistent trend that fluorescence increases at small values of κσ and reaches a maximum, then decreases at high values of κσ. For the singly charged cations, the fluorescence ratios lie on the same curve. The cation TBAF deviates somewhat from the curve and this may result from its unusually large size. Doubly charged counterions have much bigger charge to size ratio and quench the fluorescence more strongly. This screening effect is size dependent, for example, Mg^{2+} with the smallest size screens the fluorescence at a low extent than the biggest Ba^{2+} does.

Changes in the spectroscopic behavior of fluorescent polyelectrolytes with increasing solution ionic strength can be understood to arise from changes in the rigidity of the polyions. This work indicates that the chain rigidity and extent of **PP1** increases at low ionic strength, saturates, and then decreases at high ionic strength. This work would benefit from a molecular dynamics simulation to mimic the experimental conditions and confirm the conclusions.

7.7 Acknowledgements

We acknowledge support from the U.S. National Science Foundation (CHE-0415457).

7.8 References

1. Mandel, M. *"Polyelectrolytes"*, Ridel, D., Dordrecht, **1988**.

2. Hara, M. *"Polyelectrolytes: Science and Technology"*, Dekker, M., New York, **1993**.

3. Föster, S.; Schmidt, M. *Adv. Polym. Sci.*, **1995**, *120*, 51.

4. Stevens, M.; Kremer, K. *J. Chem. Phys.*, **1995**, *103*, 1669.

5. Barrat, J.-L.; Joanny, J.-F. *Adv. Chem. Phys.* **1996**, *94*, 1.

6. Reed, W. F. *J. Chem. Phys.*, **1994**, *101*, 2515.

7. Reed, W. F. *"Macroion Characterization"*, ACS Symp. Ser., **1994**, *548*, 297.

8. Wang, D.; Lal, J.; Moses, D.; Bazan, G. C.; Heeger, A. J. *Chem. Phys. Lett.*, **2001**, *348*, 411.

9. deGennes, P.G. *"Scaling Concepts in Polymer Physics"*, **1985**, 2nd edn., Cornell University Press, Ithaca.

10. Stevens, M. and Kremer, K. *J. Chem. Phys.*, **1995**, *103*, 1669.

11. a) Stevens, M. and Kremer, K. *Macromol.*, **1993**, *26*, 4717; b) Stevens, M. and Kremer, K. *Phys. Rev. Lett.*, 1993, 71, 2228.

12. Debye, P. and Hückel, E. *Phys. Z.*, **1923**, *24*, 185.

13. Holm, C.; Joanny, J. F.; Kremer, K.; Netz, R. R.; Reineker, P.; Seidel, C.; Vilgis, T. A.; Windler, R. G. *Adv. Polym. Sci.*, **2004**, *166*, 67.

14. Stevens, M. J. and Plimpton, S. J. *Eur. Phys. J. B*, **1998**, *2*, 341.

15. Deserno, M. and Holm, C. *Macromol.*, **2000**, *33*, 199.

16. Deserno, M. and Holm, C. *Molecular Physics*, **2002**, *100*, 2941.

17. Deserno, M.; Arnold, A.; Holm, C. *Macromol.*, **2003**, *36*, 249.

18. Vlachy, V. Annu. *Rev. Phys. Chem.*, **1990**, *50*, 145.

19. Wall, F. T. and Berkowitz, J. *J. Chem. Phys.*, **1956**, *26*, 114.

20. Linse, P.; Gunnarson, G.; Jönsson, B. *J. Phys. Chem.*, **1982**, *86*,413.

21. Wennerström, H.; Jönsson, B.; Linse, P. *J. Chem. Phys.*, **1982**, *76*, 4665.

22. Verwey, E. J. W.; Overbeek, J. T. G.; *"The Theory of the Stability of Lyophobic Colloids"*, **1965**, New York: Elsevier.

23. Belloni, L. *J. Chem. Phys.*, **1986**, *85*, 519.

24. Vlachy, Y. and Prausnitz, J. M. *J. Phys. Chem.*, **1992**, *96*, 6465.

25. Blum, L. *Mol. Phys.*, **1975**, *30*, 1529.

26. Sheu, E.; Wu, C. F.; Chen, S. H.; Blum, L. *Phys. Rev. A*, **1985**, *32*, 493

27. Belloni, L. *Chem. Phys.*, **1985**, *99*, 43.

28. Linse, P. *J. Chem. Phys.*, **1991**, *94*, 3817.

29. Friedman, H. L. *"A Course in Statistical Mechanics"*, **1985**, Englewood Cliffs, NJ: Prentice-Hall

30. Valchy, V.; Marshall, C. H.; Haymet, A. D. *J. J. Am. Chem. Soc.*, **1989**, *111*, 4160.

31. Kim, S.; Jackiw, J.; Robinson, E.; Schanze, K. S.; Reynolds, J. R.; Baur, J.; Rubner, M. F. ; Boils, D. *Macromolecules*, **1998**, *31*, 964.

32. GPC studies were performed by Polymer Source Inc., Quebec CANADA.

33. Liu, M.; Kaur, P.; Waldeck, D. H.; Xue, C.; Liu, H. *Langumuir*, **2005**, *21*, 1687.

34. Liu, M.; Waldeck, D. H.; Oliver, A. M.; Head, N. J. and Paddon-Row, M. N. *J. Am. Chem. Soc.*, **2004**, *126*, 10778.

35. NIST Chemistry WebBook, www.nist.gov/chemistry.

36. A) Platt, J. R., et al, "*Systematics of the Electronic Spectra of Conjugated Molecules: A Source Book*", **1964**, John Wiley and Sons, New York; B) Platt, J. R., et al, "*Free-electron Theory of Conjugated Molecules: A Source Book*", **1964**, John Wiley and Sons, New York.

Chapter 8 Conclusion

Electron transfer reactions are the fundamental and ubiquitous chemical processes. Nonadiabatic electron transfer in donor-bridge-acceptor (DBA) molecules can be viewed as electron tunneling through a barrier that is determined by the orbitals of the atoms along a path between the donor (*D*) and acceptor (*A*) groups. The U-shaped DBA systems under investigation provide unique insight into the nature of nonadiabatic electron transfer processes, which involves electron tunneling through noncovalent contacts. The tunneling efficiency during this process is quantified by the electronic coupling matrix element, $|V|$, which characterizes the electronic interaction between an electron donor and acceptor.

The studies of the electron transfer reaction of the U-shaped molecules in chapters 2 and 3 is focused on understanding the mechanism switch from nonadiabatic electron transfer reaction to a solvent controlled electron transfer reaction. Specifically, in solvents with rapid dielectric response, such as acetonitrile which has a low viscosity and fast relaxation time, the electron transfer mechanism is nonadiabatic. In solvents with a 'slow' dielectric response, such as N-methylacetamide and N-methylpropionamide which have high viscosities and slow relaxation times, the electron transfer mechanism changes and is controlled by the solvent's relaxation, called the 'solvent friction' limit. A detailed investigation on electron transfer as a function of solvent and temperature were used to understand how the electron transfer mechanism switches. This finding is the first experimental example to require that both electron displacement and atom displacements be treated equally in electron transfer reactions, which goes against the commonly-held assumption that the reaction rate is controlled by either the electron's movement or atom's movement.

Two types of motions may be important for the switch in electron transfer mechanism: one is rearrangement of solvent molecules during the reaction and another is motion of the pendant group, that is, conformational gating. To distinguish the importance of the solvation motion, the dynamic Stoke-Shift in these slow solvents were measured to obtain the solvation time. If the electron transfer is limited by the solvent friction, the electron transfer rate should correlate with the solvation time; but if it proceeds by electron tunneling, it will not. As a fact, the low temperature rate constants correlate with the solvation rate, $1/\tau_s$, as determined through dynamic Stokes-Shift measurements. At high temperature the rate constant is independent of $\tau_{s.}$. A comparison of Zusman prediction provides good agreement of the effective electronic coupling with that found for nonadiabatic electron transfer, using the semi-classical equation. The adiabaticity parameter g, which can be defined from Zusman's criterion, predicts that the solvent friction limit applies in these slow relaxation solvents. The characteristics of electron transfer at low temperature also matches with Sumi and Marcus prediction and the electron transfer appears to lie in the narrow reaction window limit of the Sumi-Marcus treatment because of the ratio of $\lambda_v/\lambda_0 \sim 0.5$ and the nonexponentiality of the locally excited state's population decay.

Chapter 4 describes a study of three new U-shaped molecule systems with the same electron donor and electron acceptor, but different pendant moiety. These new systems investigate whether rotation of the pendant group changes the electronic coupling and effects the reaction. The results show that placement of the aromatic moiety in the cleft gives electronic couplings that do not vary significantly with alkylation. The small variation of the electronic coupling with the amount of alkyl substitution and the related geometric changes of the pendant group in the cleft suggest that modulation of the electron tunneling probability by changes in the

phenyl ring geometry is not the cause of the change of the electron transfer mechanism from nonadiabatic to solvent controlled reaction.

Chapters 6 and 7 demonstrate that the fluorescence emission of a conjugated polyelectrolyte is highly sensitive to the binding of protein and dendrimers. A detailed study of how the polyelectrolyte's fluorescence intensity changes as a function of analyte concentrations explores that the quenching mechanism is mainly due to the conformation changes of the polyelectrolyte. A comparison of the different analytes confirms that the quenching mechanism is controlled by the electrostatic interactions between the macromolecular analytes and the polyelectrolytes. The ionic strength studies indicate that the conformation of polyelectrolyte varies with the environment and this variation causes an increase of the fluorescence intensity with increasing ionic strength and the extent of the enhancement correlates with the sizes and charges of the ions.

In summary, this thesis consists of studies into photoinduced electron transfer systems and the result demonstrates how the pendant moiety efficiently mediates the electronic coupling. By varying the solvent systems from 'fast' response solvents to 'slow' response solvents, a switch of the electron transfer mechanism is observed. The fluorescence quenching mechanism of polyelectrolyte with different analytes has been investigated and internal conversion rather than electron transfer, dominates the quenching of the polyelectrolyte. The sensitivity of the quenching is dependent on the size and the charge of the analytes.

Appendix

A. Cryostat vacuum system operation

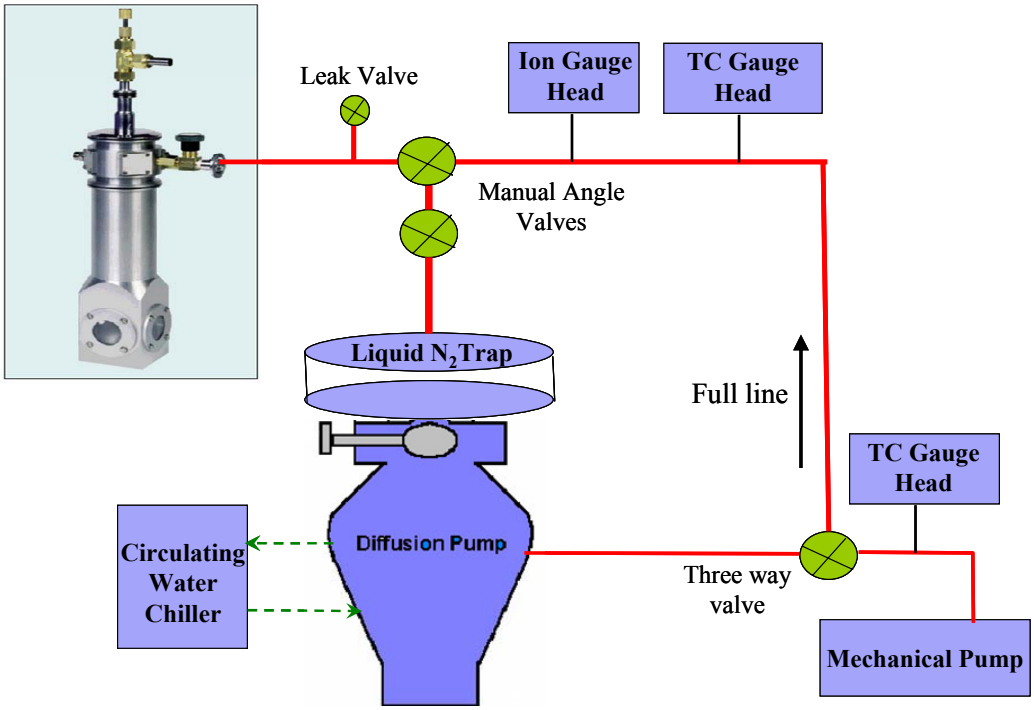

Cryostat vacuum system contains several major components: a cryostat, a mechanical pump, a diffusion pump, a water chiller, two manual valves, a three-way valve, a leak valve, two TC gauges and one ion gauge. The function of the mechanical pump is to pump down the full line as well as to facilitate the diffusion pump. Normally, the vacuum can reach less than 100 mTorr when only the mechanical pump is running. The diffusion pump can provide much higher vacuum and for this system, the normal vacuum can remain around 2×10^{-6} Torr with liquid nitrogen in the trap.

The procedure to operate this system is as following:

1. Turn on the mechanical pump.

2. Turn the three-way valve to the full line and pump down the full line until vacuum is below 100 mTorr (check TC gauge). Make sure the manual valve in the full line and the valve on the cryostat are both opened.
3. Switch the three-way valve toward the diffusion pump and wait until the vacuum is less than 50 mTorr (check TC gauge).
4. Turn on the water chiller and the diffusion pump and wait for about half hour to one hour to warm the diffusion pump up. Make sure the manual valve on the top of the diffusion top is closed.
5. Recheck the vacuum of the full line to make sure the vacuum is below 100 mTorr. Otherwise, switch the three-way valve to the full line and pump it down to 100 mTorr again.
6. Before opening the manual valve, double check the three-way valve and verify that it is toward the diffusion pump.
7. Open the manual valve on the top of the diffusion pump slowly and watch the vacuum reading on the TC gauge controller. When the reading is below zero, turn on the ion gauge.
8. Pump the system with the diffusion pump for a couple of hours and watch the reading of the vacuum until it is stable.
9. Fill the liquid nitrogen trap on the top of the diffusion pump.
10. Fill the cryostat with liquid nitrogen and change the temperature to an appropriate temperature.
11. The three-way valve is always toward the diffusion pump during the experiment.

12. Before turning off the system, make sure that all the liquid nitrogen has gone (suggest leaving the system overnight).
13. Turn off the ion gauge and close the manual valve on the top of the diffusion pump.
14. Turn off the diffusion pump and cool it down.
15. Turn off the water chiller.
16. Turn off the mechanical pump.

B. Solvent purification

The solvent N-methylacetamide (NMA) was purchased from Aldrich, and N-methylpropionamide (NMP) was purchased from TCI America. NMA and NMP were fractionally distilled three times using a vigreux column under vacuum. In the distillation process, several points need to be emphasized.

1. Distill high boiling point solvents NMA and NMP under the vacuum.
2. Increase the temperature of the silicon oil very slowly and keep the oil temperature less than 130 ºC all the time.
3. Collect the first distillate in one flask until the distilling temperature is stable.
4. Switch to another flask after the temperature has been stable for couple of minutes.
5. The temperature might increase after sometime because of the pump's fluctuation. If the temperature increases 5 ºC higher, switch to another flask.
6. Don't collect all of the distillate (leave couple of milliliter liquid in the original flask) and turn off the heating.
7. After the temperature of the glassware is cooled down, turn off the vacuum and vent the system.
8. For distilling NMA and NMP, it is necessary to repeat the distillation multiple times until the fluorescence is cut down to the least. (compare the fluorescence spectrum of different distillate to decide whether it is necessary to repeat the distillation, but two times of distillation is strongly recommended)